CANADIAN THESES ON MICROFICHE

I.S.B.N.

THESES CANADIENNES SUR MICROFICHE

National Library of Canada
Collections Development Branch

Canadian Theses on
Microfiche Service

Ottawa, Canada,
K1A 0N4

Bibliothèque nationale du Canada
Direction du développement des collections

Service des thèses canadiennes
sur microfiche

NOTICE

The quality of this microfiche is heavily dependent upon the quality of the original thesis submitted for microfilming. Every effort has been made to ensure the highest quality of reproduction possible.

If pages are missing, contact the university which granted the degree.

Some pages may have indistinct print especially if the original pages were typed with a poor typewriter ribbon or if the university sent us a poor photocopy.

Previously copyrighted materials (journal articles, published tests, etc.) are not filmed.

Reproduction in full or in part of this film is governed by the Canadian Copyright Act, R.S.C. 1970, c. C-30. Please read the authorization forms which accompany this thesis.

THIS DISSERTATION
HAS BEEN MICROFILMED
EXACTLY AS RECEIVED

AVIS

La qualité de cette microfiche dépend grandement de la qualité de la thèse soumise au microfilmage. Nous avons tout fait pour assurer une qualité supérieure de reproduction.

S'il manque des pages, veuillez communiquer avec l'université qui a conféré le grade.

La qualité d'impression de certaines pages peut laisser à désirer, surtout si les pages originales ont été dactylographiées à l'aide d'un ruban usé ou si l'université nous a fait parvenir une photocopie de mauvaise qualité.

Les documents qui font déjà l'objet d'un droit d'auteur (articles de revue, examens publiés, etc.) ne sont pas microfilmés.

La reproduction, même partielle, de ce microfilm est soumise à la Loi canadienne sur le droit d'auteur, SRC 1970, c. C-30. Veuillez prendre connaissance des formules d'autorisation qui accompagnent cette thèse.

LA THÈSE A ÉTÉ
MICROFILMÉE TELLE QUE
NOUS L'AVONS REÇUE

NL-339 (r. 82/08)

Canada

A CLASS OF POWER AND BANDWIDTH EFFICIENT TRANSMISSION TECHNIQUES FOR DIGITAL RADIO COMMUNICATIONS SYSTEMS

by

THO LE-NGOC

A Thesis
Submitted to the School of Graduate Studies
University of Ottawa
in Partial Fulfillment of the Requirements
for the Degree of Doctor of Philosophy

Department of Electrical Engineering
University of Ottawa
Ottawa, Canada
February 1983

UNIVERSITÉ D'OTTAWA
UNIVERSITY OF OTTAWA

DEDICATED TO MY PARENTS

ABSTRACT

A new class of power and bandwidth efficient transmission techniques for digital radio communications systems is presented.

At first, a new class of Intersymbol-Interference and Jitter-Free (IJF) baseband signals having fast spectral roll-off and low-out-of-band energy emission is introduced. The generation and detection of IJF baseband signals are discussed. Their spectral properties and error probability performance are analytically and experimentally investigated.

These IJF baseband signals are then combined with quadrature-amplitude modulation schemes. The resulting modulation techniques are called IJF-Quadrature-Phase-Shift-Keying (IJF-QPSK) and IJF-Offset QPSK. The power spectral density function of *hardlimited* IJF-QPSK and IJF-Offset QPSK signals is derived. Spectral properties and error probability performance of IJF-QPSK and IJF-Offset QPSK schemes in other nonlinear channels with adjacent-channel and co-channel interference are studied using computer simulation and experimental methods.

The carrier recovery (CR) and symbol timing recovery (STR) aspects and implementation feasibility of IJF-QPSK and IJF-Offset QPSK modems are also investigated.

Experimental, simulation and theoretical results are in agreement. The results indicate that the IJF-Offset QPSK modulation technique provide less spectrum spreading and better performance than QPSK, Offset QPSK and MSK in narrow-band nonlinear channels. Potential applications of IJF-Offset QPSK schemes in digital radio communications systems are discussed.

RESUME

Une nouvelle classe de techniques de transmission s'appliquant aux communications numériques par système hertzien est présentée. Ces techniques se caractérisent par une bonne efficacité spectrale ainsi que de bonnes performance en terme de probabilité d'erreur.

Tout d'abord, une nouvelle classe de signaux en bande de base caractérisée par l'absence d'interférence entre symboles et de gigue (en anglais appelés "Intersymbol-Interference and Jitter-Free (IJF)") est introduite. Du point de vue spectral, ces signaux présentent une forte décroissance asymptotique ainsi qu'une faible énergie rayonnée en dehors de la bande utile. La génération et la détection de ces signaux sont étudiées. Leur propri étés spectrales et performances en terme de probabilité d'erreur sont obtenues à la fois analytiquement et expérimentalement.

Ensuite, ces signaux en bande de base servent à définir de nouvelles techniques de modulation avec deux porteuses en quadrature appelées IJF-Quadrature Phase Shift Keying (IJF-QPSK) et IJF-Offset QPSK.

L'expression analytique de la densité spectrale de puissance des signaux IJF-QPSK et IJF-Offset QPSK est obtenue après passage de ceux-ci dans un limiteur dur. Les propriétés spectrales et performances en terme de probabilité d'erreur sont étudiées expérimentalement et par simulation sur ordinateur, pour d'autres types de canaux non-linéaires sujets aux interférences des canaux adjacents ou en polarisation croisée.

Les récupérations de porteuse et de fréquence rythme sont également examinées, ainsi que la faisabilité des modems IJF-QPSK et IJF-Offset-QPSK.

Les résultats théoriques, expérimentaux et de simulation sont en bon accord. Ces résultats montrent que la modulation TJF-Offset QPSK donne lieu à un étalement de spectre plus faible et à de meilleures performances que les modulations QPSK, Offset-QPSK et MSK pour des canaux non-linéaires à bande étroite. Les applications potentielles aux communications numériques par système hertzien sont finalement discutées.

ACKNOWLEDGEMENTS

I wish to express my sincere gratitude to my thesis supervisor, Dr. Kamilo Feher for his guidance throughout this research, and for his advice and constructive criticism during the preparation of this thesis.

I also wish to thank Mr. Patrick Vandamme for his helpful discussions, Mr. Hiep Pham Van for his assistance in obtaining some laboratory measurements, and Mrs. Marie Berryman for typing this thesis.

Finally, I wish to express my deep appreciation to my wife for her constant encouragement during the course of this study.

TABLE OF CONTENTS

LIST OF FIGURES

LIST OF TABLES

CHAPTER ONE: INTRODUCTION

The need for power and bandwidth efficient modulation schemes has led to the extensive use of phase-shift keying (PSK) in digital transmission systems. Since power spectra of PSK signals exhibit sidelobes that may interfere with adjacent channels, a certain amount of filtering is necessary at the transmitter. However, this filtering may result in a great amount of envelope fluctuation in the signal, which leads to a considerable out-of-band spectral regeneration due to the AM/AM and AM/PM nonlinear effects of the transmit high power amplifiers (HPA).

As a precaution against spectral regeneration, the transmit HPA may have to operate below saturation in an approximately linear region. This incurs the penalty that an HPA designed for greater power output would have to be used, with the consequent technological and economic problems. Post-HPA filtering, to control spectral regrowth, may be impractical at high radio frequency-to-bit rate ratios due to the high selectivity requirements (e.g. 6 GHz to 64 kb/s). It also may not be used when there is a frequency agility requirement, which is of particular interest in a number of applications. One of the solutions to this problem is the use of combined pulse shaping/modulation schemes to provide transmitted RF signals having low spectral regrowth in nonlinear

channels.

In this thesis we introduce and investigage a new class of power and bandwidth efficient transmission techniques for digital radio communications systems.

1.1 THESIS OUTLINE

Following this introductory chapter, in Chapter 2, a literature survey of digital quadrature phase modulation techniques is presented in historical progression from the widely known Quadrature-Phase-Shift-Keying (QPSK), Offset-QPSK (OQPSK), and Minimum-Shift Keying (MSK), to recently developed digital modulation schemes. This survey shows that new discoveries using combined pulse shaping/modulation techniques could lead to improvements in power and bandwidth efficiencies of communications systems.

In Chapter 3, we introduce a new class of Intersymbol-Interference and Jitter Free (IJF) baseband signals having fast spectral roll-off and low out-of-band energy emission. Its spectral properties and error probability (P_e) performance in an additive white gaussian noise (AWGN) environment are analytically examined.

This new class of power and bandwidth efficient IJF baseband signals is combined with quadrature phase modulation schemes. The resulting modulation techniques are called IJF-QPSK and IJF-Offset QPSK.

The spectral properties of IJF-QPSK and IJF-Offset QPSK signals in linear and nonlinear channels are studied in Chapter 4. We derive the power spectral density (PSD) function of *hardlimited* IJF-QPSK and IJF-Offset QPSK signals using a 16-state Markov chain model. The effects of the time offset between inphase and quadrature baseband components on the spectral regrowth are presented. Spectral properties of IJF-QPSK and IJF-Offset QPSK signals in other nonlinear channels are also investigated and compared to those of QPSK, OQPSK and MSK signals.

Chapter 5 presents the studies of P_e performance of IJF-QPSK and IJF-Offset QPSK modems (modulator/demodulator) in linear and nonlinear channels. Effects of co-channel and adjacent-channel interference on the P_e performance of IJF-QPSK and IJF-Offset QPSK modems are investigated. The performance of these modems in illustrative Single-Channel-Per-Carrier (SCPC), Time-Division-Multiple-Access (TDMA) and On-Board regenerative systems is evaluated and compared to that of QPSK, Offset-QPSK and MSK modems.

Synchronization aspects of IJF-QPSK and IJF-OQPSK demodulators are presented in Chapter 6. Pattern-noise in carrier and symbol timing recovery loops is analytically studied. Effects of static phase and timing error in recovered carrier and symbol timing signals are also investigated.

In Chapter 7, some modified schemes are introduced to further improve the spectral properties of IJF-quadrature modulated signals. Spectral properties and P_e performance of these modified scheme are presented.

Chapter 8 contains final conclusions and suggestions for future research.

Appendix includes the listings and descriptions of simulation routines.

1.2 RESEARCH CONTRIBUTIONS

The major contributions of our research include the introduction of a new class of power and bandwidth efficient transmission techniques for digital radio communications systems. Some specific contributions are summarized below:

* Introduction of a new class of Intersymbol-Interference and Jitter Free (IJF) baseband signals which have low out-of-band energy and fast spectral roll-off.

* Investigation of the error probability performance of IJF baseband signals in an AWGN environment with transversal, decision-feedback and raised-cosine-type receivers.

* Introduction of new non-constant-envelope quadrature modulation schemes, named IJF-QPSK and IJF-Offset QPSK,

which use these IJF baseband signals.

* Investigation of the spectral properties of IJF-QPSK and IJF-OQPSK signals in hardlimited and other nonlinear channels.

* Investigation of the error probability performance of IJF-QPSK and IJF-Offset QPSK modems in a complex interference environment.

* Investigation of the carrier and symbol timing recovery aspects of IJF-QPSK and IJF-Offset QPSK demodulators, and introduction of a fast symbol timing recovery (STR) scheme.

* Investigation of the implementation feasibility, and potential applications of IJF-QPSK and IJF-Offset QPSK modems in digital radio communications systems.

CHAPTER TWO:

A LITERATURE REVIEW OF DIGITAL QUADRATURE PHASE MODULATION TECHNIQUES

SUMMARY:

The aim of this chapter is to review major contributions that have been published in the field of power and bandwidth efficient modulation techniques related to our research topic.

This literature review is presented in historical progression from the widely known QPSK, Offset-QPSK and MSK modulation schemes, to the recently developed digital modulation schemes. This historical review gives us some insight into understanding the evolution of power and bandwidth efficient modulation schemes applied to nonlinear channels, and, furthermore, the motivation, results, inadequacies, and incompleteness of the earlier work. With this overview, we are able to justify the needs and objectives of our investigation of a new class of power and bandwidth efficient transmission techniques for digital radio communications systems.

2.1 QPSK, OFFSET-QPSK, AND MSK MODULATION SCHEMES

Quatrature-Phase-Shift-Keying (QPSK), Offset-QPSK, and Minimum-Shift-Keying (MSK) modulation techniques are among the most widely used techniques in digital radio communications systems, and particularly in digital satellite systems.

The spectral properties and error probability performance of these modulation schemes, in both linear and nonlinear channels, have been investigated in considerable depth by many authors [1-23]. The most important properties of these modulation schemes are summarized in the following paragraphs, with the emphasis on parameters which yield the difference in spectral spreading caused by nonlinear amplification of the QPSK, OQPSK and MSK signals. With the comprehension of the effects of these parameters on the spectral spreading, we are able to understand the motivation in searching for other power and bandwidth efficient modulation techniques, as applied to nonlinear channels.

QPSK is frequently used because of its bandwidth efficiency, low E_b/N_o requirement for good error probability performance, and relatively simple hardware design. Since the power spectrum of a QPSK signal exhibits sidelobes that may interfere with adjacent channels, a certain amount of filtering is necessary at the transmitter. However, this filtering leads to a great amount of signal envelope fluctuation and hence a considerable spectral

spreading due to the AM/AM and AM/PM nonlinear effects of the transmit high-power amplifier (HPA).

Offset-QPSK (OQPSK), also known as Staggered-QPSK (SQPSK), was shown to retain relatively low spectral sidelobes after undergoing nonlinear amplification [2]. The main difference between conventional and offset-QPSK schemes is in the alignment of the in-phase and quadrature baseband components of the modulated signals. This difference in time alignment in the baseband components does not change the power spectral density of the modulated signal and hence in linear channel both QPSK and OQPSK spectra have the same shape. However, the two modulated signals respond differently when they undergo bandlimiting and then nonlinear amplification. Because of the coincident alignment of the two baseband components in QPSK modulation, an instantaneous phase transition of 180° can take place, hence the bandlimited QPSK signal exhibits 100% envelope fluctuation. In Offset-QPSK, the two baseband signals cannot change their states simultaneously. One of the baseband signals has data transitions in the middle of the symbol interval of the other baseband signal, eliminating the possibility of instantaneous phase transitions of 180°. Thus, the bandlimited Offset-QPSK signal has a much smaller envelope fluctuation than the QPSK signal. Consequently, the absence of fast phase transitions (180°) and hence of the high frequency content means that nonlinear amplification will not fully regenerate the high frequency components originally removed by the bandlimiting filter.

Spectral advantages possessed by Offset-OQPSK stem mainly from the fact that Offset-QPSK avoids the large phase transitions of 180° associated with the QPSK format. This suggests that further suppression of spectral spreading in bandlimited-nonlinear applications can be obtained, if the Offset-QPSK signal format can be modified to avoid step phase transitions altogether. This can be thought of as an obvious motivation for designing constant-envelope modulation schemes with continuous phase. Minimum-Shift-Keying (MSK) introduced by Doelz and Heald [4], is one such scheme.

Minimum-Shift-Keying (MSK) is considered as a form of Offset-QPSK in which the symbol pulse shape is a half-cycle sinusoid rather than the usual rectangular form [5]. It can also be viewed as a special case of continuous-phase-frequency-shift keying (CPFSK) [6,7] with the frequency deviation ratio equal to 0.5. In this view, it is also known as Fast-FSK (FFSK) because it can transmit faster pulse trains than any other ordinary FSK or binary PSK (BPSK) of equal bandwidth and signal-to-noise ratio [8]. Owing to its constant envelope and continuous phase nature an unfiltered MSK signal, when nonlinearly amplified, suffers no significant spectral spreading in the bandwidth of interest, and provides faster spectral roll-off and lower high-order spectral sidelobes than the filtered OQPSK signal. However, its spectral main-lobe is 50% wider than that of unfiltered QPSK, and Offset-QPSK signals [5]. Therefore,

it causes some difficulties to determine whether or not the MSK scheme provides better power and bandwidth efficiencies than the QPSK and Offset-QPSK schemes. Attempting to answer this question, many authors [3,5,10-23] have investigated the spectral spreading and error probability performance of QPSK, Offset-QPSK and MSK systems in various nonlinear channel models including adjacent-channel interference effects. Most of these investigations have been performed with the aid of computer simulations. The comparative results are usually expressed in terms of E_b/N_o requirements for given error probability performance and channel spacings. These results also depend on the parameters used in the simulation models, such as the transmit and receive channel filters, and nonlinear devices. In general, it has been demonstrated that MSK provides better performance for wide channel-spacings and worse performance for narrow channel-spacings, relative to QPSK and OQPSK.

So far it has been shown that the baseband pulse shape, phase transition and envelope fluctuation of a modulated signal are the most important parameters which affect the spectral properties of the modulated, filtered and amplified signals. For this reason, efforts have been expended to search for different pulse shapes, phase transition and envelope fluctuation characteristics which yield power and bandwidth efficient modulation techniques. Based on envelope fluctuation, these modulation techniques are classified in two categories: constant-envelope and non-constant-envelope modulation techniques.

2.2 CONSTANT-ENVELOPE MODULATION TECHNIQUES

In recent years, several authors have studied and introduced techniques to generate an entire class of constant-envelope MSK-type modulated carriers whose spectral properties are more desirable in some applications than those of MSK or Offset-QPSK. These studies are classified in two main categories: one considers MSK as a special case of Offset-QPSK, (section 2.2.1) and the other as a special form of Continuous Phase Frequency Shift Keying (CPFSK) (Section 2.2.2).

2.2.1 Constant Envelope Quadrature Amplitude Modulation Schemes

From the view of a special case of Offset-QPSK, the MSK-type modulated carrier can be decomposed into two antipodal pulse streams, modulating respectively the in-phase and quadrature carrier components as illustrated in Fig. 2.1. The modulated carrier is given by

$$y(t) = x_I(t)\cos\omega_c t + x_Q(t-T_s/2)\sin\omega_c t \qquad (2.1)$$

where

$$x_I(t) = \sum_{n=-\infty}^{+\infty} a_n p(t-nT_s)$$

$$x_Q(t) = \sum_{m=-\infty}^{+\infty} b_m p(t-mT_s)$$

S/P: *Serial-to-Parallel Converter*

T_b: *bit interval*, $T_b = T_s/2$

T_s: *symbol interval*

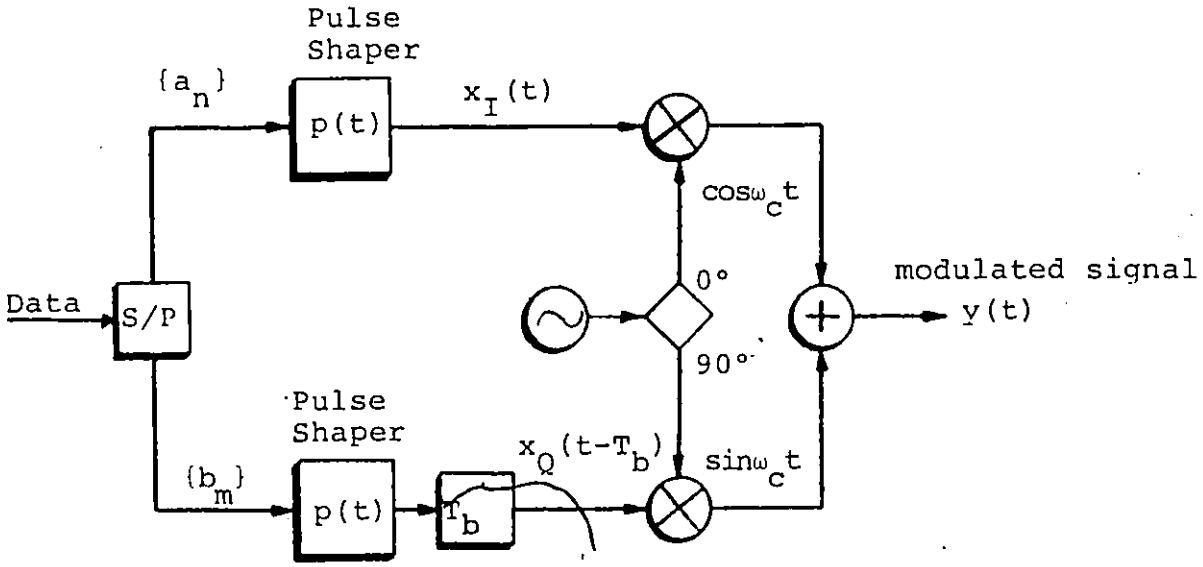

Fig. 2.1: BLOCK DIAGRAM OF A QUADRATURE AMPLITUDE MODULATOR

are the in-phase and quadrature pulse streams respectively,

$a_n, b_m = \pm 1$ with probability of 1/2

$p(t)$ is a single-interval pulse, i.e.

$p(t) = 0$ for $|t| > T_s/2$, and

T_s is the symbol interval

The constant-envelope property of the modulated carrier is retained if $p(t)$ satisfies the following constraints [28]

$$p(t) = p(-t) \tag{2.2a}$$

$$p^2(t) + p^2(T_s/2-t) = 1 \tag{2.2b}$$

for $0 \leq |t| \leq T_s/4$

For the well-known MSK modulated carrier, the pulse $p(t)$ is

$$p(t) = \begin{cases} \cos \frac{\pi t}{T_s}, & |t| \leq T_s/2 \\ 0, & |t| > T_s/2 \end{cases}$$

The power spectrum of the MSK-type modulated carrier has the same shape as that of the pulse $p(t)$ [24-25]. Thus the spectral properties of the MSK-type modulated signal can be improved by using bandwidth-efficient pulse shapes $p(t)$. With this purpose in mind, a number of authors [26-31], to name only some of the contributors, have proposed different pulse shapes,

p(t), to improve the spectral properties of the modulated signal y(t) in retaining its envelope constanoy (i.e. satisfying Eqs. 2.2a and b).

Amoroso [26] proposed a class of pulse shapes represented by

$$p(t) = \begin{cases} \cos\left[\frac{\pi t}{T_s} - U\sin\frac{4\pi t}{T_s}\right], & |t| \leq T_s/2 \\ 0, & |t| > T_s/2 \end{cases} \tag{2.3}$$

where U is constant in the range (0,1/2). Note that for U=0 the MSK signal is obtained.

The resulting modulation techniques is called Sinusoidal Frequency-Shift-Keying (SFSK) by the fact that the modulator can be synthesized by applying a keyed sinewave to a linear integrator followed by a linear frequency modulator (i.e. CPFSK modulator structure as shown in Fig. 2.2).

Following in the same path, Simon [27] derived a set of conditions on the input pulse shapes, and derived the general power spectral density of these pulse shapes. Rabzel and Pasupathy [28] and Bazin [29] presented classes of pulse shapes having sharp spectral roll-off by applying the properties of pulse with many continuous derivatives, i.e. searching for pulse shapes p(t) which

(i) satisfy Eqs. (2.2a and b), i.e., the constant-envelope conditions

and (ii) have N continuous derivatives.

It is noted this approach is based on the following well-known theorem [52]: "If p(t) has N continuous derivatives, then its Fourier transform P(f) decays assymptotically as $|f|^{-(N+2)}$, and its power spectrum $|P(f)|^2$ as $|f|^{-2(N+2)}$".

Boutin *et al* [30] and Deshpande and Wittke [31] presented classes of pulse shapes which attain a low out-of-band power fraction, using prolate spheroidal wave functions, i.e. searching for pulse shapes p(t) which

(i) satisfy Eqs. (2.2a and b)

and (ii) have maximum in-band-to-total energy ratio $r = \frac{E_B}{E_T}$ where the in-band energy is

$$E_B = \int_{-B}^{+B} |P(f)|^2 df,$$

the total energy is

$$E_T = \int_{-T_s/2}^{+T_s/2} |p(t)|^2 dt$$

P(f) is the Fourier transform of p(t) and [-B, +B] is a chosen bandwidth.

The results of the studies mentioned above [26-31], indicate that the spectra of the obtained constant-envelope

MSK-type signals have lower side-lobes but wider main-lobes than that of QPSK (or Offset-QPSK) signals: the spectral side-lobes of these constant-envelope modulated signals are further reduced relative to those of the MSK signal, but their spectral main-lobes are still similar to that of the MSK signal (i.e., in the range of 1.5 X the symbol rate). Hence they are not attractive in narrow channel-spacing systems (i.e. systems in which the difference of the center frequencies of adjacent channels is smaller than the bit rate frequency).

2.2.2 CPFSK Modulation Schemes

Figure 2.2 shows the block diagram of a binary Continuous-Phase-Frequency-Shift -Keying (CPFSK) modulator. The binary CPFSK signal can be expressed as [32,33].

$$y(t) = \cos(\omega_c t + \psi(t)) \tag{2.4}$$

The phase $\psi(t)$ is

$$\psi(t) = \sum_{i=-\infty}^{+\infty} 2\pi h_i c_i \int_{-\infty}^{t} g(x-iT_b)dx \tag{2.5}$$

where c_i is the i^{th} bit,

$c_i = \pm 1$ with equal probability of 1/2.

h_i is the modulation index during the i^{th} bit interval

VCO: Voltage Controlled Oscillator

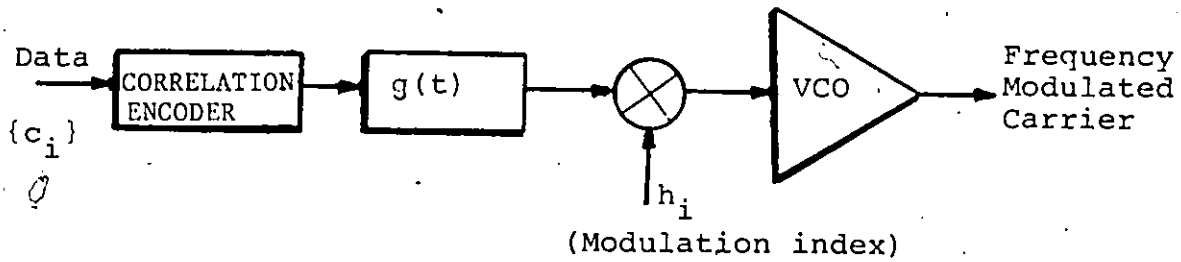

Fig. 2.2: BLOCK DIAGRAM OF A CPFSK MODULATOR

T_b is the bit interval i.e. $T_b = \frac{1}{2}T_s$, and
$g(t)$ is the baseband pulse shape.

The amplitude of $g(t)$ is chosen so that the maximum phase change over the i^{th} bit interval is $c_i h_i \pi$ radians. To obtain a CPFSK modulated carrier, the phase $\psi(t)$ should be a continuous function of time t, which implies that the baseband pulse shape $g(t)$ should not contain any impulses.

Efforts have been recently expended to search for various baseband pulse shapes $g(t)$, modulation index h_i, and correlation between symbols [32-43] to improve the system performance. CPFSK systems can be classified in the following manner:

(a) Full-Response CPFSK Systems

Full-Response CPFSK systems are those with the baseband pulses $g(t)$ limited within one bit interval T_b.

(i) Linear-Phase, Constant-h: In this case the baseband pulse shape $g(t)$ is a single-interval rectangular pulse defined as

$$g(t) = \begin{cases} \frac{1}{2T_b}, & |t| \leq T_b/2 \\ 0, & |t| > T_b/2 \end{cases}$$

The well-known MSK scheme can be considered as a special case of the linear-phase full-response CPFSK scheme with the modulation index $h=0.5$,

(ii) Linear Phase, Multi-h: The error probability performance or spectral properties of the above systems can be further improved by considering schemes with different modulation index h_i for each symbol interval. In [34-35] schemes with a set of cyclic values of the modulation index h_i, used in the modulator were considered.

(iii) Smooth Baseband Pulse Shape $g(t)$: Another method of improving the power spectra of the linear phase system is to use continuous baseband pulse shapes $g(t)$, or better still pulse shapes with one or more continuous derivatives. Only constant-h schemes have been considered with smooth pulses. SFSK modulation scheme [26] is an example of this type with $g(t)$ having one continuous derivative.

Spectral properties of Full-Response CPFSK signals can be summarized as follows. As the baseband pulse $g(t)$ is smoother (i.e. has a higher number of continuous derivatives) the power spectrum of the Full-Response CPFSK signal rolls off faster and its mainlobe becomes wider. A higher average modulation index, h, gives wider spectral mainlobe. The spectral main-lobes of these Full-Response CPFSK signals are still wider than that of QPSK (or Offset-QPSK) signal. For this reason, the Full-Response CPFSK signals are not attractive in systems which require a narrow

adjacent channel spacing.

Bounds on the error probability performance of Full-Response CPFSK systems in linear channels have been computed in these studies using their Euclidean distance properties [32,36]. It has been shown that these systems with $h=0.5$ have the same error performance as MSK and QPSK. However, the performance of these systems in a nonlinear multi-channel environment has not been documented in the readily available literature.

(b) Partial-Response CPFSK Systems

Partial-Response CPFSK systems are those with the baseband pulses $g(t)$ wider than one bit interval T_b. Only constant-h schemes have been considered for partial-response CPFSK systems [33,39,41-43,91].

(i) Linear Phase: Partial-Response CPFSK systems with linear phase were considered in [41-42]. For these systems the baseband pulses $g(t)$ are piecewise constant, providing piecewise linear phase trajectories.

(ii) Smooth Pulses: Partial-Response CPFSK schemes based on smooth multiple-interval baseband pulses $g(t)$ have been considered in [39,41-43]. The Tamed-Frequency Modulation (TFM), introduced by deJager and Dekker [39],

can be considered as a case of Partial-Response CPFSK with a smoothed pulse shape $g(t)$.

In principle, the power spectrum of the TFM signal is improved by correlating the phase shifts so that the phase shift over a bit interval is a function of one or more previous bits and the present bit. In other words the TFM scheme makes use of the correlative level coding techniques [51] in the phase shifts of the modulated signal. Rhodes [43] extended this technique to a scheme called Frequency-Shift-Offset-Quadrature (FSOQ) modulation. Mulwijk [41] generalized further this correlative encoded FM technique to a class of Correlative Phase Shift Keying (CORPSK) modulation techniques.

With smooth, multiple-interval baseband pulses, $g(t)$, Partial-Response CPFSK modulation schemes provide power spectra having both narrow main-lobes and fast roll-off. For $g(t)$ occupying more than 4-bit intervals, the spectral main-lobes of the corresponding CPFSK signals are compatible with that of QPSK and their spectral roll-off is steeper. However, to obtain the best error probability performance signal detectors must be coherent. Reference signals (i.e. carrier and clock) must then be generated in the receiver. For CPFSK modulation techniques, the extraction of these reference signals is rather complicated in most cases. Furthermore, phase variations are small due to multi-level correlation, demanding careful carrier and clock synchronization. In summary, the cost of the spectral

improvement of CPFSK schemes increases the system complexity and synchronization problems.

2.3 NON-CONSTANT ENVELOPE PSK-TYPE MODULATION TECHNIQUES

A constant-envelope modulated carrier would not undergo major spectral spreading effects caused by nonlinear amplification. For this reason, efforts have been expended in the search for constant-envelope bandwidth-efficient modulation techniques as presented in Section 2.2. Alternately, non-constant envelope bandwidth-efficient modulation techniques can be attractive in nonlinear channel applications if they can provide low spectral spreading caused by nonlinear amplification.

Prabhu [46] proposed bandwidth-efficient PSK-type modulation schemes with overlapping baseband pulses. The modulator block diagram for this type of modulation is similar to that shown in Fig. 2.1 but the baseband pulse $p(t)$ is now wider than one symbol interval. For equiprobable binary data the power spectrum of the modulated signal has the same shape as that of the overlapping baseband pulse $p(t)$ [24-25]. Hence the spectral advantages are obtained by the fact that overlapping baseband pulses have a better bandwidth efficiency than non-overlapping pulses of the same form [45].

As an extension of Prabhu's work, Austin and Chang [47] studied furthermore the spectral properties and error probability

performance of the Quadrature Overlapped Raised-Cosine (QORC) and Staggered QORC (SQORC) schemes in linear and nonlinear single-channel environment. The block diagram of the SQORC modulator is similar to that shown in Fig. 2.1 with the double interval raised-cosine pulse

$$p(t) = \begin{cases} \frac{1}{2}\left(1+\cos\frac{\pi t}{T_s}\right), & |t| \leq T_s \\ 0, & |t| > T_s \end{cases}$$

where T_s is the symbol interval.

The results of [47] show that the SQORC scheme has lower (better) spectral spreading, due to a saturated high-power amplifier (HPA) than OQPSK and MSK schemes.

Amoroso [48] presented a class of "quasi-bandlimited" double-interval pulses $p(t)$ which can be used in PSK-type modulation schemes. It is expressed as

$$p(t) = \begin{cases} \left[\frac{\sin(\pi t/T_s)}{\pi t/T_s}\right]^n, & -T_s \leq t \leq T_s \\ 0, \text{ otherwise} \end{cases}$$

These pulses approach band limitation with increasing n because the truncated energy outside $[-T_s, +T_s]$ is a rapidly decreasing

function of n. This can be seen by noting that the unlimited pulse $\frac{\sin \pi t/T_s}{\pi t/T_s}$ with $-\infty<t<+\infty$ is strictly bandlimited [24].

Amoroso also proposed a method of generating a constant-envelope modulated carrier by introducing an ideal hardlimiter after the modulator [48]. This ideal hardlimiter removes the carrier envelope fluctuations but also introduces impairments due to signal distortions.

In the studies mentioned above [46-48], it has been shown that pulse-overlapping PSK-type signals provide low spectral spreading caused by nonlinear amplification. They have spectral main-lobes compatible to that of QPSK and faster spectral roll-off.

2.4 SUMMARY

So far, major contributions in the field of digital modulation techniques, most pertinent to our research topic, have been reviewed . Baseband pulse shapes, phase transitions and envelope fluctuations are among the major parameters which affects the power spectra of modulated signals in nonlinear channels.

Based on the fact that a constant-envelope modulated signal undergoes no significant spectral regeneration caused by nonlinear amplification, many authors have proposed different baseband pulse shapes, and smooth phase transitions to improve the spectral properties of constant-envelope modulated signals. The results of these studies show that significant spectral improvements are only obtained when baseband pulses occupy more than 4 bit intervals. The cost of the spectral improvement of these constant-envelope modulation schemes increases the system complexity and synchronization problems. On the other hand, some authors have also studied non-constant-envelope modulation schemes which yield less spectral regeneration than QPSK, OQPSK and MSK in nonlinear channels.

In these studies the spectral properties and/or error probability performance in a single-channel environment were investigated. However, the error probability performance in a complex interference (e.g. adjacent-channel, co-channel interference) environment, synchronization aspects and hardware feasibility of proposed modulation schemes have not been studied in detail.

In the following chapters, we introduce and study the properties of a new class of power and bandwidth efficient transmission techniques for digital radio communications systems. Our studies include the spectral properties, error probability

performance in a complex interference environment, carrier and symbol timing recovery aspects, hardware feasibility, and potential applications of the proposed class of digital transmission techniques.

CHAPTER THREE

A CLASS OF POWER AND BANDWIDTH EFFICIENT INTERSYMBOL-INTERFERENCE AND JITTER-FREE (IJF) BASEBAND SIGNALS

SUMMARY:

In this chapter, a new class of power and bandwidth efficient Intersymbol-Interference and Jitter-Free (IJF) baseband signals is introduced and studied. These signals can be generated by a generalized Nonlinear Switching Filter (NLSF).

The power spectral density (PSD) function of baseband signals generated by a generalized NLSF is derived using a 4-state Markov chain model. It is shown that this PSD function can be expressed in terms of the Fourier transform of a double-interval even pulse when the baseband signals satisfy the Intersymbol-Interference and Jitter Free (IJF) conditions. These results stimulate the search of pulse shapes which yield IJF baseband signals having steep spectral roll-off and low out-of-band energy emission. A new class of such signals and their spectral properties are described in this chapter.

The error probability (P_e) performance of IJF baseband signals in an additive white gaussian noise (AWGN) environment is analytically evaluated. Linear transversal, decision-feedback, and raised-cosine-type receivers are investigated.

Experiments are also performed to verify the analytical results.

3.1 PROPERTIES OF ISI AND JITTER-FREE (IJF) SIGNALS

3.1.1. Spectral Analysis of Generalized NLSF Signals Using a Markov Chain Model

The Non-Linear-Switching-Filter (NLSF) shown in Fig. 3.1a was introduced by Feher [54] to generate a bandwidth efficient base-band signal. Hardware implementation of this NLSF was reported in [49,50,54,71,89].

As an extension of the NLSF concept, consider a *generalized* NLSF shown in Fig. 3.1b.

The input to the generalized NLSF is a Non-Return-to-Zero (NRZ) signal

$$x(t) = \sum_{n=-\infty}^{+\infty} x_n g(t-nT_s) \qquad (3.1)$$

where T_s is the symbol interval,

$$g(t-nT_s) = \begin{cases} 1 & \text{for } |t-nT_s| < T_s/2 \\ 0 & \text{elsewhere} \end{cases}$$

and

$x_n = +A$ or $-A$ with probability of 1/2

The generalized NLSF output signal is represented by

S1,S2,S3,S4: Analog switches to select SINE, COSINE, DC+, and DC- respectively

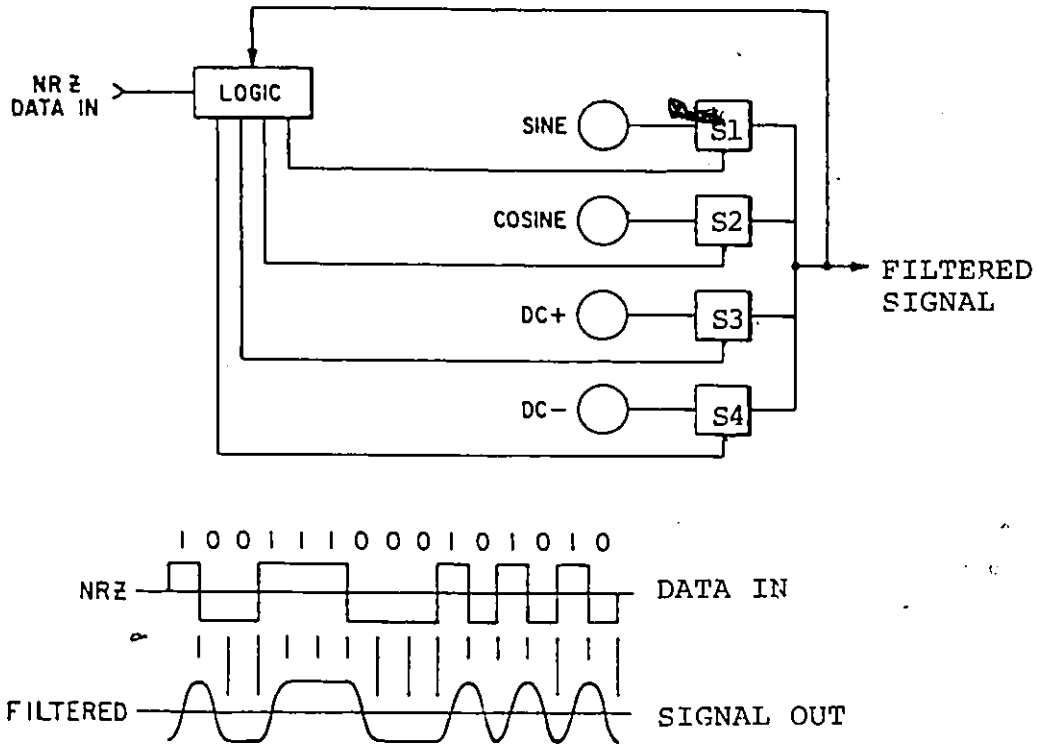

Fig. 3.1a: BLOCK DIAGRAM OF A NONLINEAR SWITCHING FILTER

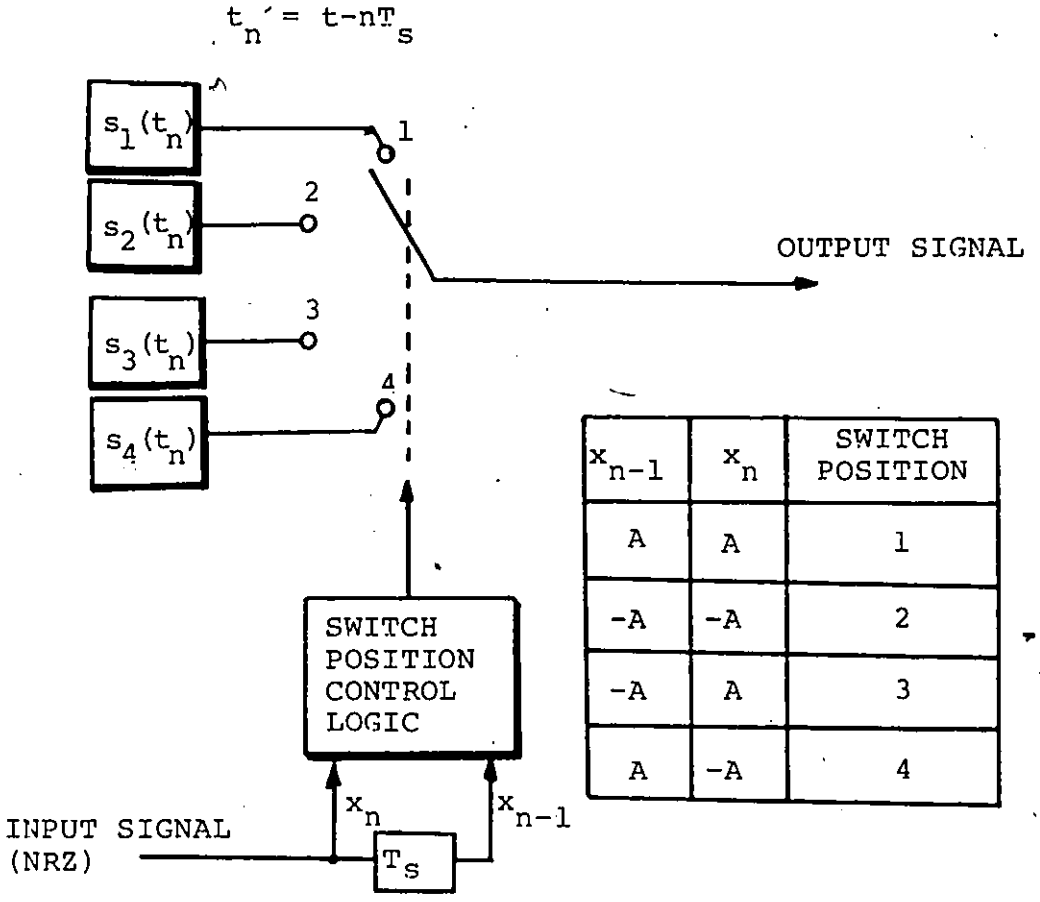

x_{n-1}	x_n	SWITCH POSITION
A	A	1
-A	-A	2
-A	A	3
A	-A	4

Fig. 3.1b: BLOCK DIAGRAM OF A *GENERALIZED* NONLINEAR SWITCHING FILTER

$$y(t) = \sum_{n=-\infty}^{+\infty} y_n(t) \tag{3.2a}$$

where

$$y_n(t) = \begin{cases} s_1(t-nT_s) = s_e(t-nT_s), & \text{if } x_{n-1}=x_n=+A \\ s_2(t-nT_s) = -s_e(t-nT_s), & \text{if } x_{n-1}=x_n=-A \\ s_3(t-nT_s) = s_o(t-nT_s), & \text{if } x_{n-1}=-A,\ x_n=+A \\ s_4(t-nT_s) = -s_o(t-nT_s), & \text{if } x_{n-1}=+A,\ x_n=-A \end{cases} \tag{3.2b}$$

and

$s_e(t)$ and $s_o(t)$ are single-interval pulses of duration T_s, i.e.

$$s_e(t) = s_o(t) = 0 \quad \text{for} \quad |t| > T_s/2$$

Figure 3.2 shows an illustrative measured eye diagram and the corresponding power spectrum of a waveform processed by a NLSF.

Every T_s seconds, the NLSF outputs an elementary signal $y_n(t)$ from the set of 4 basic signals $\{s_1(t-nT_s), s_2(t-nT_s), s_3(t-nT_s), s_4(t-nT_s)\}$, determined by the previous elementary signal $y_{n-1}(t)$ and present input x_n. Therefore, the NLSF can be statistically represented by a 4-state Markov chain as shown in Fig. 3.3. The encoded signal $y(t)$ is characterized by the set of stationary probabilities:

$$\{p_i,\ i=1,2,3,4\}$$

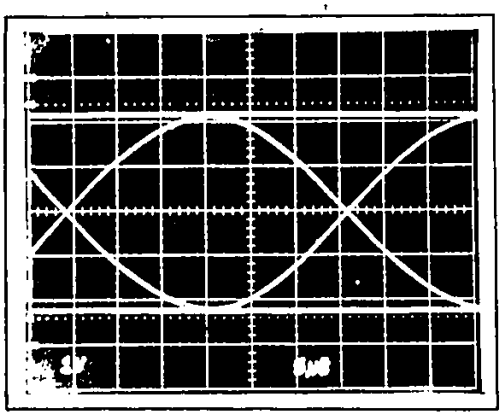

(a) Measured eye diagram (bit rate: 32 kb/s)

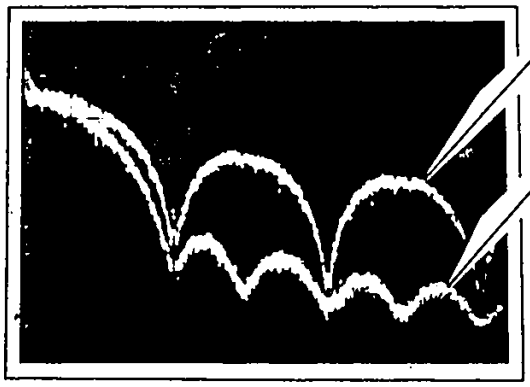

(b) Measured power spectrum (bit rate: 32 kb/s)
Vertical: 10 dB/ div
Horizontal: 10 kHz/div
(starting at 0 Hz)

Fig. 3.2 : WAVEFORM PROCESSED BY A NLSF

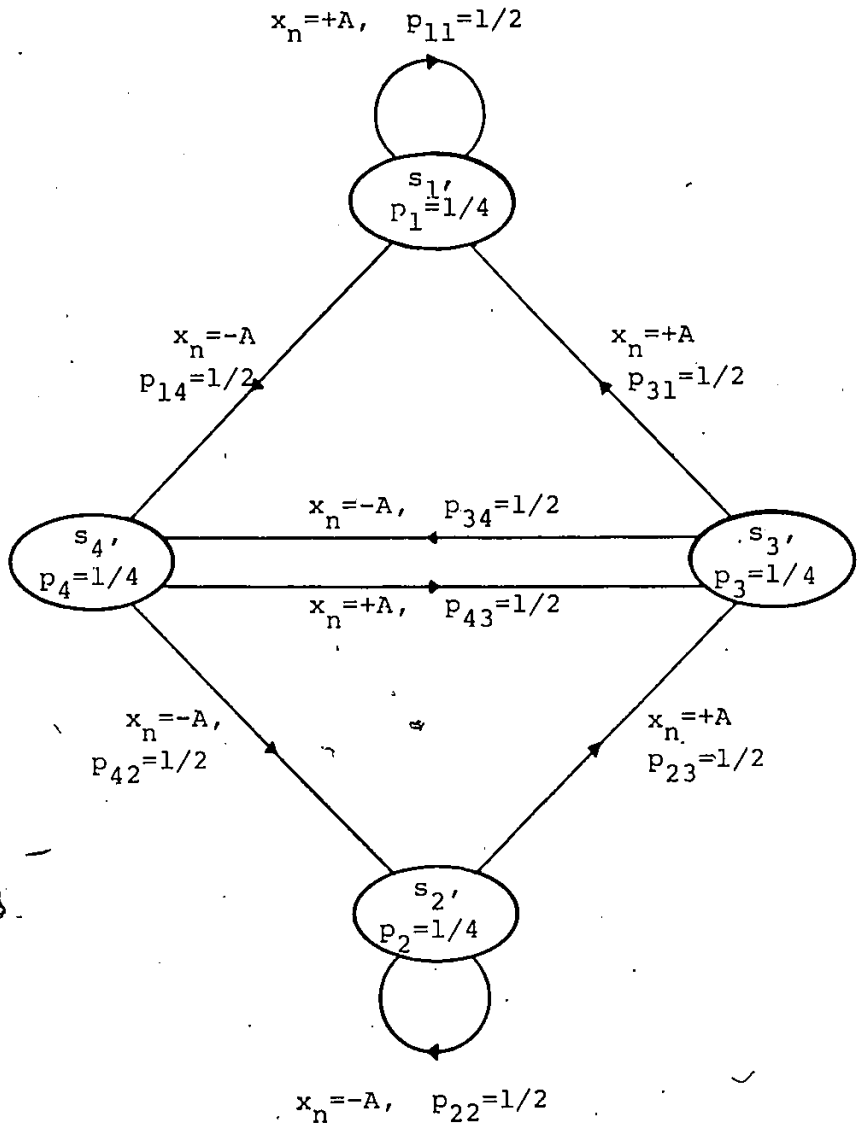

Fig. 3.3: 4-STATE MARKOV CHAIN REPRESENTATION OF THE NLSF PROCESSING

and the set of transition probabilities

$$\{p_{ik},\ i,\ k=1,2,3,4\}$$

where the states are the basic signals s_i, $i=1,2,3,4$ and the stationary and transition probabilities are defined as

$$p_i = P\{y_n(t) = s_i(t-nT_s)\}$$

$$p_{ik} = P\{y_n(t) = s_k(t-nT_s) \,|\, y_{n-1}(t) = s_i(t-(n-1)T_s)\}$$

for $i,\ k=1,2,3,4$

Based on Eq. (3.2b) and Fig. 3.3, p_i's and p_{ik}'s are derived as

$$p_i = 1/4 \quad \text{for} \quad i=1,2,3,4 \tag{3.3a}$$

$$P = \begin{bmatrix} p_{11} & p_{12} & p_{13} & p_{14} \\ p_{21} & p_{22} & p_{23} & p_{24} \\ p_{31} & p_{32} & p_{33} & p_{34} \\ p_{41} & p_{42} & p_{43} & p_{44} \end{bmatrix} = \frac{1}{2} \begin{bmatrix} 1 & 0 & 0 & 1 \\ 0 & 1 & 1 & 0 \\ 1 & 0 & 0 & 1 \\ 0 & 1 & 1 & 0 \end{bmatrix} \tag{3.3b}$$

From this statistical description, the power spectral density (PSD) of the encoded signal $y(t)$ is given by [55]

$$Y(f) = \frac{1}{T_s^2} \sum_{n=-\infty}^{+\infty} \left| \sum_{i=1}^{4} p_i S_i\left(\frac{n}{T_s}\right) \right|^2 \delta\left(f-\frac{n}{T_s}\right) + \frac{1}{T_s} \sum_{i=1}^{4} p_i |S_i(f)|^2$$

$$+ \frac{2}{T_s} \mathrm{Re}\left[\sum_{i=1}^{4} \sum_{k=1}^{4} p_i S_i^*(f) S_k(f) S_{ik} \right] \qquad (3.4)$$

where

$S_i(f)$ is the Fourier transform of $s_i(t)$,

$S_i^*(f)$ is the complex conjugate of $S_i(f)$

$S_{ik} = \sum_{n=1}^{\infty} p_{ik}^{(n)} e^{-j2\pi nfT_s}$

$p_{ik}^{(n)}$ is the ik^{th} entry of the n-step transition matrix P^n,

$P^n = \underbrace{P \times P \times P \times \ldots \times P}_{n \text{ times}}$

and

Re [...] is the real part of [...]

From Eq . (3.2b) it follows that

$$S_1(f) = -S_2(f) = S_e(f)$$

$$S_3(f) = -S_4(f) = S_o(f)$$

and

$$P^n = \{p_{ik}^{(n)}\} = \frac{1}{4} \begin{bmatrix} 1 & 1 & 1 & 1 \\ 1 & 1 & 1 & 1 \\ 1 & 1 & 1 & 1 \\ 1 & 1 & 1 & 1 \end{bmatrix} \quad \text{for} \quad n=2,3, \ldots$$

By substituting $S_e(f)$, $S_o(f)$, p_i's and $p_{ik}^{(n)}$'s into Eq. (3.4), and simplifying it, the PSD function of the NLSF signal $y(t)$ is obtained as

$$Y(f) = \frac{1}{T_s}\left[|S_e(f)|^2+|S_o(f)|^2 + Re\{(S_e(f)-S_o(f))(S_e(f)+S_o(f))^* e^{-j2\pi fT_s}\}\right] \tag{3.5}$$

for any given pair of $s_e(t)$ and $s_o(t)$.

3.1.2 ISI and Jitter Free (IJF) Signals

Equation (3.5) represents the general PSD function of a NLSF signal y(t) for a given pair of $s_e(t)$ and $s_o(t)$. Let $s_e(t)$ and $s_o(t)$ be *even* and *odd* pulses respectively. Their Fourier transforms satisfy the following equations

$$S_e(f) = S_e^*(f) \text{ : purely real}$$

and

$$S_o(f) = -S_o^*(f) \text{ : purely imaginary}$$

In this case, Eq.(3,5) can be rewritten as

$$Y(f) = \frac{1}{2T_s}\left[S_e^2(f)-S_o^2(f)+Re\{(S_e(f)-S_o(f))^2 e^{-j2\pi fT_s}\} \right]$$

$$= \frac{1}{2T_s}\{S_e^2(f)-S_o^2(f)+ [S_e^2(f)+S_o^2(f)]\cos 2\pi fT_s + j2S_e(f)S_o(f)\sin 2\pi fT_s\}$$

or

$$Y(f) = \frac{1}{T_s}\left[S_e(f)\cos\pi fT_s + jS_o(f)\sin\pi fT_s \right]^2 \tag{3.6}$$

By defining an *even double-interval* pulse s(t) of duration $2T_s$ as

$$s(t) = \begin{cases} \frac{1}{2}\left[s_e(|t|-T_s/2) - s_o(|t|-T_s/2)\right], & |t|<T_s \\ 0, \text{ elsewhere} \end{cases} \tag{3.7}$$

or equivalently,

$$s_e(t) = \begin{cases} \frac{1}{2}\left[s(t-T_s/2) + s(t+T_s/2) \right] & ,|t|<T_s \\ \\ 0, \text{ elsewhere} \end{cases} \tag{3.8a}$$

and

$$s_o(t) = \begin{cases} \frac{1}{2}\left[s(t-T_s/2) - s(t+T_s/2) \right] & ,|t|<T_s \\ \\ 0, \text{ elsewhere} \end{cases} \tag{3.8b}$$

From Eqs.(3.8a,b), it can be shown that

$$S_e(f) = S(f)\cos\pi fT_s$$

and

$$S_o(f) = -jS(f)\sin\pi fT_s$$

where S(f) is the Fourier transform of s(t).

Equation (3.6) can be simplified as

$$Y(f) = \frac{1}{T_s}\,|S(f)|^2 \tag{3.9}$$

In order to obtain an *intersymbol-interference and jitter-free* (IJF) signal, y(t), the even double-interval pulse s(t) has to satisfy the following IJF condition [25]

$$s(T_s) = s(-T_s) \tag{3.10a}$$

or equivalently,

$$|s_e(T_s/2)| = |s_o(T_s/2)| \tag{3.10b}$$

In fact, for a given pair of even and odd pulse shapes, $s_e(t)$ and $s_o(t)$, the IJF signal $y(t)$ can be also generated by overlapping the double-interval pulse $s(t)$ defined by Eq. (3.7).

The IJF signal encoder can be designed using a transversal filter as shown in Fig. 3.4a. The encoder pulse response is illustrated in Fig. 3.4b. The input NRZ rectangular pulse is sampled into $(2N+1)$ samples at intervals of d where $d = \frac{T_s}{N}$. Each sample $p(t-id)$ is multiplied by the weighting coefficient b_i, for $i=-N, -(N-1), \ldots, -1, 0, +1, \ldots, (N-1), N$. The weighted samples are then summed by an analog adder to form a staircase pulse $s'(t)$

$$s'(t) = \sum_{i=-N}^{+N} b_i p(t-id) \tag{3.11}$$

where

$$b_i = s(id),$$

$s(t)$ is defined by Eq. (3.7), and

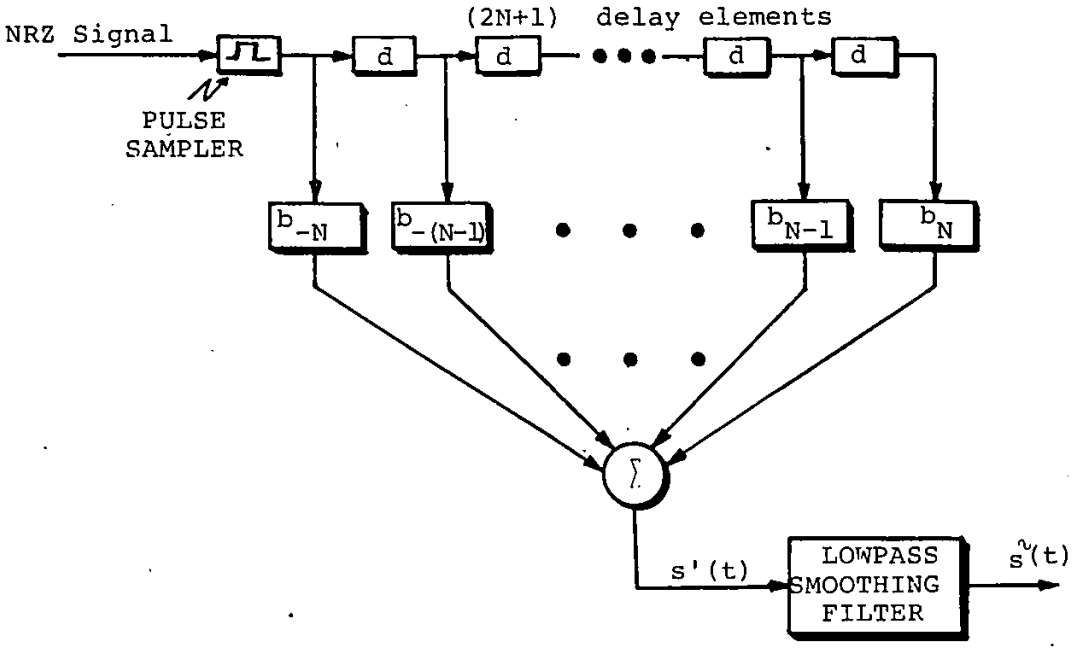

(a) BLOCK DIAGRAM OF AN IJF ENCODER USING THE TRANSVERSAL FILTER

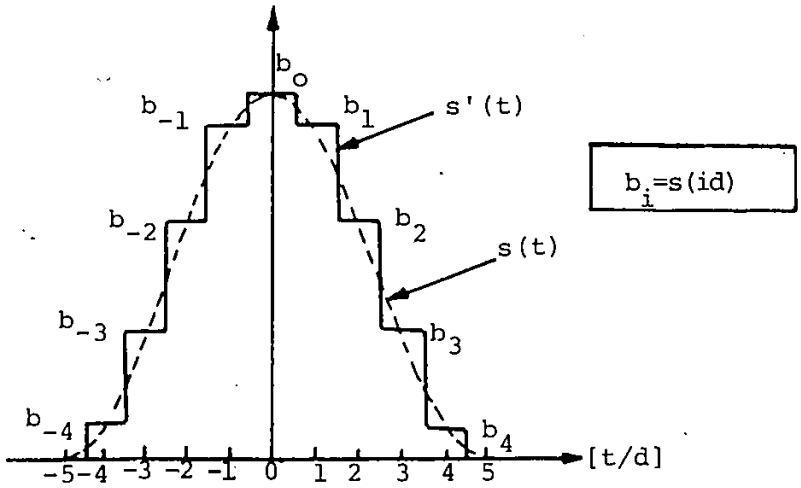

(b) AN EXAMPLE OF THE ENCODER PULSE RESPONSE WITH N=5 and $s(t) = \frac{1}{2}(1+\cos\frac{\pi t}{T_s})$

Fig. 3.4: PRACTICAL IMPLEMENTATION OF AN IJF ENCODER USING THE DOUBLE-INTERVAL PULSE OVERLAPPING TECHNIQUE

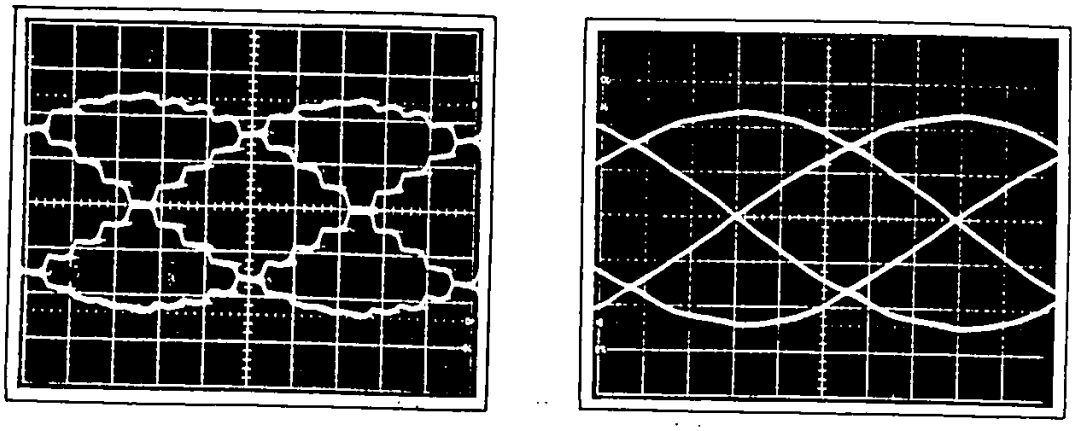

(a) Signalling element: $s(t) = \cos\frac{\pi t}{2T_s}$

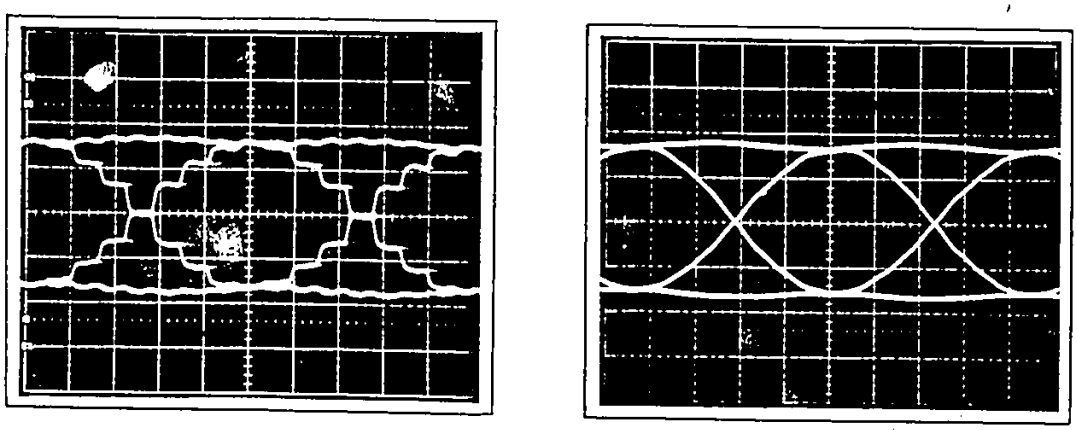

(b) Signalling element: $s(t) = \frac{1}{2}\ (1+\cos\frac{\pi t}{T_s})$

Fig. 3.5: MEASURED EYE DIAGRAMS OF ILLUSTRATIVE IJF SIGNALS GENERATED BY USING THE OVERLAPPING PULSE CONCEPT

Notes: Simple Binary Transversal Filters have been employed for for the signal generation. Eye diagrams were *measured prior to* and *after a* first-order "smoothing" filter. This filter follows the transversal filter and is included to remove higher order frequency components.

$$p(t-id) = \begin{cases} 1, & -\frac{d}{2} < t-id \leq \frac{d}{2} \\ 0, & \text{elsewhere} \end{cases}$$

The staircase pulse $s'(t)$ is finally smoothed by a low-pass filter. The filtered pulse $\tilde{s}(t)$ is an *approximation* of the double-interval impulse response $s(t)$. As N increases, $\tilde{s}(t)$ approaches $s(t)$.

Illustrative measurement results are presented in Fig. 3.5.

The pulse overlapping and NLSF processing techniques give the same result. For low bit rate applications (e.g. less than 200 kb/s) the NLSF hardware is simpler, while for higher bit rate applications implementation of transversal filters to generate overlapped pulses is simpler.

3.2 PULSE SHAPES FOR BANDWIDTH-EFFICIENT IJF SIGNALS:

Equation (3.9) shows that the power spectral density (PSD) of the baseband IJF signal has the same shape as the Fourier transform of the double-interval pulse $s(t)$. This section presents the *search for pulse shapes* $s(t)$ *satisfying the IJF conditions* given by Eqs. (3.10a and b), and resulting in

1) *fast spectral roll-off* (Section 3.2.1)

and

2) *Low out-of-band energy* (Section 3.2.2)

3.2.1 A Sub-Class of IJF Signals Having Fast Spectral Roll-Off

Consider a double-interval even pulse $s(t)$ represented as the sum of $(N+2)$ orthogonal even functions

$$s(t) = \begin{cases} \sum_{k=0}^{N+1} a_k \cos(k \frac{\pi t}{n_o T_s}), & \text{for } |t| \leq T_s \\ 0, & \text{elsewhere} \end{cases} \qquad (3.12)$$

where

T_s is the symbol interval

$n_o = 2,3 \ldots$

It is well-known that if $s(t)$ has N continuous derivatives, then its Fourier transform $S(f)$ decays assymptotically as $|f|^{-(N+2)}$ and its power spectrum $|S(f)|^2$ as $|f|^{-2(N+2)}$ [56]. Since the orthogonal functions $\cos(k \frac{\pi t}{n_o T_s})$ have an infinite number of continuous derivatives on $(-\infty, +\infty)$, $s(t)$ also has an infinite number of derivatives for $|t| < T_s$. For continuity of N derivatives at the end-points, $t = \pm T_s$, the necessary and sufficient condition is

$$s^{(i)}(\pm T_s) = 0, \quad i=0,1,2, \ldots, N \qquad (3.13)$$

where

$s^{(i)}(t)$ is the i^{th} derivative of $s(t)$.

From Eqs. (3.12) and (3.13), this condition can be expressed as

$$a_o + \sum_{k=1}^{N+1} a_k \cos\left(k \frac{\pi}{n_o}\right) = 0 \qquad (3.14a)$$

$$\sum_{k=1}^{N+1} a_k (k)^i \sin\left(k \frac{\pi}{n_o}\right) = 0, \quad \text{for} \quad i=1,3,5, \ldots \qquad (3.14b)$$

and

$$\sum_{k=1}^{N+1} a_k (k)^i \cos\left(k \frac{\pi}{n_o}\right) = 0, \quad \text{for} \quad i=2,4,6, \ldots \qquad (3.14c)$$

Substituting the Fourier transform of $s(t)$ defined by Eq. (3.12) into Eq. (3.8), the PSD function of the IJF signal is obtained as

$$Y(f) = \frac{1}{T_s} \Big| a_o \frac{\sin 2\pi f T_s}{f T_s} + 4n_o \sum_{k=1}^{N+1} \frac{a_k}{k^2 - 4n_o^2 (f T_s)^2}$$

$$\left[k \sin \frac{\pi k}{n_o} \cos 2\pi f T_s - 2n_o \left(\cos \frac{\pi k}{n_o}\right) f T_s \sin 2\pi f T_s\right] \Big|^2 \qquad (3.15)$$

where the coefficient a_k's satisfy Eqs. (3.14 a, b, c) for $k=0,1,2, \ldots, (N+1)$

We studied classes of IJF signals with $n_o=2,3,4, \ldots,$

and found that the spectral characteristics of IJF signals having the same N and different n_o's are similar. For this reason only one particular class of IJF signals with $n_0=2$ is described.

The double-interval even pulse $s(t)$ for $n_o=2$ is

$$s(t) = \begin{cases} \sum_{k=0}^{N+1} a_k \cos\left(k \frac{\pi t}{2T_s}\right), & |t| \leq T_s \\ 0, & \text{elsewhere} \end{cases} \tag{3.16}$$

From Eqs. (3.14a-c) and (3.15), the normalized power spectral density function of $y(t)$ is derived as

$$\frac{Y(x)}{Y(o)} = \begin{cases} \left|\frac{\sin 2\pi x}{2\pi x} \cdot \prod_{p=1}^{\frac{N+1}{2}} \frac{p^2}{p^2-4x^2}\right|^2, & \text{for odd } N \\ \left|\cos 2\pi x \cdot \prod_{p=1}^{\frac{N}{2}+1} \frac{(2p-1)^2}{(2p-1)^2-16x^2}\right|^2, & \text{for even } N \end{cases} \tag{3.17}$$

where

$$x = fT_s$$

Figure 3.6 shows a number of double-interval pulses, $s(t)$, and eye diagrams of corresponding IJF signals. The power spectra of these IJF signals are illustrated in Fig. 3.7. As N increases, the spectral roll-off of the corresponding IJF signal is faster for high frequencies but the main lobe becomes wider. As a result, the choice of an IJF signal depends on the trade-off between the main lobe occupancy and side-lobe roll-

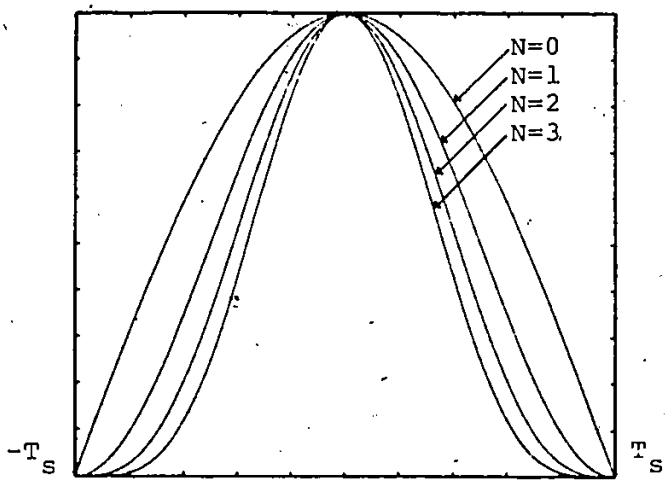

(a) double-interval pulse s(t)

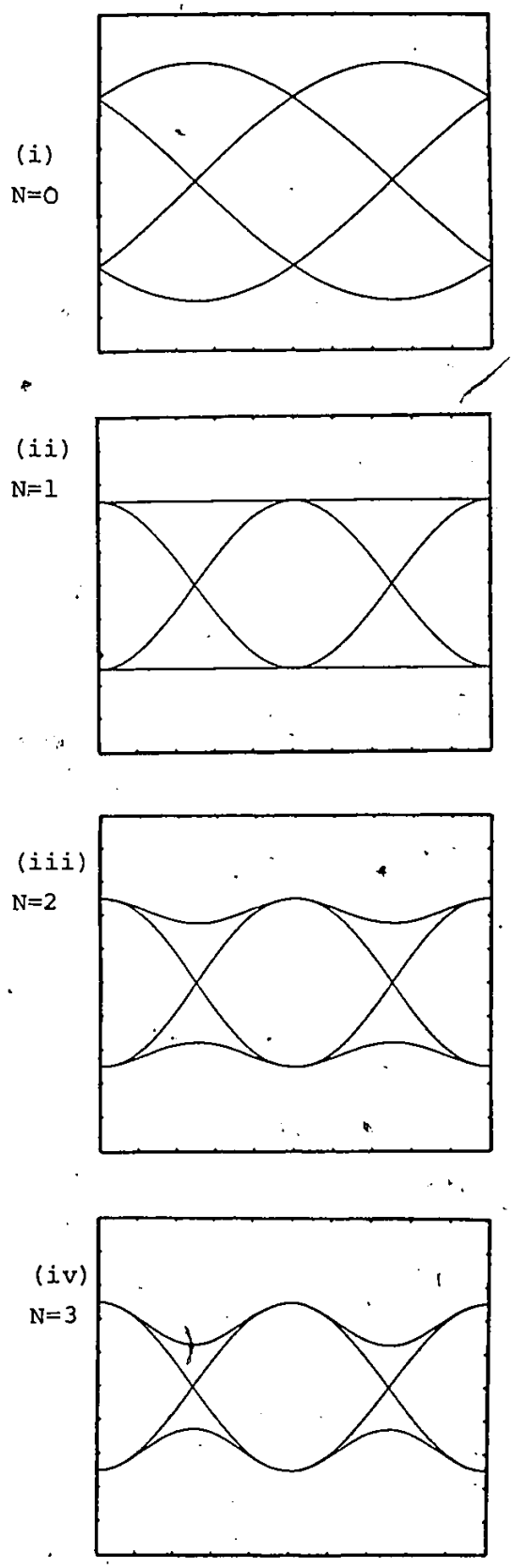

(b) Eye diagrams

Fig. 3.6: SOME IJF SIGNALS HAVING FAST SPECTRAL ROLL-OFF

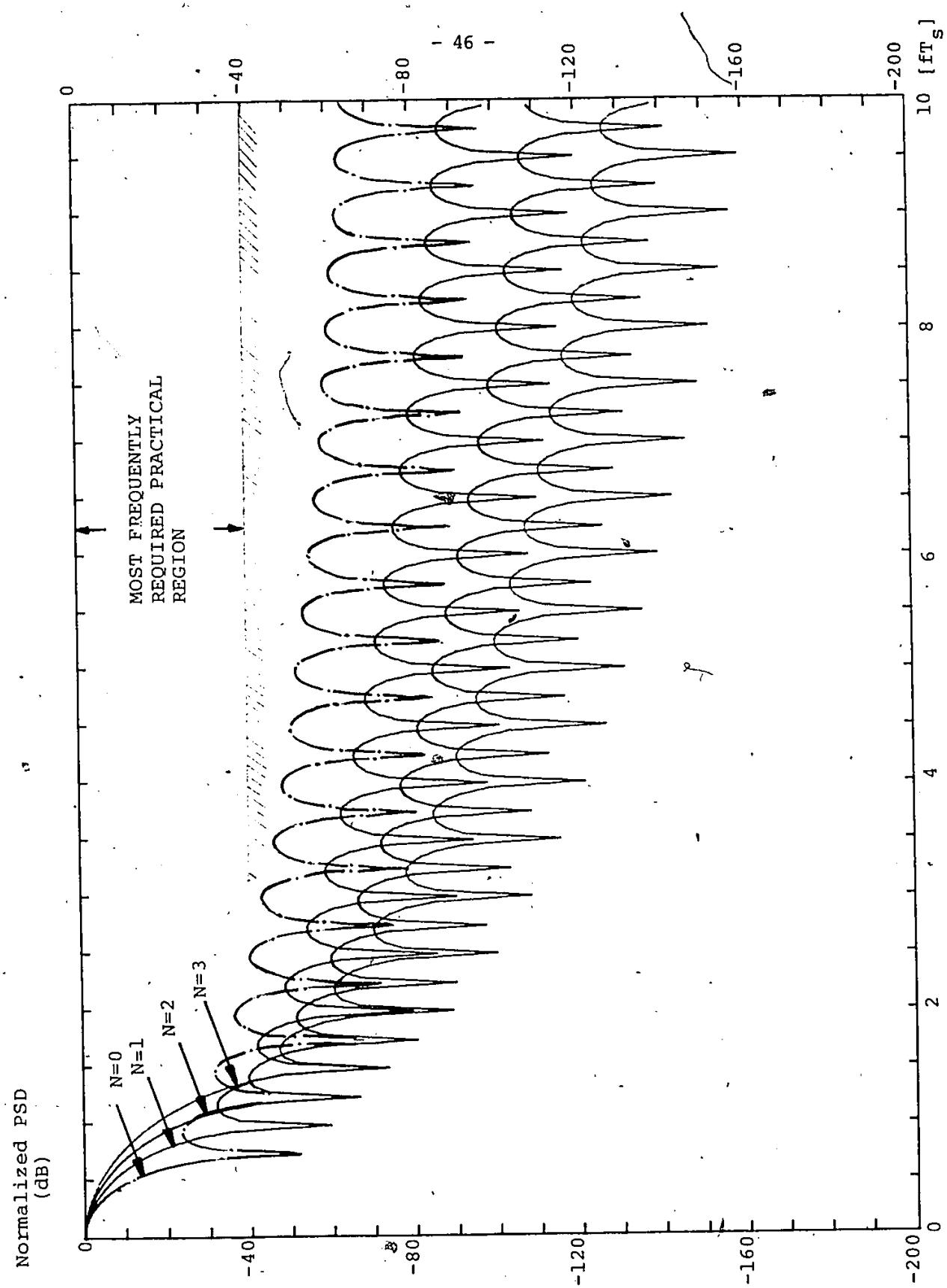

Fig. 3.7: NORMALIZED POWER SPECTRA OF IJF SIGNALS HAVING FAST SPECTRAL ROLL-OFF

off. In most practical applications, a spectral density of more than 40 dB below the highest spectral density (near 0 Hz) can often be neglected [89]. For this reason, IJF signals corresponding to N=0 and N=1 are more attractive.

The double-interval pulses $\bar{s}_0(t)$, $\bar{s}_1(t)$ corresponding to N=0 and N=1 are

$$\bar{s}_0(t) = \begin{cases} \cos \frac{\pi t}{2T_s}, & |t| \leq T_s \\ 0, & \text{elsewhere} \end{cases} \tag{3.18a}$$

and

$$\bar{s}_1(t) = \begin{cases} \frac{1}{2}(1+\cos \frac{\pi t}{T_s}), & |t| \leq T_s \\ 0, & \text{elsewhere} \end{cases} \tag{3.18b}$$

As shown in Fig. 3.8a, the first null frequency of $\bar{s}_0(t)$ is at $0.75/T_s$, while that of $\bar{s}_1(t)$ is at $1/T_s$. However, the asymptotic spectral roll-off of $\bar{s}_0(t)$ is of the order of $|f|^{-4}$ while that of $\bar{s}_1(t)$ is of the order of $|f|^{-6}$. Both of them show spectral advantages over the NRZ signal (Figs. 3.8a,b).

Note that $\bar{s}_1(t)$ is also called overlapped raised-cosine pulse and used in the QORC modulation scheme [47].

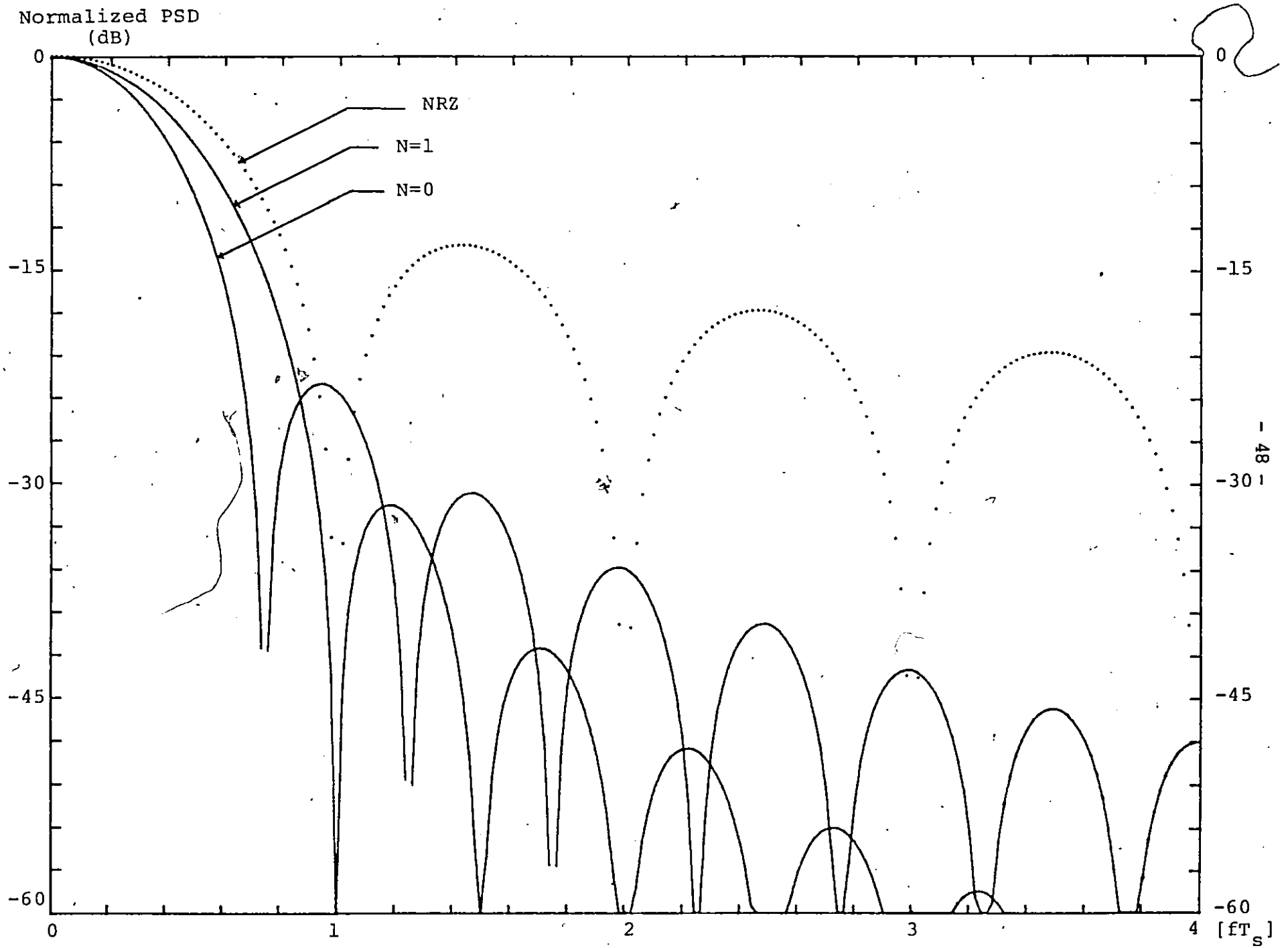

Fig. 3.8a: NORMALIZED POWER SPECTRA OF IJF SIGNALS HAVING FAST SPECTRAL ROLL-OFF

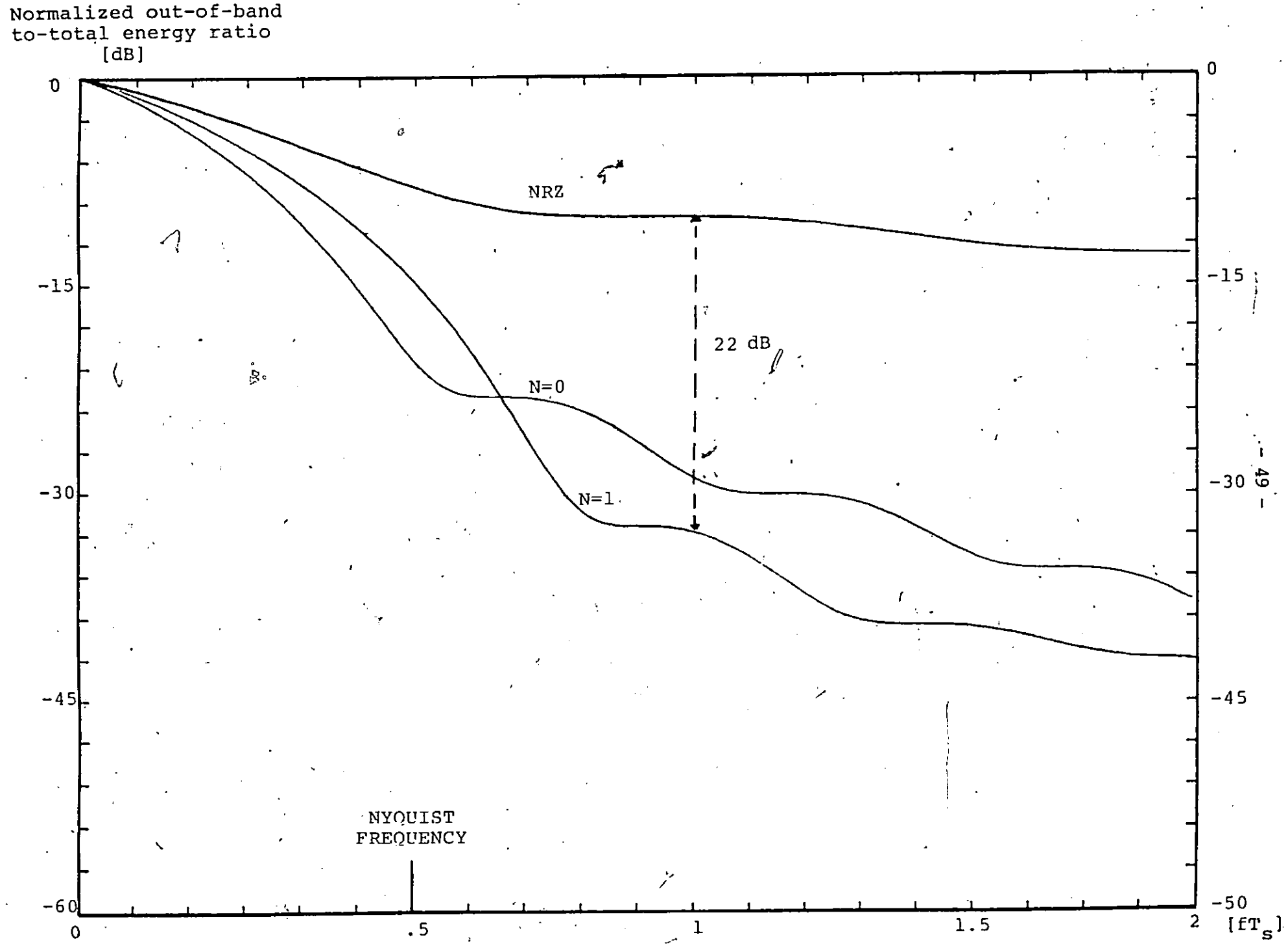

Fig. 3.8b: OUT-OF-BAND-TO-TOTAL ENERGY RATIO OF IJF (N=0 AND N=1) SIGNALS

3.2.2. A Sub-Class of IJF Signals Having Low Out-of-Band Energy

Consider the double-interval even pulse $s(t)$ satisfying the IJF conditions, Eqs. (3.9a and b). The total energy E_o is

$$E_o = \int_{-T_s}^{+T_s} |s(t)|^2 \, dt \tag{3.19}$$

and its energy E_B in a given frequency band $[-B, +B]$ is

$$E_B = \int_{-B}^{+B} (S(f) \cdot S^*(f)) \, df \tag{3.20}$$

where $S(f)$ is the Fourier transform of $s(t)$

and $S^*(f)$ is the complex conjugate of $S(f)$

Since $s(t)$ is real-valued,

$$S^*(f) = \int_{-T_s}^{+T_s} s(t) \, e^{j2\pi ft} dt$$

Hence Eq. (3.20) can be written as

$$E_B = \int_{-B}^{+B} \iint_{-T_s}^{+T_s} s(t)s(v)e^{-j2\pi f(t-v)} dv \, dt \, df$$

$$= \iint_{-T_s}^{+T_s} s(t)s(v) \, \frac{\sin 2\pi B(t-v)}{(t-v)} \, dv \, dt \tag{3.21}$$

Let η be defined as the inband to total energy ratio,

$$\eta = E_B/E_o \tag{3.22a}$$

From Eq. (3.21) it can be written as

$$\eta = \frac{1}{E_o} \int_{-T_s}^{+T_s} \int s(t)s(v) \frac{\sin 2\pi B(t-v)}{(t-v)} dv\, dt$$

$$= \int_{-T_s}^{+T_s} \int s(t)s(v) \frac{\sin 2\pi B(t-v)}{(t-v)} dv\, dt \tag{3.22b}$$

where E_o is normalized to unity. Minimizing the out-of-band energy is equivalent to maximizing the in-band energy fraction η. The maximum value of η, occurs when $s(t)$ is one of the eigenfunctions corresponding to the largest eigenvalue of the integral equation [57]:

$$\eta s(v) = \int_{-T_s}^{+T_s} \int s(t) \frac{\sin 2\pi B(t-v)}{(t-v)} dt \tag{3.23}$$

where $\frac{\sin 2\pi B(t-v)}{(t-v)}$ is the Kernel of the integral equation, and $s(t)$ must satisfy Eqs. (3.9a,b).

Eq. (3.23) can be solved with the aid of the prolate spheroidal wave functions [58]. The solution, however, is fairly complex. Alternatively, it can be solved using the following sampled approach [59,60].

Let the double-interval pulse $s(t)$ be represented by a

sampled waveform:

$$z(t) = \sum_{m=-M}^{+M} z_m \delta(t-md) \tag{3.24}$$

where

$$z_m = s(md),$$
$$d = T_s/M$$

and $\delta(t)$ is an impulse function.

Its Fourier transform is

$$Z(f) = \sum_{m=-M}^{+M} z_m e^{-j2\pi mfd} = \underline{z}^T \underline{p} \tag{3.25}$$

where $\underline{z}$ and $\underline{p}$ are $(2M+1)$ column vectors, i.e.

$$\underline{z}^T = [z_{-M}, z_{-(M-1)}, \ldots, z_o, \ldots z_{M-1}, z_M]$$

$$\underline{p}^T = [p_{-M}, p_{-(M-1)}, \ldots, p_o, \ldots, p_{M-1}, p_M]$$

and

$$p_m = e^{-j2\pi fmd}$$

Following the derivation given in [59,60], the inband energy fraction η is given by

$$\eta = \frac{\underline{z}^T R \underline{z}}{\underline{z}^T \underline{z}} \tag{3.26}$$

where R is a $(2M+1)\times(2M+1)$ matrix,

$$R = [r_{ik}],\ i,\ k=-M\ldots,0,\ldots,+M$$

$$r_{ik} = \frac{1}{(i-k)} \sin 2\pi \frac{i-k}{M} c$$

and

$$c = BT_s$$

The problem is to search for the eigenvector $\underline{z}_o$ corresponding to the maximum eigenvalue η_o of the equation

$$\eta \underline{z}^T \underline{z} = \underline{z}^T R \underline{z} \tag{3.27}$$

where $\underline{z}$ must satisfy the ISI- and jitter-free conditions (Eqs. (3.10a and b)), i.e.

$$z_m = z_{-m}, m=0,1,\ldots,M-1$$

and

$$z_M = z_{-M}=0$$

Eq. (3.27) is solved for the cases $M=20$ and $c=.5,\ .55,\ .60,\ldots,1$. The shapes of these double-interval pulses, $s(t)$, and eye diagrams of the corresponding IJF signals are illustrated in Fig. 3.9.

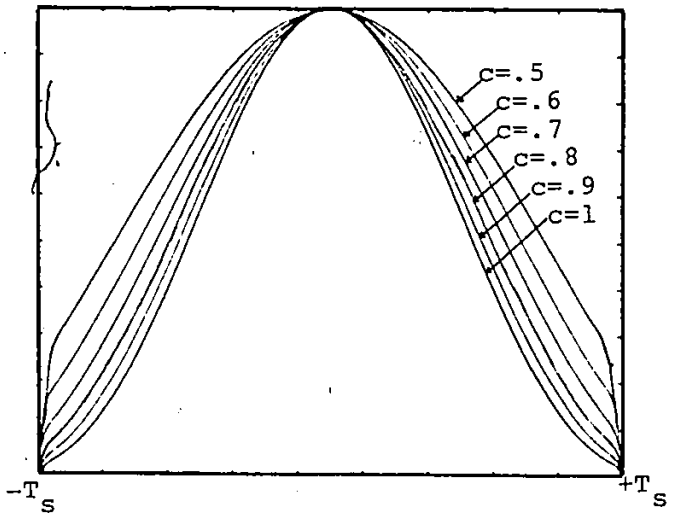

(a) double-interval pulse s(t)

(b) Eye diagrams

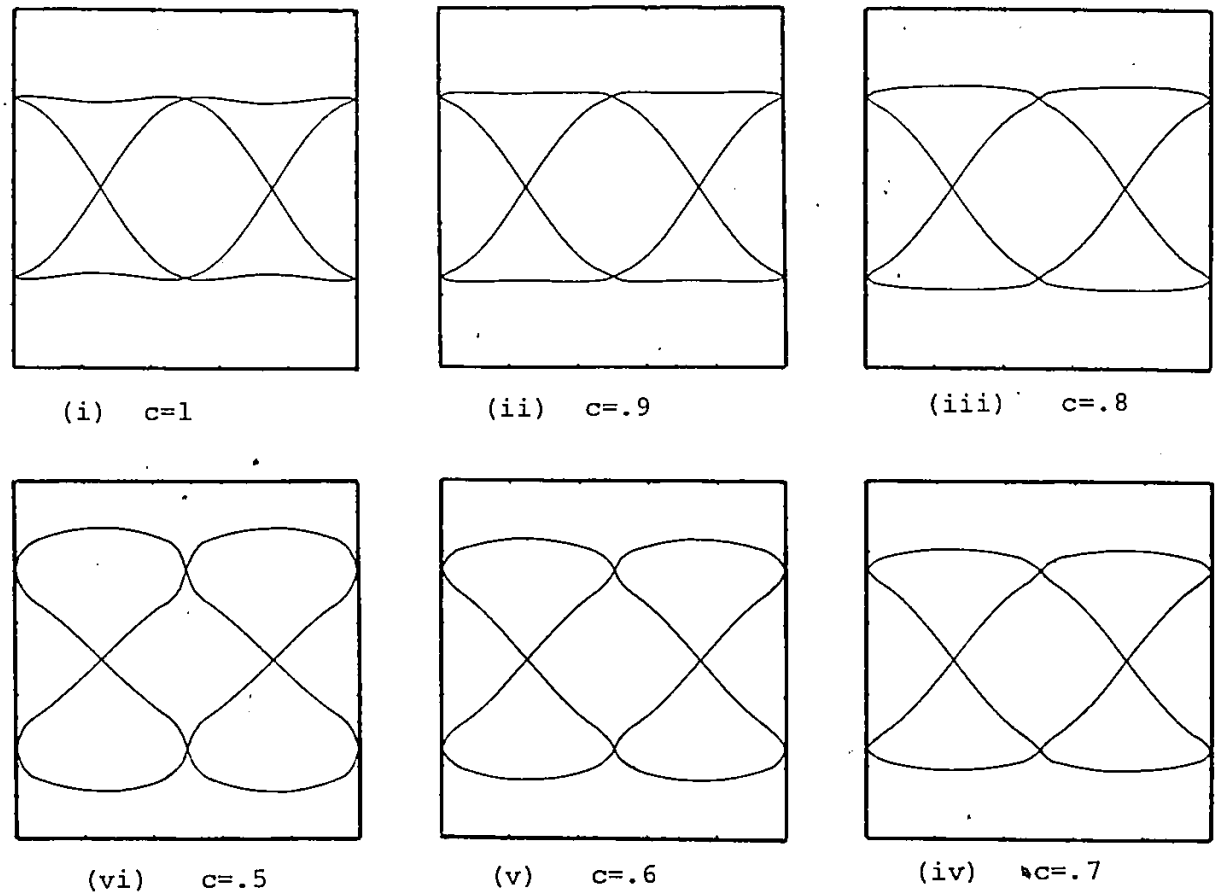

Fig. 3.9: IJF SIGNALS HAVING LOW OUT-OF-BAND ENERGY

Figure 3.10a shows the power spectral densities of these IJF signals. As c increases, the spectral mainlobe of the IJF signal becomes wider and its sidelobes get lower. Compared to the NRZ signals, these IJF signals show significant spectral advantages in terms of power spectrum (Fig. 3.10a) and out-of-band to inband energy ratio (Fig. 3.10b).

Figures 3.10a, b provide the necessary information to select an IJF signal for a specific application. For operational systems, an allowable out-of-band-to-in-band energy ratio is specified. A number of IJF signals that meet the requirement can be selected from Fig. 3.10b. Then Fig. 3.10a can be used to select an IJF signal based on the trade-off between the mainlobe occupancy and sidelobe level. For example, in digital Single-Channel-Per-Carrier (SCPC) satellite systems that satisfy the INTELSAT specifications [62], the required out-of-band-to-in-band energy ratio of the chosen signal must be lower than -26 dB for $BT_s=0.7$ where [-B, +B] is the specified RF bandwidth and $1/T_s$ is the symbol rate (i.e. power content at frequencies greater than or equal to 22.5 kHz must be greater than 26 dB down from the in-band signal power for the 64 kb/s QPSK signal [62, page 27]). Fig. 3.10b indicates that the IJF signals with c=0.70, 0.75 meet this requirement. From Fig. 3.10a, the IJF signal for c=0.75 is a suitable choice with the mainlobe occupancy of $0.87/T_s$ and highest sidelobe level of -32 dB. Note that the overlapped raised-cosine pulse (Fig. 3.8, case N=1) used in QORC modulation scheme [47] does not meet with this out-

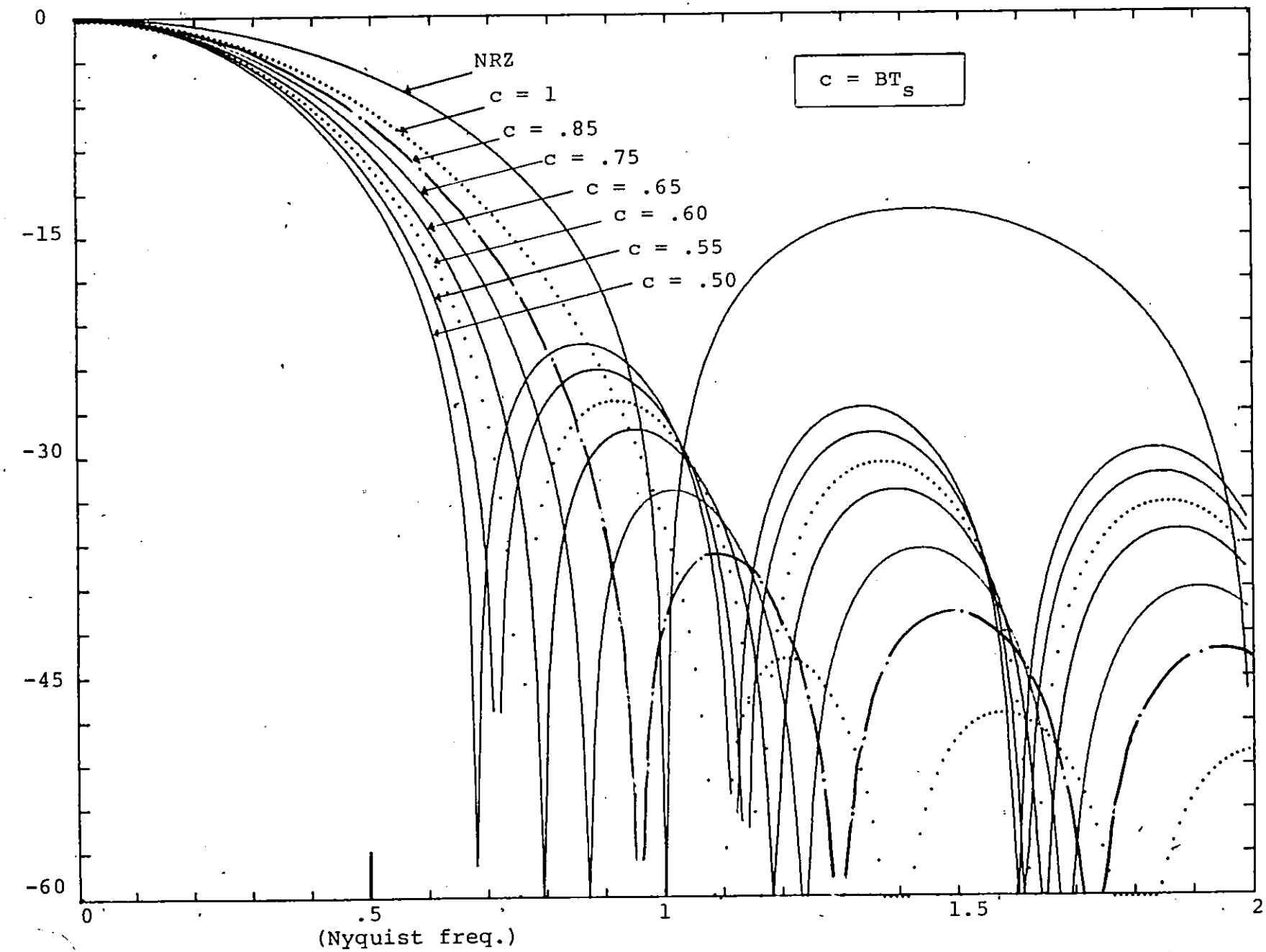

Fig. 3.10a: NORMALIZED POWER SPECTRA OF IJF SIGNALS HAVING LOW OUT-OF-BAND ENERGY

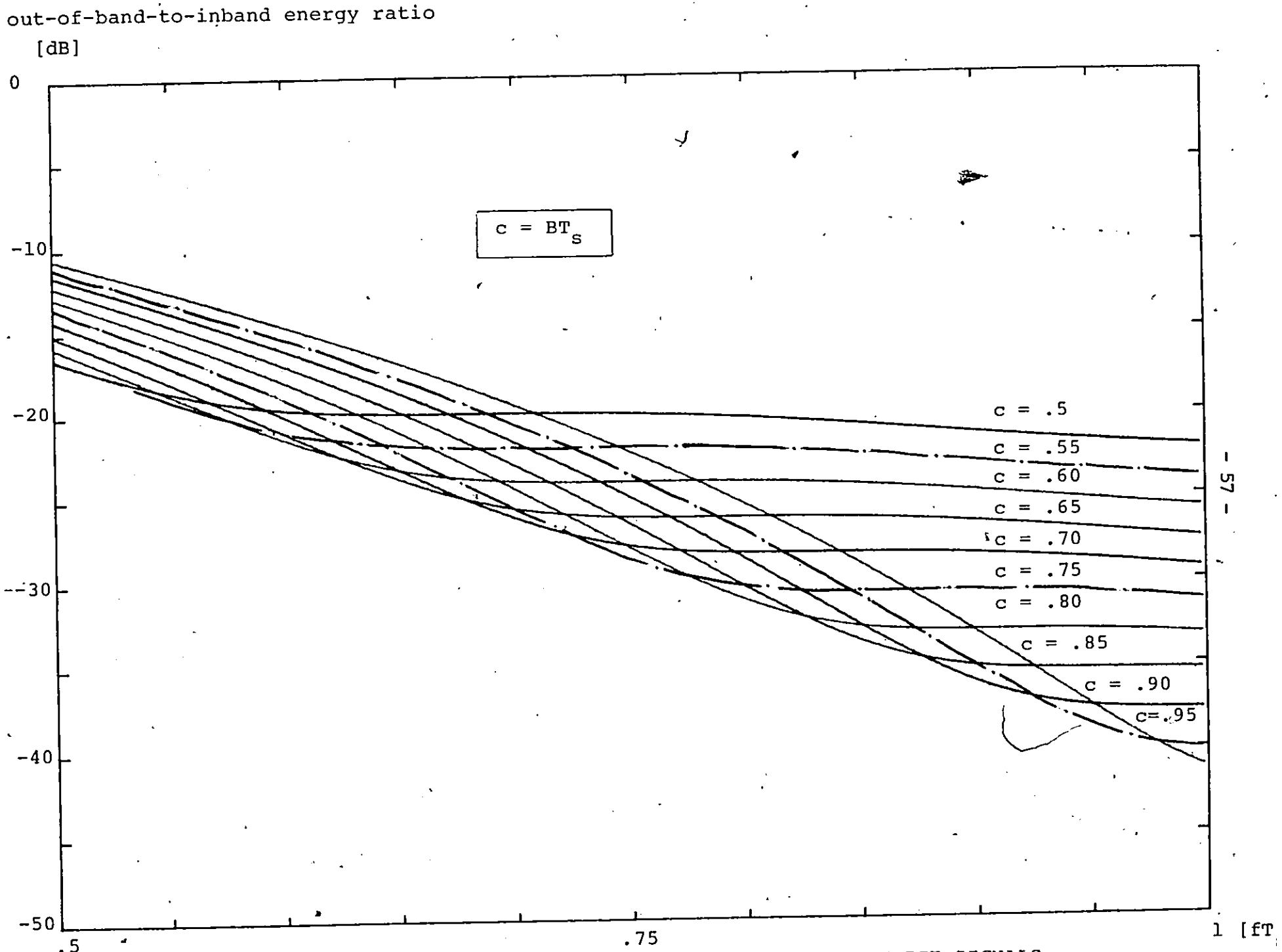

Fig. 3.10b: OUT-OF-BAND-TO-INBAND ENERGY RATIOS OF IJF SIGNALS HAVING LOW OUT-OF-BAND ENERGY

of-band emission requirement.

3.3 ERROR PROBABILITY (P_e) PERFORMANCE:

Figure 3.11 shows a model of an additive white gaussian noise (AWGN) linear baseband channel. The signal r(t), at the input of the receiver is

$$r(t) = y(t)+n(t) \tag{3.28}$$

where y(t) is the transmitted IJF signal, and n(t) is the AWGN with a double-sided spectral density $N_o/2$. Due to the overlapping pulses, the optimum maximum likelihood receiver is known to be a set of matched filters, the number of which depends exponentially on the length of the message [25].

Though theoretically meaningful, this approach has a very limited practical interest due to the excessive complexity required. Another derivation has been given by Forney [63], in which the received signal is processed by a recursive structure using the Viterbi Algorithm. However, the implementation of such a receiver still remains complex and can only be justified when classical receivers such as linear or nonlinear transversal equilizers cannot be designed to achieve a satisfactory performance.

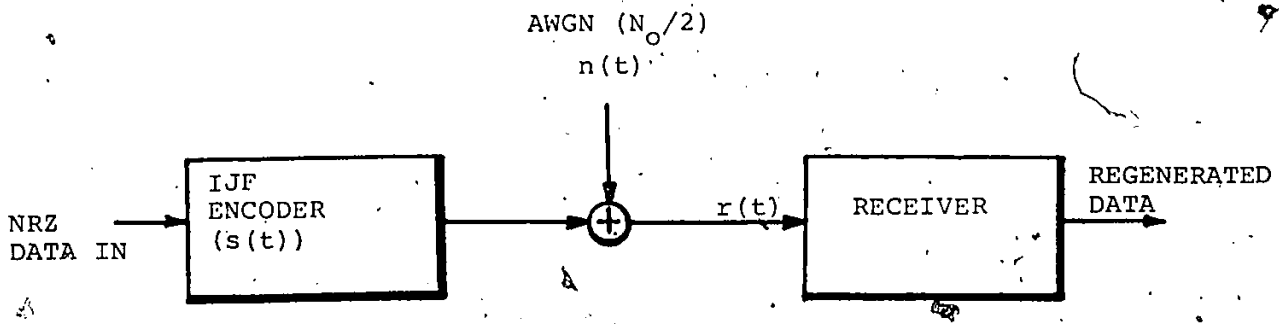

Fig. 3.11: IJF LINEAR BASEBAND MODEL

In this section, the error probability (P_e) performance of the IJF baseband channels using

(i) Linear transversal receivers,

(ii) Decision-Feedback receivers,

and (iii) Raised-cosine-type receivers

is analytically evaluated. The receiver structures are illustrated in Figs. 3.12a-c.

3.3.1. Linear Transversal Receiver

The coefficients of the different transversal filters can be optimized under several criteria. The most commonly used are the minimum-mean-square-error (MMSE) and the minimum average error probability under the constraint of no ISI. It has been shown that the latter gives the same results as the MMSE criterion, under the condition of a reasonably high signal to noise ratio (SNR) [8]. Its performance being independent of the SNR, it is more convenient to use it when comparing different transmission schemes. That is what we do in the sequel.

The matched filter impulse response is given by the expression of the *IJF double-interval* pulse shape at the transmitter, i.e., $\bar{s}_N(t)$. The impulse response at the output of the matched filter is expressed as the autocorrelation function of $\bar{s}_N(t)$,

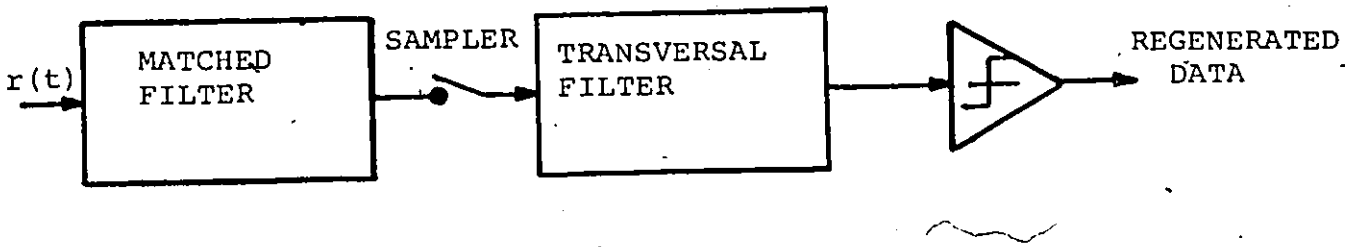

(a) LINEAR TRANSVERSAL FILTER

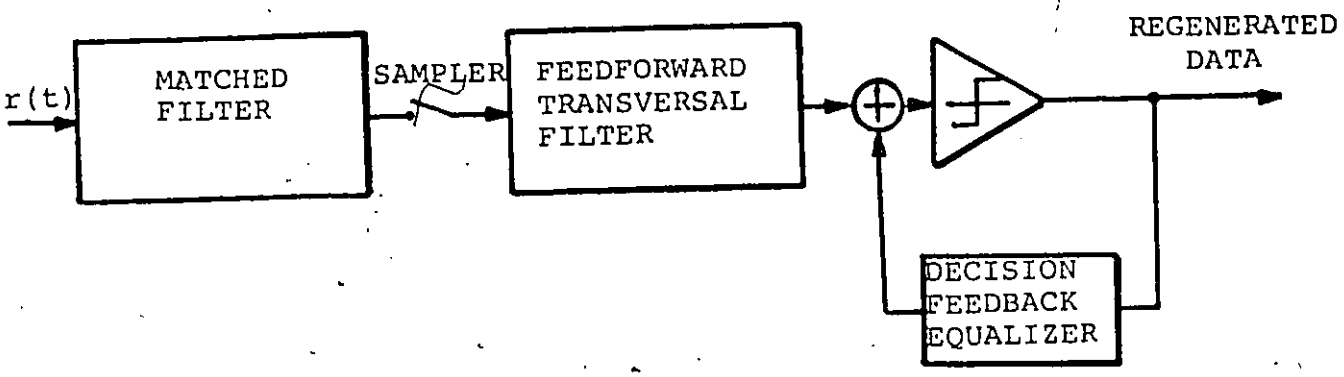

(b) NONLINEAR DECISION-FEEDBACK FILTER

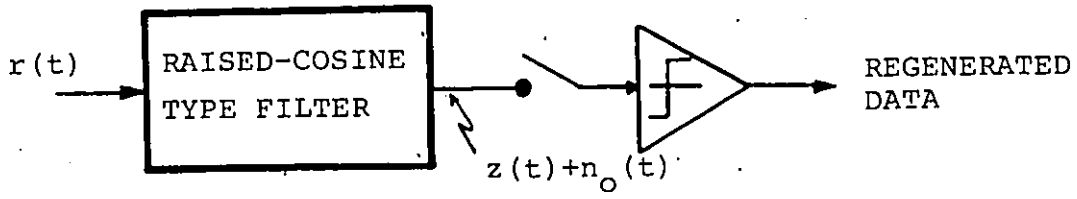

(c) RAISED-COSINE TYPE RECEIVER

Fig. 3.12: RECEIVER STRUCTURES

$$\bar{R}_N(t) = \int_{-\infty}^{+\infty} \bar{s}_N(\tau)\bar{s}_N(t+\tau)d\tau \qquad (3.29)$$

Three particular cases of interest are given, for a class of IJF signals having fast spectral roll-off properties with N=0,1,2 shown by Eq. (3.16), i.e.

$$\bar{s}_0(t) = \cos\frac{\pi t}{2T_s}, \qquad |t| \le T_s \qquad (3.30a)$$

$$\bar{s}_1(t) = \frac{1}{2}\left(1+\cos\frac{\pi t}{T_s}\right), \qquad |t| \le T_s \qquad (3.30b)$$

$$\bar{s}_2(t) = \frac{1}{4}\left(3\cos\frac{\pi t}{2T_s} + \cos\frac{3\pi t}{2T_s}\right), \qquad |t| \le T_s \qquad (3.30c)$$

Since the basic pulses are limited to $[-T_s, +T_s]$, $\bar{R}_N(t)$ is finite over an interval $[-2T_s, +2T_s]$ and is zero elsewhere. Their normalized expressions are

$$\bar{R}_0(t) = \left(1-\frac{|t|}{2T_s}\right)\cos\frac{\pi|t|}{2T_s} + \frac{1}{\pi}\sin\frac{\pi|t|}{2T_s}, \quad |t| \le 2T_s \qquad (3.31a)$$

$$\bar{R}_1(t) = \frac{1}{3}\left(2-\frac{|t|}{T_s}\right)\left[1+\frac{1}{2}\cos\frac{\pi|t|}{T_s}\right] + \frac{1}{2\pi}\sin\frac{\pi|t|}{T_s}, \quad |t| \le 2T_s \qquad (3.31b)$$

$$\bar{R}_2(t) = \frac{1}{2}\left[\frac{1}{10}\left(2-\frac{|t|}{T_s}\right)\left(9\cos\frac{\pi|t|}{2T_s} + \cos\frac{3\pi|t|}{2T_s}\right)\right.$$

$$\left. + \frac{9}{10\pi}\sin\frac{\pi|t|}{2T_s} + \frac{11}{30\pi}\sin\frac{9\pi|t|}{2T_s}\right], \quad |t| \le 2T_s \qquad (3.31c)$$

The infinite-length transversal filter is used to eliminate ISI

residues in the matched filter impulse response. The error probability versus the energy per bit to noise spectral density ratio (E_b/N_o) is obtained by relating the signal energy per bit to the amplitude of the impulse response at the sampling time and the noise spectral density to its variance at the output of the filter. It can be expressed as [25]

$$P_e = \frac{1}{2} \operatorname{erfc} \sqrt{\frac{E_b}{N_o F}} \tag{3.32}$$

where

$$\operatorname{erfc}(x) = \frac{2}{\sqrt{\pi}} \int_x^{\infty} e^{-u^2} du$$

and F represents the performance comparison factor between the IJF transmission techniques and the optimum binary transmission scheme (i.e. $P_e=\frac{1}{2} \operatorname{erfc}\sqrt{\frac{E_b}{N_o}}$). By normalizing the autocorrelation function so that $\bar{R}(o)=1$, the performance comparison factor, F, is given by

$$F = \frac{\sigma^2}{(N_o/2)} \tag{3.33}$$

where σ^2 is the noise variance at the output of the infinite-length transversal filter.

The sampled and normalized autocorrelation function is expressed in z- domain as

$$R(z) = \rho z^{-1} + 1 + \rho z$$

$$R(z) = (p-qz)\ (p-qz^{-1}) \tag{3.34}$$

where

$$\rho = \bar{R}(\pm T_s) < 1/2,$$

p and q satisfy the following properties

$$p^2 + q^2 = 1$$

$$pq = -\rho$$

$$|p| > |q|$$

The z-transform of the linear transversal filter impulse response approximates the inverse of R(z),

$$T(z) = \frac{1}{R(z)} = \frac{1}{p-qz} \cdot \frac{1}{p-qz^{-1}} \tag{3.35}$$

The first term $\frac{1}{p-qz}$ represents an infinite length anticausal transversal filter which can be made realizable by assuming an appropriate truncation and delay. This filter is often referenced as a pre-whitening filter [63] since the noise samples at its output are independent and have a variance $N_o/2$.

The second term $\frac{1}{p-qz^{-1}}$ represents a semi-infinite-length transversal filter,

$$\frac{1}{p-qz^{-1}} = \frac{1}{p} \sum_{m=0}^{\infty} \left(\frac{q}{p}\right)^m z^{-m} \tag{3.36}$$

The noise variance σ^2 at the output of this transversal filter can be obtained as [25]

$$\sigma^2 = \frac{N_o}{2} \sum_{m=0}^{\infty} \left[\frac{1}{p} \left(\frac{q}{p}\right)^m\right]^2 = \frac{N_o}{2} \frac{1}{p^2-q^2} \tag{3.37}$$

From Eqs. (3.33, 3.37) the performance comparison factor can be expressed in (dB) as

$$F^{TF}\ (dB) = -10 \log_{10} (p^2-q^2) = -5\log_{10}(1-4\rho^2) \tag{3.38}$$

This factor represents the necessary increase of the E_b/N_o to get the same error probability as with optimum binary transmission techniques.

In the derivation of Eq. (3.38) an infinite length transversal filter was assumed. It is of interest to consider the performance expected from a realizable filter, i.e., to consider the effect of the truncation of this infinite transversal filter. Compared with the infinite length case, the performance with a finite-length transversal filter is influenced by the following:

(i) Dependence of the noise variance on the length of the transversal filter

(ii) Variation of the amplitude of the overall impulse response

(iii) Residual ISI

Fig. 3.13 illustrates the numerical results obtained for the three IJF signals represented by Eqs. 3.30a-c. It is interesting to note that even a low number of taps (typically 5) leads to small performance degradations.

3.3.2. Decision-Feedback Equalizer

A more attractive structure is given by the decision feedback equalizer (DFE). This equalizer incorporates a feedforward and a feedback path, such as shown in Fig. 3.12b.

It is known that this receiver always gives better theoretical performance than the linear receiver, neglecting the error propagation effect [70]. This is mainly explained by the absence of noise enhancement in the feedback part of the receiver. The degradation due to the error propagation effect depends on the number of feedback taps and on their amplitude. Since we are looking for the optimum DFE under the constraint of no ISI, the feed-forward part is the whitening filter previously discussed and the feedback part reduces to only one tap. So the error propagation has a slight effect on the global performance. The feedback tap eliminates the ISI component from the *past symbol* represented

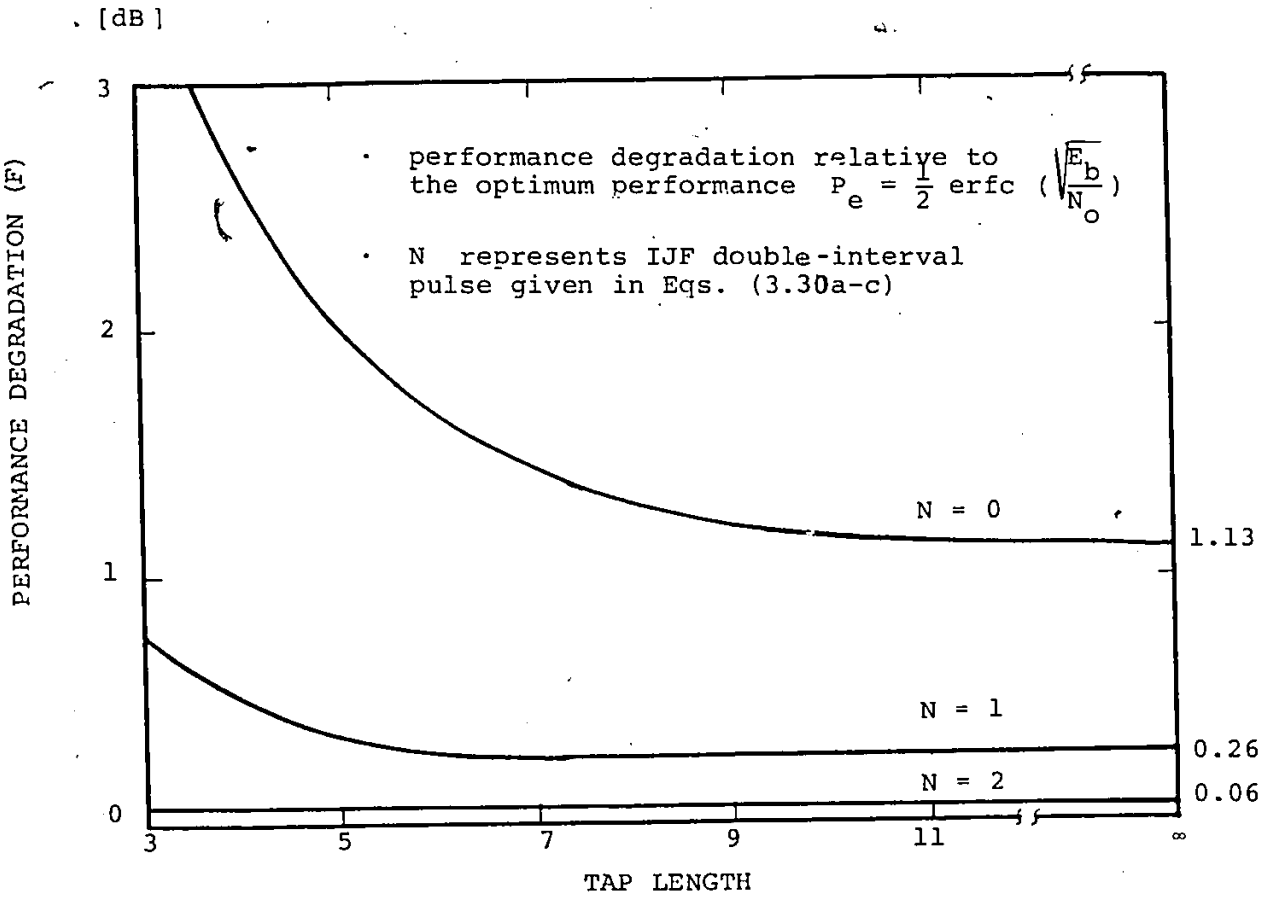

Fig. 3.13: P_e PERFORMANCE OF LINEAR TRANSVERSAL FILTERS VERSUS TAP LENGTH

by $(-qz^{-1})$. The amplitude of the signal at the sampling time is p<1. Therefore the comparison factor for the *optimum* DFE is given by

$$F_{(dB)}^{DFE} = -20 \log (p) = -10\log_{10}\{(1+(1-4\rho^2)^{\frac{1}{2}})/2\} \tag{3.39}$$

representing the loss due to the amplitude attenuation at the sampling time. The results for the DFE versus the number of taps of the forward filter are displayed in Fig. 3.14. A significant improvement has been achieved compared with the linear transversal filter. Furthermore the DFE requires fewer taps than the linear transversal equalizer for the same P_e performance.

3.2.3 Raised-Cosine-Type Receiver

The receiver filter shown in Fig. 3.12c is a raised-cosine-type filter having a linear phase response and the following amplitude characteristics.

$$G(x) = \frac{R(x,\alpha)}{S(x)} \tag{3.40}$$

where

$x = fT_s$

$S(x)$ is the Fourier transform of $s(t)$ and $s(t)$ is defined by Eq. (3.7)

and

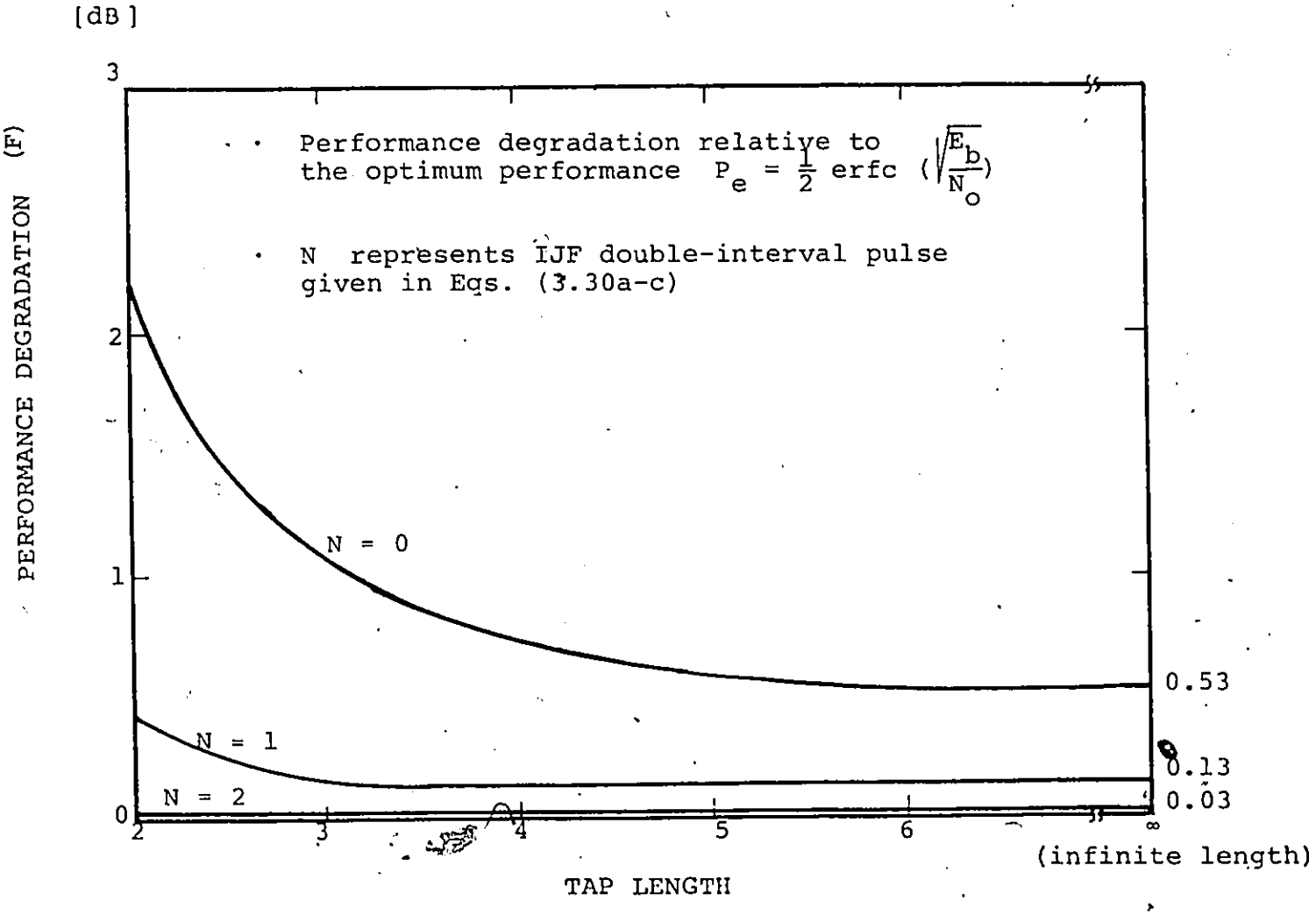

Fig. 3.14: P_e PERFORMANCE OF NONLINEAR DECISION-FEEDBACK FILTERS VERSUS TAP LENGTH

$R(x,\alpha)$ is the amplitude response of a raised-cosine filter, i.e.

$$R(x,\alpha) = \begin{cases} 1, & \text{for } 0 \le x \le \frac{1}{2}(1-\alpha) \\ \frac{1}{2}\left(1-\sin\frac{\pi}{\alpha}\left(x-\frac{1}{2}\right)\right), & \text{for } \frac{1}{2}(1-\alpha) \le x \le \frac{1}{2}(1+\alpha) \\ 0, & \text{for } x \ge \frac{1}{2}(1+\alpha) \end{cases}$$

The output of the raised-cosine type filter can be represented as

$$v(t) = z(t)+n_o(t) \tag{3.41}$$

where $z(t)$ is the noise-free, filtered signal component, and $n_o(t)$ is the filtered noise component.

It can be shown that the noise-free filtered signal component $z(t)$ prior to detection is ISI-free. The error probability P_e is given by [25,24].

$$P_e = \frac{1}{2}\,\mathrm{erfc}\left(\frac{A}{\sigma\sqrt{2}}\right) \tag{3.42}$$

where A is the peak amplitude of $z(t)$ at the sampling instants and σ^2 is the power of the filtered noise, $n_o(t)$.

The average energy per bit E_b of the transmitted IJF signal $y(t)$ is

$$E_b = A^2 \int_{-T_s}^{+T_s} s^2(t)\, dt \qquad (3.43a)$$

Note that $s(t)$ is normalized so that $s(o)=1$.

The power of the filtered noise is

$$\sigma^2 = \frac{N_o}{T_s} \int_0^{\frac{1+\alpha}{2}} G^2(x,\alpha)\, dx \qquad (3.43b)$$

where $\frac{N_o}{2}$ is the double-sided spectral density of the AWGN.

Substituting Eqs. (3.43a,b) into Eq. (3.42) yields

$$P_e = \frac{1}{2} \operatorname{erfc} \left(\frac{1}{\rho} \sqrt{\frac{E_b}{N_o}}\right) \qquad (3.44a)$$

where

$$\rho^2 = \frac{1}{T_s} \int_{-T_s}^{+T_s} s^2(t)dt. \int_0^{\frac{1+\alpha}{2}} G^2(x,\alpha)dx \qquad (3.44b)$$

It is noted that ρ^2 represents the degradation in P_e performance of the IJF signal relative to the optimum performance, i.e.,

$$P_e = \frac{1}{2} \operatorname{erfc} \left(\sqrt{\frac{E_b}{N_o}}\right).$$

For example, if the double interval pulse

$$s(t) = \frac{1}{2}(1+\cos\frac{\pi t}{T_s})$$

is chosen, then the amplitude response of the receive filter is

$$G(x,\alpha) = R(x,\alpha) \cdot \frac{(1-4x^2)2\pi x}{\sin 2\pi x}$$

Figure 3.15a shows the plots of $G(x,\alpha)$ for the different values of the roll-off factor (α). The E_b/N_o degradation (ρ^2) as a function of the roll-off factor (α) for this receive filter is plotted in Fig. 3.15b. It is shown that the best performance (i.e. lowest degradation) is obtained with $\alpha=0.6$ and the degradation compared to the theoretical optimum performance is negligible.

3.3.4 Comparision of Measured and Analytical P_e Performance Results

The P_e performance of an IJF baseband channel (Fig. 3.11) is also experimentally evaluated. As an illustrative example, the double-interval pulse

$$s(t) = \frac{1}{2}(1+\cos\frac{\pi t}{T_s})$$

is used. The bit rate is

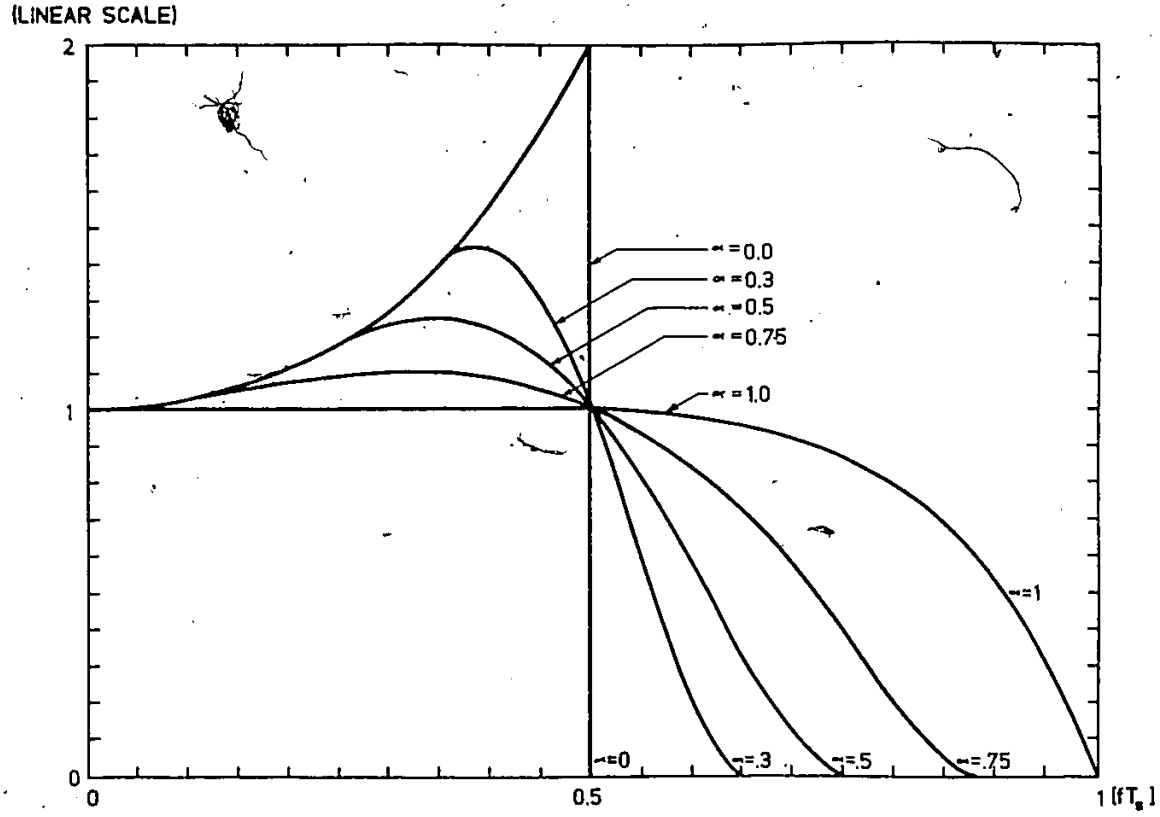

(a) AMPLITUDE RESPONSE

(b) PERFORMANCE DEGRADATION VERSUS ROLL-OFF FACTOR

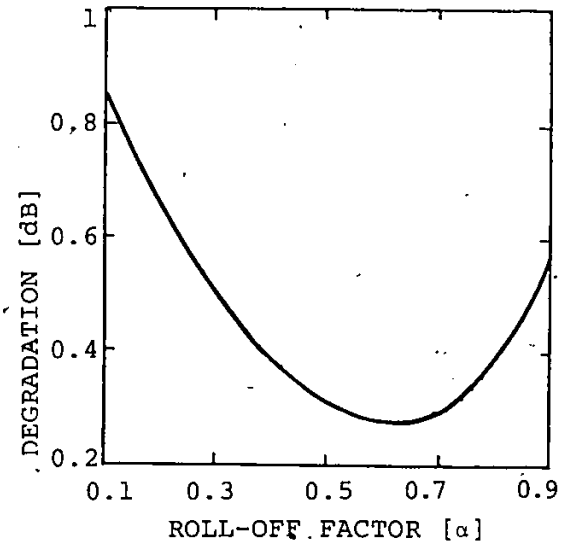

Fig. 3.15: RAISED-COSINE-TYPE FILTER FOR $s(t) = \frac{1}{2}(1+\cos\frac{\pi t}{T_s})$

$$\frac{1}{T_s} = 32 \text{ kb/s}$$

The receive filter is an equalized 4th order Butterworth which approximates the raised-cosine-type filter with $\alpha=0.4$ (Fig. 3.15a).

The measured result is shown in Fig. 3.16. The E_b/N_o degration compared to the theoretical optimum performance is 0.5 dB and in agreement with the computed result shown in Fig. 3.15b (E_b/N_o degradation = 0.4 dB for $\alpha = 0.4$).

Parts of this chapter were presented in [61, 79].

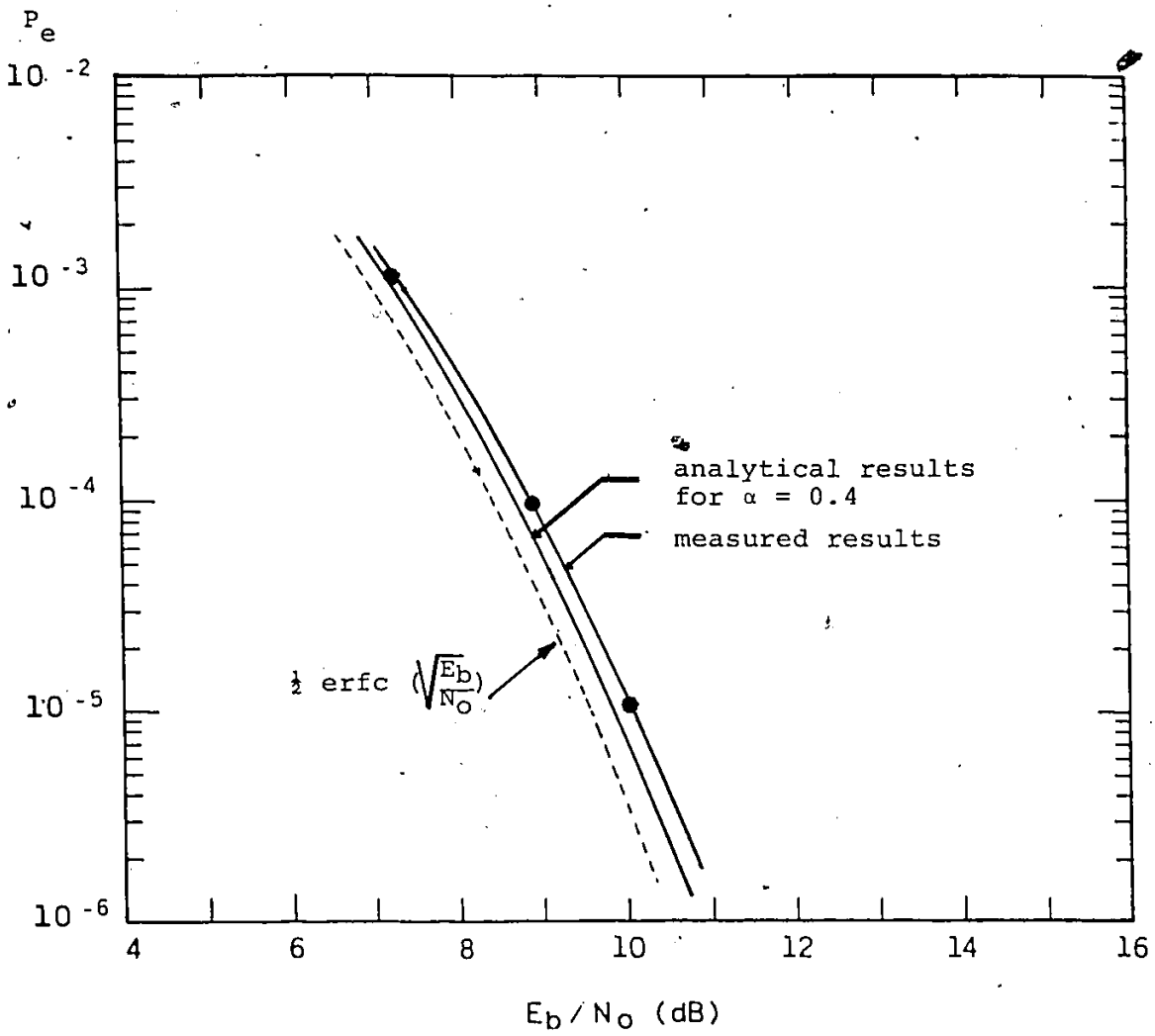

Fig. 3.16: MEASURED PERFORMANCE OF AN IJF SIGNAL (N=1)

CHAPTER FOUR:
IJF-QUADRATURE MODULATION TECHNIQUES: SPECTRAL PROPERTIES

SUMMARY:

IJF baseband signals introduced in the previous chapter are combined with quadrature phase modulation techniques. The resulting modulation schemes are called IJF-Quadrature-Phase-Shift-Keying (IJF-QPSK) and IJF-Offset QPSK (IJF-OQPSK).

The spectral properties of these IJF-quadrature modulated signals in linear and nonlinear channels are studied. Their envelope fluctuations are also investigated. A 16-state Markov chain model is used to derive the power spectral density function of hardlimited IJF-quadrature modulated signals. The spectrum spreading action of the ideal hardlimiter and the effects of the time offset between inphase and quadrature baseband components are examined. Experiments and computer simulations are performed to verify analytical results. Spectral properties of IJF-quadrature modulated signals in other nonlinear channels are also investigated using simulation techniques.

The results demonstrate that the described IJF-OQPSK schemes have attractive spectral properties in comparison to other digital modulation techniques.

4.1 PROPERTIES OF IJF-QUADRATURE MODULATED SIGNALS

The block diagram of an IJF-quadrature modulator is shown in Fig. 4.1. The NRZ input signal $x(t)$ is serial-to-parallel converted into two NRZ data streams $x_I(t)$ and $x_Q(t)$. The symbol interval T_s of $x_I(t)$ or $x_Q(t)$ is twice of the bit interval T_b of $x(t)$.

The data stream $x_Q(t)$ is delayed by d where $0 \leq d < T_s$ to produce $x_Q(t-d)$. NRZ signals $x_I(t)$ and $x_Q(t-d)$ are encoded into IJF signals $y_I(t)$ and $y_Q(t)$ respectively. The IJF signals $y_I(t)$ and $y_Q(t)$ modulate the quadrature carriers, $\cos 2\pi f_c t$ and $\sin 2\pi f_c t$, are then summed to produce the IJF-quadrature modulated signal $z(t)$,

$$z(t) = y_I(t) \cos 2\pi f_c t + y_Q(t) \sin 2\pi f_c t \qquad (4.1)$$
$$= A(t) \cdot \cos[2\pi f_c t + \phi(t)]$$

where $A(t)$ and $\phi(t)$ are the envelope and phase of the IJF-quadrature modulated signal,

$$A(t) = \sqrt{y_I^2(t) + y_Q^2(t)} \qquad (4.2a)$$

and

$$\phi(t) = -\tan^{-1}\left(\frac{y_Q(t)}{y_I(t)}\right) \qquad (4.2b)$$

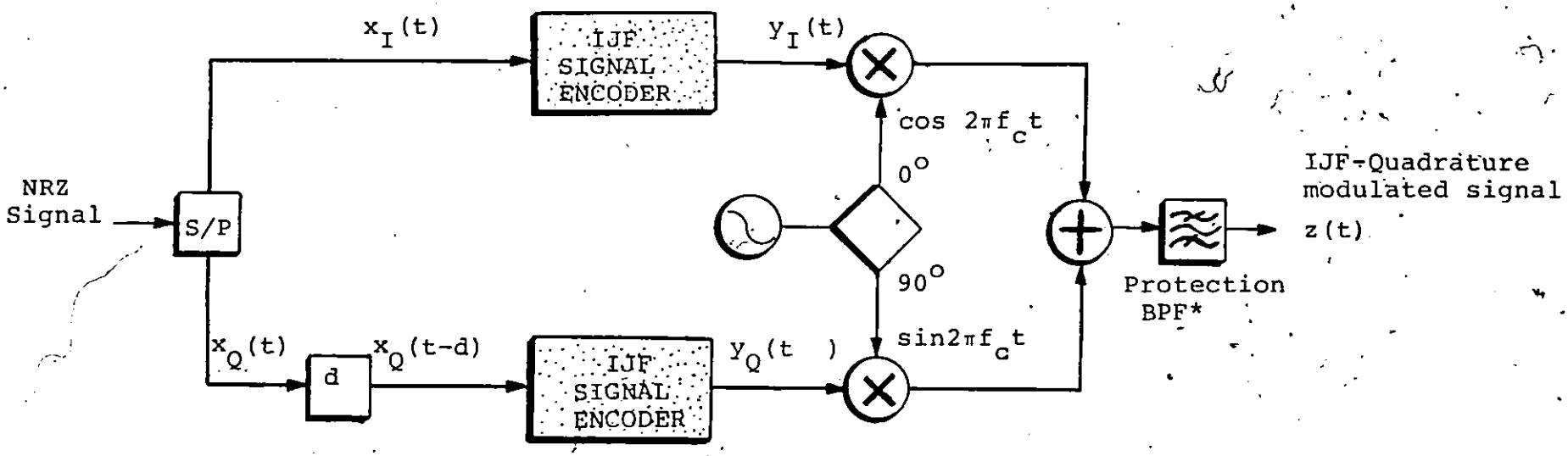

(* Protection BPF removes higher-order intermodulation products)

Fig. 4.1: BLOCK DIAGRAM OF AN IJF-QUADRATURE MODULATOR

The modulation scheme is called IJF-QPSK for $d=0$ and IJF-Offset QPSK for $d=T_b$. It is noted that the modulator requires no extra *transmit shaping filters* except IJF encoders.

Based on Eq. (3.9) and the structure of the quadrature modulator, the PSD function of the IJF-quadrature modulated signal $z(t)$ can be obtained from:

$$Z(f) = K|S(f-f_c)|^2 \tag{4.3}$$

where K is a constant and $S(f)$ is the Fourier transform of $s(t)$ defined by Eq. (3.7).

Figs. 4.2a and b show the envelope fluctuation, and signal space diagram of the IJF-QPSK signal respectively. Since the transition times in $y_I(t)$ and $y_Q(t)$ coincide, the envelope of the IJF-QPSK signal exhibits serious fluctuations.

By delaying the data stream $x_Q(t)$ by T_b relative to $x_I(t)$, the resultant IJF-OQPSK signal exhibits a maximum envelope fluctuation of 3 dB as shown in Figs. 4.3a, and b.

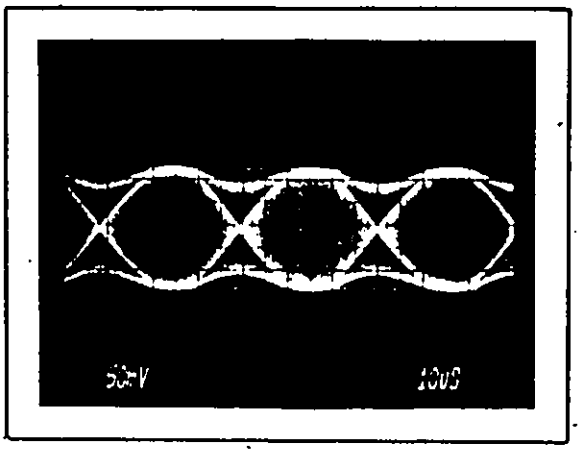

- *bit rate:* 64 kb/s
- *carrier frequency:* 512 kHz

(a) MEASURED IJF-QPSK SIGNAL (N=1)

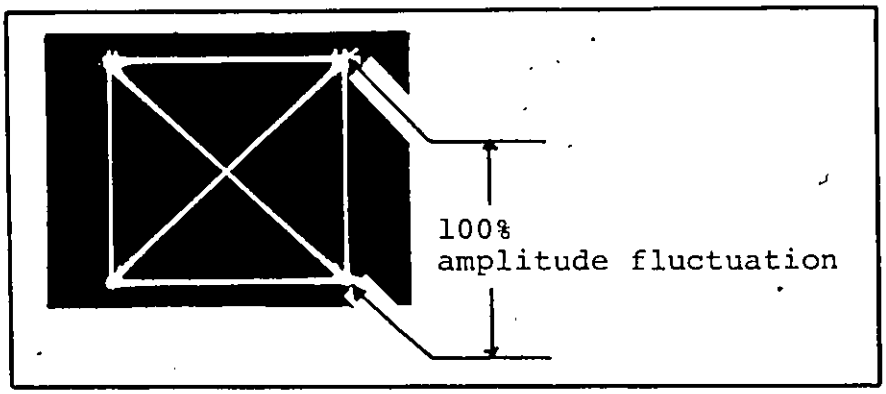

(b) MEASURED SIGNAL SPACE DIAGRAM

Fig. 4.2: ENVELOPE FLUCTUATION OF AN IJF-QPSK SIGNAL

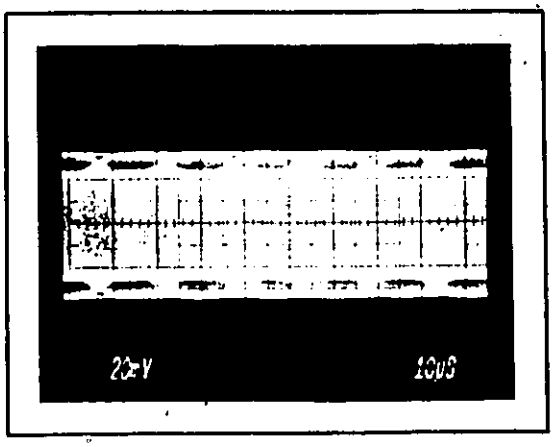

- *bit rate:* 64 kb/s
- *carrier frequency:* 512 kHz

(a) MEASURED IJF-OFFSET QPSK SIGNAL

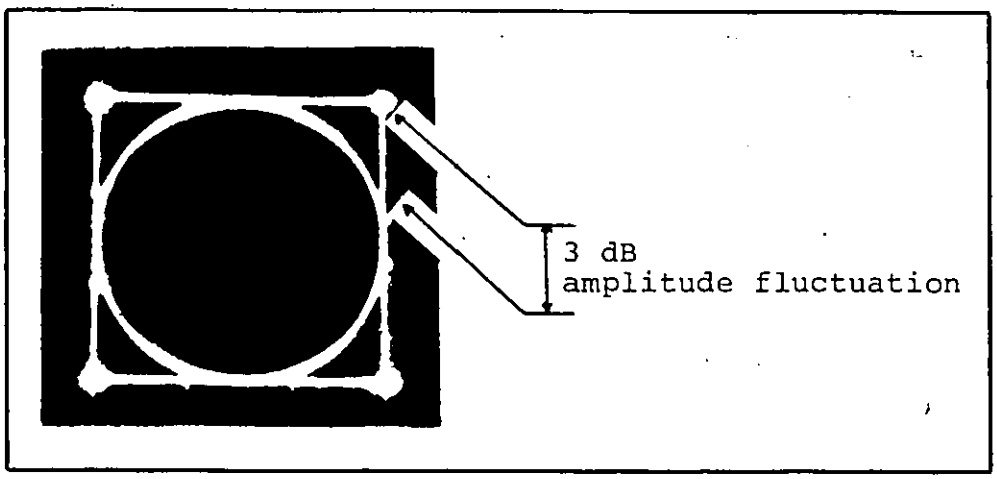

(b) MEASURED SIGNAL SPACE DIAGRAM

Fig. 4.3: ENVELOPE FLUCTUATION OF AN IJF-OFFSET QPSK SIGNAL

4.2 PROPERTIES OF HARDLIMITED IJF-QUADRATURE MODULATED SIGNALS

To maximize power efficiency, the HPA (high power amplifier) has to operate in a nonlinear mode. Consider the IJF-quadrature modulator followed by a saturated HPA shown in Fig. 4.4a. The saturated HPA may be modelled as an ideal hardlimiter that produces a constant output envelope and no change to the phase of the IJF-quadrature modulated signal [74]. The transfer characteristic of the ideal hardlimiter is shown in Fig. 4.4b. Such a model closely approximates Gunn and Impatt diode injection locked amplifiers and is a reasonable first order approximation of saturated HPAs in general.

The hardlimited IJF-quadrature modulated signal $z'(t)$ can be represented as [5]*

$$z'(t) = y'_I(t) \cos 2\pi f_c t + y'_Q(t) \sin 2\pi f_c t \qquad (4.4)$$

$$= C \cos(2\pi f_c t + \Phi'(t))$$

where $y'_I(t)$ and $y'_Q(t)$ are inphase and quadrature equivalent baseband components of the hardlimited IJF quadrature modulated

---

* *The first harmonic (fundamental) of the hardlimited signal is considered as an approximation of practical RF devices.*

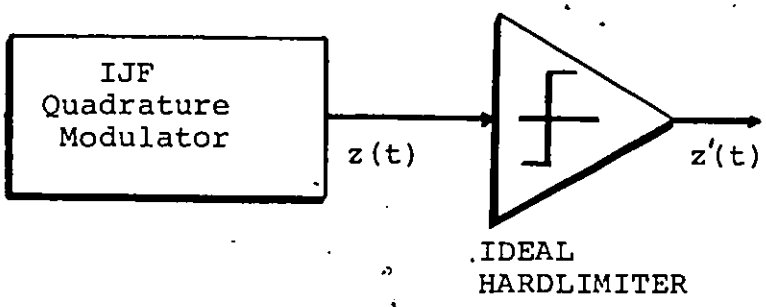

Fig. 4.4a: BLOCK DIAGRAM OF AN IJF QUADRATURE MODULATOR FOLLOWED BY A HARDLIMITER

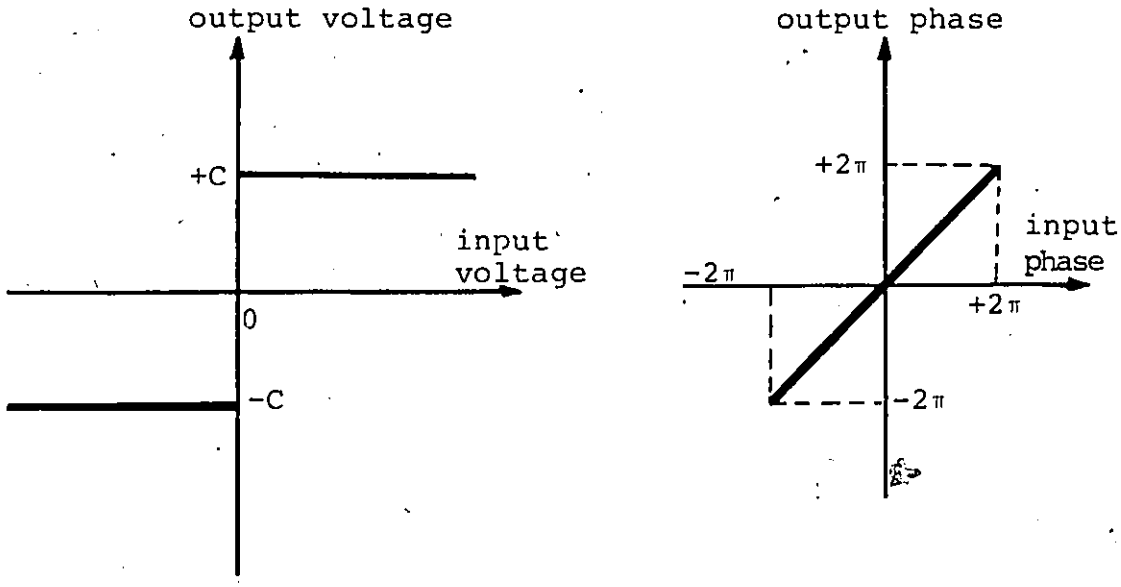

(i) AMPLITUDE (ii) PHASE

Fig. 4.4b: TRANSFER CHARACTERISTICS OF AN IDEAL HARDLIMITER

signal and

$$y'^2_I(t) + y'^2_Q(t) = C^2: \text{ constant} \tag{4.5}$$

and

$$\phi'(t) = -\tan^{-1}\left\{\frac{y'_Q(t)}{y'_I(t)}\right\} \tag{4.6a}$$

Since the ideal limiter has no memory,

$$\phi'(t) = \phi(t) \tag{4.6b}$$

From Eqs. (4.2b), (4.6a,b), it can be shown that

$$\frac{y'_Q(t)}{y'_I(t)} = \frac{y_Q(t)}{y_I(t)} \tag{4.7}$$

By substituting Eq. (4.7) into Eq. (4.5), it follows that

$$y'_I(t) = \frac{Cy_I(t)}{\sqrt{y_I^2(t) + y_Q^2(t)}} \tag{4.8a}$$

and

$$y'_Q(t) = \frac{Cy_Q(t)}{\sqrt{y_I^2(t) + y_Q^2(t)}} \tag{4.8b}$$

Eqs. (4.8a,b) indicate that for any change in $y_I(t)$ (or $y_Q(t)$), $y'_Q(t)$ (or $y'_I(t)$) are affected. In other words, hard-limiting introduces *crosstalk* between the inphase and quadrature equivalent baseband components [74].

Figs. 4.5a, b show the measured eye diagram of $y_I'(t)$ and $y_Q'(t)$ (at the output of the demodulation lowpass filters and signal space diagram of the hardlimited IJF-QPSK signal respectively. Since the transitions in $y_I(t)$ and $y_Q(t)$ occur at the same time, the eye diagrams of the inphase and quadrature equivalent baseband components, $y_I'(t)$ and $y_Q'(t)$, of the hardlimited IJF-QPSK signal *remain ISI and jitter free*. However the hardlimiter introduced sharp transitions in $y_I'(t)$ and $y_Q'(t)$. This implies that the high frequency spectral components of the *hardlimited* IJF-QPSK signal are higher than those of the IJF-QPSK.

Figs. 4,6a,b show the measured eye diagrams of $y_I'(t)$ and $y_Q'(t)$ and signal space diagram of the hardlimited IJF-OQPSK signal. Since the transition in $y_I(t)$ (or $y_Q(t)$) occurs at the maximum eye opening point of $y_Q(t)$ (or $y_I(t)$), the inphase to quadrature *crosstalk* introduces *intersymbol interference (ISI)*. As shown in Figs. 4.6a,b the peak-to-peak ISI is 3 dB.

4.3 DERIVATION OF THE POWER SPECTRAL DENSITY FUNCTION OF HARDLIMITED IJF-QUATRATURE MODULATED SIGNALS

Let the baseband component $y_I'(t)$ (or $y_Q'(t-d)$), represented as the sum of an infinite number of single-interval pulse shapes $q(t_n)$ defined in one symbol interval $[(n-\frac{1}{2})T_s, (n+\frac{1}{2})T_s]$, i.e.

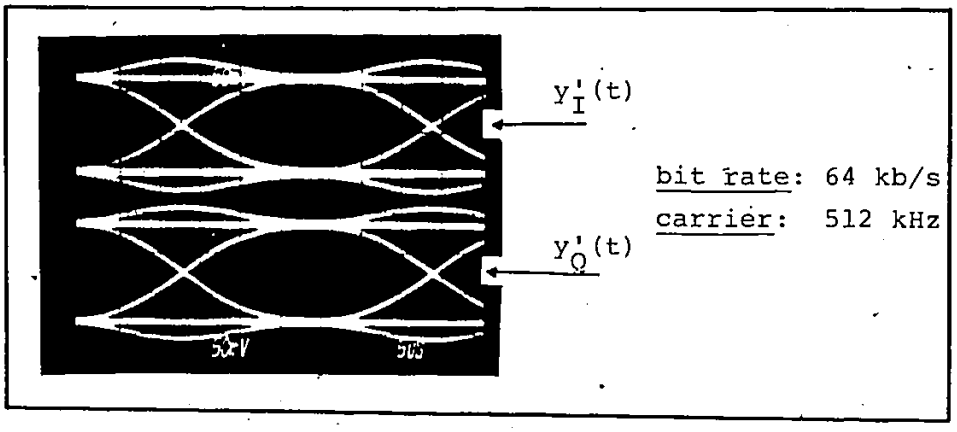

(a) MEASURED EYE DIAGRAMS OF $y'_I(t)$ and $y'_Q(t)$
(at the outputs of the demodulator lowpass filters)

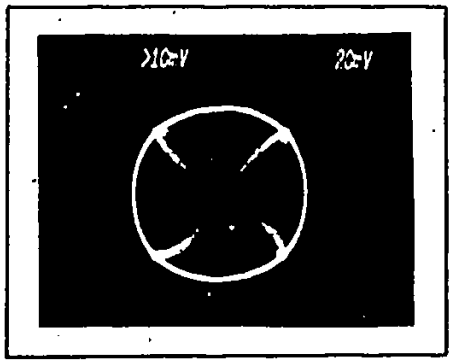

NOTES:
- the circle indicates a constant envelope
- traces inside the circle represent sharp transitions in $y'_I(t)$ and $y'_Q(t)$

(b) MEASURED SIGNAL SPACE DIAGRAM OF HARDLIMITED IJF-QPSK SIGNAL

Fig. 4.5: EFFECTS OF HARDLIMITING ON AN IJF-QPSK SIGNAL

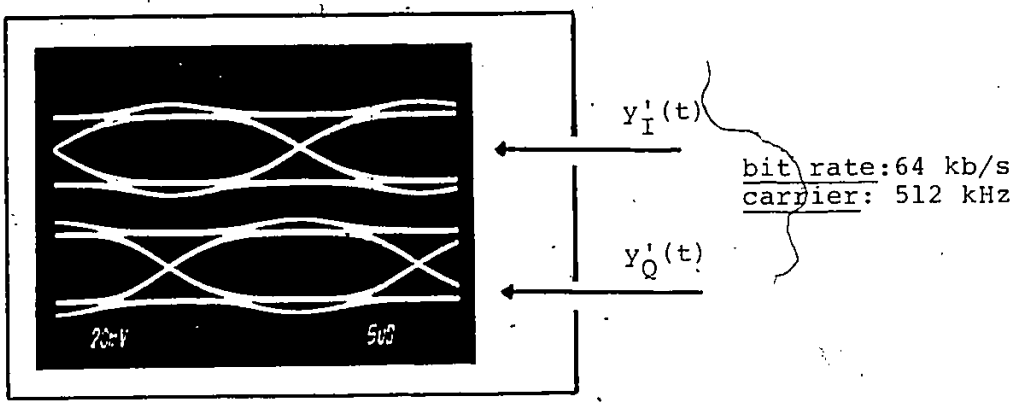

(a) MEASURED EYE DIAGRAMS OF $Y'_I(t)$ and $y'_Q(t)$
(at the outputs of the demodulator lowpass filters)

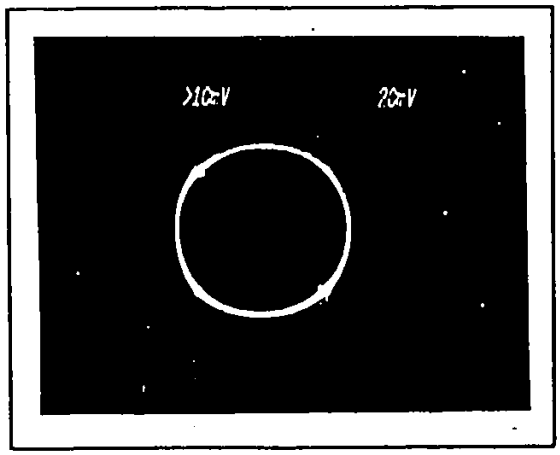

NOTES:

- *the circle indicate a constant envelope*
- *there are no traces inside the circle as opposed to Fig. 4.5b.*

(b) MEASURED SIGNAL SPACE DIAGRAM OF A HARDLIMITED IJF-OFFSET QPSK SIGNAL

Fig. 4.6: EFFECTS OF HARDLIMITING ON AN IJF-OFFSET QPSK SIGNAL

$$y_I'(t) = \sum_{n=-\infty}^{+\infty} q(t_n), \quad t_n = t - nT_s \tag{4.9}$$

From Eqs. (4.8a and b), it can be shown that $q(t_n)$ belongs to the set $\{v_i(t_n), i=1...16\}$ where $v_i(t_n)$ are represented by

$$v_j(t_n) = -v_{17-j}(t_n) = C \frac{s_e(t_n)}{\sqrt{s_e^2(t_n)+s_j'^2(t_n)}} \tag{4.10a}$$

$$v_{j+4}(t_n) = -v_{13-j}(t_n) = C \frac{s_o(t_n)}{\sqrt{s_o^2(t_n)+s_j'^2(t_n)}} \tag{4.10b}$$

where $j = 1,2,3,4,$

$s_e(t)$, $s_o(t)$ are defined by Eqs. (3.2a and b), and pulse shapes $s_j'(t_n)$, $j = 1,2,3,4$ are

$$s_1'(t_n) = \begin{cases} s_e(-t_n-d), & \text{for } -T_s/2 \le t_n < d-T_s/2 \\ s_e(t_n-d), & \text{for } d-T_s/2 \le t_n < T_s/2 \end{cases} \tag{4.11a}$$

$$s_2'(t_n) = \begin{cases} s_o(-t_n-d), & \text{for } -T_s/2 \le t_n < d-T_s/2 \\ -s_o(t_n-d), & \text{for } d-T_s/2 \le t_n < T_s/2 \end{cases} \tag{4.11b}$$

$$s_3'(t_n) = \begin{cases} s_o(-t_n-d), & \text{for } -T_s/2 \le t_n < d-T_s/2 \\ s_e(t_n-d), & \text{for } d-T_s/2 \le t_n < T_s/2 \end{cases} \tag{4.11c}$$

$$s_4'(t_n) = \begin{cases} s_e(-t_n-d), & \text{for } -T_s/2 \le t_n < d-T_s/2 \\ -s_o(t_n-d), & \text{for } d-T_s/2 \le t_n < T_s/2 \end{cases} \tag{4.11d}$$

In each symbol interval, $q(t_n)$ is chosen from the set $\{v_i(t_n), i=1,2,\ldots,16\}$. The waveshape of $q(t_n)$ is dependent on the waveshape of the previous $q(t_{n-1})$ and $y_I(t_n)$ and $y_Q(t_n)$. The stationary probabilities

$$p_i = P\{q(t_n) = v_i(t_n)\}, \quad i=1,2,\ldots,16$$

and transition probabilities

$$p_{ik} = P\{q(t_n) = v_k(t_n) | q(t_{n-1}) = v_i(t_{n-1})\}, \quad i,k = 1,2,\ldots,16$$

can be obtained by investigating the encoding law of $y_I(t)$, $y_Q(t)$ (Eq. (2.2b)) and construction of $v_i(t_n)$, $i=1,2,\ldots,16$, i.e.,

$$p_i = \frac{1}{16}, \quad i=1,2,\ldots,16 \tag{4.12a}$$

and p_{ik}'s are arranged as entries in the 16×16 transition matrix

$$P = \{p_{ik}, \ i,k=1,2,\ldots,16\} = \frac{1}{4}\begin{bmatrix} A & O & A & O \\ A & O & A & O \\ O & B & O & B \\ O & B & O & B \end{bmatrix} \tag{4.12b}$$

where A, B are 4×4 matrices,

$$A = \begin{bmatrix} 1 & 0 & 0 & 1 \\ 0 & 1 & 1 & 0 \\ 1 & 0 & 0 & 1 \\ 0 & 1 & 1 & 0 \end{bmatrix} \qquad B = \begin{bmatrix} 0 & 1 & 1 & 0 \\ 1 & 0 & 0 & 1 \\ 0 & 1 & 1 & 0 \\ 1 & 0 & 0 & 1 \end{bmatrix}$$

and O is a 4×4 null matrix

The PSD function of $y_I(t)$ is given by [55,64]

$$Y(f) = \frac{1}{T_s^2} \sum_{n=-\infty}^{+\infty} \left| \sum_{i=1}^{16} p_i V_i\left(\frac{n}{T_s}\right) \right|^2 \delta\left(f - \frac{n}{T_s}\right)$$

$$+ \frac{1}{T_s} \sum_{i=1}^{16} p_i \left| V_i(f) \right|^2$$

$$+ \frac{2}{T_s} R_e \left\{ \sum_{i=1}^{16} \sum_{k=1}^{16} p_i V_i^*(f) V_k(f) V_{ik} \right\} \qquad (4.13)$$

where $V_i(f)$ is the Fourier transform of $v_i(t)$, $i=1,\ldots,16$, $V_i^*(f)$ is the complex conjugate of $V_i(f)$,

$$V_{ik} = \sum_{n=1}^{\infty} p_{ik}^{(n)} e^{-j2n\pi fT_s},$$

$p_{ik}^{(n)}$ is the ik^{th} entry in the matrix P^n,

$$P^n = \underbrace{PxPx\ldots xP}_{n \text{ times}}$$

and $Re\{\ldots\}$ is the real part of $\{\ldots\}$

Substituting values of $V_i(f)$'s, V_{ik}'s and p_i's into Eq. (4.13) yields

$$Y(f) = \frac{1}{8T_s} \{ 2 \sum_{i=1}^{8} |V_i(f)|^2 + Re\{ (V_1(f)+V_4(f)-V_5(f)-V_8(f)]^2$$

$$+ [V_2(f)+V_3(f)-V_6(f)-V_7(f)]^2) e^{-j2\pi fT_s} \} \qquad (4.14a)$$

It can be shown that the hardlimited IJF-quadrature modulated signal $z'(t)$ has the same spectral shape as the baseband component $y'_I(t)$ (or $y'_Q(t)$), i.e. its normalized PSD function can be represented by

$$\begin{aligned} Z_n(x) = Z_o\{2 \sum_{i=1}^{8} |V_i(x)|^2 \\ + R_e\{([V_1(x)+V_4(x)-V_5(x)-V_8(x)]^2 \\ +[V_2(x)+V_3(x)-V_6(x)-V_7(x)]^2)e^{-j2\pi x}\}\} \end{aligned} \qquad (4.14b)$$

where Z_o is a normalizing coefficient chosen such that

$$Z_n(0) = 1$$

and

$$x = (f-f_c)T_s$$

Equation 4.14b represents the general power spectral density function of the hardlimited IJF-quadrature modulated signal with a given offset value, d. Equations (4.11a-d) indicate that different values of d result in different sets of pulse shapes $s'_i(t_n)$, i=1,2,...,4 and, hence for the same IJF quadrature modulated signal z(t), the spectral regrowth of the hardlimited IJF quadrature modulated signal z'(t) depends on the offset value, d, between I and Q baseband components.

As an illustrative example, the spectral regrowth of the hardlimited IJF quadrature modulated signal having the IJF

double-interval pulse $s(t) = \frac{1}{2}(1+\cos(\frac{\pi t}{T_s}))$ is investigated with different values of d using Eq. (4.14b). The results shown in Fig. 4.7 indicate that the minimum spectral regrowth of the hard-limited IJF-quadrature modulated signal is obtained at $d = T_s/2$.

It is also noted that the spectral regrowth is the same for 2 different offset values, d and (T_s-d).

Figure 4.8 shows the computed eye diagrams of the equivalent baseband components of the hardlimited IJF-quadrature modulated signal with different values of d using Eqs. (4.8a,b). Note the IJF conditions applied to the transmitted baseband eye diagrams. However, after quadrature modulation, nonlinear amplification and demodulation the signals contain intersymbol-interference (ISI) and jitter. Fig. 4.8 shows that the ISI introduced by the I and Q crosstalk effect increases with d. It is maximum (3 dB peak-to-peak) at $d = T_s/2$ and zero at d=0.

Both spectral spreading, and I and Q crosstalk affect the P_e performance of the IJF-quadrature modulated signals. These effects will be discussed in Chapter 5.

Figure 4.9 shows the power spectra of a class of IJF-OQPSK signals having fast spectral roll-off, after the hardlimiter. These power decay assymptotically as $|f-f_c|^{-2(N+2)}$ where N is called the roll-off order defined by Eqs. (3.12). It is seen

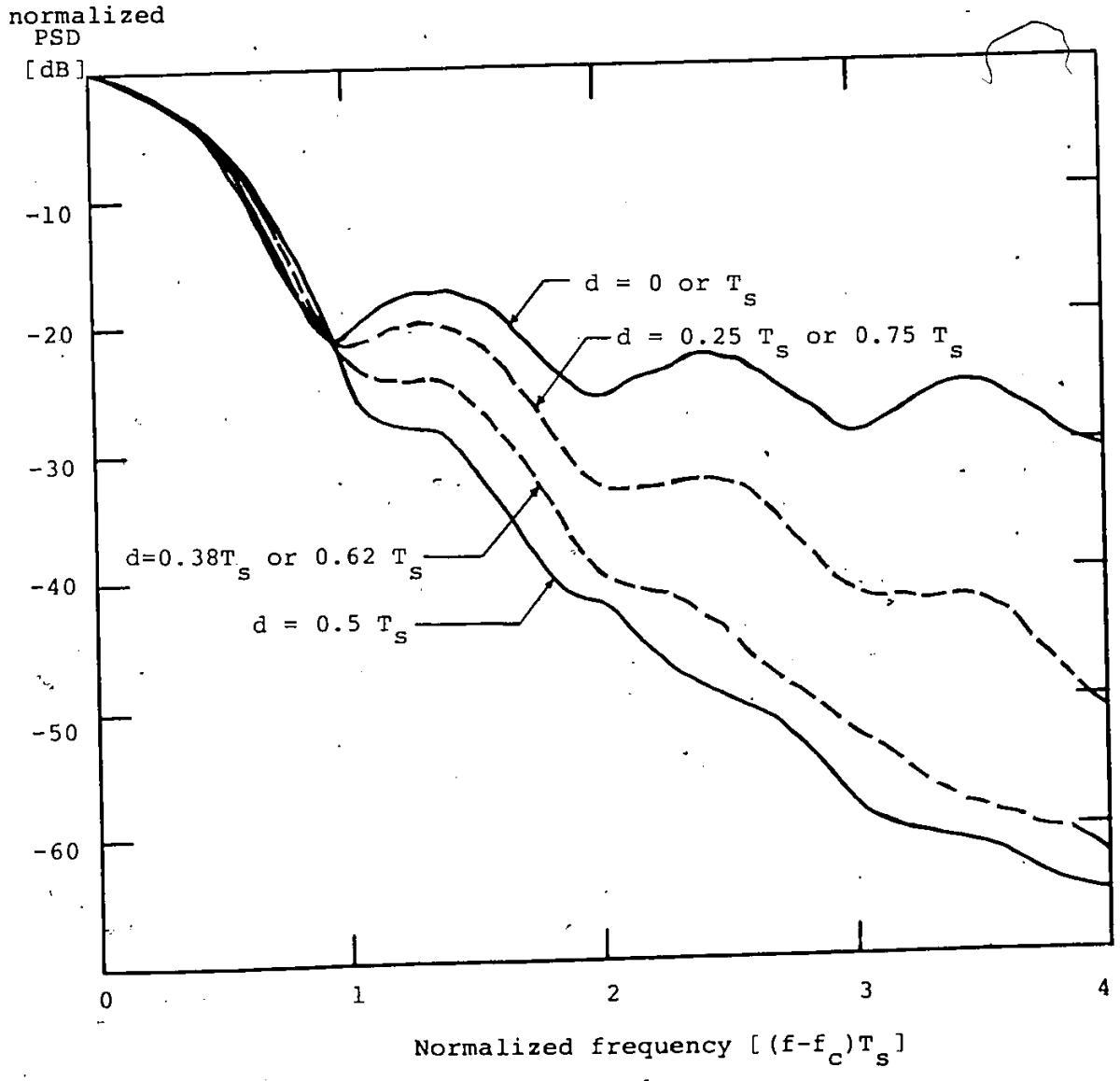

Fig. 4.7: POWER SPECTRA OF HARDLIMITED IJF-QUADRATURE MODULATED SIGNALS WITH DIFFERENT VALUES d

(for $s(t) = \frac{1}{2}(1 + \cos\frac{\pi t}{T_s})$)

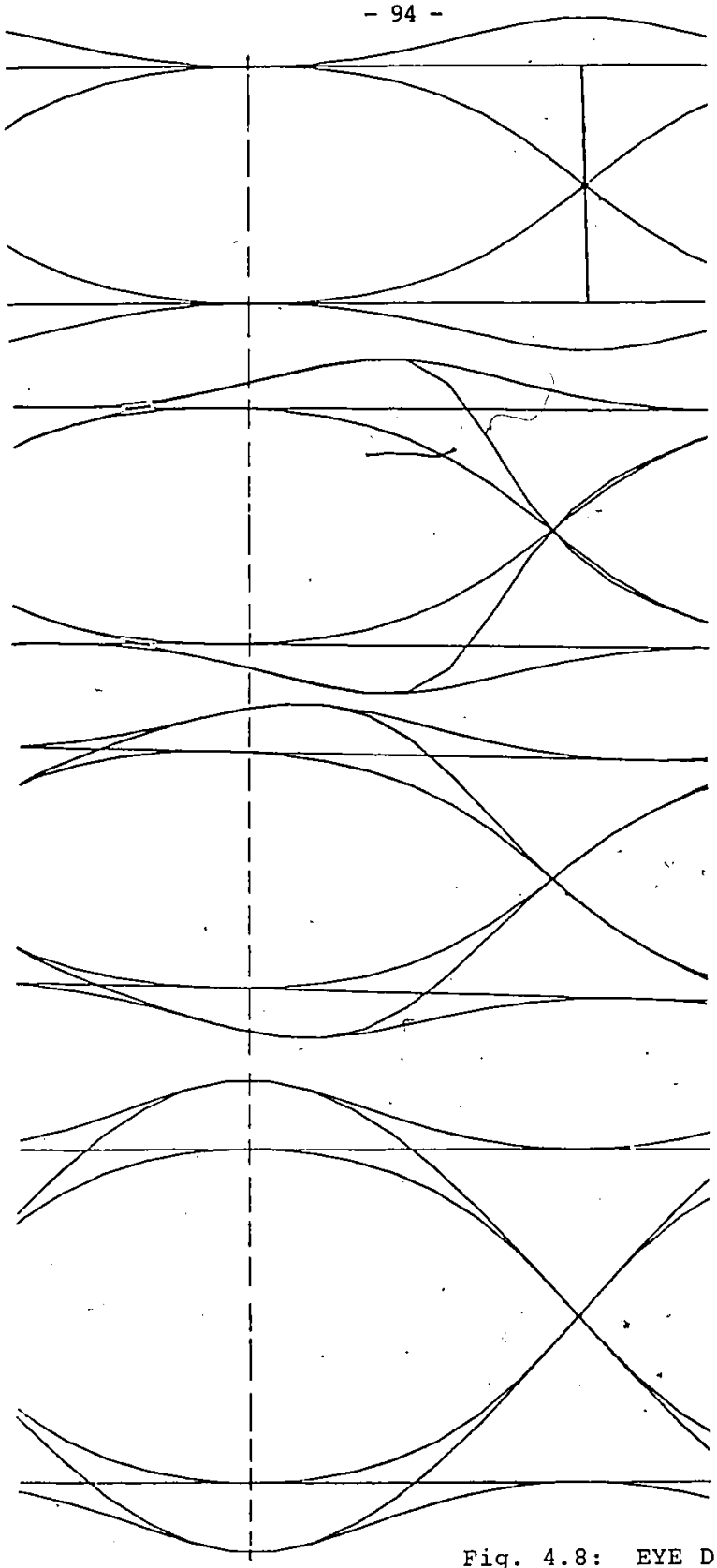

Fig. 4.8: EYE DIAGRAMS OF THE DEMODULATED BASEBAND COMPONENTS OF HARDLIMITED IJF-QUADRATURE MODULATED SIGNALS

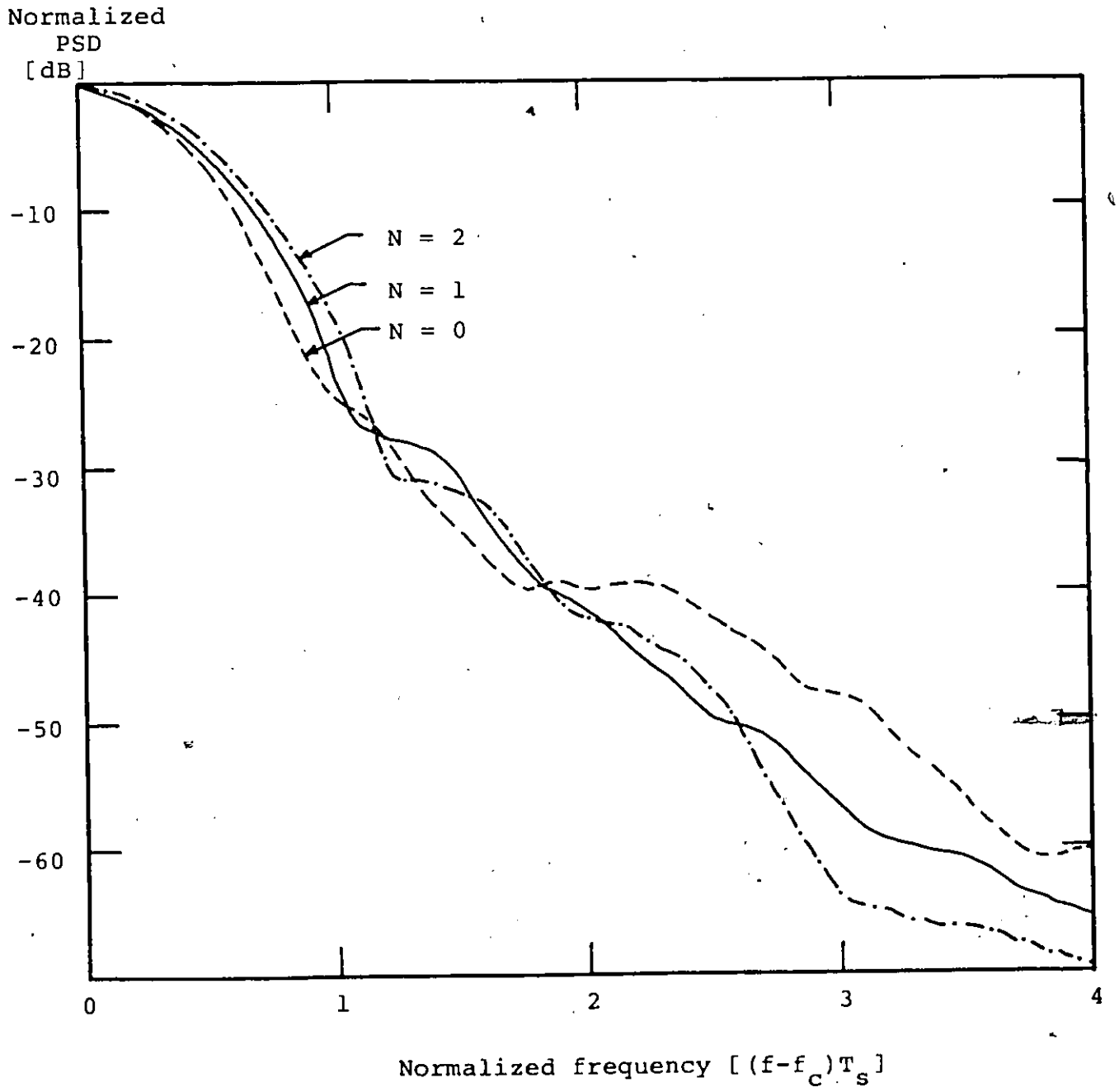

Fig. 4.9: POWER SPECTRA OF HARDLIMITED IJF-OFFSET QPSK SIGNALS

in Fig. 4.9 that the steep spectral roll-off property is still preserved after the hardlimiter. Figure 4.9 also indicates that the hardlimited IJF-OQPSK signal having $s(t) = \cos \frac{\pi t}{2T_s}$ (i.e. N=0) exhibits the lowest spectral spreading in the frequency band $0 \leq |f-f_c| \leq 2/T_s$.

4.4 EXPERIMENTAL AND COMPUTER SIMULATION RESULTS

The block diagram of the experimental model of the IJF-quadrature modulator is shown in Fig. 4.1 where two offset values, $d=0$ and $d=T_s/2$, are used. The IJF encoder has the double-interval pulse $s(t) = \frac{1}{2}(1+\cos \frac{\pi t}{T_s})$ that is $N=1$. In our down-scaled experimental set-up the bit rate and the carrier frequency are 64 kb/s and 512 kHz respectively.

The measured signal space diagrams of the IJF-quadrature modulated signals with $d=0$ and $d=T_s/2$ (Figs. 4.2b, 4.3b) show that for $d=0$ the IJF-quadrature modulated signal exhibits 100% amplitude fluctuation while for $d=T_s/2$, its maximum amplitude fluctuation is only $\sqrt{2}$ (or 3 dB). For this reason, the IJF-quadrature modulated signal, with $d=0$, has a more significant spectral regrowth than the hardlimited IJF-Offset-QPSK (i.e. $d=T_s/2$) as shown in Fig. 4.10.

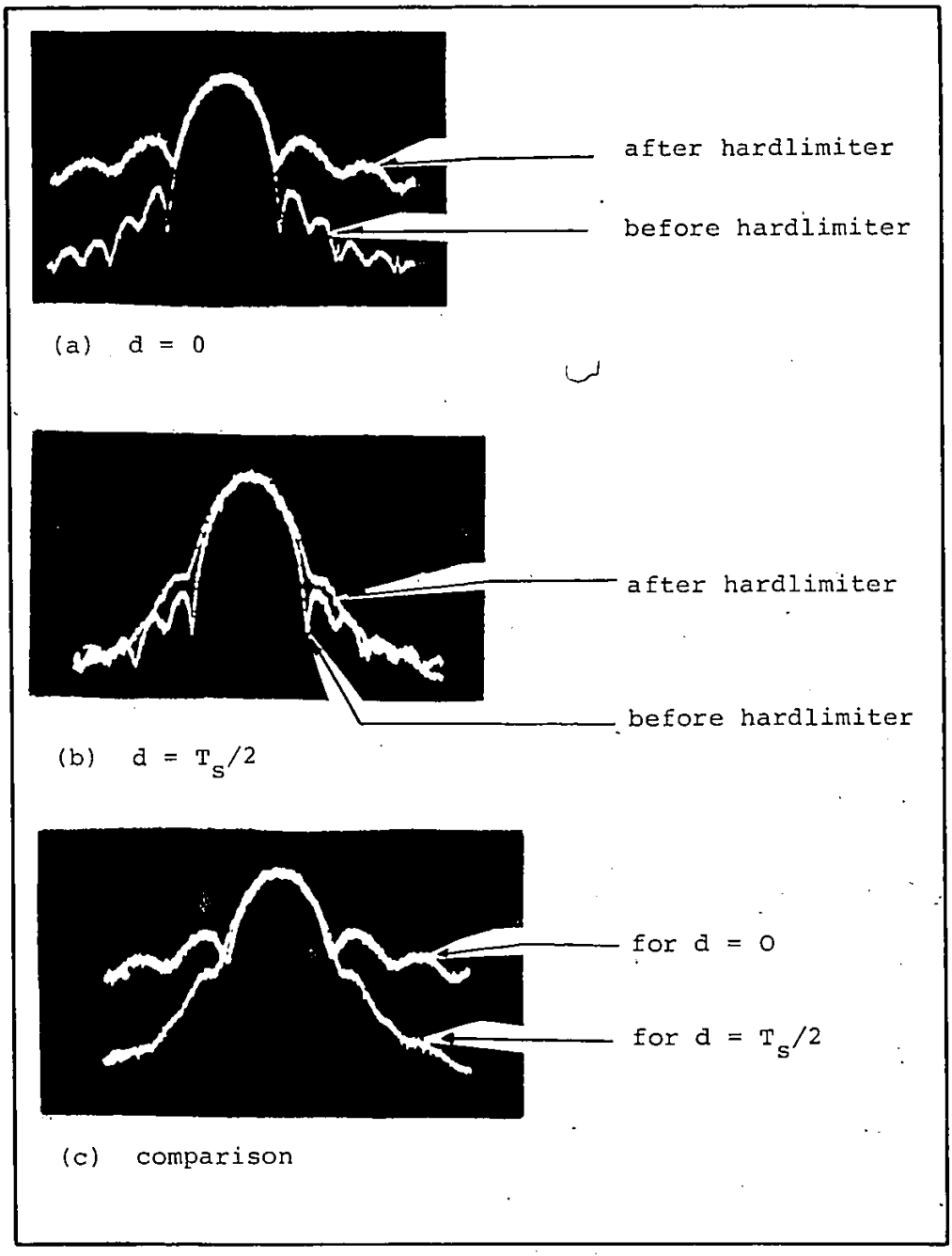

Fig. 4.10: MEASURED POWER SPECTRA OF THE IJF-QPSK AND IJF-OQPSK SIGNALS
(bit rate: 64 kb/s, carrier frequency: 512 kHz)

The equivalent complex baseband model of the IJF-quadrature modulator used in the computer simulation is shown in Fig. 4.11. Fig. 4.12 shows spectral regrowth of the hardlimited IJF-OQPSK ($d=T_s/2$) obtained by computer simulation (solid line), theoretical derivation (dashed line) and experiments (dotted line). It is seen that the simulation and theoretical results are identical, and in a close agreement with the experimental results.

As a next step the ideal hardlimiter in the simulation model (Fig. 4.11) is replaced by the high-power amplifier (HPA) having the AM/AM and AM/PM characteristics shown in Fig. 4.13. The simulation results (Fig. 4.14) shows that the IJF-Offset-QPSK signal exhibits similar spectral regrowth whether this regrowth is caused by a practical model of a saturated HPA or by an ideal hardlimiter. In the case of IJF-QPSK a significant difference exists.

The spectral regrowth of the hardlimited IJF-OQPSK signal if compared to that of hardlimited QPSK, OQPSK, and MSK. The transmit shaping filters used for these modulated signals are described in Table 4.1. The results of Fig. 4.15 show that the hardlimited IJF-OQPSK signal has more significant spectral advantages than the hardlimited QPSK, OQPSK and MSK signals.

The *hardlimited* IJF-Offset QPSK signal has a constant envelope. Its power spectrum is compared to those of other constant-envelope modulated signals such as TFM [39], FSOQ [43], and

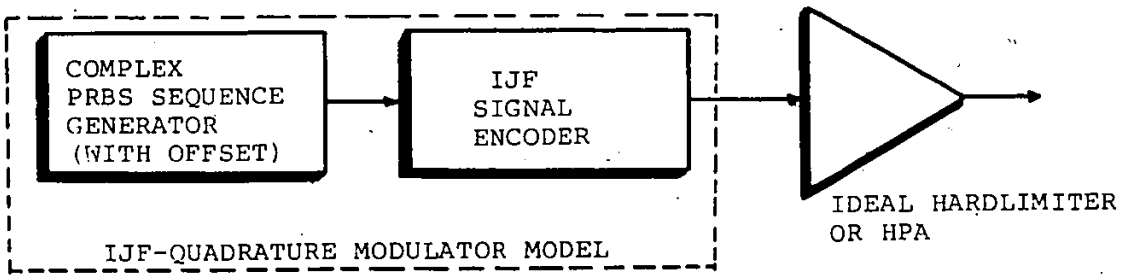

Fig. 4.11: EQUIVALENT COMPLEX BASEBAND MODEL OF THE IJF QUADRATURE MODULATOR

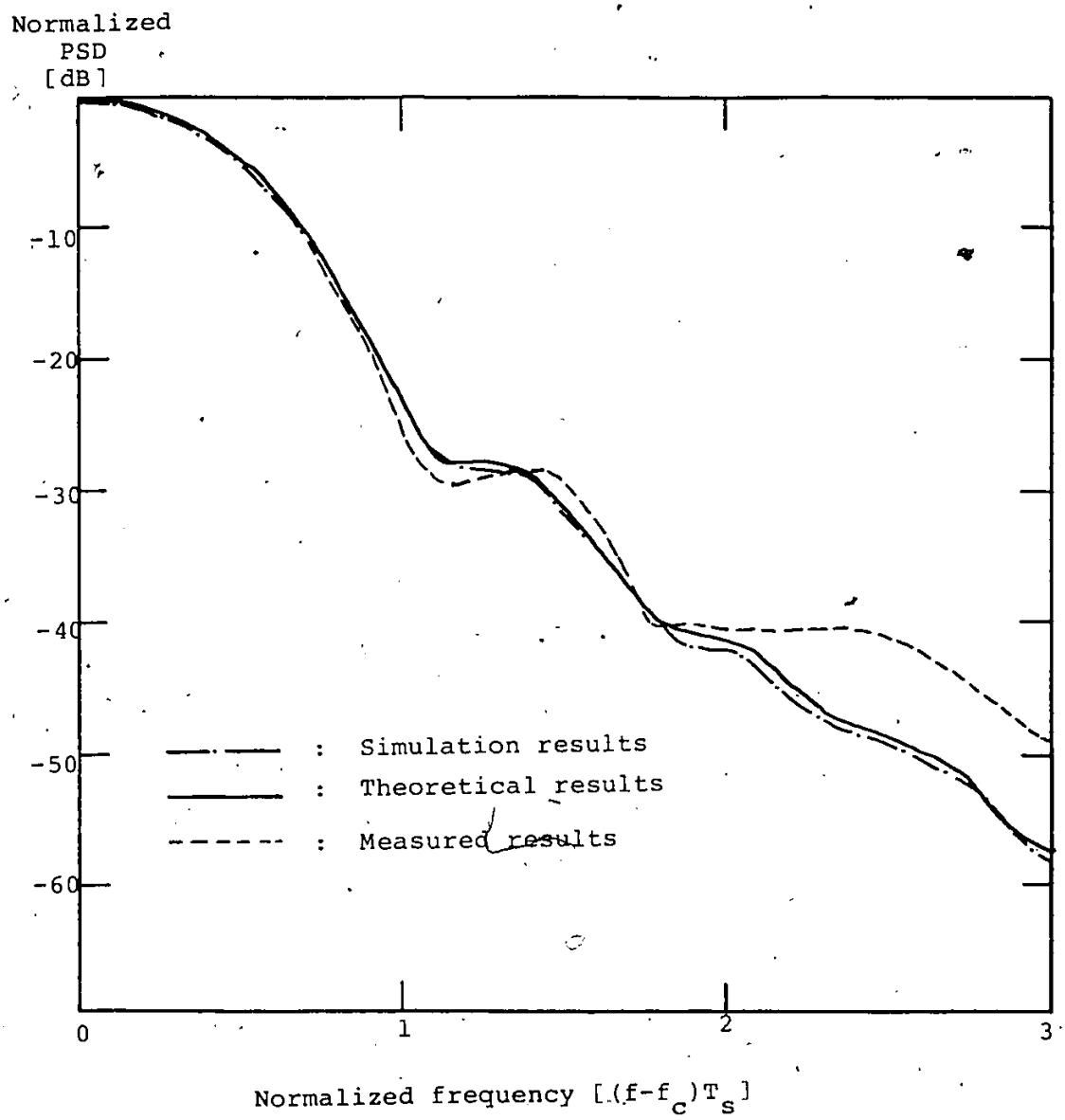

Fig. 4.12: COMPARISON OF THEORETICAL, MEASURED AND SIMULATION RESULTS ON THE SPECTRUM SPREADING OF A HARDLIMITED IJF-OQPSK SIGNAL

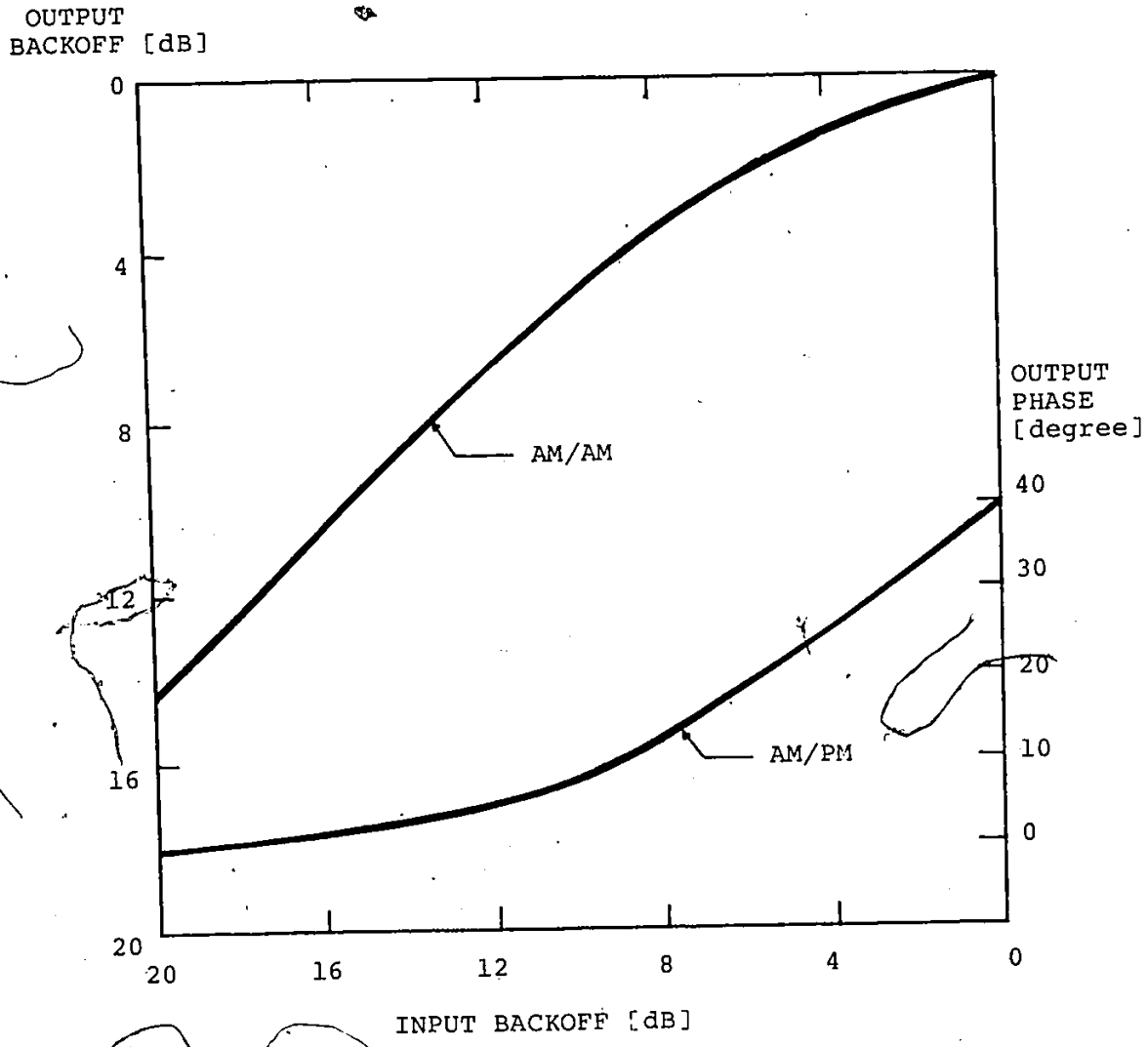

Fig. 4.13: NONLINEAR CHARACTERISTICS OF A HIGH-POWER AMPLIFIER (Recommended for Intelsat V TDMA simulator [73]).

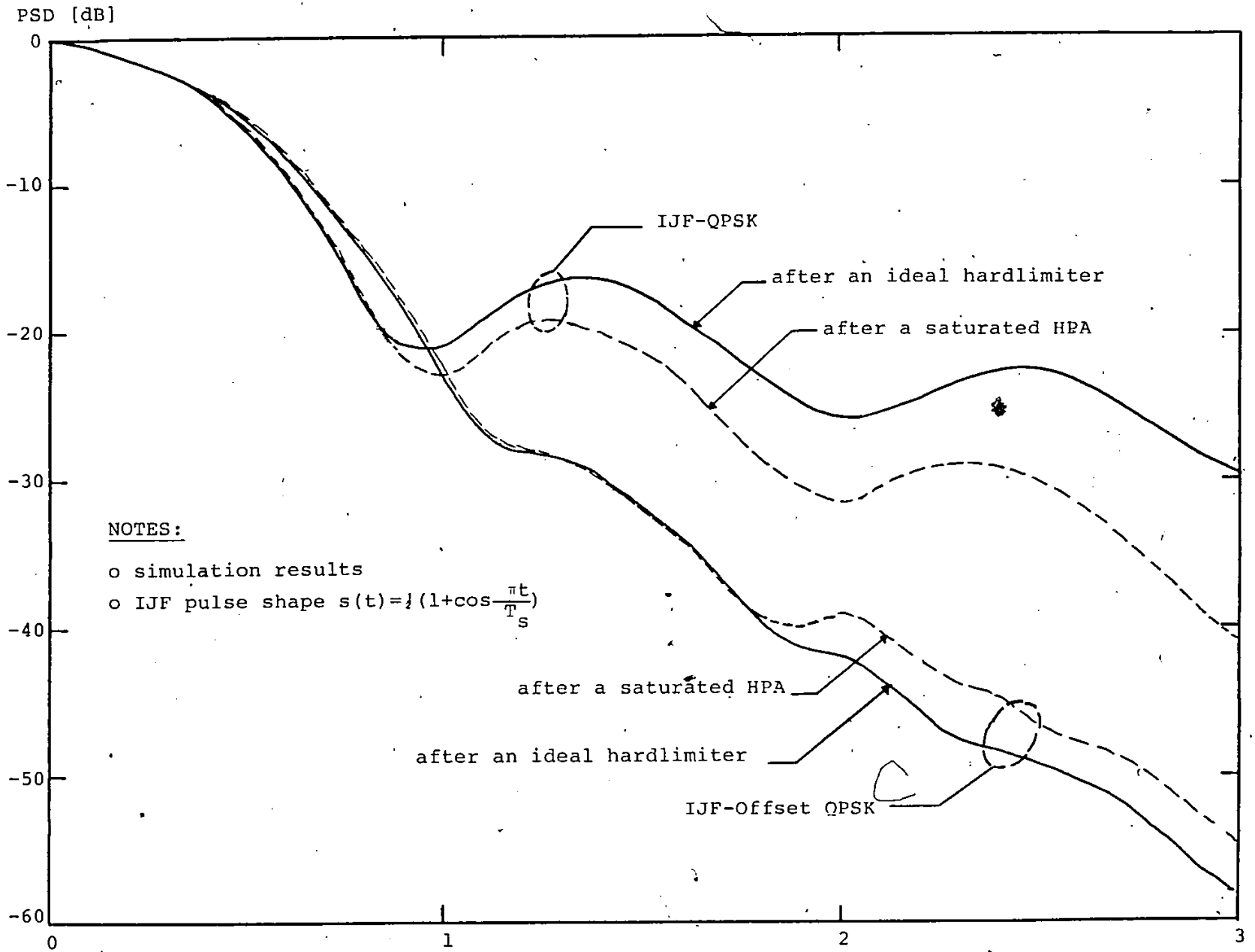

Fig.4.14: SPECTRAL SPREADING COMPARISON OF IJF-QPSK AND IJF-OFFSET QPSK SIGNALS

Modulation scheme	Transmit filter
QPSK, OQPSK	$\frac{x}{\sin x}$ equaliser + square-root of the raised cosine filter with roll-off factor $\alpha=0.4$
MSK	5th order Butterworth filter with $f_{3dB} = \pm \frac{0.5}{T_s}$, where $1/T_s$ is the symbol rate
IJF-OQPSK with $s(t) = \frac{1}{2}(1+\cos\frac{\pi t}{T_s})$	Nil

Table 4.1: TRANSMIT SHAPING FILTERS FOR QPSK, OQPSK, MSK AND IJF-OQPSK SIGNALS

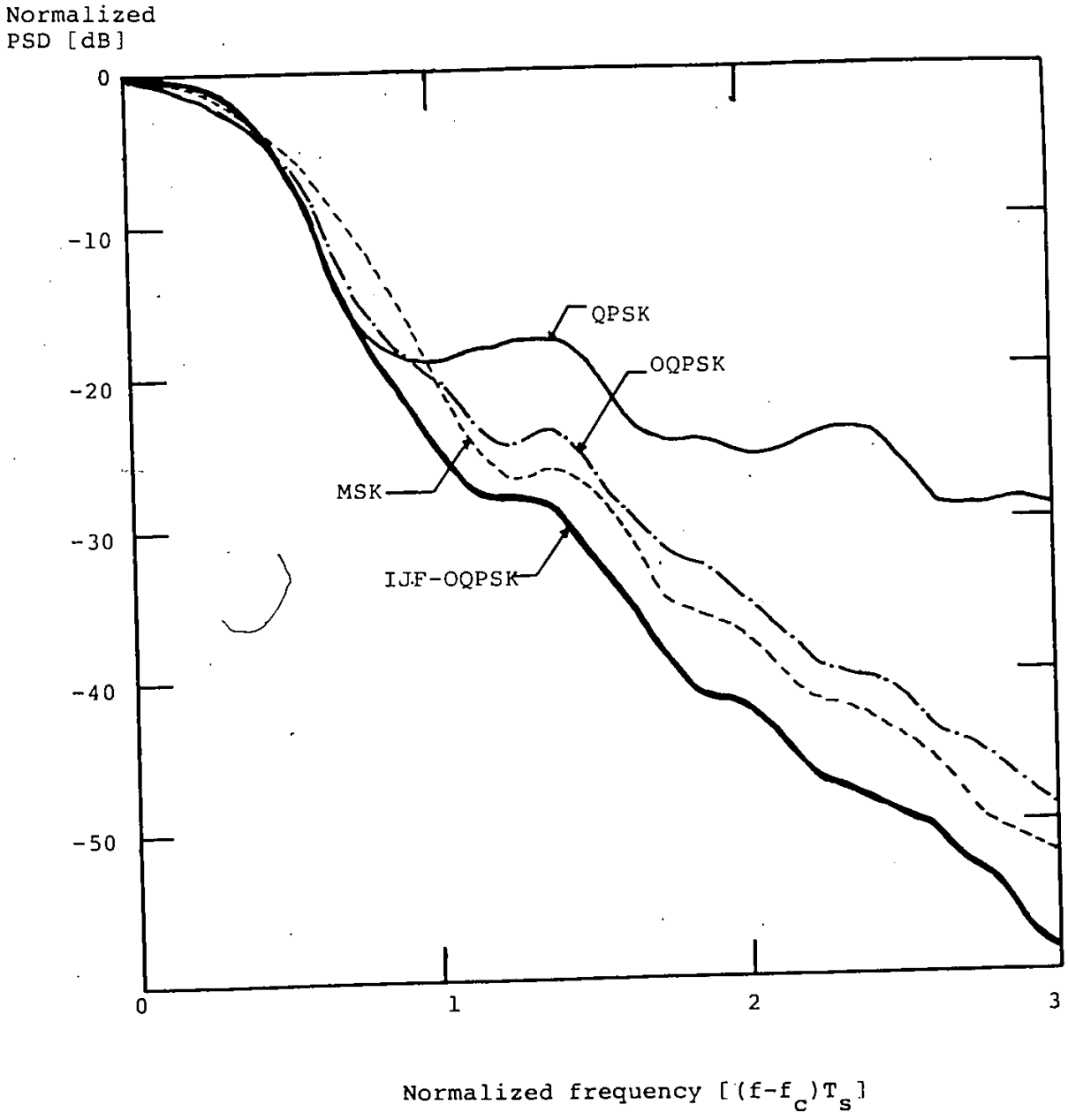

Fig. 4.15: COMPARISON OF POWER SPECTRA OF HARDLIMITED QPSK, OQPSK, MSK AND IJF-OQPSK SIGNALS

(Transmit shaping filters for different modulation schemes are described in Table 4.1).

hardlimited quasi-bandlimited keying [48]. Fig. 4.16 shows the spectral comparison, taking the power spectral density at the carrier frequency as the 0dB reference. It is indicated that for the frequency region within the bit rate frequency, the IJF-OQSK with N=0 has better (lower) power spectrum.

NOTE: *Parts of Chapter 4 were published in [65, 66].*

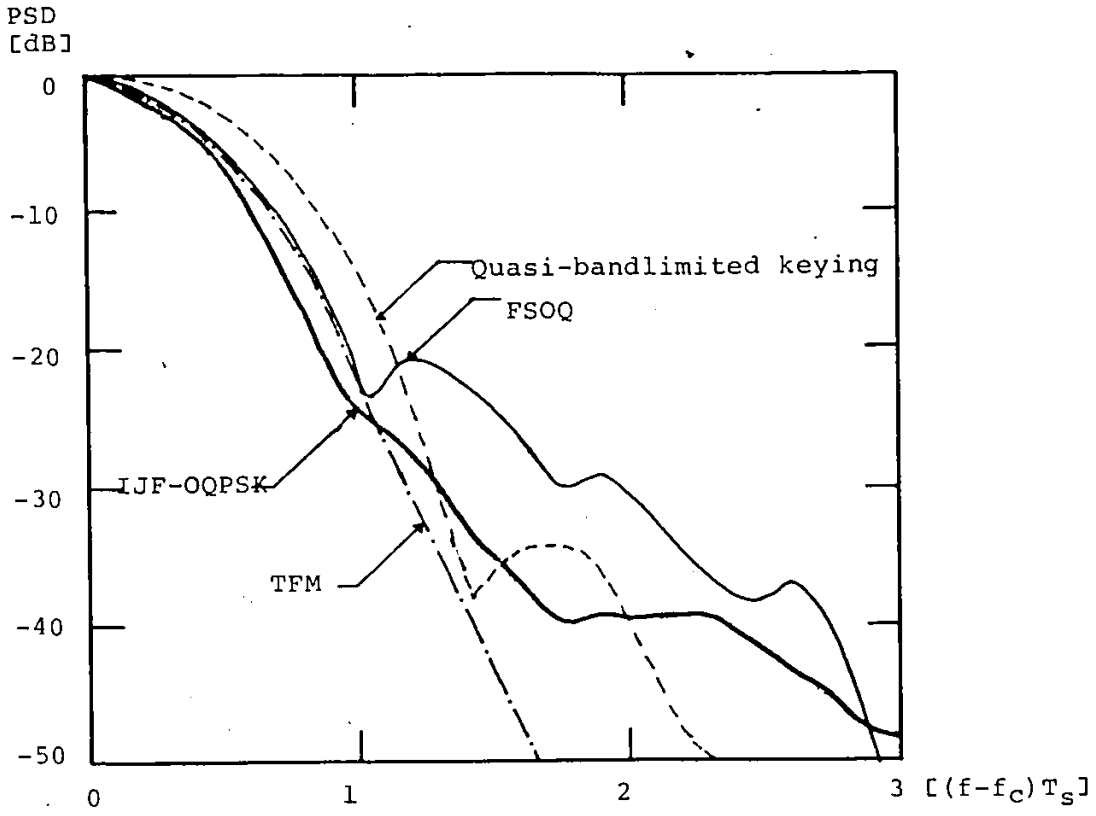

Notes:
- o IJF-OQPSK, Quasi-bandlimited keying signals are hardlimited.
- o For IJF-OQPSK signal, N = 0.
- o For Quasi-bandlimited keying signal, n = 3

Fig. 4.16: NORMALIZED POWER SPECTRA OF VARIOUS CONSTANT-ENVELOPE MODULATED SIGNALS

CHAPTER FIVE:
IJF-QUADRATURE MODULATION TECHNIQUES: ERROR PROBABILITY PERFORMANCE

SUMMARY:

In this chapter, the error probability (P_e) performance of IJF-quadrature modulated signals in an additive white gaussian noise environment is presented.

The P_e performance of IJF-QPSK and IJF-Offset QPSK modems in linear, hard-limited, and cascaded nonlinear channels is provided. The detection filter is a raised-cosine type filter previously described in Section 3.2.3.

Effects of co-channel and adjacent-channel interference on the P_e performance of IJF-QPSK and IJF-Offset QPSK modems are investigated using simulation techniques.

Potential applications of IJF-Offset QPSK modems in power efficient stations for Single-Channel-Per-Carrier (SCPC), Time-Division-Multiple-Access (TDMA), and On-Board Regenerative systems are studied. Performance comparison of IJF-Offset QPSK, QPSK, OQPSK, and MSK are presented.

Experimental results are in agreement with simulation results.

5.1. P_e PERFORMANCE OF IJF-QPSK AND IJF-OFFSET QPSK IN AN AWGN SINGLE-CHANNEL ENVIRONMENT

5.1.1 P_e Performance of IJF-QPSK and IJF-Offset QPSK in Linear, and Hardlimited Channels

The single-channel model of an IJF quadrature modem (modulator-demodulator) is shown in Fig. 5.1. As an illustrative example, the double-interval pulse shape used in the IJF encoders, $s(t) = \frac{1}{2}(1+\cos\frac{\pi t}{T_s})$, is selected for our study. The modulator has no extra transmit shaping filter. The receive filter used in the demodulator is a raised-cosine type filter, as previously described in Section 3.2.3.

In a *linear channel*, it was shown that, for both IJF-QPSK and IJF-Offset QPSK, the receive filter having a roll-off factor $\alpha=0.6$ provides a negligible degradation of 0.28 dB compared to the theoretical optimum performance.

Figure 5.2 illustrates the P_e performance of the IJF quadrature modulated signals in a *hardlimited single-channel* model. It is seen that the IJF-QPSK (i.e. $d=0$) out-performs the IJF-OQPSK (i.e. $d=T_s/2$). This is explained by the fact, that in the sampling instants the baseband components of the hardlimited IJF-QPSK have less intersymbol interference (ISI) than those of the hardlimited IJF-OQPSK due to the inphase-to-quadrature cross-talk effects (Fig. 4.8).

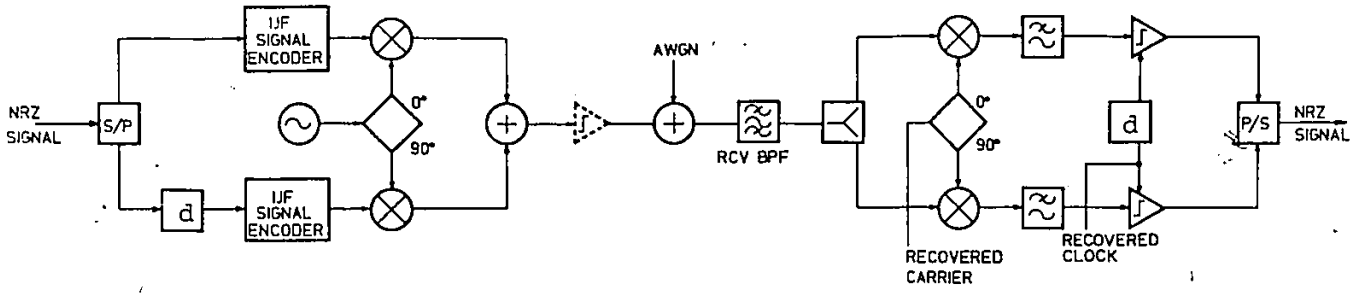

(a) MODULATOR (b) DEMODULATOR

Fig. 5.1: BLOCK DIAGRAM OF IJF QUADRATURE MODULATOR/ DEMODULATOR IN AN AWGN ENVIRONMENT

The performance of the IJF-Offset QPSK modem is also experimentally evaluated. The bit rate is 64 kb/s and the carrier frequency is 512 kHz. The measured results, Fig. 5.3, are in agreement with the simulation results (Fig. 5.2).

However, as shown in Fig. 4.7, the hardlimited IJF-OQPSK signal has much less spectral spreading than the hardlimited IJF QPSK signal. For this reason, in the hardlimited multi-channel system the IJF-OQPSK signal leads to a higher carrier-to-interference (C/I) ratio and hence a smaller adjacent-channel-interference (ACI) caused P_e degradation than the IJF-QPSK. This will be demonstrated in Section 5.2.

5.1.2 P_e Performance of the IJF-OQPSK Modem in a Cascaded Non-Linear Channel (TDMA Application)

The TDMA transmission technique has been introduced to achieve higher efficiency and flexibility in satellite communications systems [89]. Due to the single-carrier-per-transponder mode of operation TDMA transmission reduces the nonlinear effects of the transponder TWTA by avoiding intermodulation products encountered in FDMA systems. However, it still undergoes degradation caused by the combined effects of the bandlimited environment of the transponder channel, and the cascaded nonlinearities of the earth station HPA and transponder TWTA. It is this degradation that limits an efficient use of earth station and satellite power amplifiers, that is, introduces an

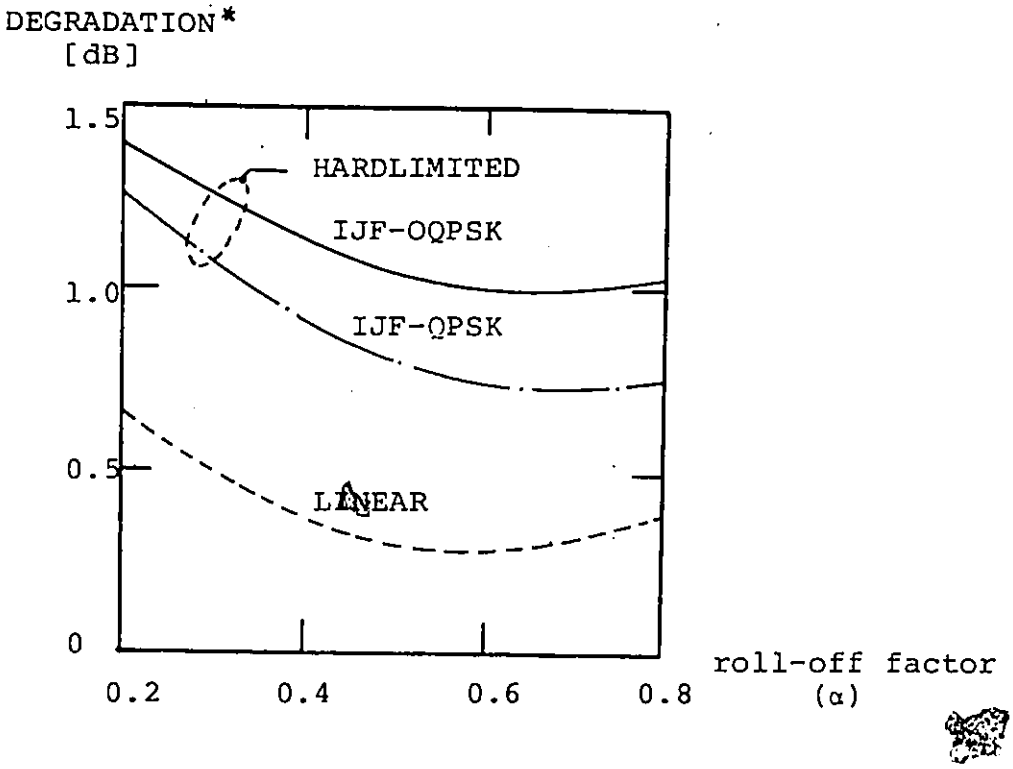

(* *Degradation relative to the optimum performance:* $E_b/N_o = 8.4dB$ *for* $P_e=10^{-4}$)

Fig. 5.2: PERFORMANCE DEGRADATION OF IJF-QPSK AND IJF-OQPSK MODEMS IN A SINGLE-CHANNEL SYSTEM

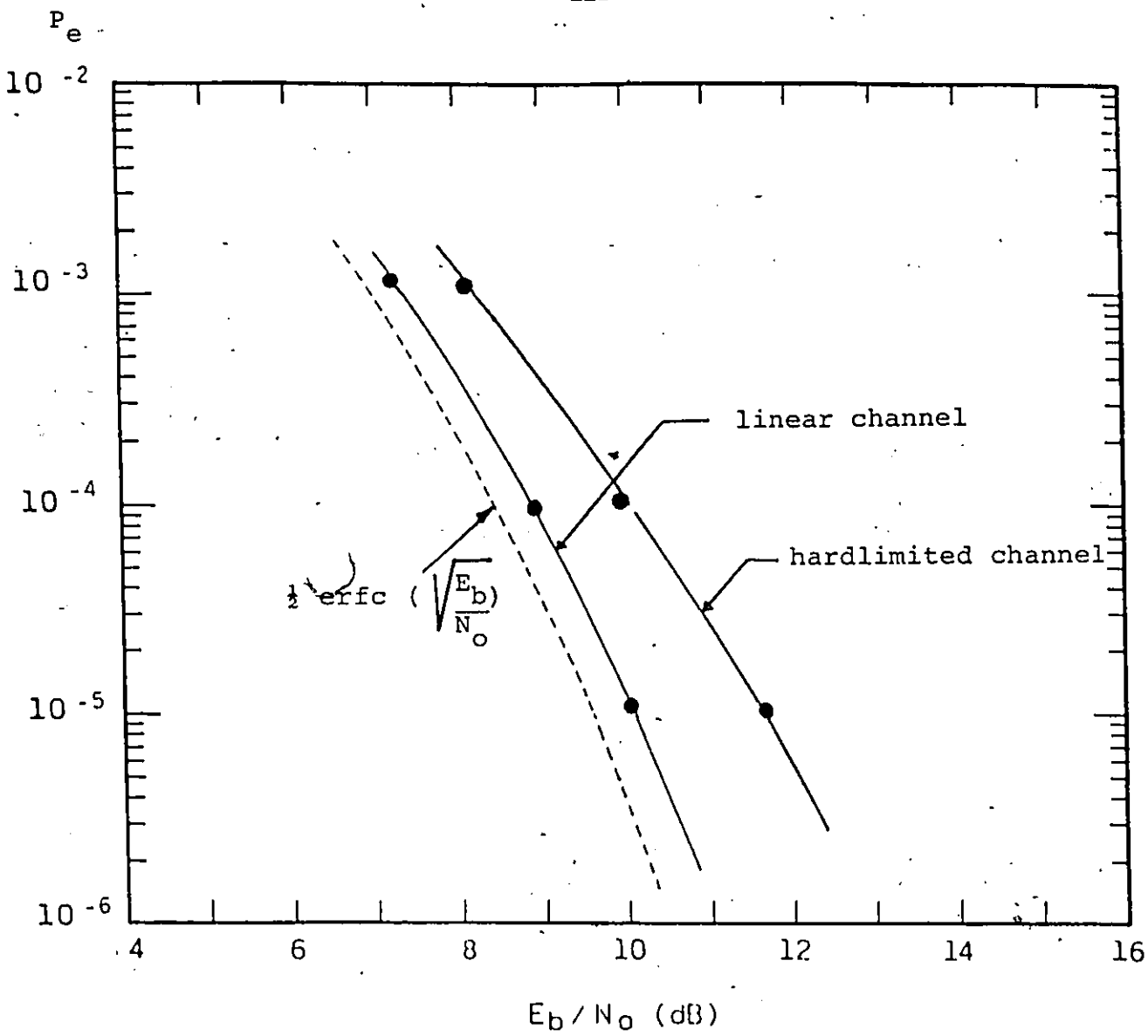

Fig. 5.3: MEASURED PERFORMANCE OF AN IJF-OQPSK MODEM IN AN AWGN ENVIRONMENT

NOTES:
- *bit rate:* 64 kb/s
- *carrier frequency:* 512 kHz
- *received BPF:* 4th order Butterworth with phase equalization approaching the raised-cosine type BPF with α=0.4

output power back-off requirement.

Fig. 5.4 illustrates the simulation model of a cascaded nonlinear channel. The characteristics of the earth station HPA, transponder TWTA, input and output MUX filters recommended in the Intelsat V-TDMA system specifications [73] are used in the simulation. The AM/AM and AM/PM conversion characteristics of the HPA and TWTA are illustrated in Fig. 4.13. In accordance with the recommended Intelsat V satellite simulator model we assume a negligible uplink noise.

Table 5.1 summarizes the filter partitioning used for IJF-OQPSK and QPSK modems. As an illustrative example, the IJF double-interval pulse used in the IJF-OQPSK modulator is $s(t) = \frac{1}{2}(1+\cos\frac{\pi t}{T_s})$. The IJF-OQPSK modulator has no extra transmit shaping filter. The receive detection filter used in the IJF-OQPSK demodulator is a raised-cosine type filter having a roll-off factor $\alpha=0.4$. For conventional QPSK modems, we adopted one of the most frequently used filtering strategies specified for operational systems [73].

The combined effect of the AM/AM and AM/PM nonlinearities, with the imperfect amplitude and group delay characteristics of the input/output transponder MUX filters, introduces a degradation in the P_e performance of the IJF-OQPSK system. Fig. 5.5 depicts the simulation results on the P_e performance of the IJF-OQPSK modem in different illustrative cases. The P_e

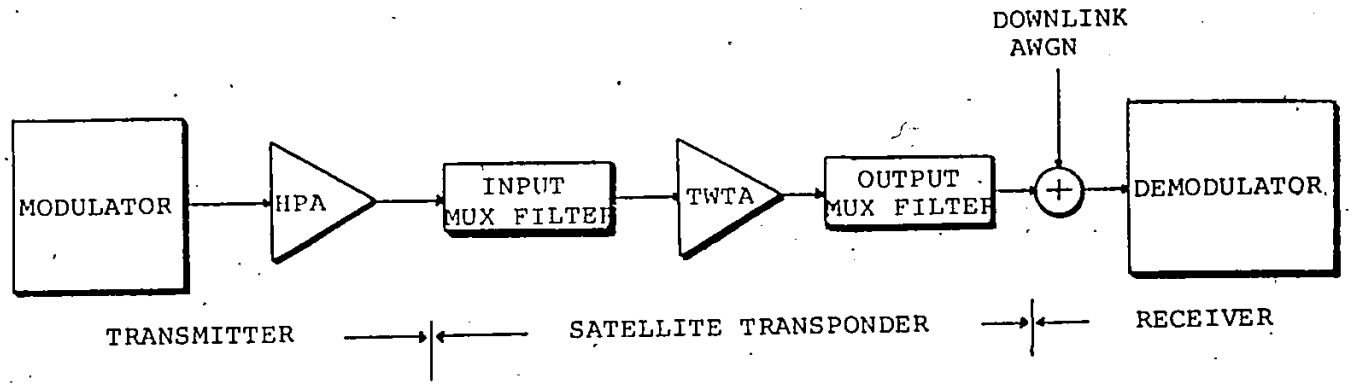

- o INPUT MUX FILTER:
  - Amplitude Response: full raised-cosine filter with roll-off factor $\alpha = 0.1$ and $f_{3dB} = f_b/3$ (single-sided)

    where f_b is the bit rate.
  - Group Delay: parabolic
- o OUTPUT MUX FILTER:
  - Amplitude Response: full raised-cosine filter with roll-off factor $\alpha = 0.2$ and $f_{3dB} = f_b/3$ (single-sided)

    where f_b is the bit rate.
  - Group Delay: parabolic

Fig. 5.4: SIMULATION MODEL OF A CASCADED NONLINEAR SATELLITE CHANNEL

Modulation Scheme Scheme	Transmit Shaping Filter	Receive Detection Filter
IJF-OQPSK with $s(t)=\frac{1}{2}(1+\cos\frac{\pi t}{T_s})$	- NIL -	Full raised-cosine filter with roll-off factor $\alpha = 0.4$ and aperture equalizer.
QPSK	Square-root of raised cosine filter with roll-off factor $\alpha = 0.4$ and $\frac{x}{\sin x}$ aperture equalizer.	Square-root of raised cosine filter with roll-off factor $\alpha = 0.4$.

Table 5.1: FILTER PARTITIONING FOR IJF-OQPSK AND QPSK MODEMS. (linear phase response is assumed)

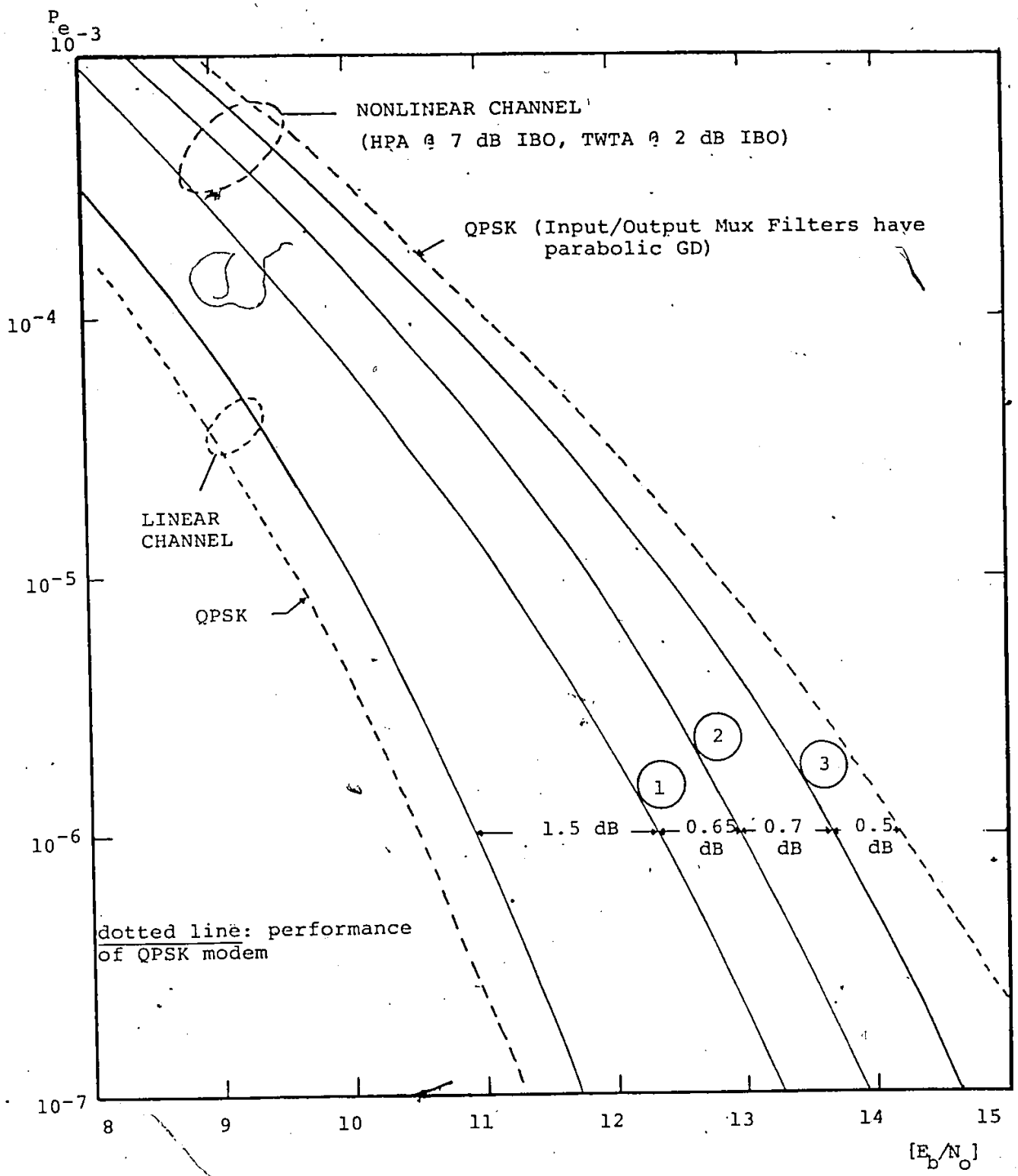

Fig. 5.5: PERFORMANCE OF THE IJF-OQPSK MODEM IN CASCADED NONLINEAR CHANNELS (Solid lines)

NOTES: Curve ① : Input and Output mux filters are excluded.
Curve ② : Input and Output mux filters have constant GD.
Curve ③ : Input and Output mux filters have parabolic GD.

degradation due to the *cascaded nonlinear* effect of the earth station HPA and transponder TWTA is 1.5 dB at $P_e=10^{-6}$ relative to a linear channel (curve 1). By introducing input and output transponder MUX filters, the IJF-OQPSK signal prior to the transponder TWTA exhibits an increased amplitude fluctuation, therefore it suffers more degradation due to AM/AM and AM/PM conversion effects of the TWTA: if the MUX filters are assumed to have a constant (ideal) group delay characteristic, then the P_e performance of the IJF-OQPSK is degraded by 0.65 dB at $P_e=10^{-6}$ relative to the case of no MUX filtering (curve 2). If *parabolic group delay* characteristics of MUX filters are assumed, then the P_e performance (curve 3) is degraded by 1.35 dB at, $P_e=10^{-6}$ relative to the case of no MUX filtering. Since a negligible uplink noise is assumed the degradation in P_e performance is related to the increase of intersymbol-interference in the received IJF-OQPSK signals prior to the single sampling detector as shown in Fig. 5.6. The P_e performance of the IJF-OQPSK modem is also compared to that of the QPSK in the same transmission link as illustrated in Fig. 5.5. While in the *linear channel* the P_e performance of the IJF-OQPSK modem is 0.4 dB worse than that of the QPSK, the IJF-OQPSK shows a "gain" of 0.5 dB at $P_e=10^{-6}$ compared to QPSK in the bandlimited and cascaded nonlinear channels.

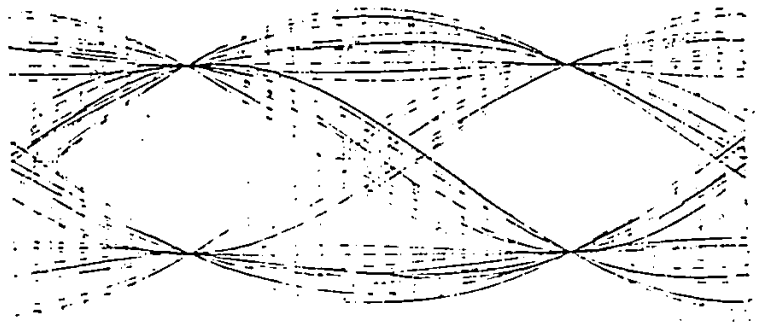

(a) LINEAR CHANNEL

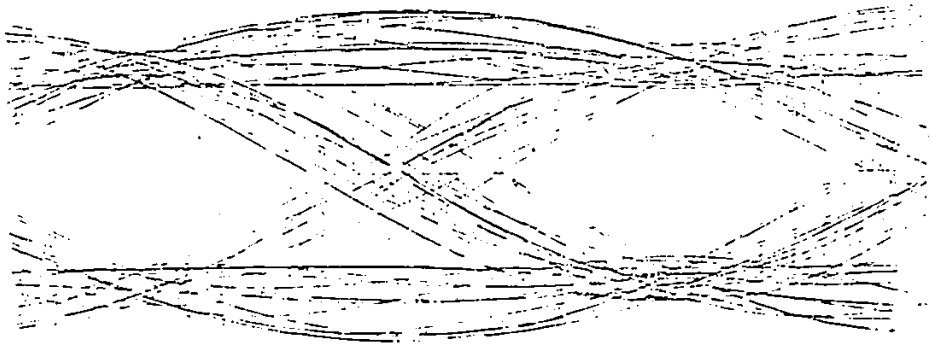

(b) NONLINEAR CHANNEL
(HPA at 7 dB IBO, TWTA at 2 dB IBO)

Fig. 5.6: EYE DIAGRAMS OF DEMODULATED IJF-OQPSK SIGNALS IN LINEAR AND CASCADED NONLINEAR CHANNELS.

5.1.3. P_e Performance of the IJF-OQPSK Modem in a Regenerative Satellite Link

Onboard regeneration techniques [75] are used to further improve the performance of satellite links using TDMA schemes. In regenerative satellite systems, the uplink and downlink are isolated by onboard demodulation-remodulation processing. This prevents the direct transfer of noise accumulated on the uplink to the downlink, and only bit errors made in the onboard detection processing of the uplink are passed onto the downlink. The isolation of the uplink and downlink also separates the effects of cascaded nonlinearities, avoiding the transfer of signal distortions from the uplink to the downlink. Fig. 5.7 shows the simulation model of a regenerative satellite link. The HPA, TWTA, and filters have the same characteristics as described in the previous section. The simulation results on the uplink and downlink P_e performance of the IJF-OQPSK modulation scheme are shown in Fig. 5.8. The regenerative satellite system provides a P_e performance gain of 2.15 dB at $P_e=10^{-6}$, relative to the conventional satellite system, equipped with IJF-OQPSK modems.

In regenerative satellite systems the total P_e performance is given by [75]

$$P_{eT} \approx P_{eD}+P_{eU}$$

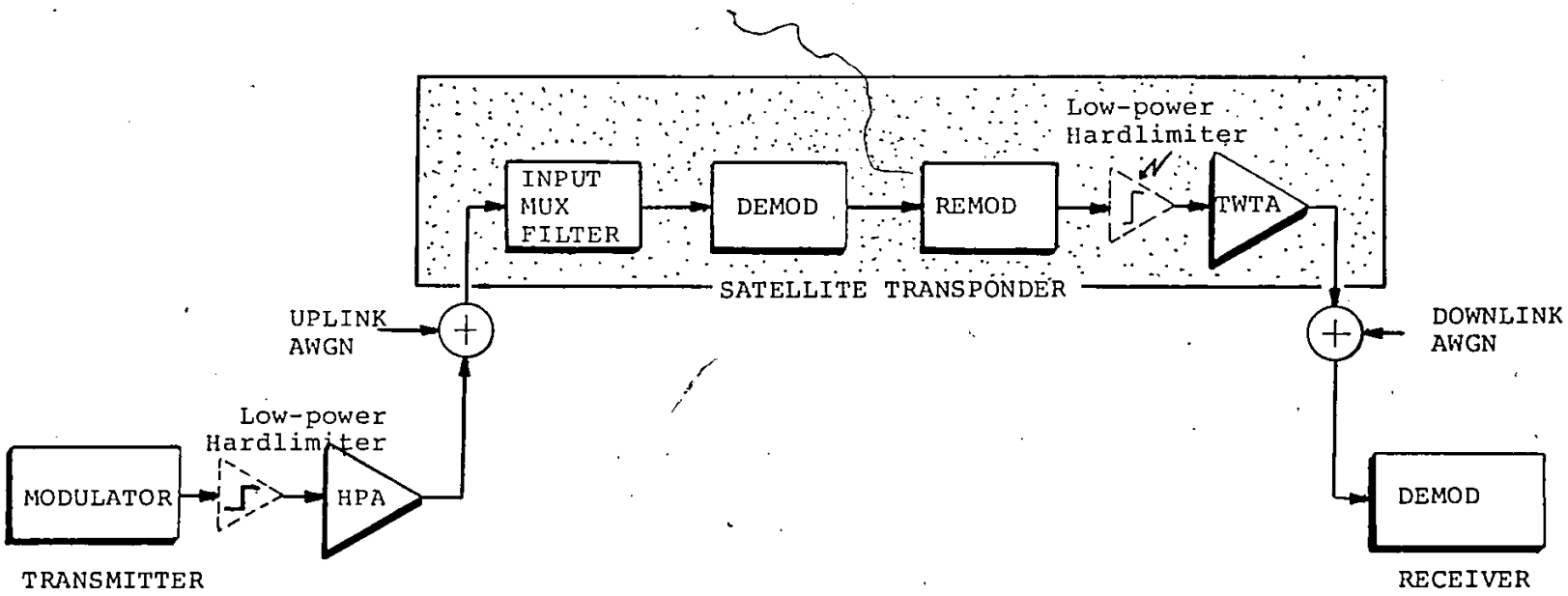

Fig. 5.7: SIMULATION MODEL OF A REGENERATIVE SATELLITE LINK

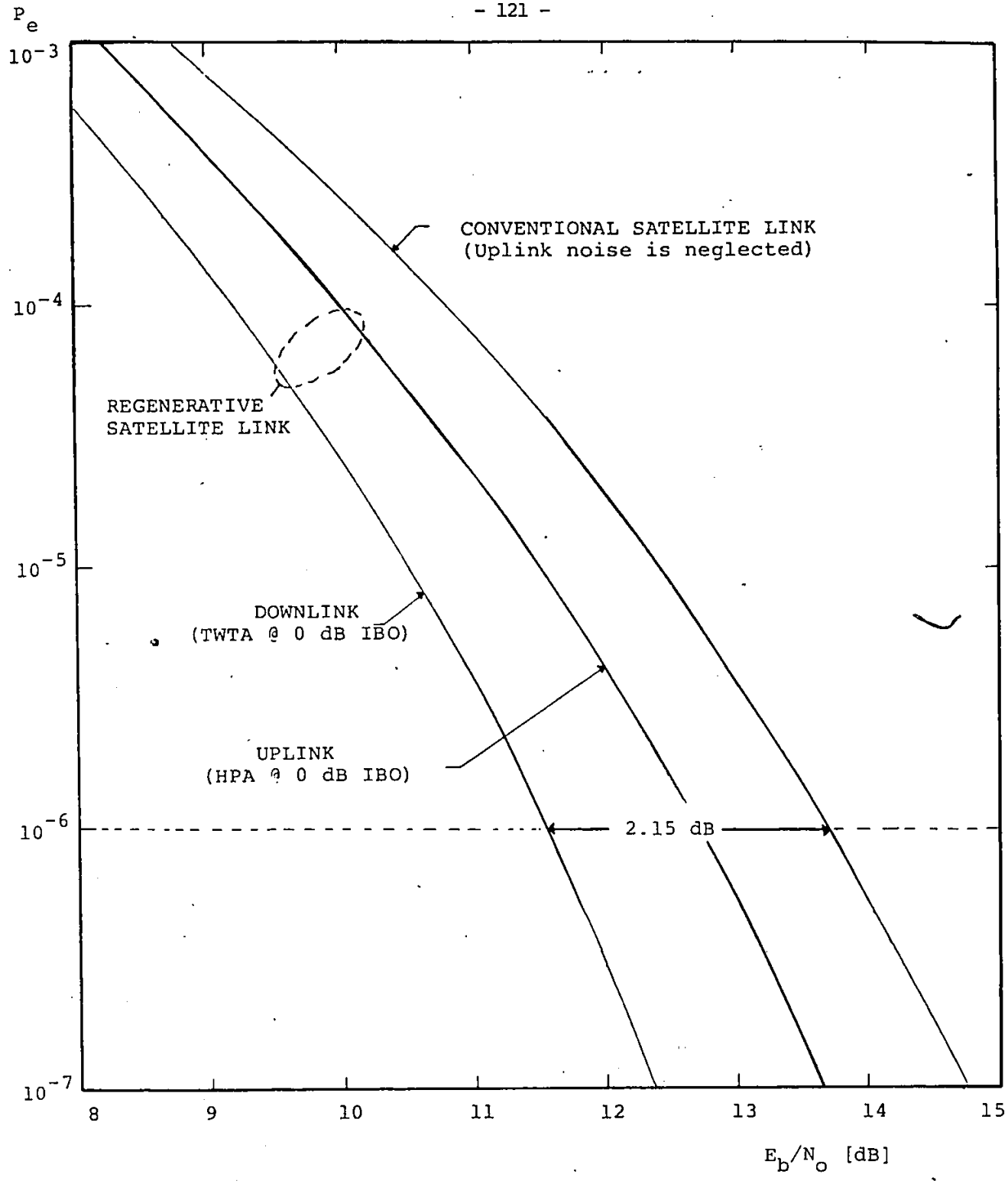

Fig.5.8a: PERFORMANCE OF CONVENTIONAL AND REGENERATIVE SATELLITE LINKS USING IJF-OQPSK MODEMS

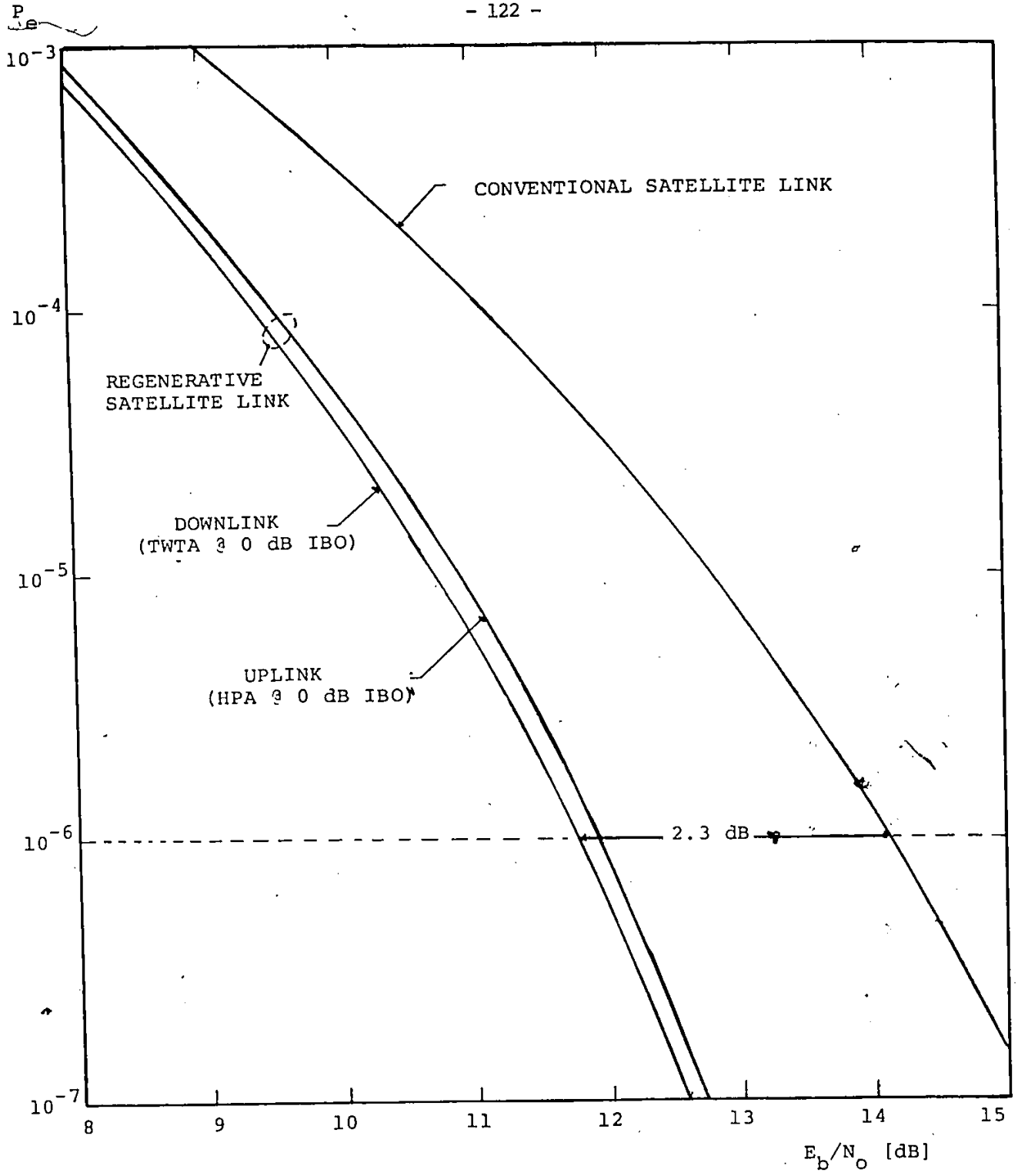

Fig. 5.8b: PERFORMANCE OF *HARDLIMITED* IJF-OQPSK MODEMS IN CONVENTIONAL AND REGENERATIVE SATELLITE SYSTEMS

where P_{eU} and P_{eD} are the uplink and downlink P_e performance respectively. This equation is used to plot the "Iso-Probability of error performance" curves for $P_{eT}=10^{-4}$ of the regenerative link using IJF-OQPSK modems, as shown in Fig. 5.9. The IJF-OQPSK modulators may be equipped with ideal *low-power hardlimiters* prior to the high-power amplifiers. The hardlimited IJF-OQPSK signal has a constant envelope, therefore does not undergo AM/AM and AM/PM conversions of the HPA and TWTA. The HPA and TWTA can operate at saturation, that is, 0 dB back-off. Consequently the system power efficiency of the transmitter is increased and the cost and weight of the HPA or TWTA in use is reduced. The simulation results shown in Fig. 5.9 indicate that the regenerative satellite system using IJF-OQPSK modems with a low-power hardlimiter is the best choice when the HPA and TWTA operate at 0 dB back-off. The results (Fig. 5.9) also show that the regenerative system using the IJF-OQPSK modem introduces a gain of 1 dB at $P_e=10^{-4}$ in both the uplink and the downlink performance, compared to the regenerative system using QPSK modems.

5.2 P_e PERFORMANCE OF IJF-QPSK AND IJF-OFFSET QPSK IN A COMPLEX INTERFERENCE ENVIRONMENT

5.2.1 Computer Simulation Model

Fig. 5.10 shows the simulation model of a multi-channel system. It is an equivalent complex baseband model of the

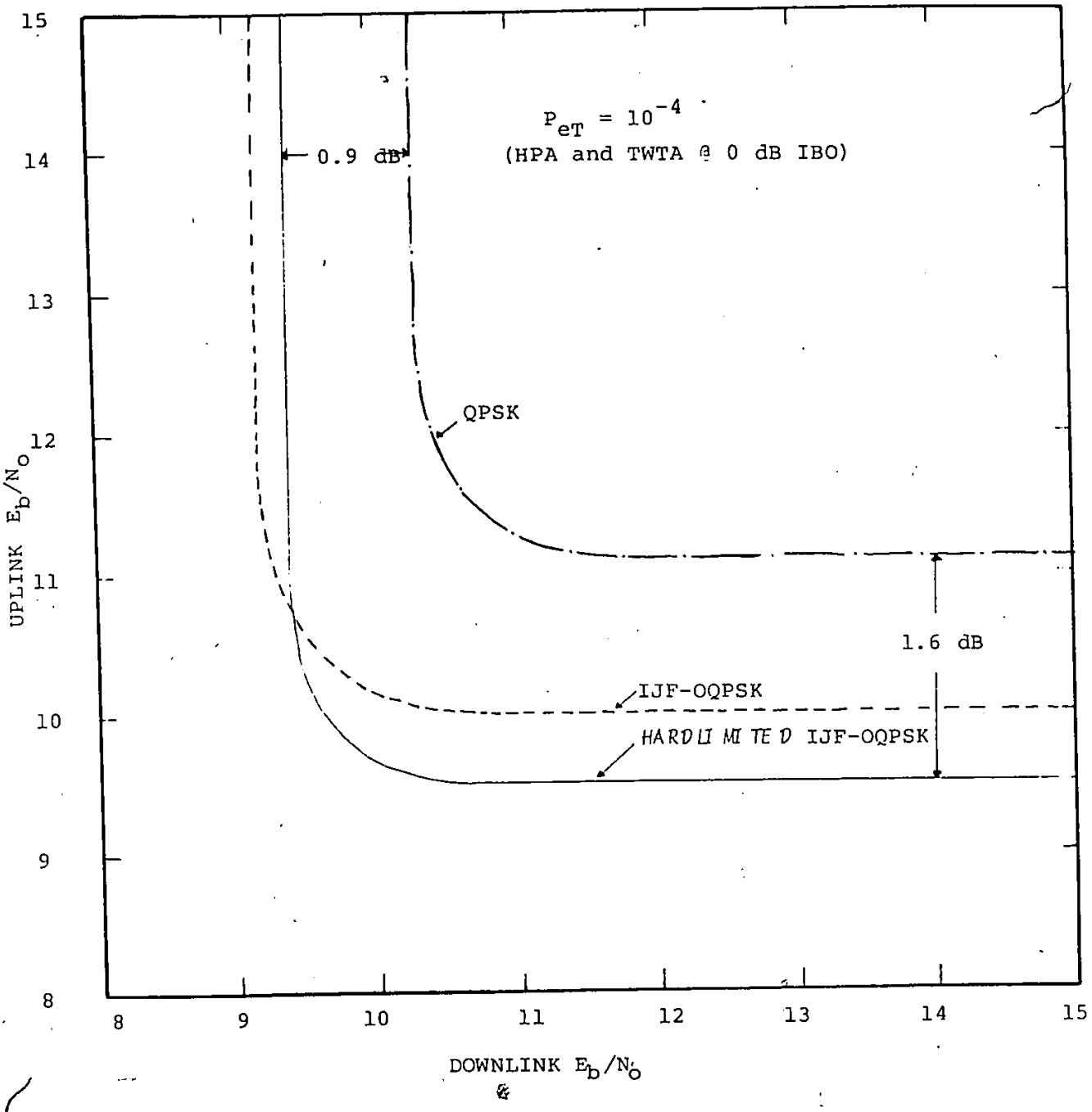

Fig.5.9: COMPARATIVE PERFORMANCE OF REGENERATIVE SATELLITE SYSTEMS USING IJF-OQPSK AND QPSK MODEMS

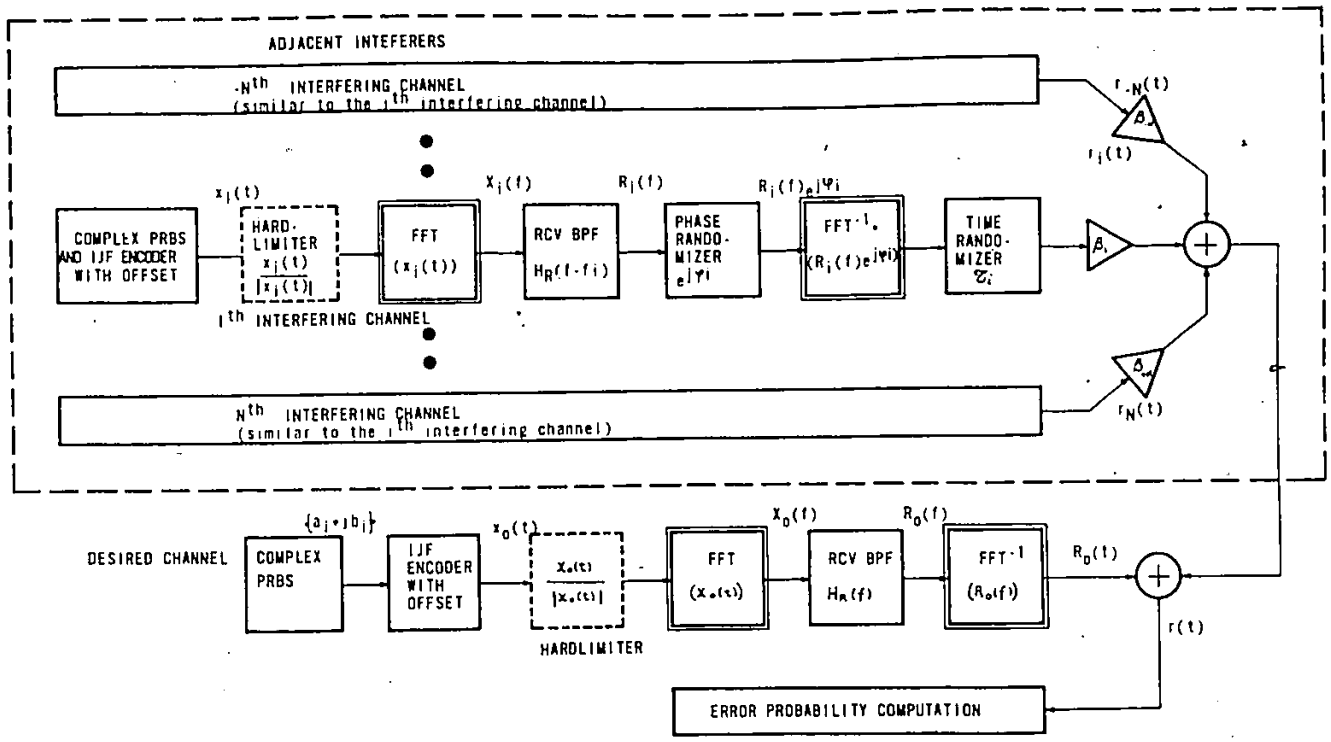

Fig. 5.10: MODEL OF THE SIGNAL PROCESSING AND P_e CALCULATION FOR A MULTI-CHANNEL IJF-OQPSK SYSTEM

modulated system. Filtering is processed in the frequency domain with the aid of Fast Fourier Transform (FFT) techniques: the receive detection filter is represented by its lowpass equivalent transfer function $H_R(f)$ for the main channel and by $H_R(f-f_i)$ for the ith interfering channel. The filtering process is performed by multiplying the Fourier transform of the complex baseband signal by the lowpass equivalent transfer function of the receive filter, i.e. the Fourier transform of the received desired signal is

$$R_o(f) = H_R(f) \cdot FFT \{x_o(t)\} \tag{5.1a}$$

and the Fourier transform of the received ith interfering signal is

$$R_i(f) = H_R(f-f_i) \cdot FFT \{x_i(t)\} \tag{5.1b}$$

where f_i represents the channel spacing between the main and the ith interfering channels. The lack of coherence between the ith interfering and main channels is included by the multiplication

$$R_i(f) \cdot e^{j\phi_i} \tag{5.2a}$$

where ϕ_i is a random variable uniformly distributed in $(0,2\pi)$.

The lack of synchronization between the ith interfering and main channels is introduced by rotating the interfering complex baseband signal $r_i(t)$ by ζ_i where ζ_i is a random variable uniformly distributed in $(0,T_s)$, and

$$r_i(t) = FFT^{-1}\{R_i(f)e^{j\phi_i}\} \tag{5.2b}$$

The *noise-free* received signal containing interchannel interference is given by

$$r(t) = r_o(t) + \sum_{i=-N}^{+N} \beta_i r_i(t) \tag{5.3}$$

where β_i represents the relative voltage difference between the ith interfering and main channels at the receiver input.

At the receive end, the corresponding real and imaginary parts, $r_I(t)$ and $r_Q(t)$, are sampled at kT_s and $(k+\frac{1}{2})T_s$ respectively. The conditional error probability in an AWGN environment for the samples $r_I(kT_s)$ and $r_Q((k+\frac{1}{2})R_s)$ is given by [25]

$$P(e|r_I(kT_s)) = \begin{cases} 1-\text{erfc}[\dfrac{r_I(kT_s)}{\sigma_n\sqrt{2}}], & \text{if } a_k r_I(kT_s) < 0 \\ \\ \dfrac{1}{2}\,\text{erfc}(\dfrac{r_I(kT_s)}{\sigma_n\sqrt{2}}) & \text{otherwise} \end{cases} \tag{5.4a}$$

$$P(e|r_Q((k+\tfrac{1}{2})T_s)) = \begin{cases} 1-\operatorname{erfc}\left[\dfrac{r_Q((k+\frac{1}{2})T_s)}{\sigma_n\sqrt{2}}\right], & \text{if } b_k \cdot r_Q[(k+\tfrac{1}{2})\tfrac{T_s}{2}] < 0 \\ \tfrac{1}{2}\operatorname{erfc}\left(\dfrac{r_Q((k+\frac{1}{2})T_s)}{\sigma_n\sqrt{2}}\right), & \text{otherwise} \end{cases} \tag{5.4b}$$

where

a_k, b_k are the $k^{\underline{th}}$ symbols in the transmitted complex pseudo-random sequence,

σ_n^2 is the noise variance,

$$\sigma_n^2 = \frac{N_o}{2}\int_{-\infty}^{+\infty}|H_R(f)|^2 df$$

and

$\frac{N_o}{2}$ is the double-sided noise spectral power density of the AWGN.

The error probability is then given by

$$P_e = \frac{1}{2M}\sum_{k=1}^{M}\{P(e|r_I(kT_s))+P(e|r_Q((k+\tfrac{1}{2})T_s))\} \tag{5.5}$$

where M is the length of the transmitted pseudo-random sequence.

5.2.2. Illustrative Simulation Results

As an illustrative example, the IJF-QPSK and IJF-Offset QPSK modems with the IJF double-interval pulse

$$s(t) = \frac{1}{2}(1+\cos\frac{\pi t}{T_s})$$

are used in the simulation model. The receive detection filter is a raised-cosine-type filter having a linear phase response and an amplitude response given by Eq. (3.40).

5.2.2.1. Performance of IJF-OQPSK Scheme in a Co-Channel Interference (CCI) Environment

A *frequency-reuse* communication system using IJF-OQPSK scheme is simulated by introducing an interfering channel centered at the same carrier frequency as the main channel (i.e. co-channel interference). Fig. 5.11 shows the effects of the co-channel interference on the performance degradation at $P_e=10^{-4}$, with different receive filter roll-off factors, α. It indicates that the receive filter with a roll-off factor $\alpha=0.6$ provides the best performance in both linear and hardlimited channels. It also shows that a C/I ratio of 26 dB is acceptable provided an increase in the E_b/N_o ratio of about 0.3 dB can be tolerated for the same P_e performance.

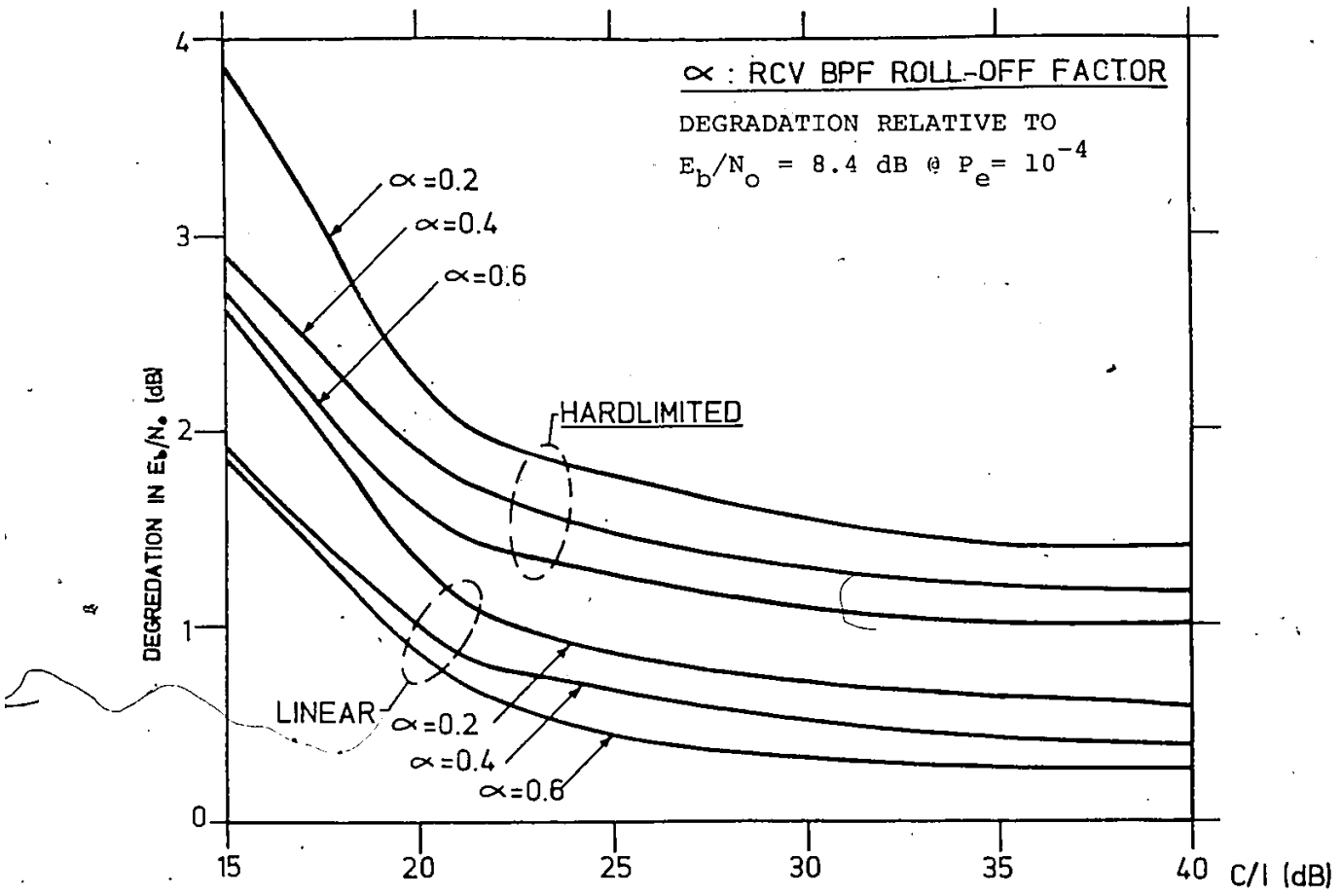

Fig. 5.11: PERFORMANCE DEGRADATION VERSUS C/I IN A CCI AND AWGN ENVIRONMENT

5.2.2.2. Performance of IJF-OQPSK Scheme in an *Adjacent Channel* Interference (ACI) Environment

Fig. 5.12 shows the results of the carrier-to-interference (C/I) power ratio versus the carrier frequency difference with two equal power channels for the region of major interest (7/12 to 9/12 of the normalized channel spacing). The receive filter having a smaller roll-off factor (α) provides better C/I ratio.

At first the effect of a *single* adjacent channel interferer on the P_e performance is investigated. As illustrated in Fig. 5.13 the simulation results indicate that for a channel spacing of less than 0.68 of the bit rate frequency the receive filter having α=0.4 provides the best performance.

The effect of two equally spaced upper and lower adjacent channels on the P_e performance of the desired IJF-OQPSK channel was also investigated. The simulation results are shown in Fig. 5.14a for *equal-power* channels, and in Fig. 5.14b when one of the two interferers is 7 dB higher than the main channel. The second case illustrates the worst-case condition of the INTELSAT SCPC system [62].

The simulation results (Figs. 5.13, 5.14a,b) indicate that a receive detection filter having α=0.4 provides the best

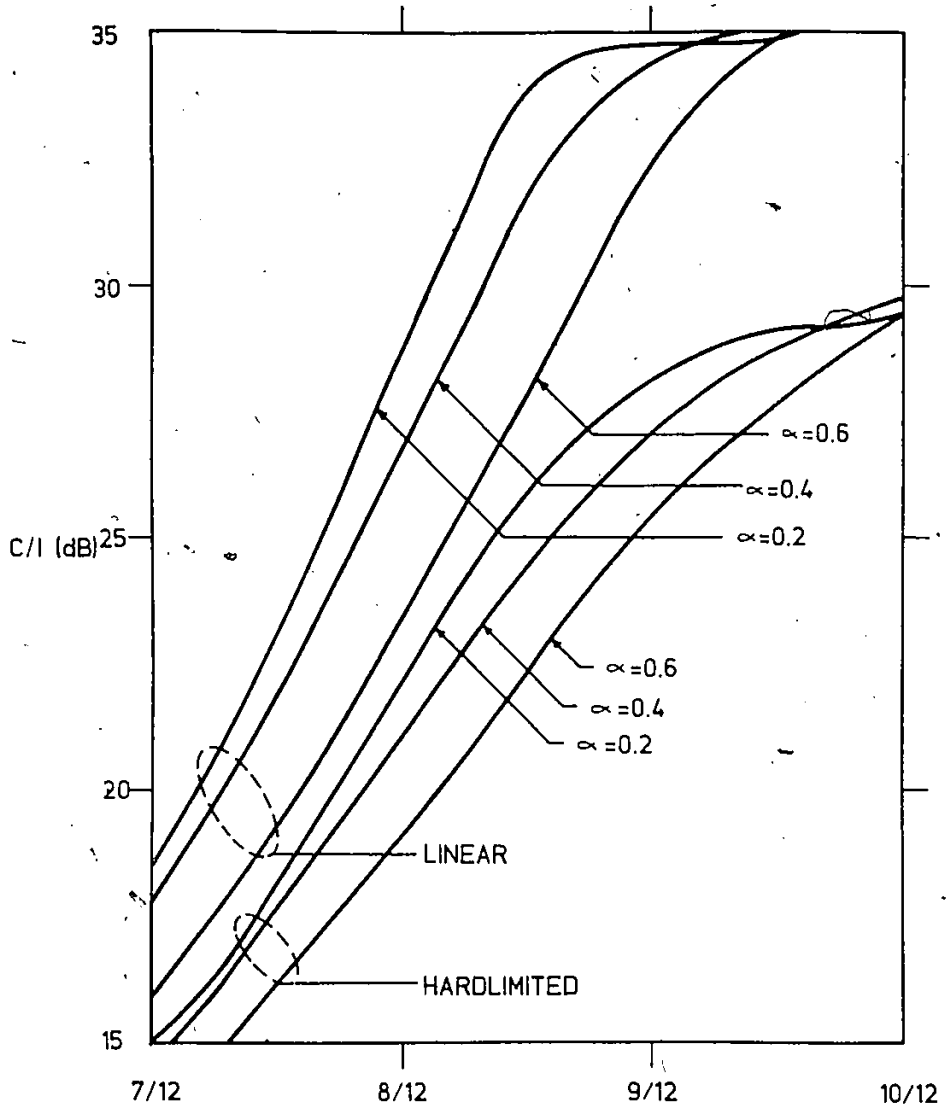

Fig. 5.12: C/I VERSUS CHANNEL SPACING
(for two equal-power channels with raised cosine-type receive filter)

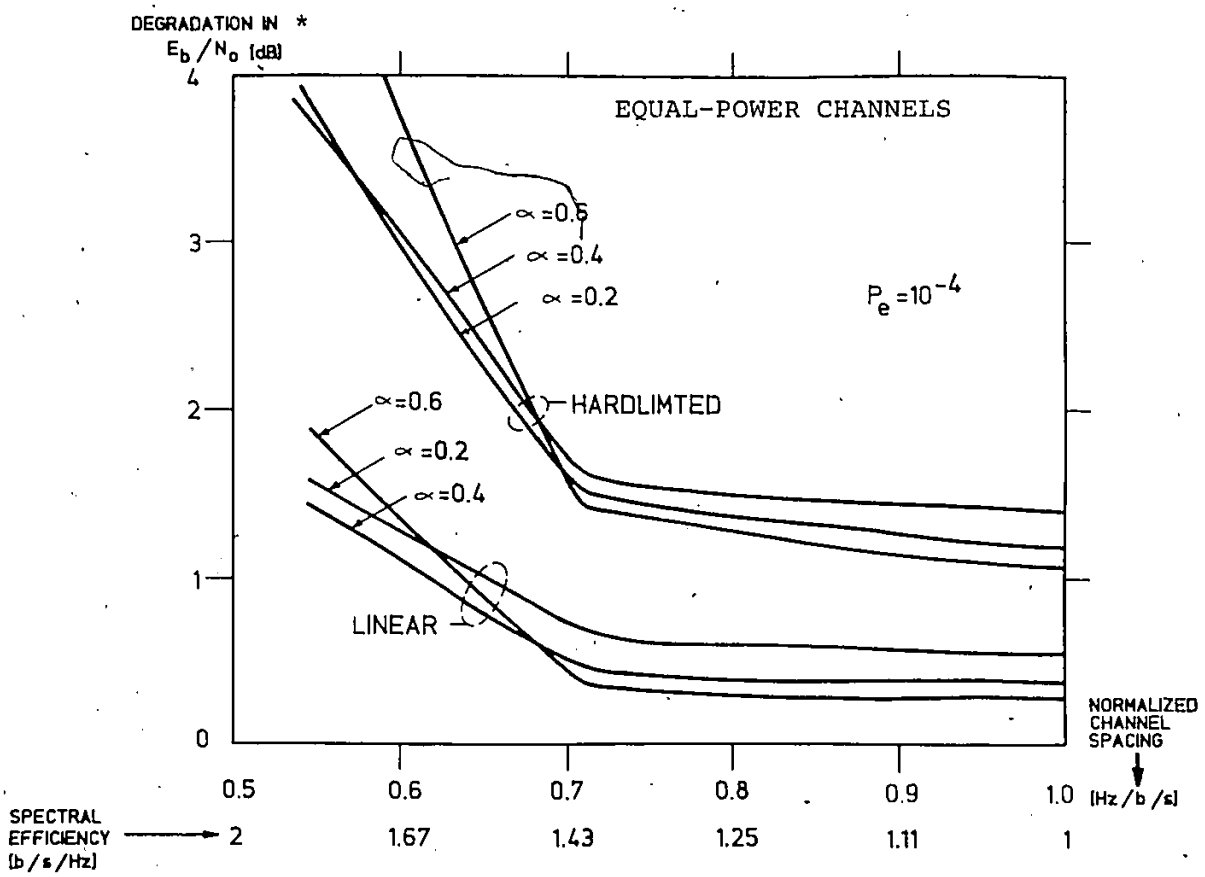

Fig. 5.13: DEGRADATION VERSUS CHANNEL SPACING IN THE CASE OF ONE ACI

(* *Degradation relative to* E_b/N_o = 8.4 dB @ $P_e = 10^{-4}$)

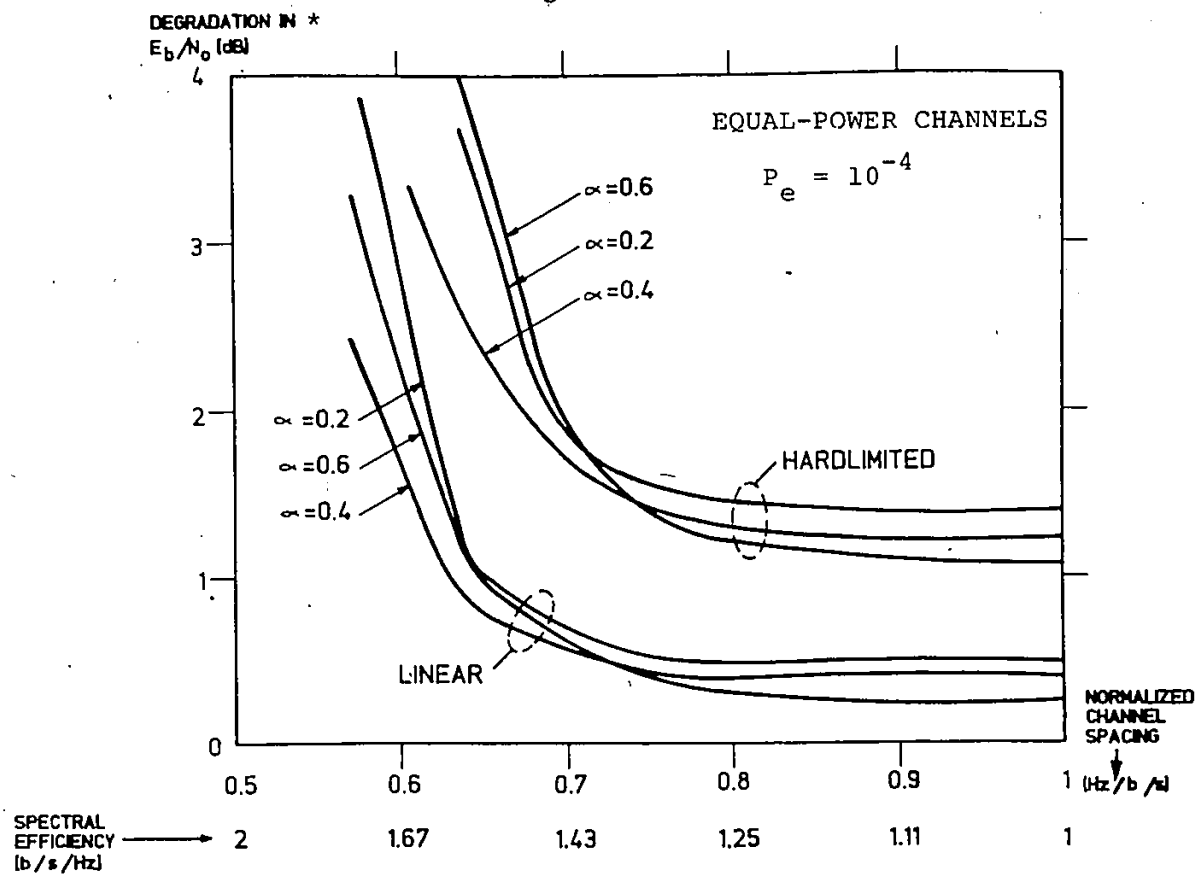

Fig. 5.14a: DEGRADATION VERSUS CHANNEL SPACING IN THE CASE OF TWO EQUAL-POWER ACI's

(* *Degradation relative to* E_b/N_o = 8.4 dB @ $P_e = 10^{-4}$)

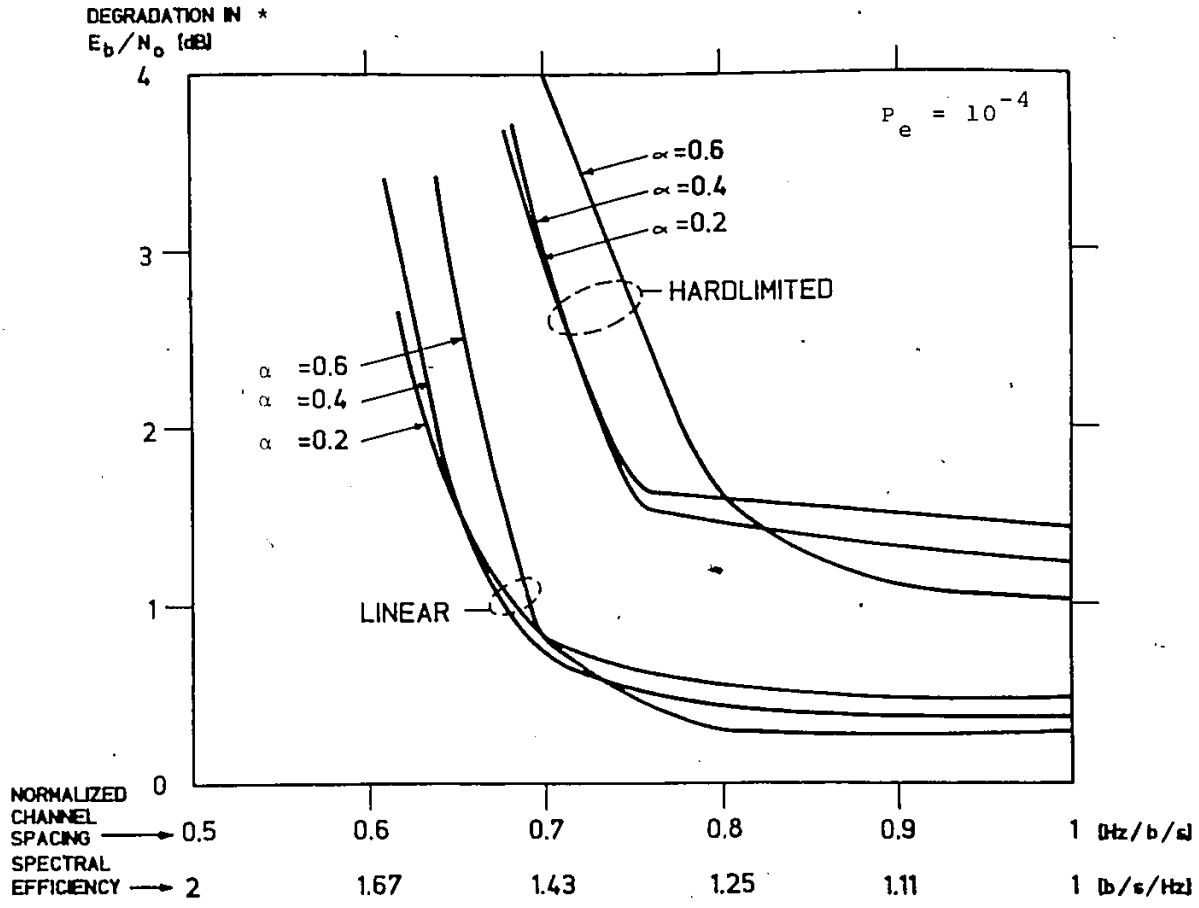

Fig. 5.14b: DEGRADATION VERSUS CHANNEL-SPACING IN THE CASE OF TWO ACI's (one ACI is 7dB higher than the main channel)

(* *Degradation relative to* $E_b/N_o = 8.4$ dB @ $P_e = 10^{-4}$)

performance for narrow channel spacings. Furthermore, the IJF-OQPSK modulation scheme can provide a spectral efficiency of 1.42 b/s/Hz with a performance degradation of less than 0.8 dB at $P_e = 10^{-4}$ in a multi-channel environment with an adjacent interferer being 7 dB higher than the desired channel in a *linear* environment (Fig. 5.14b). This approaches the current Intelsat SCPC system requirements.

5.2.3. Performance Comparison

5.2.3.1. Performance of a Saturated HPA Single Channel-Per-Carrier (SCPC) System

In a conventional multi-channel SCPC earth station, a number of modulated signals are combined at IF, upconverted to RF and amplified by a common transmit high-power amplifier (HPA). To avoid the intermodulation products the transmit HPA must operate in linear mode having a large backoff, thus a large loss in output power.

There is a growing demand on operating companies to provide SCPC earth terminals for use in remote areas for low data rate subscribers. Such terminals would typically require a *single* modulated channel only. The earth-station high-power amplifiers are expected to operate in saturation mode to obtain high-power efficiency and maximum RF output power. In such a system each satellite transponder will process a number of digitally

modulated carriers in a FDMA mode and, for this reason, operates in a linear region. Fig. 5.15 shows the block diagram of such SCPC system model with three channels. Equal channel spacing is assumed.

As shown in Fig. 4.14 the spectral regrowth of the IJF-OQPSK signal caused by a saturated HPA is less than that by an ideal hardlimiter. Hence the IJF-QPSK signal amplified by a *saturated HPA* creates less adjacent channel interference than the *hardlimited* IJF-QPSK. The performance of both IJF-QPSK and IJF-Offset QPSK modems in a *multi-channel* environment is presented in Fig. 5.16. It is confirmed that the IJF-QPSK modem with a saturated HPA has a better performance than that with an ideal hardlimiter. On the contrary, whether the IJF-Offset QPSK signal is hardlimited or amplified by a saturated HPA, it exhibits the same spectral spreading, hence creates the same ACI. Fig. 5.16 indicates that the IJF-Offset QPSK modem with an ideal hardlimiter has a slightly better performance than that with a saturated HPA. The additional E_b/N_o degradation is contributed by the AM/PM conversion of the HPA. For this reason, *a low-power hardlimiter having a negligible AM/PM effect is inserted prior to the saturated HPA in practical systems* to improve the performance.

The second set of results (Fig. 5.17) presents the E_b/N_o degradation compared to the optimum theoretical performance in a linear channel, i.e. E_b/N_o=8.4 dB at $P_e=10^{-4}$ as a function

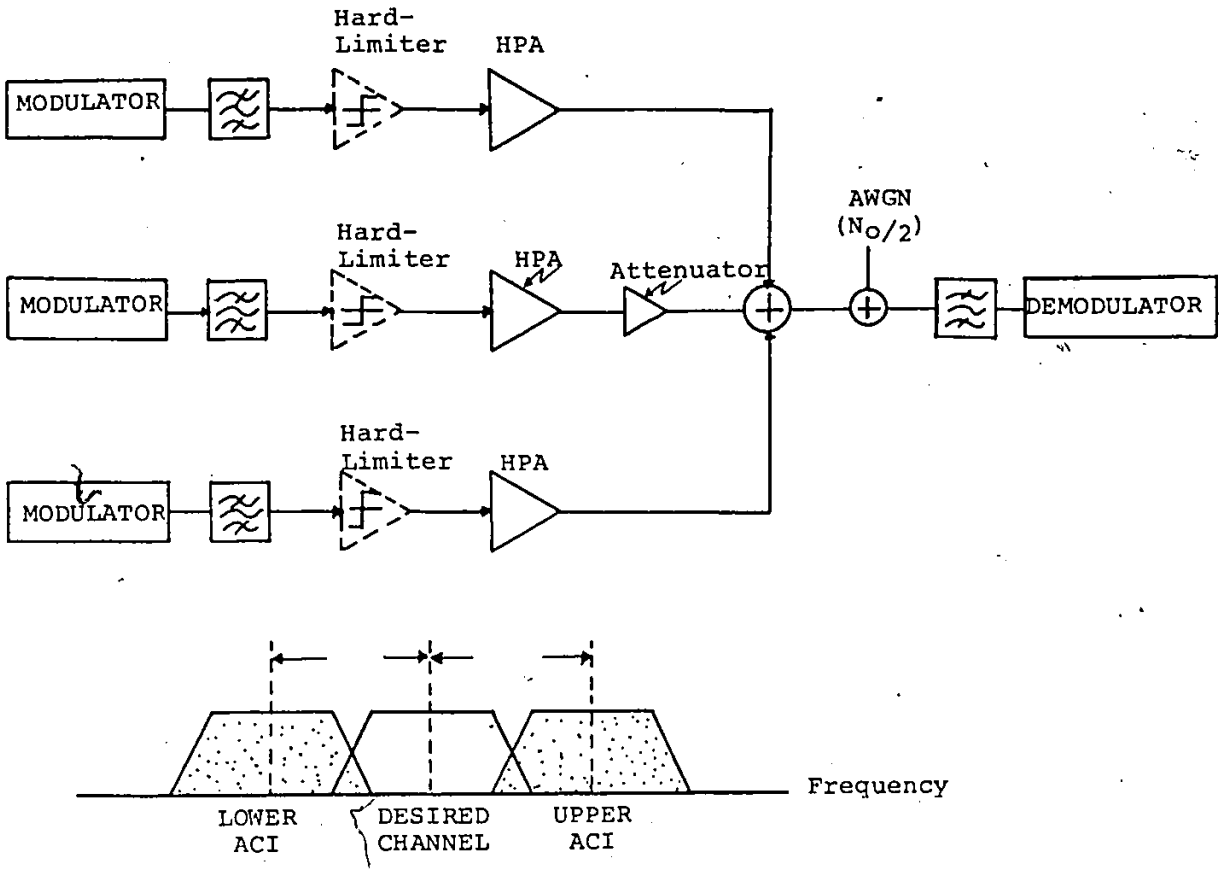

Fig. 5.15: SCPC SATELLITE SYSTEM MODEL

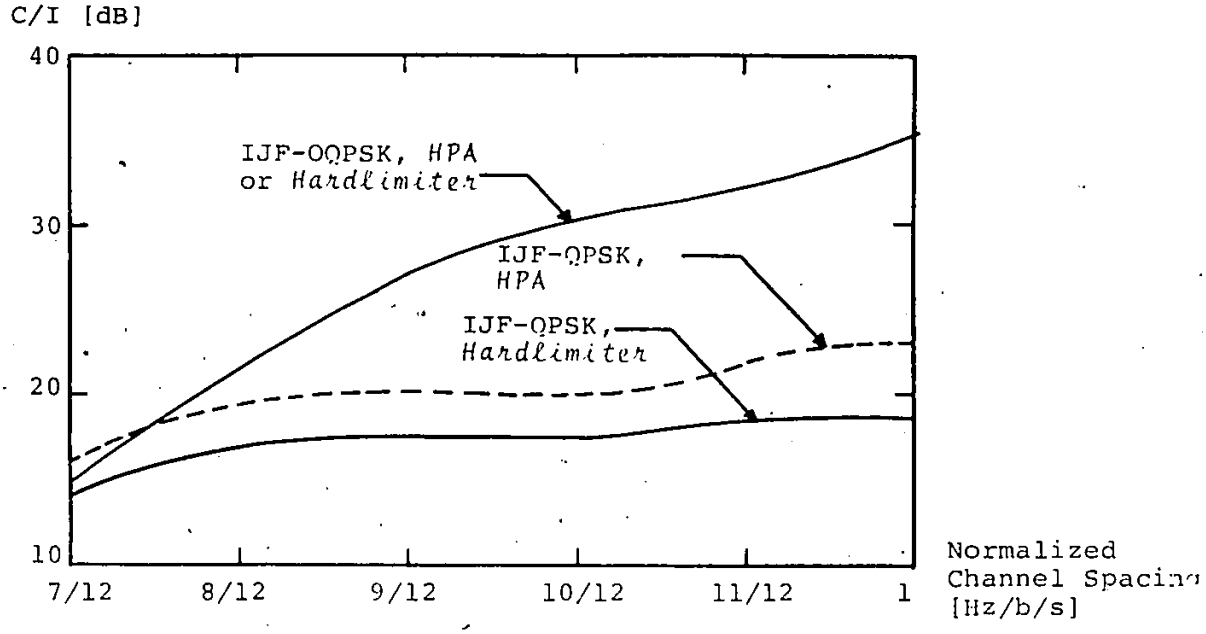

(a) Carrier-to-Interference Power ratio measured at the output of the receive BPF.

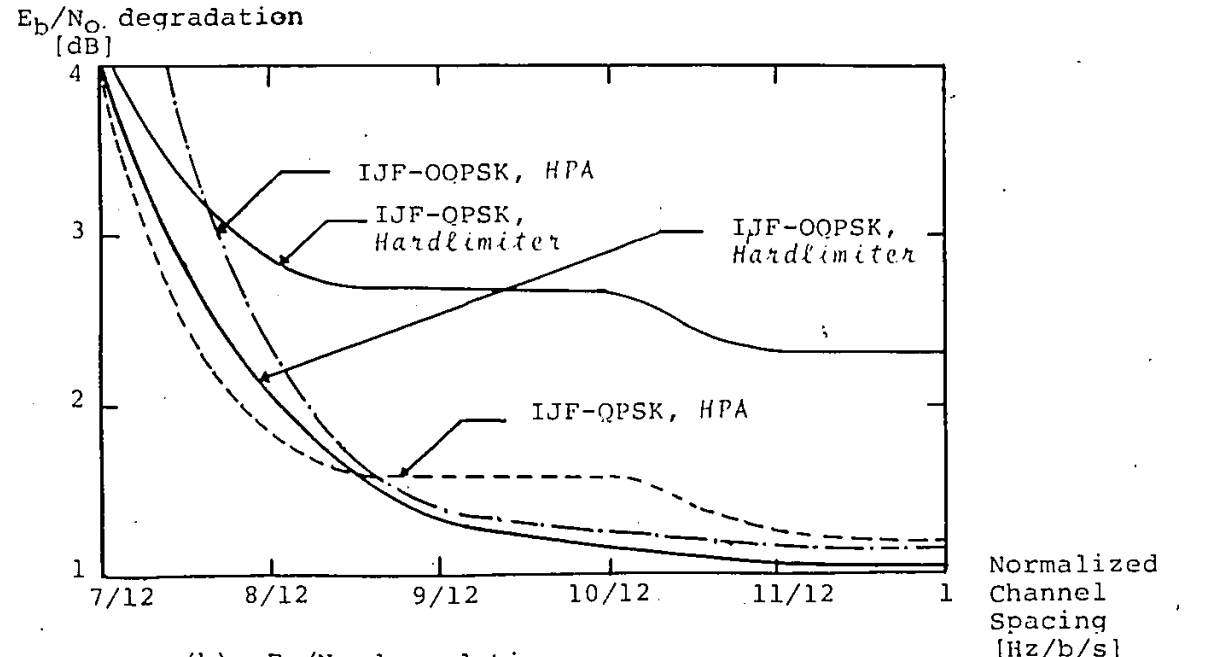

(b) E_b/N_o degradation
(relative to E_b/N_o = 8.4 dB @ $P_e=10^{-4}$)

Fig. 5.16: PERFORMANCE OF IJF-QPSK AND IJF-OFFSET QPSK MODEMS IN A MULTI-CHANNEL NONLINEAR ENVIRONMENT

(Receive detection filter: raised-cosine type with $\alpha=0.4$)

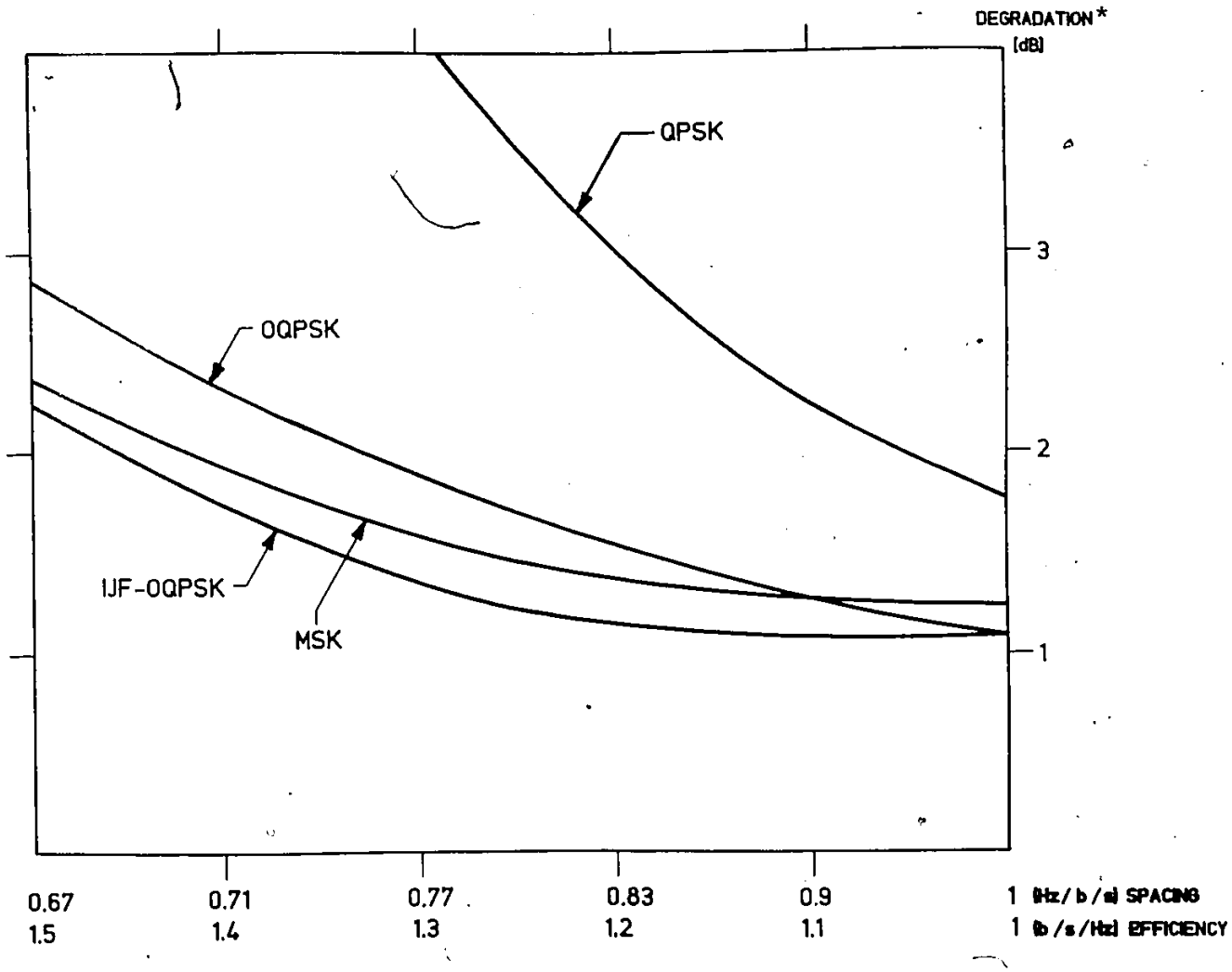

Fig. 5.17: PERFORMANCE COMPARISON OF QPSK, OQPSK, MSK AND IJF-OQPSK IN A HARDLIMITED MULTI-CHANNEL SYSTEM

(* Degradation relative to E_b/N_o = 8.4 dB @ $P_e = 10^{-4}$)

of the normalized channel spacing (i.e. channel spacing/bit rate). The desired (main) and adjacent channels are assumed to have the same power at the input of the receiver earth-station. Filter partitioning used for IJF-OQPSK, QPSK, and MSK modems is summarized in Table 5.2. For QPSK and Offset QPSK we adopt the most frequently used filtering strategies [73]. The results show that for narrow channel spacings less than the bit rate, the IJF-OQPSk system has the best performance, i.e. lowest degradation. This is explained as follows: The carrier-to-interference (C/I) ratio at the receive filter output for different modulation schemes is shown in Fig. 5.18. It is noted that the IJF-OQPSK modulation scheme provides the highest (best) C/I.

The higher C/I advantages of the IJF-OQPSK become more evident when the received modulated carrier power of the main channel is below that of the adjacent channels. This situation may occur in case of an *up-link fade* of the desired channel. Fig. 5.19 presents the E_b/N_o degradation as a function of the fade depth of the desired channel. As the main channel is attenuated, the adjacent channel interference becomes predominant and for this reason the modulation technique which creates less ACI provides better performance. As an example, for a fade depth of 12 dB of the desired channel, the IJF-OQPSK modem exhibits only 2 dB degradation; the performance degradation of QPSK modem is more than 7 dB, see Fig. 5.19b. These results indicate a significant performance improvement of the saturated HPA SCPC with IJF-OQPSK modems.

Table 5.2: FILTER PARTITIONING FOR IJF-OQPSK, QPSK, OFFSET QPSK, AND MSK (performance comparison shown in Fig. 5.17)

Modulation scheme	Transmit Shaping Filter	Receive Detection Filter
IJF-OQPSK	—— Nil ——	Full raised-cosine filter with aperture equalizer
QPSK and Offset QPSK	Square-root of raised-cosine filter with $\frac{x}{\sin x}$ equalizer	Square-root of raised-cosine filter
MSK	5th order Butterworth with $f_{3dB} = \frac{1}{2}$ bit rate	5th order Butterworth with $f_{3dB} = \frac{1}{2}$ bit rate

LINEAR PHASE RESPONSE IS ASSUMED

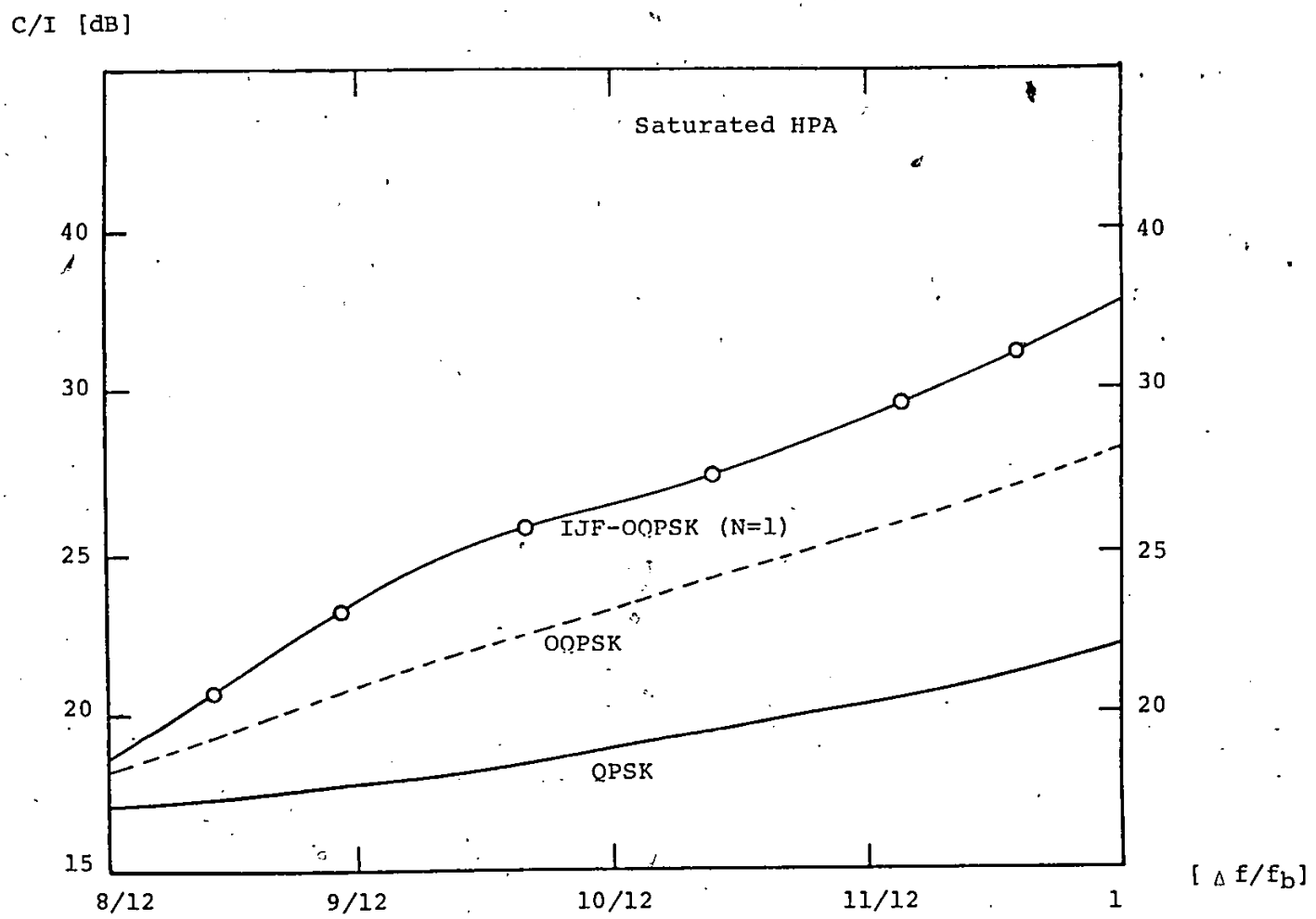

Fig.5.18: COMPARISON OF C/I OF QPSK, OQPSK, AND IJF-OQPSK MODEMS

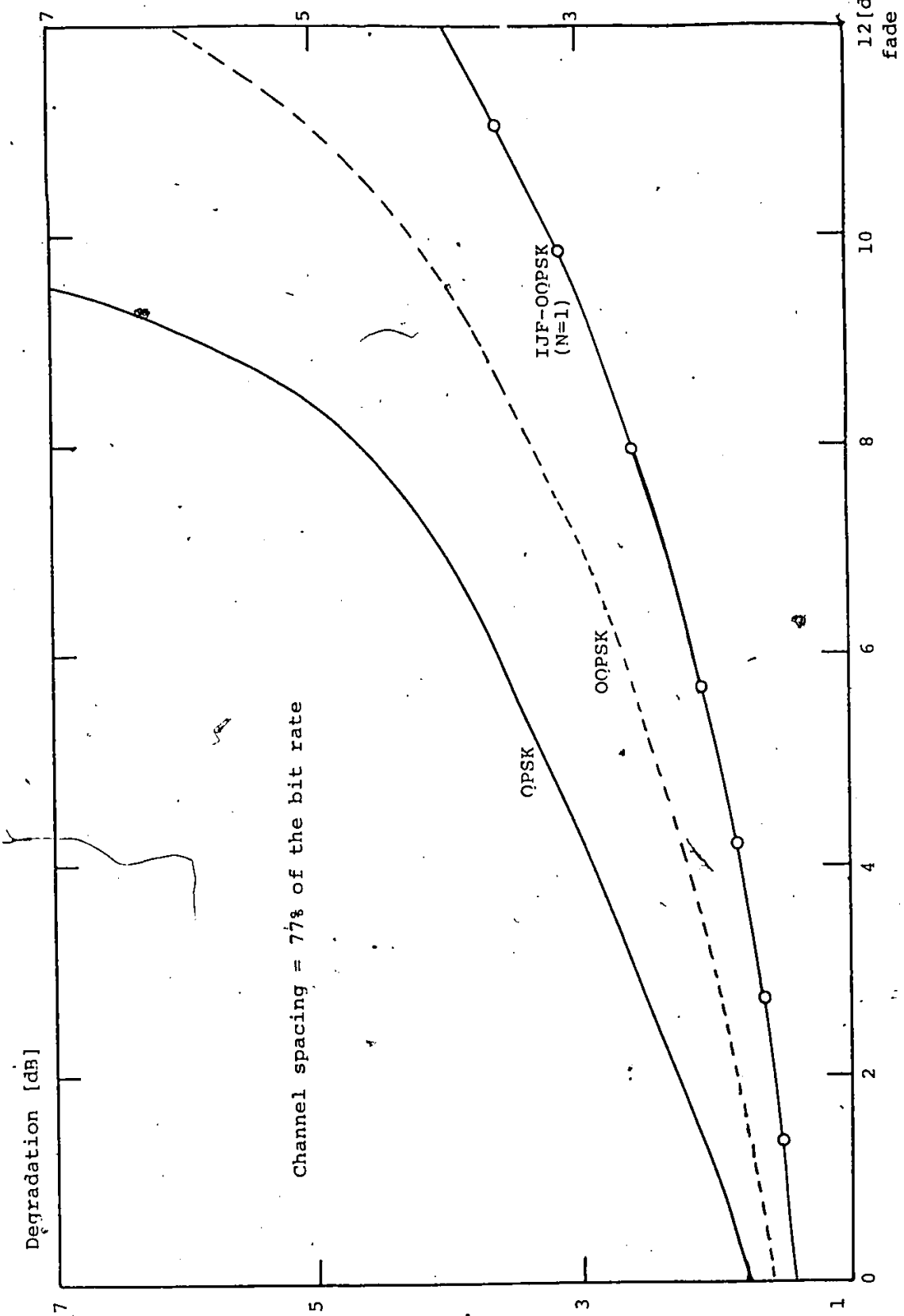

Fig. 5.19a: DEGRADATION VERSUS FADE DEPTH OF THE DESIRED CHANNEL FOR CHANNEL SPACING OF 77% OF THE BIT RATE. (compared to E_b/N_o = 8.4 dB for $P_e=10^{-4}$)

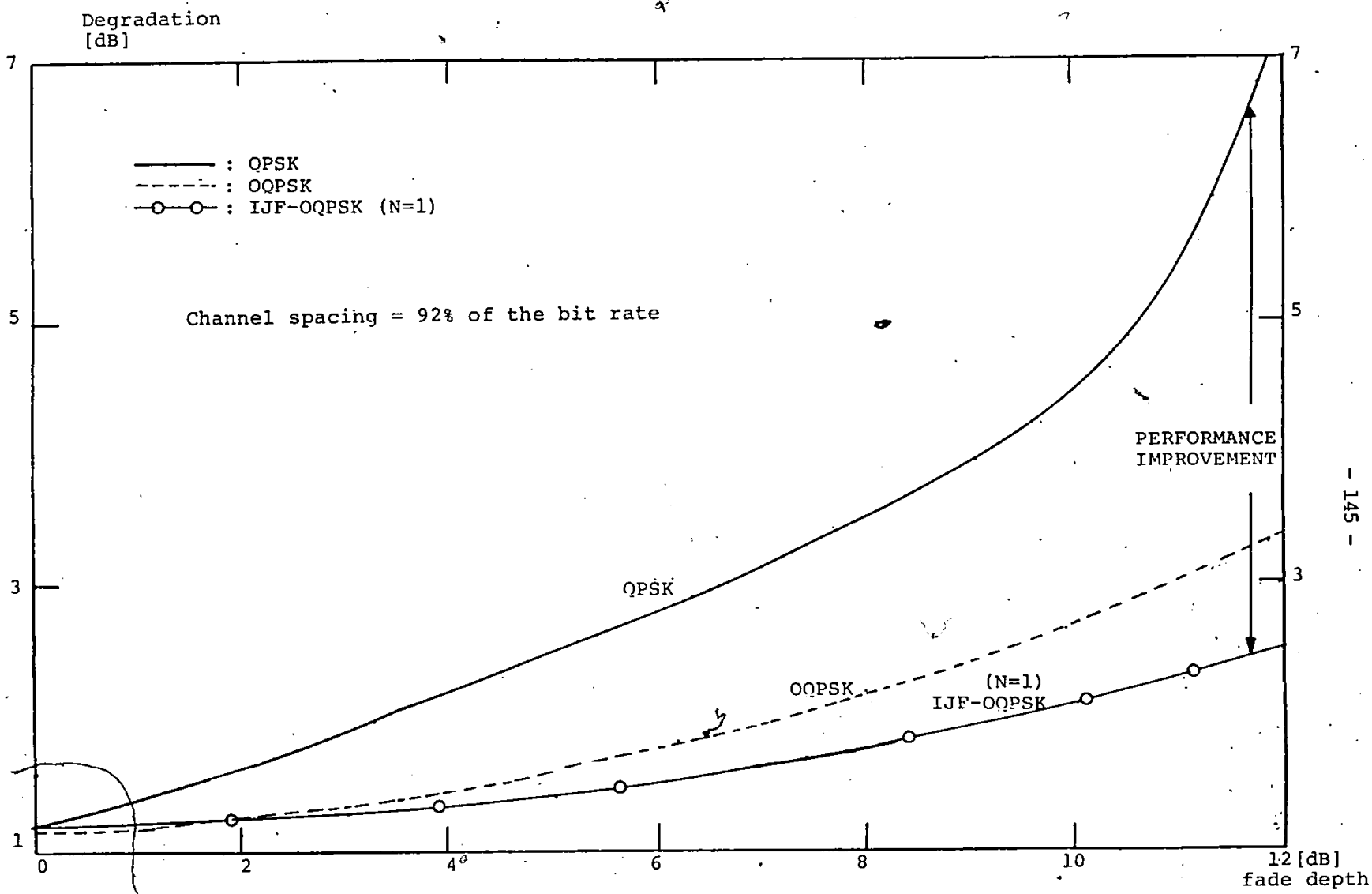

Fig. 5.19b: DEGRADATION VERSUS FADE DEPTH OF THE DESIRED CHANNEL FOR CHANNEL SPACING OF 92% OF THE BIT RATE (compared to E_b/N_o = 8.4 dB for $P_e=10^{-4}$)

5.2.3.2. Performance of an Illustrative On-Board Regenerative Satellite System

Fig. 5.20 illustrates an illustrative regenerative satellite system model with adjacent channel interference. The ACI is predominantly caused by spectral spreading of the modulated adjacent carriers.

Assume that the same modulation technique is used on the uplink and downlink. The individual link models include a saturated earth-station HPA and a saturated TWT in the satellite transponder. Otherwise, the link model is similar to that of the SCPC system presented in the previous section. Hence the individual uplink and downlink performance P_{eU} and P_{eD} can be obtained from the results given in Section 5.2.3.1. Using these results the "Iso-error probability performance" curves for the overall system performance $P_{eT}=10^{-4}$ of the regenerative system are plotted in Figs. 5.21a,b. E_b/N_o represents the required bit-energy-to-noise-density ratio of the main (desired) channel to maintain an overall error probability of 10^{-4} in the presence of two adjacent channels on both uplink and downlink. For the results in Fig. 5.21a the main and adjacent channels are assumed to have the same power at the input of the receiver. For the results in Fig. 5.21b the main channel power is lower than that of each adjacent channel by 12 dB.

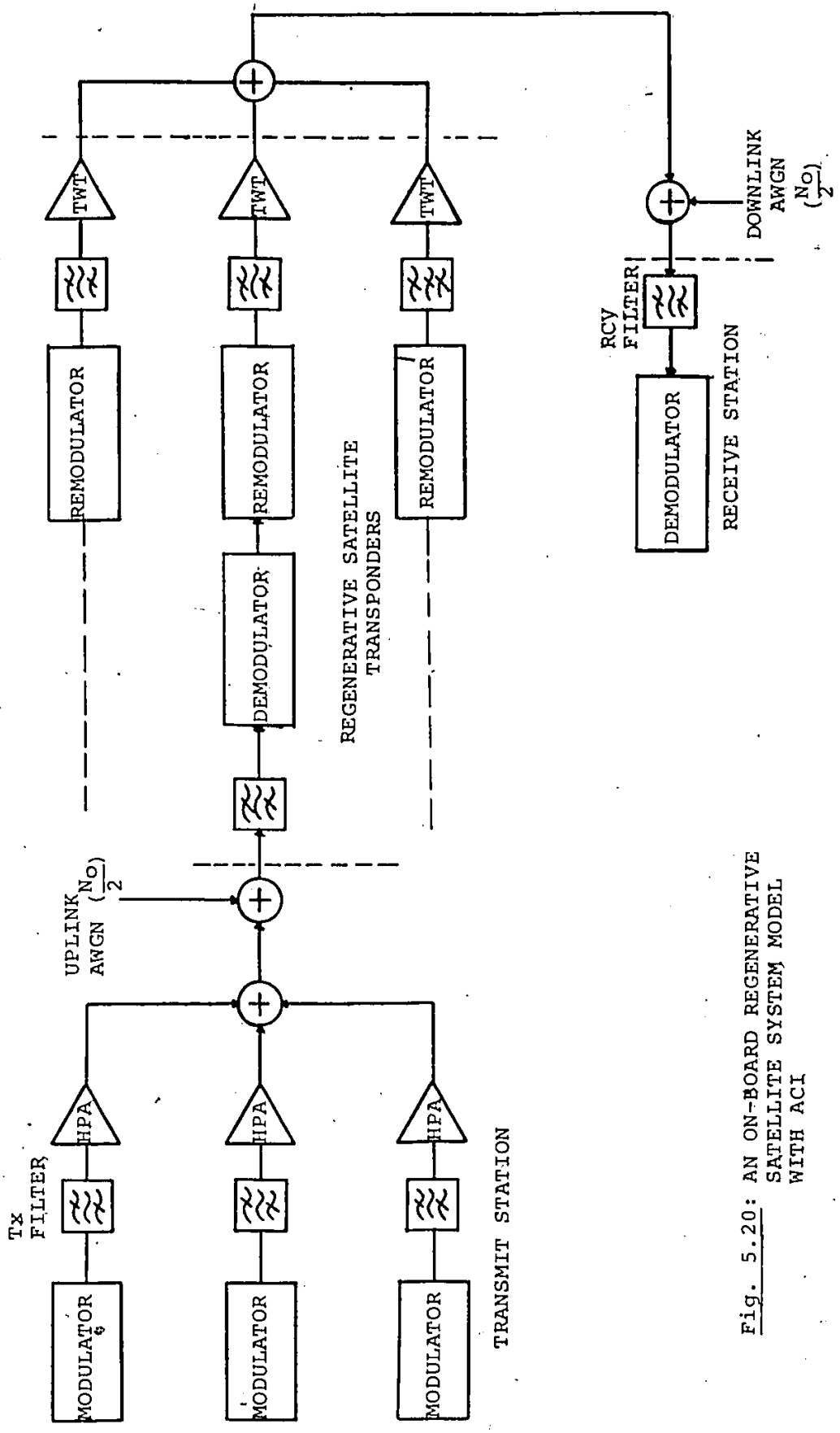

Fig. 5.20: AN ON-BOARD REGENERATIVE SATELLITE SYSTEM MODEL WITH ACI

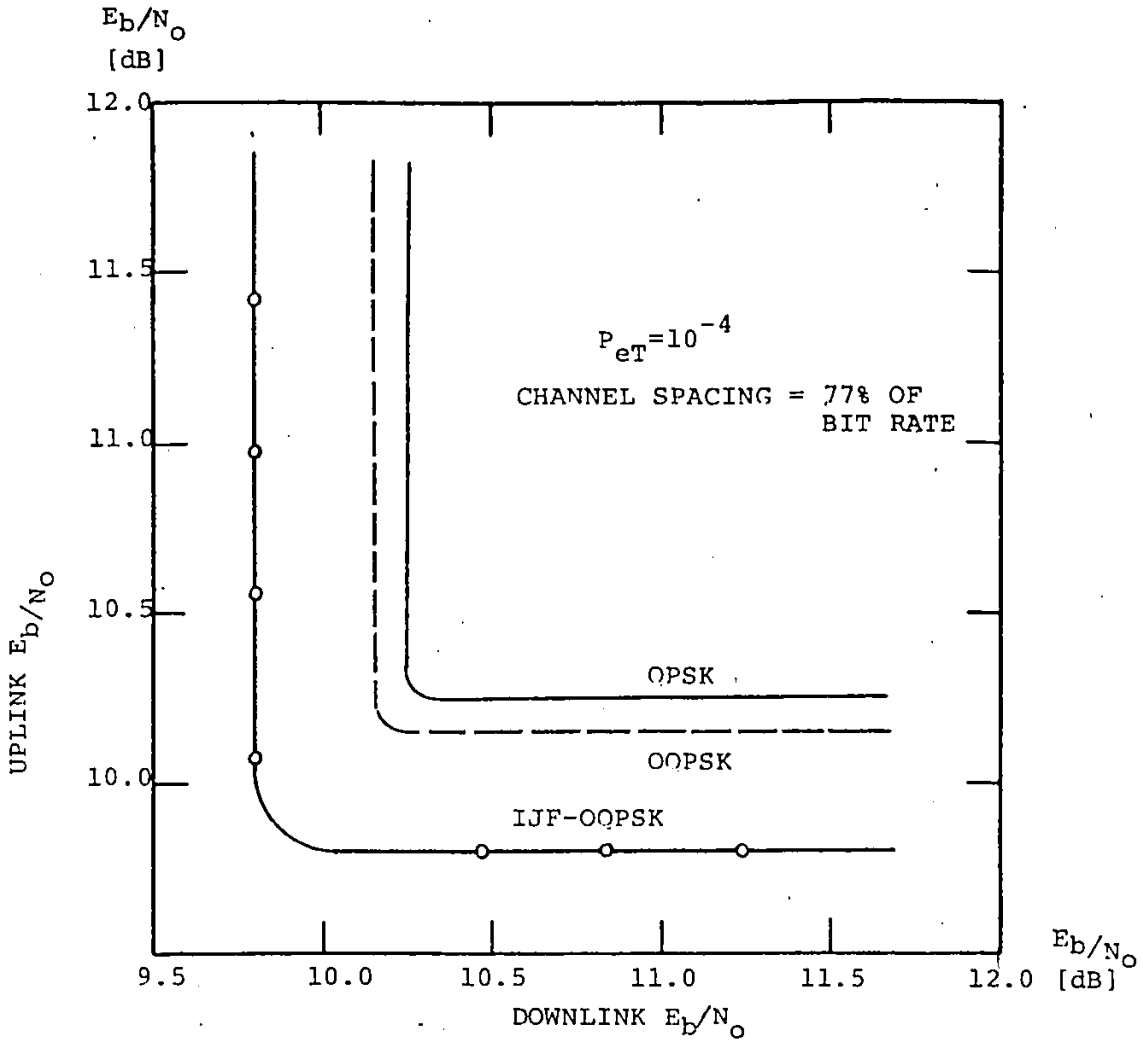

Fig.5.21a: ISO-ERROR PROBABILITY PERFORMANCE OF A REGENERATIVE SATELLITE SYSTEM WITH ACI (EQUAL POWER CHANNELS)

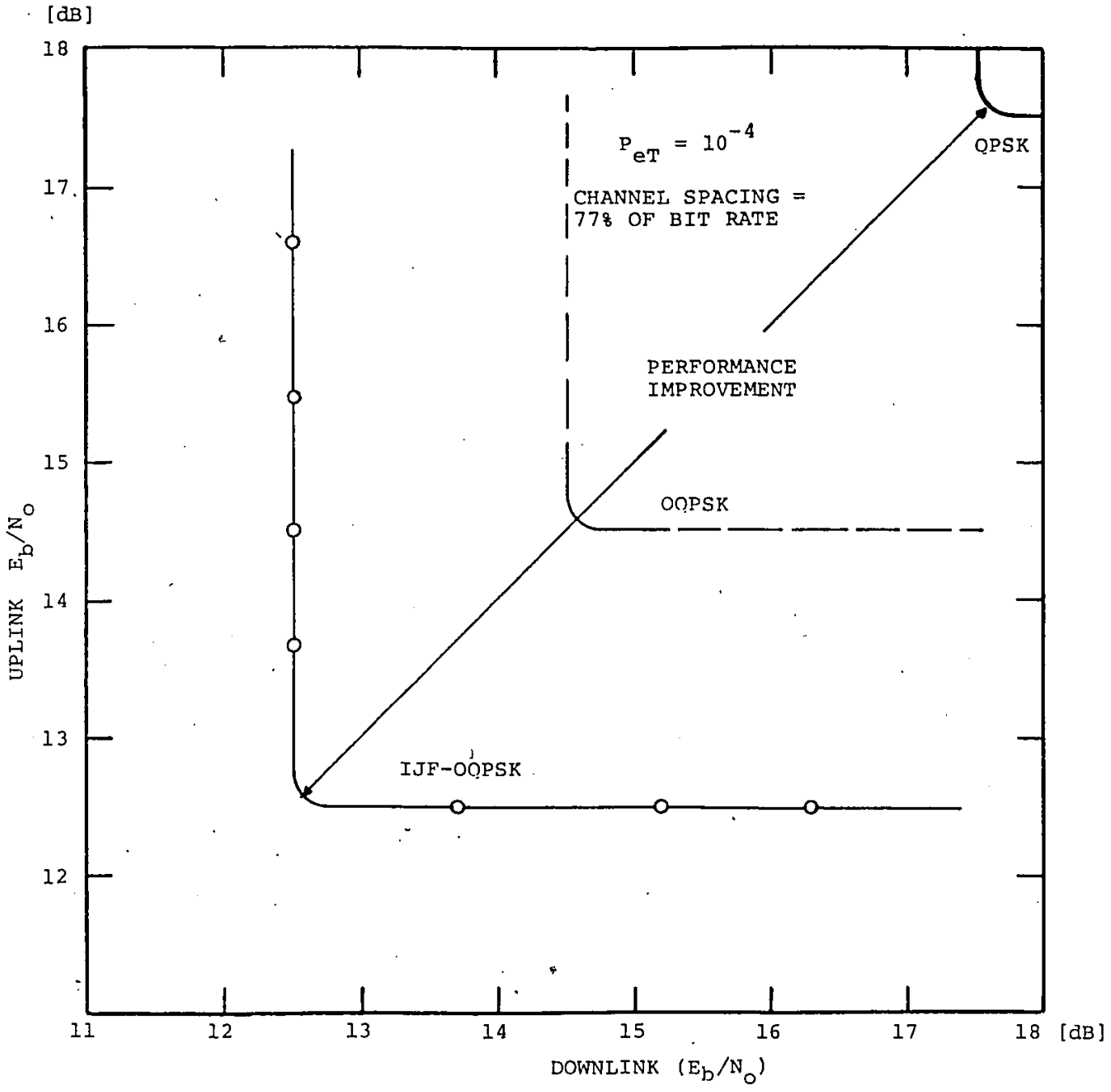

Fig. 5.21b: ISO-ERROR PROBABILITY PERFORMANCE OF REGENERATIVE SATELLITE SYSTEM WITH ACI (12 dB FADE DEPTH OF THE DESIRED CHANNEL)

Compared to QPSK and OQPSK modems, the IJF-OQPSK exhibits its improved performance specially when the main channel power is faded, i.e. it is below that of the adjacent channels.

5.2.4. Experimental Results

The experimental set-up to measure the P_e performance of an IJF-OQPSK modem in the presence of two adjacent channel interferers is shown in Fig. 5.22. The IJF double-interval pulse used in the IJF-OQPSK modem is $s(t) = \frac{1}{2}(1+\cos \frac{\pi t}{T_s})$. In the experiments the main channel IF frequency is centered at f_o = 512 kHz while the upper and lower adjacent channels are centered at (5.2 kHz + Δf_i and 512 kHz - Δf_i) respectively. The bit rate is 64 kb/s. A 6th order elliptic bandpass filter with amplitude and group delay equalization has been used as the receive detection filter. This filter approximates a raised-cosine-type filter used in simulation. Its center frequency is 512 kHz and its 3 dB-bandwidth is 37.5 kHz. Fig. 5.23 illustrates the C/I ratio (dB) versus the normalized channel spacing (Hz/b/s) at the bandpass filter output in the *hardlimited* case. The measured P_e performance of the hardlimited multiple-channel IJF-OQPSK systems is shown in Fig. 5.24. As an illustrative example of the Intelsat SCPC system, a channel spacing of 45 kHz is chosen in the experiment. The extra degradation at $P_e=10^{-4}$ due to ACI is 1.3 dB.

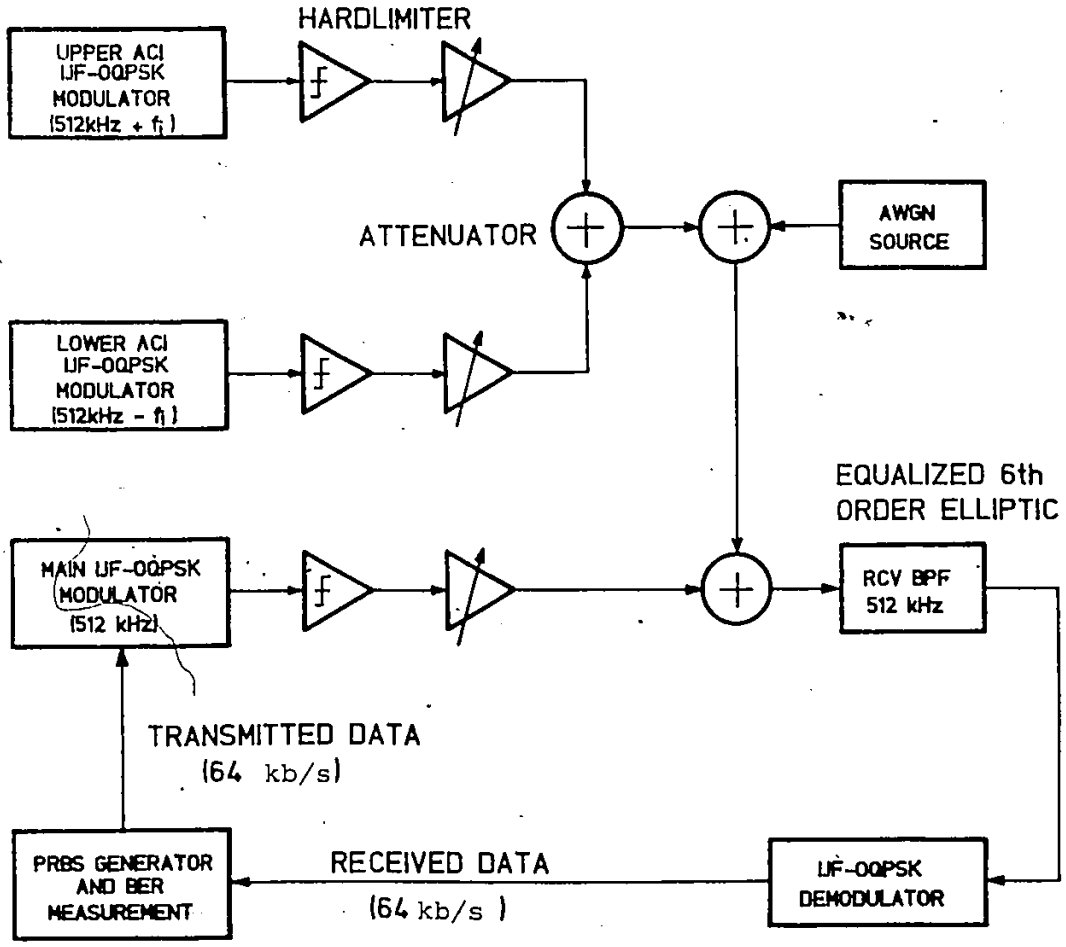

Fig. 5.22: EXPERIMENTAL SET-UP FOR A MULTI-CHANNEL IJF-OQPSK SYSTEM

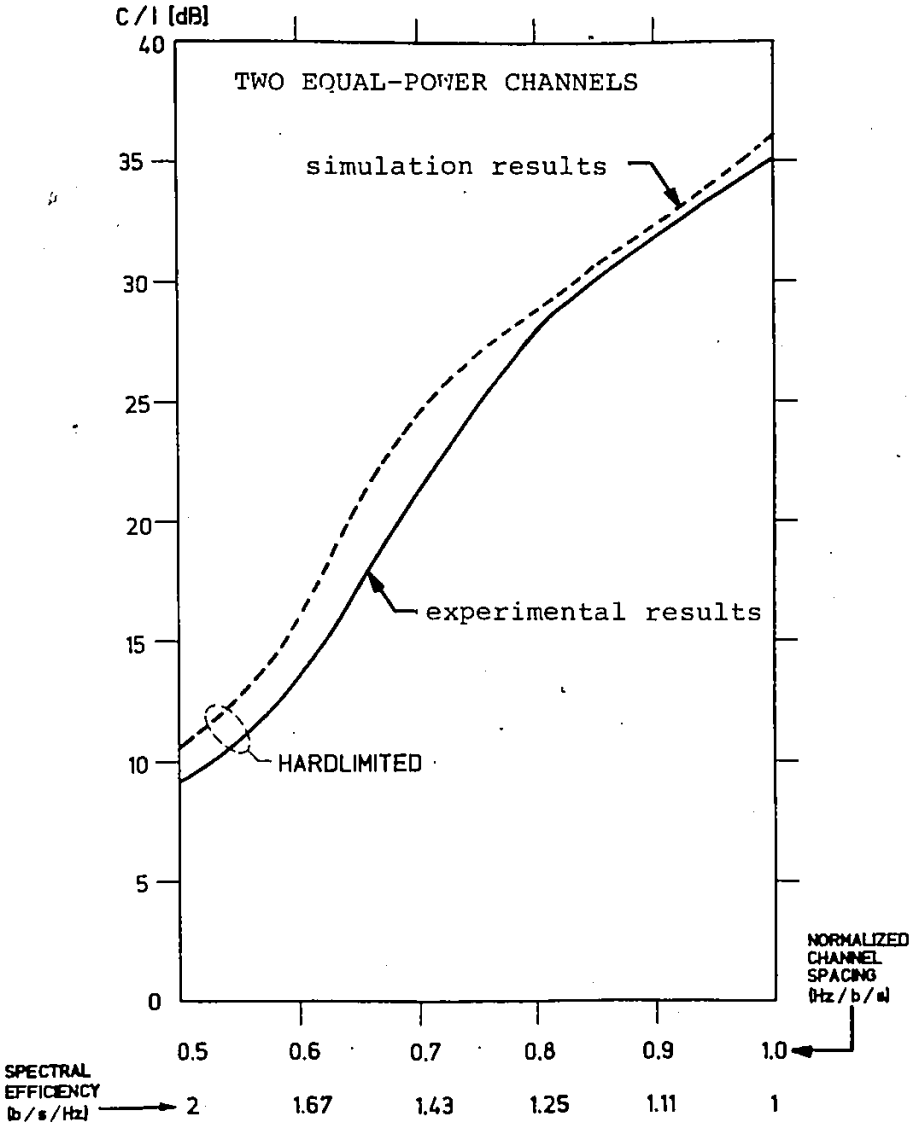

Fig. 5.23: MEASURED C/I VERSUS CHANNEL SPACING

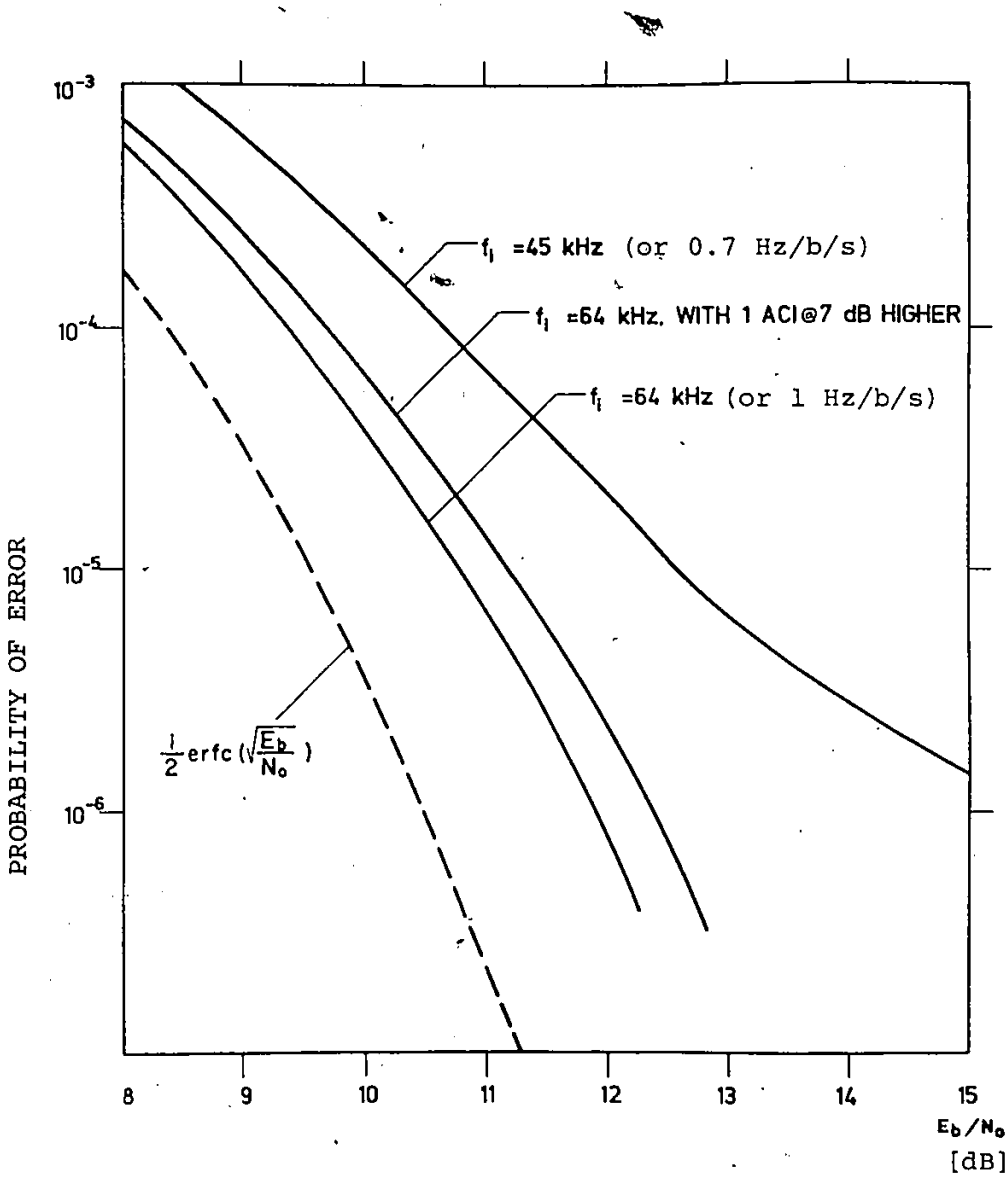

Fig. 5.24: MEASURED PERFORMANCE OF A HARDLIMITED MULTI-CHANNEL IJF-OQPSK SYSTEM

For a channel spacing of 64 kHz (1 Hz/b/s), the effects of ACI is negligible.

The comparison of measured and simulation results on the P_e performance is illustrated in Fig. 5.25. The measured and simulated results are in a close agreement.

NOTES: *Parts of this chapter were published in [65,67-69,82-84]*

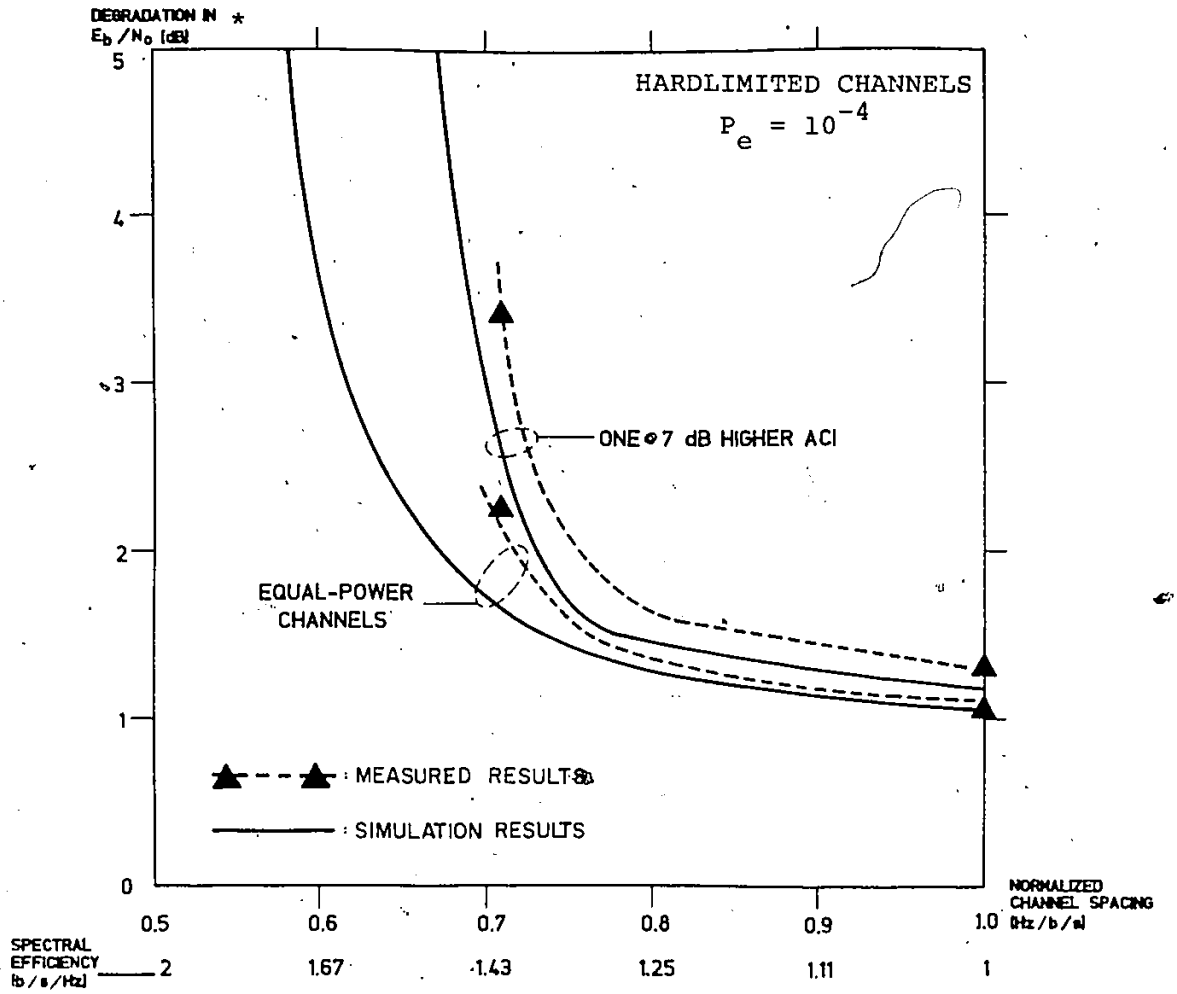

Fig. 5.25: COMPARISON OF SIMULATION AND MEASURED RESULTS

(* *Degradation relative to* $E_b/N_o = 8.4$ dB @ $P_e = 10^{-4}$)

CHAPTER SIX:
IJF-QUADRATURE MODULATION TECHNIQUES CARRIER AND CLOCK SYNCHRONIZATION

SUMMARY:

In this chapter, the carrier and clock synchronization aspects of IJF-QPSK and IJF-Offset QPSK demodulators are presented.

The power spectral density functions of recovered carrier and clock signals are derived and used to investigate the pattern-noise in different carrier and clock recovery loops. A fast digital symbol timing recovery technique is introduced and examined.

Effects of static phase and timing error in recovered signals on the P_e performance are investigated using computer simulations. Effects of the roll-off factor of the detection filter on the P_e performance in the presence of static phase and timing error are also studied.

6.1 PATTERN-NOISE IN A CARRIER SYNCHRONIZER USING THE REMODULATION TECHNIQUE

Quadrupler, remodulator (also called *reverse-modulator* or *inverse-modulator*), *Costas loop* are three widely known types of carrier synchronizers for QPSK and Offset-QPSK demodulators [87, 89,90]. Their block diagrams are shown in Figs. 6a-c. In the quadrupler (Fig. 6.1a), the fourth harmonic component of the carrier is regenerated by a fourth-power device, filtered and divided by four to produce the carrier signal. In essence, both the remodulator (Fig. 6.1b), and the Costas loop (Fig. 6.1c) remove modulation to regenerate the carrier by cross-multiplying the received (modulated) signal by the demodulated (and limited) in-phase and quadrature components. In the remodulator, this cross-multiplication is done in passband while in the Costas loop, it is performed in baseband. In other words, the Costas loop can be derived from a series of passband-to-baseband transformations on the remodulator [87]. Both the remodulator and Costas loop provide less phase jitter than the quadrupler [86,87,90]. For these reasons, in this section, the pattern-noise in the remodulator applied to IJF-QPSK and IJF-Offset QPSK demodulators is examined.

Figure 6.2 shows the complex equivalent model of the remodulator. The *noise-free* component of the received modulated signal is represented as

BPF: Bandpass filter (narrow)
PLL: Phase-locked loop

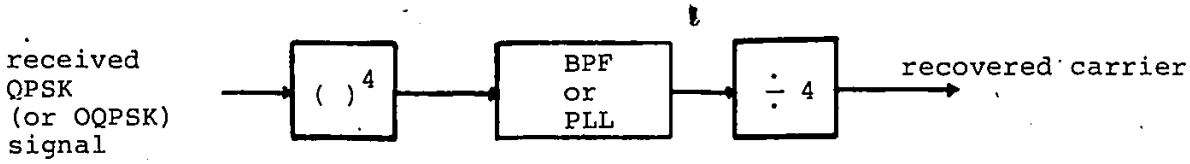

(a) QUADRUPLER

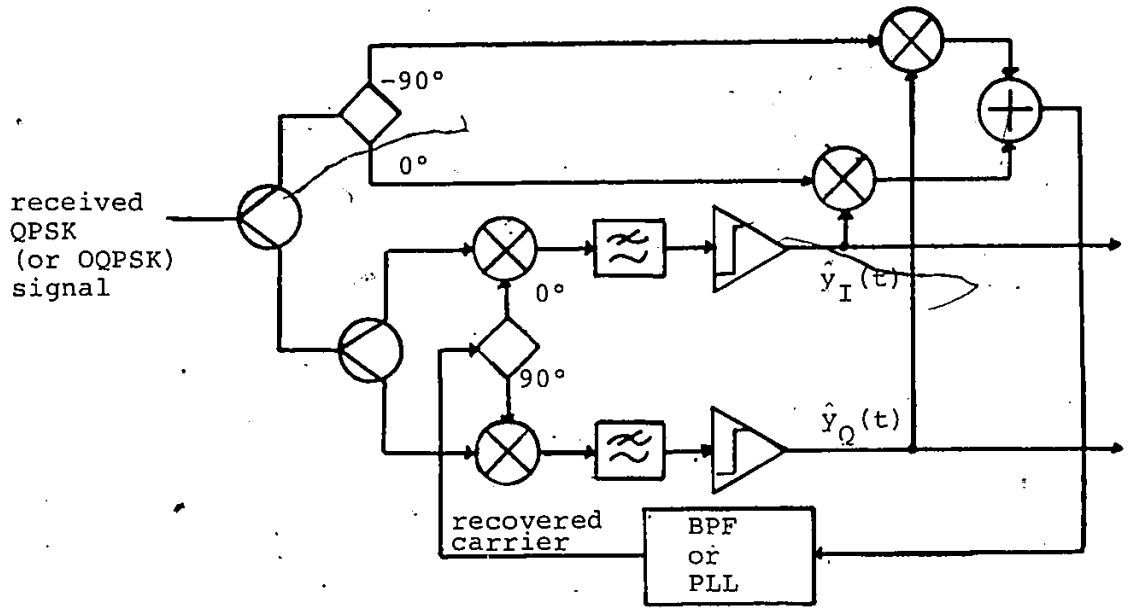

(b) REMODULATOR

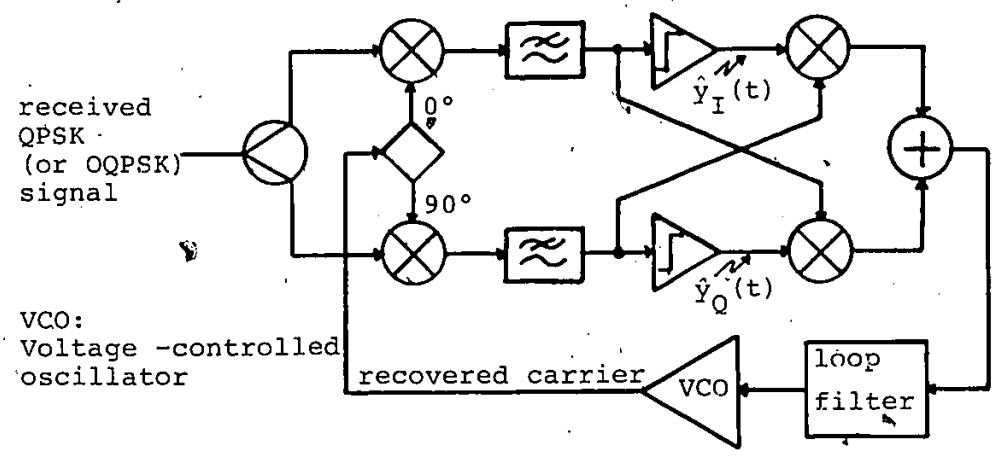

(c) COSTAS LOOP

Fig. 6.1: BLOCK DIAGRAMS OF CARRIER SYNCHRONIZERS

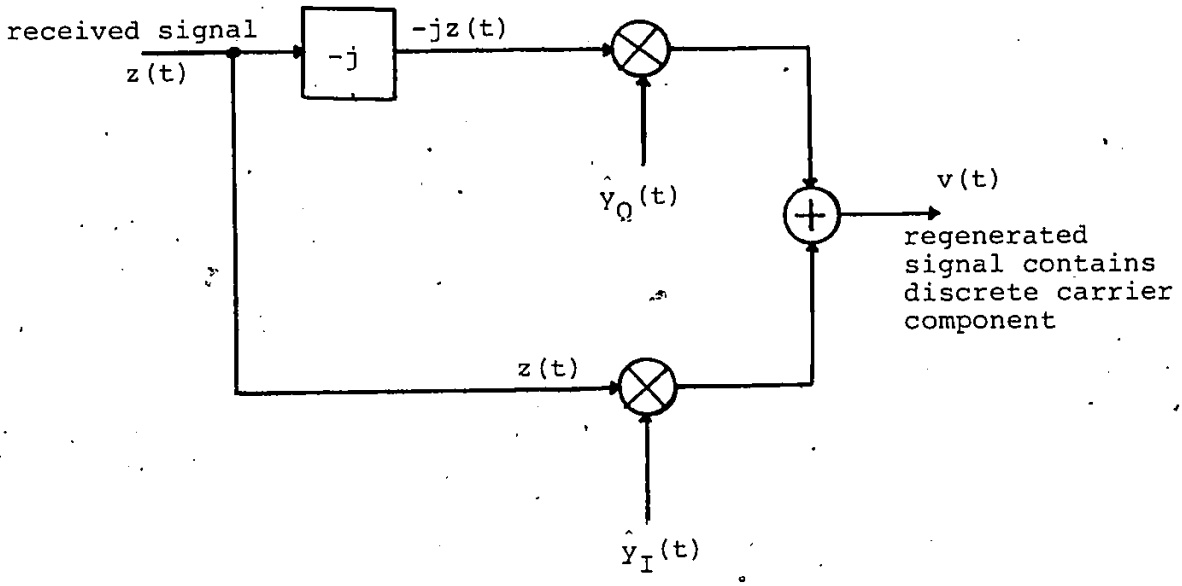

Fig. 6.2: EQUIVALENT COMPLEX MODEL OF A REMODULATOR

$$z(t) = (y_I(t)+jy_Q(t))e^{j2\pi f_c t} \qquad (6.1)$$

where $y_I(t)$ and $y_Q(t)$ represent the in-phase and quadrature components of $z(t)$ and f_c is the carrier frequency. The components $y_I(t)$ and $y_Q(t)$ are random, have zero mean and the same statistics. Hence $z(t)$ does not contain any discrete spectral component at f_c, or its harmonics.

From Fig. 6.2, the output of the remodulator can be represented as

$$\begin{aligned} v(t) &= \hat{y}_I(t) \cdot z(t) - j\hat{y}_Q(t)z(t) \\ &= \{A(t)+jB(t)\}\, e^{+j2\pi f_c t} \end{aligned} \qquad (6.2)$$

where

$$\begin{aligned} A(t) &= y_I(t)\hat{y}_I(t)+y_Q(t)\hat{y}_Q(t) \\ B(t) &= y_I(t)\hat{y}_Q(t)-\hat{y}_I(t)y_Q(t) \end{aligned}$$

are the in-phase and quadrature components of $v(t)$ and $\hat{y}_I(t)$ and $\hat{y}_Q(t)$ are demodulated in-phase and quadrature baseband signals.

$\hat{y}_I(t)$ and $\hat{y}_Q(t)$ are outputs of the comparators (Fig. 6.1b). They can be represented as

$$\hat{y}_I(t) = \text{sign}\,[y_I(t)] = \frac{|y_I(t)|}{y_I(t)} = \frac{y_I(t)}{|y_I(t)|} \tag{6.3a}$$

and

$$\hat{y}_Q(t) = \text{sign}\,[y_Q(t)] = \frac{|y_Q(t)|}{y_Q(t)} = \frac{|y_Q(t)|}{y_Q(t)} \tag{6.3b}$$

where sign [y] is sign of y.

A(t) and B(t) are then represented by

$$A(t) = |y_I(t)| + |y_Q(t)| \tag{6.4a}$$

$$B(t) = y_I(t) \cdot \text{sign}\,[y_Q(t)] - y_Q(t) \cdot \text{sign}\,[y_I(t)] \tag{6.4b}$$

The amplitudes of the in-phase and quadrature components of the carrier are given by the means of A(t) and B(t) respectively. Since $y_I(t)$ and $y_Q(t)$ have the same statistics and zero means, the mean of B(t) is also zero. Hence the desired carrier components is

$$\bar{A} = E\{A(t)\} = E\{|y_I(t)|+|y_Q(t)|\} \neq 0 \tag{6.5}$$

Equation (6.2) can be rewritten as

$$v(t) = \bar{A}e^{j2\pi f_c t} + (a(t)+jB(t))e^{j2\pi f_c t} \tag{6.6}$$

where

$$a(t) = A(t) - \bar{A}$$

$a(t)$ and $B(t)$ represent the in-phase and quadrature fluctuations respectively. They can be considered as AM and PM sidebands about the desired carrier represented by $\bar{A}e^{j2\pi f_c t}$. These fluctuations arise from the characteristics of $y_I(t)$, and $y_Q(t)$ patterns, even if the received signal $z(t)$ is perfectly noise-free. For this reason, they are usually termed *pattern-noise* (or *self-noise*, or *systematic jitter*) [87-88].

In this section we investigate the pattern-noise in the recovered carrier for IJF-QPSK and IJF-Offset QPSK demodulators by examining the power spectral density (PSD) functions of $A(t)$ and $B(t)$.

6.1.1 Power Spectra of $A(t)$ and $B(t)$ in the case of IJF-QPSK Demodulator

The noise-free component of the received IJF-QPSK, $z(t)$, is assumed to be identical to the IJF-QPSK modulated transmitted signal represented by Eq. (4.1). The baseband components, $y_I(t)$ and $y_Q(t)$, are IJF signals represented by Eqs. (3.2a and b).

$A(t)$ can be represented as

$$A(t) = \sum_{n=-\infty}^{+\infty} Q(t_n) \qquad (6.7)$$

where $t_n = t-nT_s$.

From Eqs. (3.2a,b) and (6.4a), it can be shown that $Q(t_n)$ belongs to the set $\{v_i(t_n),\ i=1,2,3,4\}$ where

$$v_1(t_n) = 2|s_o(t_n)| \tag{6.8a}$$

$$v_2(t_n) = v_3(t_n) = |s_o(t_n)|+s_e(t_n) \tag{6.8b}$$

$$v_4(t_n) = 2s_e(t_n) \tag{6.8c}$$

Following the same treatment as given in Section 4.3, we can derive the PSD function of $A(t)$. It is

$$S_A(f) = \frac{1}{T_s^2} \sum_{n=-\infty}^{+\infty} |S_1(\frac{n}{T_s}) + S_2(\frac{n}{T_s})|^2 \delta(f-\frac{n}{T_s}) + \frac{1}{2T_s}[S_1(f) - S_2(f)]^2 \tag{6.9}$$

where $S_1(f)$ and $S_2(f)$ are the Fourier transforms of $|s_o(t)|$ and $s_e(t)$ respectively.

Similarly, the PSD function of $B(t)$ can be derived as

$$S_B(f) = \frac{1}{2T_s}|W(f)|^2 \tag{6.10}$$

where $W(f)$ is the Fourier transform of

$$w(t) = \begin{cases} s_e(t)-s_o(t), & 0 \le t \le T_s/2 \\ -s_e(t)-s_o(t), & -T_s/2 \le t < 0 \\ 0, & \text{elsewhere} \end{cases}$$

From Eq. (6.9), the desired carrier is represented by the discrete spectral component at f=0, i.e.,

$$\bar{A} = \frac{1}{T_s^2} |S_1(0)+S_2(0)|^2 \cdot \delta(f)$$

Equation (6.10) indicates that B(t) does not contain any discrete spectral components as expected.

6.1.2 Power Spectra of A(t) and B(t) in the case of IJF-Offset QPSK Demodulator

Due to the time offset of $T_s/2$ between $y_I(t)$ and $y_Q(t)$, the components A(t) and B(t) for an IJF-Offset QPSK signal are different from those for an IJF-QPSK even if the same IJF double-interval pulse is used.

Let A(t) and B(t) be represented as the sums of an infinite number of single-interval pulses. Following the same treatment as given in Section 6.1.1, the PSD functions of A(t) and B(t) can be derived by using finite-state Markov chain models.

The power spectral density of $A(t)$ is

$$S_A(f) = \frac{1}{64T_s^2} \sum_{n=-\infty}^{+\infty} \left| \sum_{i=1}^{8} V_i\left(\frac{n}{T_s}\right) \right|^2 \delta\left(f - \frac{n}{T_s}\right)$$

$$+ \frac{9-4\cos^2(fT_s)}{64T_s} \sum_{i=1}^{8} |V_i(f)|^2$$

$$+ \frac{1-4\cos^2(fT_s)}{32T_s} \sum_{i=1}^{7} \sum_{k=i+1}^{8} \mathrm{Re}\{V_i^*(f)V_k(f)\}$$

$$+ \frac{1}{4T_s} \mathrm{Re}\{[\{V_1(f)+V_4(f)+V_5(f)+V_8(f)\}^* \cdot \{V_3(f)+V_4(f)+$$

$$+V_7(f)+V_8(f)\}+\{V_2(f)+V_3(f)+V_6(f)+V_7(f)\}^*\{V_1(f)+V_2(f)+$$

$$+V_5(f)+V_6(f)\}] \cdot e^{-j2\pi fT_s}\} \qquad (6.11a)$$

where

$$V_i(f) = \begin{cases} S_{a1}(f) + S_{bi}(f), & i=1,2,3,4 \\ \\ S_{a2}(f) + S_{bj}(f), & i=5,6,7,8, \text{ and } j=i-4 \end{cases} \qquad (6.11b)$$

$S_{ai}(f)$'s and $S_{bj}(f)$'s are the Fourier transforms of $s_{ai}(t)$'s and $s_{bj}(t)$'s respectively.

$$s_{a1}(t) = |s_o(t)| \qquad (6.11c)$$

$$s_{a2}(t) = |s_e(t)| \qquad (6.11d)$$

$$s_{b1}(t) = \begin{cases} s_o(t+T_s/2), & -T_s/2 \le t \le 0 \\ s_e(t-T_s/2), & 0 < t \le +T_s/2 \\ 0, & \text{elsewhere} \end{cases} \qquad (6.11e)$$

$$s_{b2}(t) = \begin{cases} s_o(t+T_s/2), & -T_s/2 \le t \le 0 \\ -s_o(t-T_s/2), & 0 < t \le +T_s/2 \\ 0, & \text{elsewhere} \end{cases} \tag{6.11f}$$

$$s_{b3}(t) = \begin{cases} s_e(t+T_s/2), & -T_s/2 \le t \le 0 \\ -s_o(t-T_s/2), & 0 < t \le +T_s/2 \\ 0, & \text{elsewhere} \end{cases} \tag{6.11g}$$

$$s_{b4}(t) = \begin{cases} s_e(t+T_s/2), & -T_2/2 \le t \le 0 \\ s_e(t-T_s/2), & 0 < t \le +T_s/2 \\ 0, & \text{elsewhere} \end{cases} \tag{6.11h}$$

The power spectral density of $B(t)$ is

$$S_B(f) = \frac{1}{8T_s} \sum_{i=1}^{8} |W_i(f)|^2$$

$$+ \frac{1}{4T_s} \mathrm{Re}\{[(W_1(f)+W_3(f)+W_5(f)+W_7(f))^* \cdot (W_6(f)+W_7(f)-W_2(f)-W_3(f)) + (W_2(f)+W_4(f)+W_6(f)+W_8(f))^* \cdot (W_1(f)+W_4(f)-W_5(f)-W_8(f))]\, e^{-j2\pi f T_s}\} \tag{6.12a}$$

where $W_i(f)$'s are the Fourier transforms of $w_i(t)$'s and

$$w_1(t) = \begin{cases} -(s_{b1}(t)+s_o(t)), & t<0 \\ s_{b1}(t)-s_o(t), & t \ge 0 \end{cases} \tag{6.12b}$$

$$w_2(t) = \begin{cases} -(s_{b3}(t)+s_o(t)), & t\leq 0 \\ s_{b3}(t)-s_o(t), & t>0 \end{cases} \tag{6.12c}$$

$$w_3(t) = \begin{cases} -s_{b4}(t)-s_o(t), & t\leq 0 \\ s_{b4}(t)-s_o(t) & t>0 \end{cases} \tag{6.12d}$$

$$w_4(t) = \begin{cases} -s_{b2}(t)-s_o(t), & t\leq 0 \\ s_{b2}(t)-s_o(t), & t>0 \end{cases} \tag{6.12e}$$

$$w_5(t) = s_{b1}(t)-s_e(t) \tag{6.12f}$$

$$w_6(t) = s_{b3}(t)-s_e(t) \tag{6.12g}$$

$$w_7(t) = s_{b4}(t)-s_e(t) \tag{6.12h}$$

$$w_8(t) = s_{b2}(t)-s_e(t) \tag{6.12i}$$

From Eq. (6.11a) the desired carrier is represented by the discrete spectral component at $f=0$, i.e.,

$$\bar{A} = \frac{1}{64T_s^2} \sum_{i=1}^{8} |V_i(0)|^2 \, \delta(f)$$

The quadrature component $B(t)$ does not contain any discrete

spectral component at carrier frequency and represents quadrature pattern-noise.

Equations (6.9), (6.10), (6.11a) and (6.12a) can be used to investigate the power spectra of A(t) and B(t) in the case of IJF-QPSK and IJF-Offset QPSK signals respectively, for different IJF pulse shapes. As an illustrative example, if the IJF double-interval pulse shape given by Eq. (3.18b) is used then

$$s_e(t) = \begin{cases} \sin \frac{\pi t}{T_s}, & -T_s/2 \leq t \leq +T_s/2 \\ 0, & \text{elsewhere} \end{cases} \tag{6.13a}$$

and

$$s_o(t) = \begin{cases} 1, & -T_s/2 \leq t \leq T_s/2 \\ 0, & \text{elsewhere} \end{cases} \tag{6.13b}$$

The PSD functions of A(t) and B(t) in case of IJF-QPSK signal are

$$S_A(x) = \frac{1}{T_s^2} \sum_{n=-\infty}^{+\infty} \left| \frac{2x+(1-8x^2)\sin\pi x}{\pi x(1-4x^2)} \right|^2 \delta(x-n)$$

$$+ \frac{1}{2T_s} \left| \frac{2x-\sin\pi x}{\pi x(1-4x^2)} \right|^2 \tag{6.14a}$$

and

$$S_B(x) = \frac{1}{2T_s} \left| \frac{1-\cos\pi x-4x^2}{\pi x(1-4x^2)} \right| \qquad (6.14b)$$

where

$$x = [f-f_c]T_s$$

Figure 6.3 illustrates the normalized spectra of A(t) and B(t). It is shown that the in-phase pattern-noise (indicated by the continuous part of $S_A(x)$ around x=0) is dominant while the quadrature pattern-noise (indicated by the continuous part of $S_B(x)$ around x=0) is very low in the vicinity of the desired carrier (x=0). It means that with a narrow bandpass filter at the output of the remodulator, the (filtered) recovered carrier contains a negligible amount of phase fluctuation. The magnitude fluctuation denoted by the continuous part of $S_A(f)$ can be easily removed by the hardlimiter.

Experiments are also performed to compare the performance of quadrupler and remodulator. Figs. 6.4a,b show the power spectra of the recovered carriers at the outputs (before bandpass filter or phase-locked loop) of the quadrupler and remodulator respectively.

The signal-to-pattern-noise ratio is defined as the power ratio of the discrete spectral component to the continuous spectral

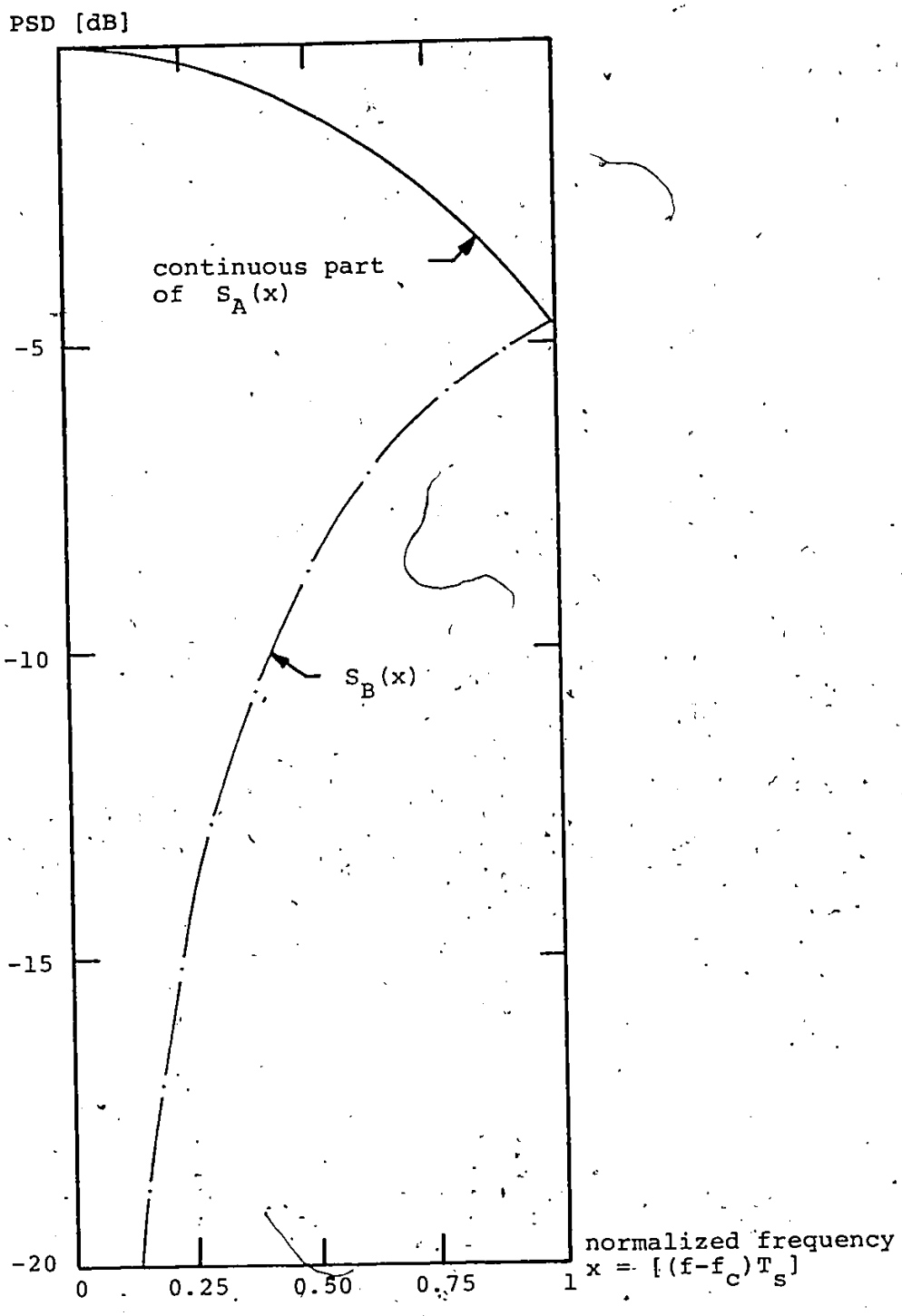

Fig. 6.3: NORMALIZED SPECTRA OF A(t) AND B(t)

POOR PRINT
Epreuve illisible

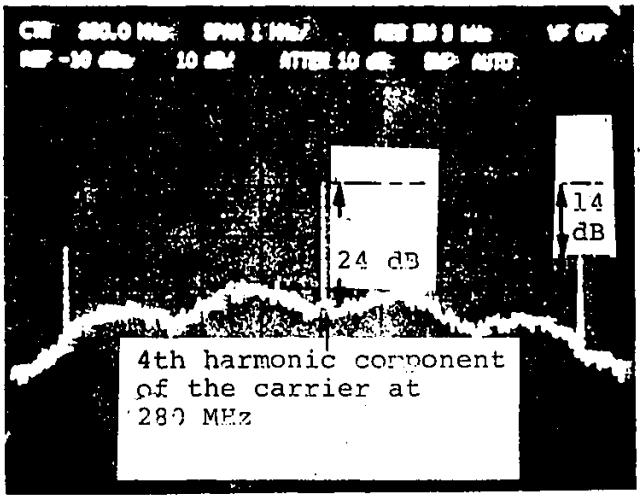

Horizontal: 1 MHz/div.
Vertical: 10 dB/div.
Res. BW: 3 kHz

(a) QUADRUPLER (case: IJF-Offset QPSK)

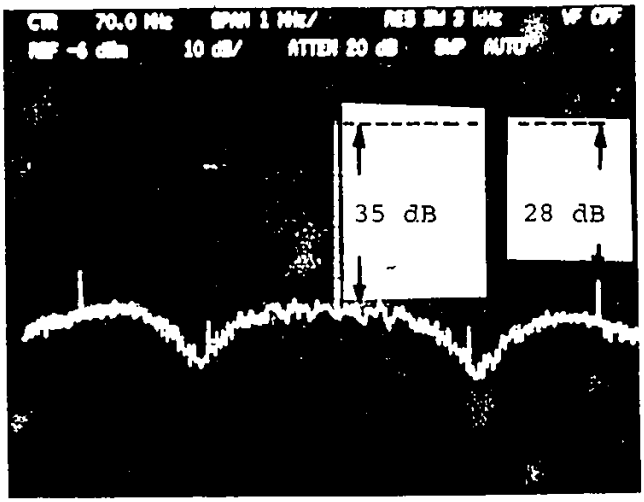

(b) REMODULATOR (case: IJF-Offset QPSK)

Horizontal: 1 MHz/div.
Vertical: 10 dB/div.
Res. BW: 3 kHz

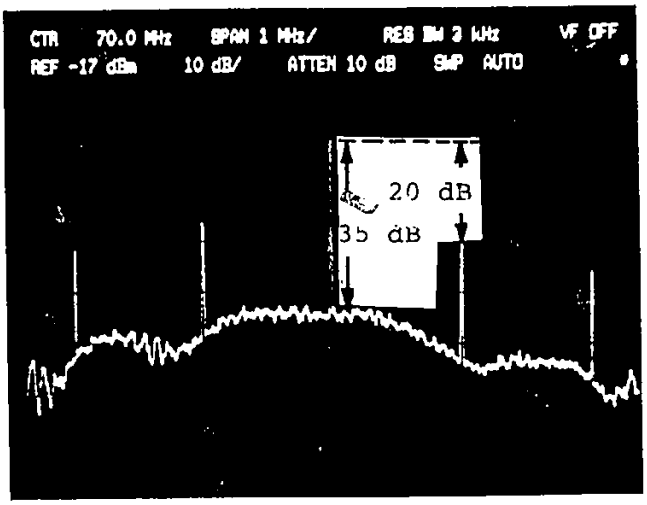

(c) REMODULATOR (case: IJF-QPSK)

Horizontal: 1 MHz/div.
Vertical: 10 dB/div.
Res. BW: 3 kHz

Fig. 6.4: MEASURED POWER SPECTRA OF RECOVERED CARRIERS BEFORE BPF OR PLL
(*bit rate:* 4.3 Mb/s, *carrier frequency:* 70 MHz)

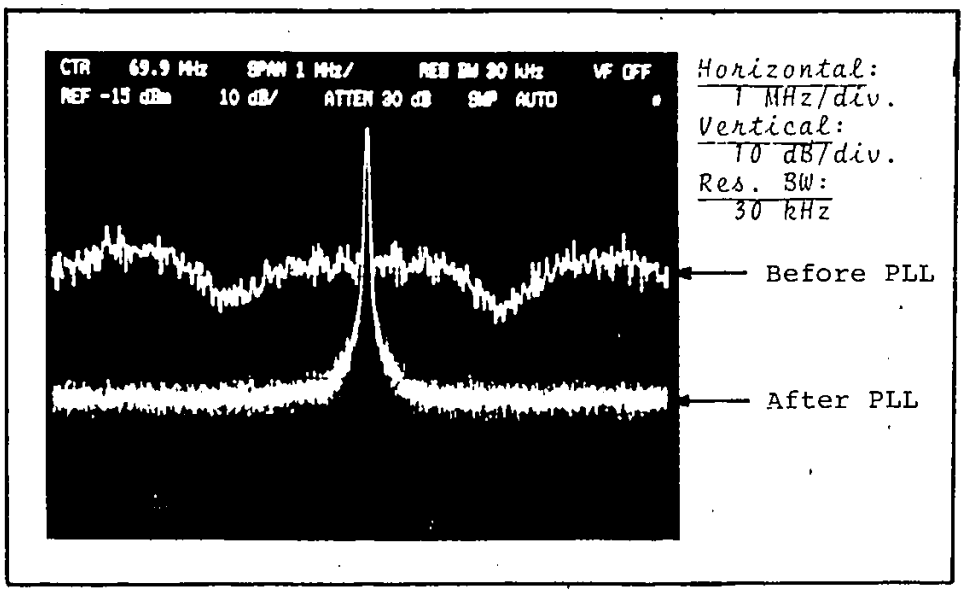

Fig. 6.5: MEASURED POWER SPECTRA OF RECOVERED CARRIER BEFORE AND AFTER PLL

bit rate: 4.3 Mb/s
carrier frequency: 70 MHz
carrier synchronizer: remodulator

component measured in a specified bandwidth. In the measured power spectra, this specified bandwidth is indicated by the resolution bandwidth of the spectrum analyzer. As shown in Fig. 6.4a,b the remodulator provides higher (better) signal-to-pattern-noise ratio, hence less phase jitter than the quadrupler.

Figure (6.4c) shows the measured power spectrum of the recovered carrier signal at the remodulator output in the case of IJF-QPSK demodulator. The signal-to-pattern-noise ratio is approximately similar (35dB in 3 kHz bandwidth) in both IJF-QPSK and IJF-Offset PSK cases except that the discrete sideband components related to the symbol rate frequency for IJF-Offset QPSK signal is lower than those for IJF-QPSK signal.

Fig. 6.5 shows the measured power spectra of the recovered carrier before and after a phase-locked loop (PLL). Pattern-noise around the discrete carrier component is filtered by the PLL.

6.2 Pattern-Noise in a Clock Synchronizer Using an Absolute-Value Technique

There is a very large number of clock synchronizer configurations. Among them, the clock synchronizer using an absolute-value device as shown in Fig. 6.6 is frequently used [87,90]. The demodulated baseband signals, $y_I(t)$ and $y_Q(t)$ are passed through absolute-value devices (e.g. full-wave rectifier). The output signal of each absolute-value device, $|y_I(t)|$ or $|y_Q(t)|$ contains discrete spectral components at the symbol rate frequency,

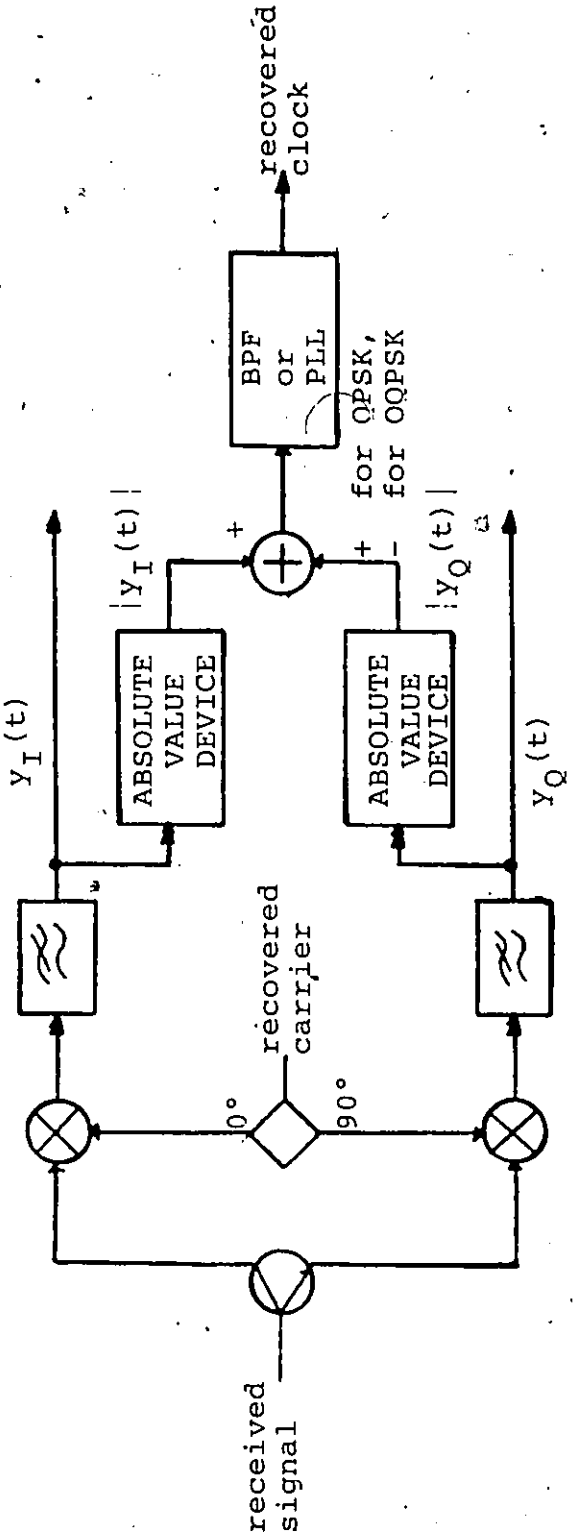

Fig. 6.6: BLOCK DIAGRAM OF A CLOCK SYNCHRONIZER USING ABSOLUTE VALUE DEVICES

$1/T_s$, and its harmonics, and a continuous spectral component. After the bandpass filter centered at $1/T_s$, the residue of the continuous spectral component may be interpreted as pattern-noise. The signal-to-pattern-noise (S/P) ratio is defined as the power ratio of the discrete spectral component at $1/T_s$ to the residue of the continuous spectral component.

By summing $|y_I(t)|$ and $|y_Q(t)|$ it is expected to obtain a better (higher) signal-to-pattern-noise ratio. However it will be shown later that it is only true for the case of IJF-QPSK, and for the case of IJF-Offset QPSK, the difference rather than the sum is required.

The signal $|y_I(t)|$ (or $|y_Q(t)|$) can be represented by

$$|y_I(t)| = \sum_{n=-\infty}^{+\infty} P(t_n), \quad t_n = t - nT_s \tag{6.15}$$

where

$$P(t_n) = \begin{cases} |s_e(t_n)| & \text{with probability of } 1/2 \\ |s_o(t_n)| & \text{with probability of } 1/2 \end{cases}$$

The power spectral density function of $|y_I(t)|$ is then derived as

$$S_{cl}(f) = \frac{1}{4T_s^2} \sum_{n=-\infty}^{+\infty} \left| S_{a1}\left(\frac{n}{T_s}\right) + S_{a2}\left(\frac{n}{T_s}\right) \right|^2 \delta\left(f - \frac{n}{T_s}\right)$$

$$+ \frac{1}{4T_s} |S_{a1}(f) - S_{a2}(f)|^2 \qquad (6.16)$$

where $S_{a1}(f)$ and $S_{a2}(f)$ are the Fourier transforms of $|s_e(t)|$ and $|s_o(t)|$ respectively (Eqs. (6.13c,d)).

The discrete spectral component at $1/T_s$ is

$$D_1(\frac{1}{T_s}) = \frac{1}{4T_s^2} |S_{a1}(\frac{1}{T_s}) + S_{a2}(\frac{1}{T_s})|^2 \qquad (6.17a)$$

Assume that the bandpass filter (BPF) is a narrow brick-wall filter centered at $1/T_s$ and having a bandwidth B, and the portion of the continuous spectral component of $S_{c1}(f)$ is approximately flat in this vicinity. Then the signal-to-pattern-noise ratio at the output of the BPF is

$$(\frac{S}{P})_1 \approx \frac{D_1(1/T_s)}{\frac{B}{4T_s}|S_{a1}(\frac{1}{T_s}) - S_{a2}(\frac{1}{T_s})|^2}$$

$$\approx \frac{1}{BT_s} \left| \frac{S_{a1}(\frac{1}{T_s}) + S_{a2}(\frac{1}{T_s})}{S_{a1}(\frac{1}{T_s}) - S_{a2}(\frac{1}{T_s})} \right|^2 \qquad (6.17b)$$

6.2.1 Case of IJF-QPSK Signals

Now consider the composite signals

$$c_2(t) = |y_I(t)| + |y_Q(t)| \qquad (6.18a)$$

and

$$c_3(t) = |y_I(t)| - |y_Q(t)| \tag{6.18b}$$

for the case of IJF-QPSK demodulator.

Following the same treatment as in Section 6.1, the PSD functions of $c_2(t)$ and $c_3(t)$ can be derived using a finite-state Markov chain models and given by

$$S_{c2}(f) = \frac{1}{T_s^2} \sum_{n=-\infty}^{+\infty} \left| S_{a1}\left(\frac{n}{T_s}\right) + S_{a2}\left(\frac{n}{T_s}\right) \right|^2 \delta\left(f - \frac{n}{T_s}\right)$$

$$+ \frac{1}{2T_s} \left| S_{a1}(f) - S_{a2}(f) \right|^2 \tag{6.19a}$$

and

$$S_{c3}(f) = \frac{1}{2T_s} \left| S_{a1}(f) + S_{a2}(f) \right|^2 \tag{6.19b}$$

Eq. (6.19b) shows that $c_3(t)$ does not contain any discrete component. From Eq. (6.19a), the signal-to-pattern-noise ratio for $c_2(t)$ is

$$\left(\frac{S}{P}\right)_2 \approx \frac{2}{BT_s} \left| \frac{S_{a1}\left(\frac{1}{T_s}\right) + S_{a2}\left(\frac{1}{T_s}\right)}{S_{a1}\left(\frac{1}{T_s}\right) - S_{a2}\left(\frac{1}{T_s}\right)} \right|^2 \tag{6.20a}$$

Comparing Eqs. (6.17b) and (6.20a), we have

$$\left(\frac{S}{P}\right)_2 = 2\left(\frac{S}{P}\right)_1 \tag{6.20b}$$

i.e. in the case of IJF-QPSK signals, the sum $(|y_I(t)|+|y_Q(t)|)$ can be used to improve the signal-to-pattern-noise ratio by 3 dB (twice).

6.2.2 Case of IJF-Offset QPSK Signals

Consider the composite signals

$$c_4(t) = |y_I(t)|+|y_Q(t)| \tag{6.21a}$$

and

$$c_5(t) = |y_I(t)|-|y_Q(t)| \tag{6.21b}$$

for the case of IJF-Offset QPSK demodulator.

Due to the time offset of $T_s/2$ between $|y_I(t)|$ and $|y_Q(t)|$, $c_4(t)$ and $c_5(t)$ are different from $c_2(t)$ and $c_3(t)$ although Eqs. (6.18a,b) and Eqs. (6.21a,b) are similar.

Following the same treatment given in Section 6.1.2 the PSD functions of $c_4(t)$ and $c_5(t)$ can be derived with the aid of finite-state Markov chain models. The discrete spectral components of these PSD functions are

$$D_{c4}(f) = \frac{1}{4T_s^2} \sum_{n=-\infty}^{+\infty} \left| [S_{a1}(\frac{n}{T_s}) + S_{a2}(\frac{n}{T_s})] + [S_{b2}(\frac{n}{T_s}) + S_{b4}(\frac{n}{T_s})] \right|^2 \cdot \delta(f - \frac{n}{T_s}) \qquad (6.22a)$$

and

$$D_{c5}(f) = \frac{1}{4T_s^2} \sum_{n=-\infty}^{+\infty} \left| [S_{a1}(\frac{n}{T_s}) + S_{a2}(\frac{n}{T_s})] - [S_{b2}(\frac{n}{T_s}) + S_{b4}(\frac{n}{T_s})] \right|^2 \cdot \delta(f - \frac{n}{T_s}) \qquad (6.22b)$$

where $S_{a1}(f)$, $S_{a2}(f)$, $S_{b2}(f)$, and $S_{b4}(f)$ are the Fourier transforms of $s_{a1}(t)$, $s_{a2}(t)$, $s_{b2}(t)$ and $s_{b4}(t)$ respectively.

The pulse shapes $s_{a1}(t)$, $s_{a2}(t)$, $s_{b2}(t)$ and $s_{b4}(t)$ are defined by Eqs. (6.11c,d,f,h). These pulse shapes are even functions and their Fourier transforms satisfy the following equations:

$$S_{a1}(f) + S_{a2}(f) = R(f) \qquad (6.23a)$$

and

$$S_{b2}(f) + S_{b4}(f) = R(f)\cos\pi f T_s - I(f)\sin\pi f T_s \qquad (6.23b)$$

where

$$R(f) = 2\mathrm{Re}\{\int_0^{T_s/2} (s_o(t)+s_e(t))e^{-j2\pi ft}\,dt\},$$

$$I(f) = 2\mathrm{Im}\{\int_0^{T_s/2} (s_o(t)+s_e(t))e^{-j2\pi ft}\,dt\},$$

$\mathrm{Re}\{\cdots\}$= Real part of $\{\cdots\}$,

and $\mathrm{Im}\{\cdots\}$ = Imaginary part of $\{\cdots\}$.

Substituting Eqs. (6.23a,b) into Eqs. (6.22a,b), we obtain

$$D_{c4}(f) = \frac{1}{4T_s^2} \sum_{n=-\infty}^{+\infty} |R(f)\cdot[1+\cos n\pi]|^2\, \delta(f-\frac{n}{T_s}) \qquad (6.24a)$$

and

$$D_{c5}(f) = \frac{1}{4T_s^2} \sum_{n=-\infty}^{+\infty} |R(f)[1-\cos n\pi]|^2\, \delta(f-\frac{n}{T_s}) \qquad (6.24b)$$

Consider the discrete spectral component at the symbol rate frequency, i.e. $f=1/T_s$ or $n=1$

$$D_{c4}(\frac{1}{T_s}) = \frac{1}{4T_s^2} |R(\frac{1}{T_s})[1-\cos\pi]|^2\, \delta(f-\frac{1}{T_s}) = 0 \qquad (6.25a)$$

and

$$D_{c5}(\frac{1}{T_s}) = \frac{1}{4T_s^2} |R(\frac{1}{T_s})[1-\cos\pi]|^2\, \delta(f-\frac{1}{T_s})$$

$$= \frac{1}{T_s^2}|R(\frac{1}{T_s})|^2\delta(f-\frac{1}{T_s}) = \frac{1}{T_s^2}|S_{a1}(\frac{1}{T_s})+S_{a2}(\frac{1}{T_s})|^2\delta(f-\frac{1}{T_s}) \qquad (6.25b)$$

Equations (6.25a,b) shows that in the case of IJF-Offset

QPSK signals, the difference $(|y_I(t)|-|y_Q(t)|)$ is required. The sum $(|y_I(t) + y_Q(t)|)$ does not contain the discrete spectral component at the symbol rate frequency.

The continuous part of the PSD function of $c_5(t)$ is derived as

$$C_{c5}(f) = \frac{1}{2T_s} |S_{a1}(f)-S^*_{a2}(f)|^2 \qquad (6.25c)$$

From Eqs. (6.25b,c) the signal-to-pattern-noise ratio for $c_5(t)$ at the output of the zonal bandpass filter is

$$(\frac{S}{P})_5 \approx \frac{D_{c5}(1/T_s)}{B \cdot C_{c5}(\frac{1}{T_s})} = \frac{2}{BT_s} \left| \frac{S_{a1}(\frac{1}{T_s})+S_{a2}(\frac{1}{T_s})}{S_{a1}(\frac{1}{T_s})-S_{a2}(\frac{1}{T_s})} \right|^2 \qquad (6.25d)$$

Comparing Eqs. (6.17b) and (6.25d), we have

$$(\frac{S}{P})_5 = 2(\frac{S}{P})_1 \qquad (6.25e)$$

i.e., In the case of IJF-Offset QPSK signals, the difference $(|y_I(t)|-|y_Q(t)|)$ can be used to improve the signal-to-pattern-noise ratio by 3 dB (twice)

6.3 Pattern-Noise in a Clock Synchronizer Using a Digital Technique

A digital clock synchronizer, shown in Fig. 6.7, was introduced and examined in [76,77,85]. The signals $y'_I(t)$ and $y'_Q(t)$

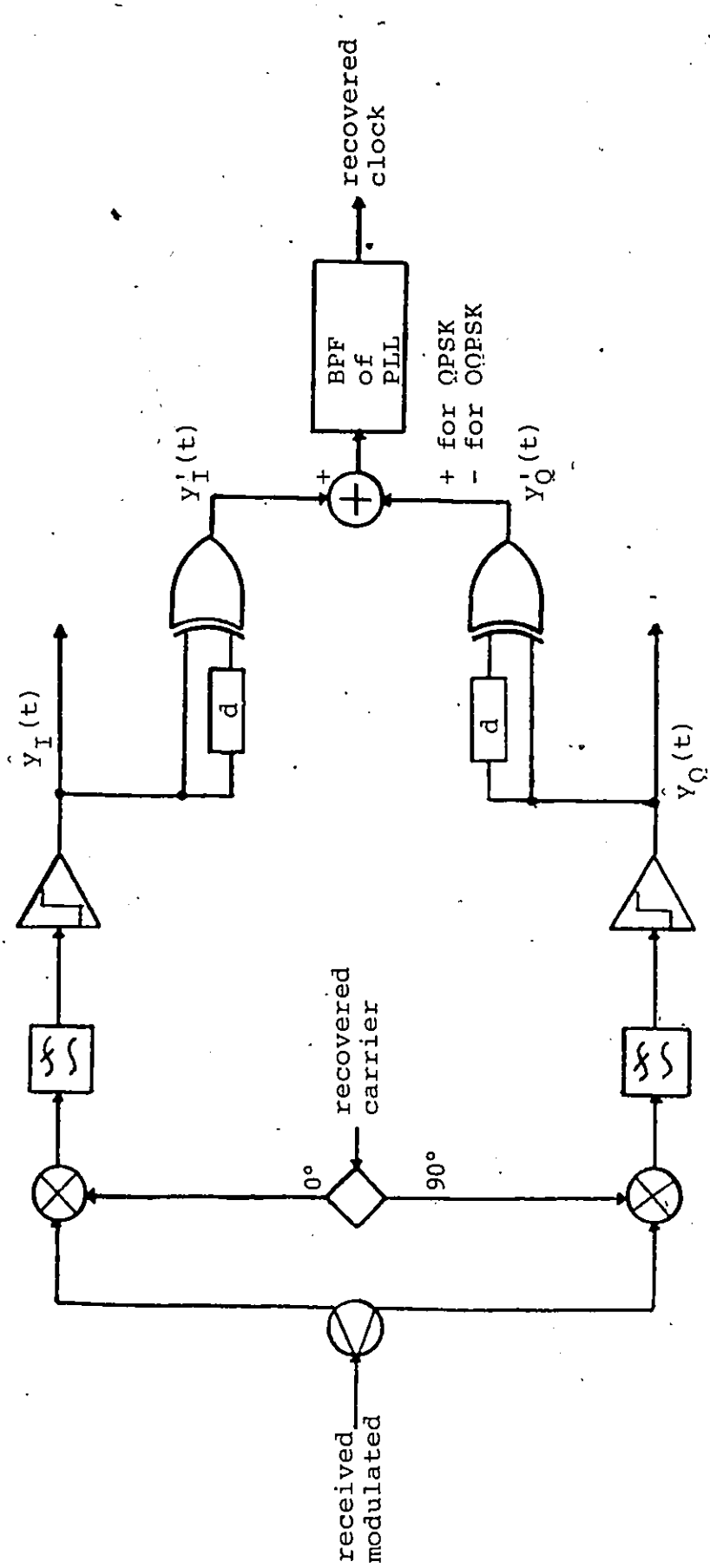

Fig. 6.7: BLOCK DIAGRAM OF A CLOCK SYNCHRONIZER USING A DIGITAL TECHNIQUE

are similar to Return-to-Zero (RZ) signals which contain discrete spectral components at the symbol rate frequency, $1/T_s$, and its harmonics. The signal $y_I'(t)$ (or $y_Q'(t)$) is represented as

$$y_I'(t) = \sum_{n=-\infty}^{+\infty} P(t_n), \quad t_n = t = nT_s \tag{6.26}$$

where

$$P(t_n) = \begin{cases} v(t_n) & \text{with probability of } 1/2 \\ 0 & \text{with probability of } 1/2 \end{cases}$$

$$v(t_n) = \begin{cases} 1, & 0 \le t_n \le d \\ 0, & \text{elsewhere} \end{cases}$$

The PSD function of $y_I'(t)$ can be derived as [85].

$$S_{c5}(f) = \frac{2d^2}{T_s} \cdot \text{sinc}^2(\pi f d) + \frac{d^2}{T_s^2}\delta(f) + \frac{2d^2}{T_s^2}\sum_{m=1}^{+\infty} \text{sinc}^2\left(\frac{m\pi d}{T_s}\right)\delta\left(f - \frac{m}{T_s}\right) \tag{6.27a}$$

Fig. 6.8 shows a measured power spectra $S_{c6}(f)$ for $d = \frac{T_s}{2}$ and $\frac{1}{T_s} = 1.2$ MHz.

The signal-to-pattern-noise ratio at the output of the zonal BPF is

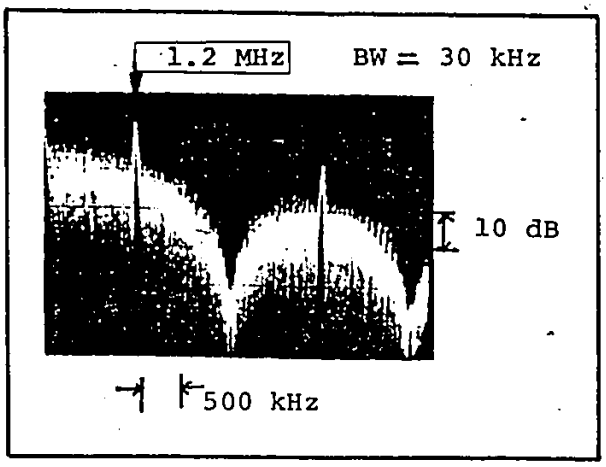

- *delay:* $d = T_s/2$
- *symbol rate:* $\frac{1}{T_s} = 1.2$ MHz

Fig. 6.8: MEASURED POWER SPECTRUM OF $y'_I(t)$ (or $y'_Q(t)$)

$$\left(\frac{S}{P}\right)_6 \approx \frac{1}{BT_s} \tag{6.27b}$$

Equation (6.27b) indicates that the signal-to-pattern-noise ratio is not dependent on the delay d. *Hence d can be chosen as small as possible to obtain fast clock recovery.*

In the following paragraphs, we will demonstrate that this signal-to-pattern-noise ratio can be improved by 3 dB by taking the sum $(y_I'(t)' + y_Q'(t))$ for IJF-QPSK signals and the difference $(y_I'(t)-y_Q'(t))$ for IJF-Offset QPSK signals.

6.3.1 Case of IJF-QPSK Signals

Consider the composite signals

$$c_7(t) = y_I'(t) + y_Q'(t) \tag{6.28a}$$

and

$$c_8(t) = y_I'(t) - y_Q'(t) \tag{6.28b}$$

for IJF-QPSK signals.

The PSD functions of $c_7(t)$ and $c_8(t)$ are derived as

$$S_{c7}(f) = \frac{d^2}{T_s^2} \sum_{n=-\infty}^{+\infty} \text{sinc}^2\left(\frac{\pi nd}{T_s}\right)\delta\left(f-\frac{n}{T_s}\right) + \frac{d^2}{2T_s}\text{sinc}^2(\pi fd) \tag{6.29a}$$

and

$$S_{c8}(f) = \frac{d^2}{2T_s} \operatorname{sinc}^2 (\pi f d) \qquad (6.29b)$$

Equations (6.29a,b) show that for IJF-QPSK signals, only the sum $(y'_I(t)+y'_Q(t))$ contains discrete spectral components useful to symbol timing recovery. The signal-to-pattern-noise ratio at the output of the zonal bandpass filter is

$$\left(\frac{S}{P}\right)_7 \approx \frac{\frac{d^2}{T_s^2} \operatorname{sinc}^2\left(\frac{\pi d}{T_s}\right)}{B \cdot \frac{d^2}{2T_s} \operatorname{sinc}^2\left(\frac{\pi d}{T_s}\right)} = \frac{2}{BT_s} \qquad (5.29c)$$

Comparing Eqs. (6.27b) and (6.29c), we obtain

$$\left(\frac{S}{P}\right)_7 = 2\left(\frac{S}{P}\right)_6 \qquad (6.29d)$$

Equation (6.29d) shows that by summing $(y'_I(t)+y'_Q(t))$, the signal-to-pattern-noise ratio is improved by 3dB (twice) for IJF-QPSK signals.

6.3.2 Case of IJF-Offset QPSK Signals

Now consider the composite signals

$$c_9(t) = y'_I(t) + y'_Q(t) \qquad (6.30a)$$

and

$$c_{10}(t) = y'_I(t) - y'_Q(t) \qquad (6.30b)$$

for IJF-Offset QPSK signals.

The signals $c_9(t)$ and $c_{10}(t)$ are not similar to $c_7(t)$ and $c_8(t)$ due to the timing offset of $T_s/2$ between $y_I'(t)$ and $y_Q'(t)$.

The PSD functions of $c_9(t)$ and $c_{10}(t)$ are derived as

$$S_{c9}(f) = \frac{d^2}{T_s^2} \sum_{n=-\infty}^{+\infty} \text{sinc}^2\left(\frac{2\pi nd}{T_s}\right) \delta\left(f - \frac{2n}{T_s}\right) + \frac{d^2}{2T_s} \text{sinc}^2(\pi fd) \tag{6.31a}$$

and

$$S_{c10}(f) = \frac{d^2}{T_s^2} \sum_{n=-\infty}^{+\infty} \text{sinc}^2\left(\frac{\pi(2n+1)d}{T_s}\right) \delta\left(f - \frac{2n+1}{T_s}\right) + \frac{d^2}{2T_s} \text{sinc}^2(\pi fd) \tag{6.31b}$$

Equation (6.31a) indicates that $c_9(t)$ does not contain the discrete spectral component at the symbol rate frequency $1/T_s$. From Eq. (6.31b), the signal-to-pattern-noise ratio for $c_{10}(t)$ is

$$\left(\frac{S}{P}\right)_{10} \approx \frac{\frac{d^2}{T_s^2} \text{sinc}^2\left(\frac{\pi d}{T_s}\right)}{B \cdot \frac{d^2}{2T_s} \text{sinc}^2\left(\frac{\pi d}{T_s}\right)} = \frac{2}{BT_s} \tag{6.31c}$$

Comparing Eqs. (6.27b) and (6.31c), we obtain

$$\left(\frac{S}{P}\right)_{10} = 2\left(\frac{S}{P}\right)_6 \tag{6.31d}$$

This means that for IJF-Offset QPSK signal, only the difference $(y'_I(t) - y'_Q(t))$ can be used to generate the discrete spectral component at the symbol rate frequency, and the signal-to-pattern-noise ratio is improved by 3 dB (twice).

We note that the results of Section 6.3 can be applied to conventional QPSK and Offset-QPSK signals as well.

6.4 Effect of Static Phase Frror in the Carrier Synchronizer on the Performance

Figure 6.9 illustrates the simulation model used to study the effect of static phase error in the carrier synchronizer on the error probability (P_e) performance of IJF-QPSK and IJF-Offset QPSK modems in both linear and hardlimited channels.

Let the noise-free component of the received modulated signal at the output of the received detection filter be represented by its equivalent complex envelope.

$$r(t) = r_I(t) + j\, r_Q(t) \qquad (6.32a)$$

For a static phase error of Φ degrees in the recovered carrier, the demodulated in-phase and quadrature components are

$$r'_I(t) = \mathrm{Re}\{r(t) \cdot e^{j\Phi}\}$$

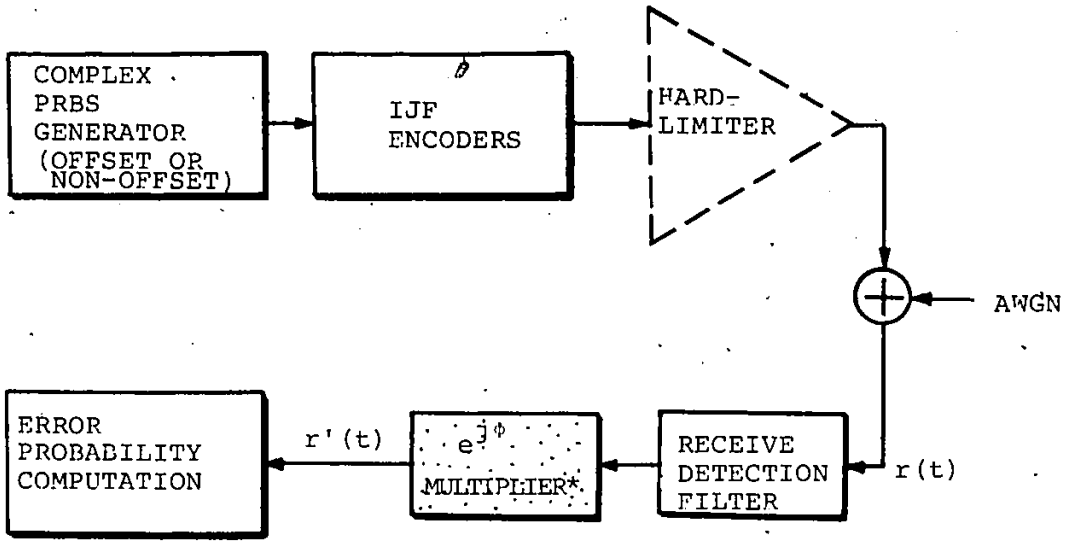

Fig. 6.9: SIMULATION MODEL USED TO STUDY THE EFFECT OF STATIC PHASE ERROR

* ϕ: *static phase error*

$$= r_I(t)\ \cos\phi - r_Q(t)\ \sin\phi \qquad (6.32b)$$

and $r'_Q(t) = \mathrm{Im}\{r(t)e^{j\phi}\}$

$$= r_I(t)\sin\phi + r_Q(t)\cos\phi \qquad (6.32c)$$

Equations (6.32b,c) show that the static phase error in the recovered carrier causes degradation in P_e performance for two reasons:

- Amplitudes of the desired components ($r_I(t)$ or $r_Q(t)$) are reduced by a factor of $\cos\phi$
- Crosstalk between the in-phase and quadrature components proportional to $\pm \sin\phi$ appears as an additional Intersymbol-Interference.

Figures 6.10a, b, and c show the simulation results of IJF-QPSK and IJF-Offset QPSK modems in both linear and hardlimited channels. The double-interval IJF pulse $s(t) = \frac{1}{2}(1+\cos\frac{\pi t}{T_s})$ is used. The receive detection filter is a raised-cosine type filter described in Chapter 3. The results are presented in terms of E_b/N_o requirements for given P_e versus the static phase error for different roll-off values (α) of the receive detection filter. They indicate that the degradation due to static phase error is similar for different cases.

The results show that additional performance degradation due

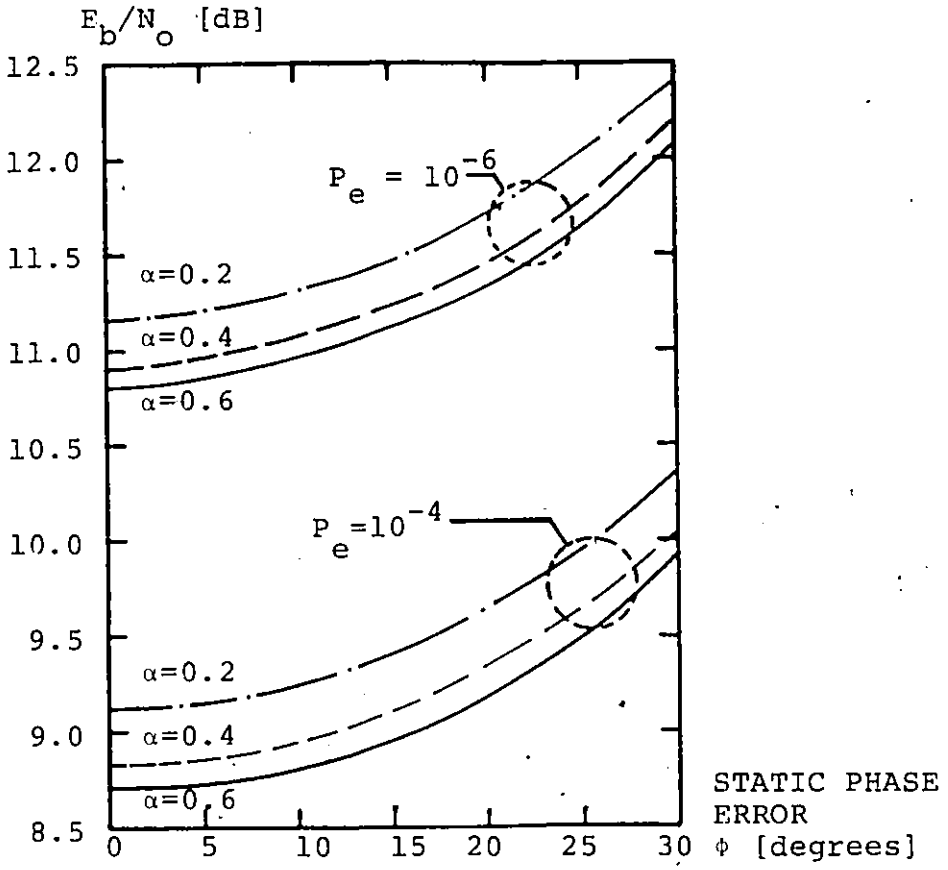

Fig. 6.10a: E_b/N_o VERSUS STATIC PHASE ERROR: IJF-QPSK AND IJF-OQPSK MODEMS IN A *LINEAR* CHANNEL

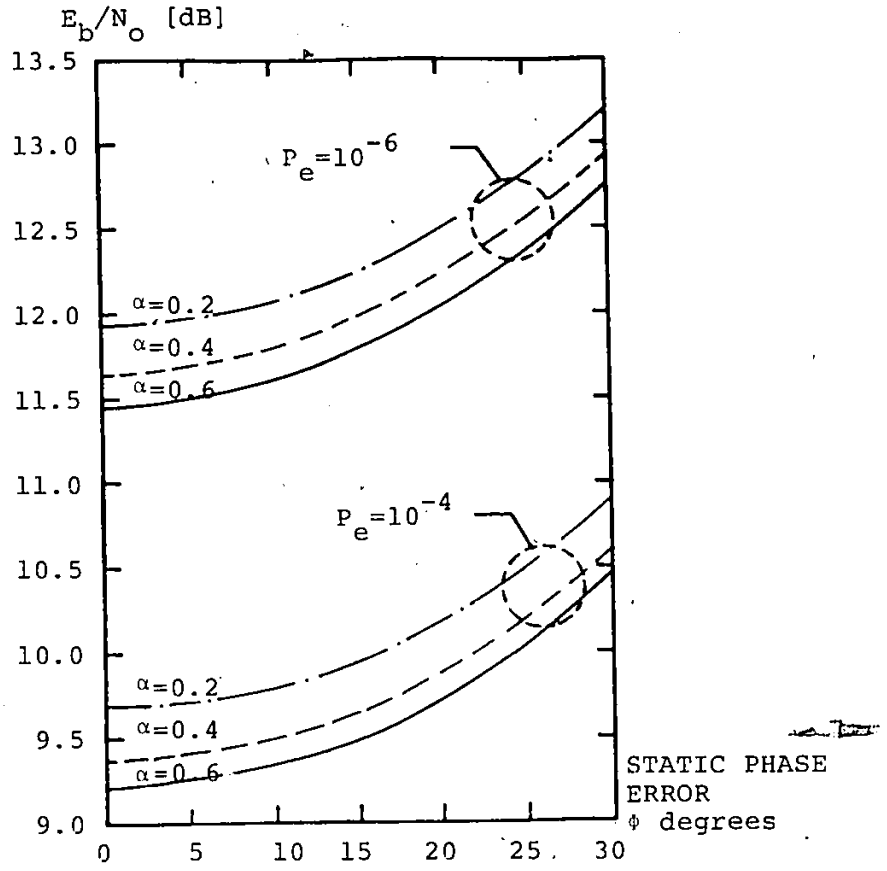

Fig. 6.10b: E_b/N_o VERSUS STATIC PHASE ERROR: IJF-QPSK MODEM IN A *HARDLIMITED* CHANNEL

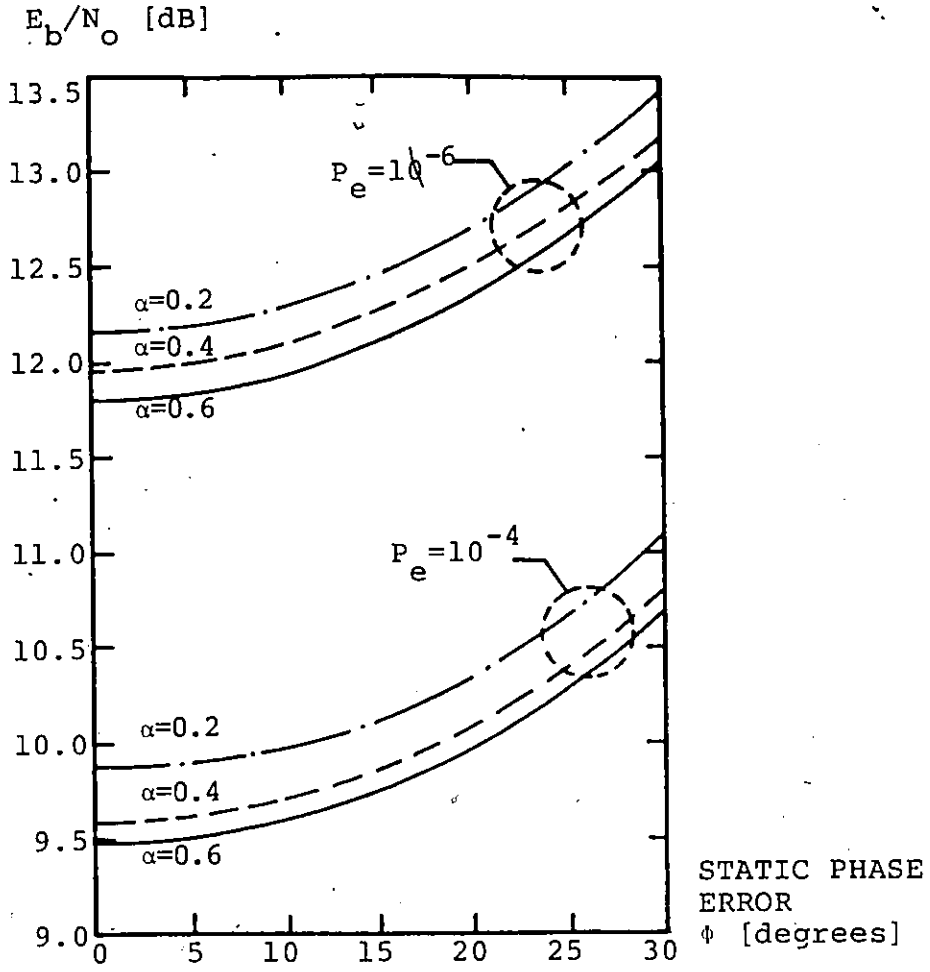

Fig. 6.10c: E_b/N_o VERSUS STATIC PHASE ERROR: IJF-OFFSET QPSK MODEM IN A *HARDLIMITED* CHANNEL

to static phase error is similar in both IJF-QPSK and IJF-Offset QPSK demodulators. At lower P_e performance ($P_e=10^{-6}$), the degradation due to static phase error becomes more severe.

6.5 Effect of Static Timing Error in the Clock Synchronizer on the Performance

Figure 6.11 illustrates the simulation model used to study the effect of static timing error in the clock synchronizer on the P_e performance of IJF-QPSK and IJF-Offset QPSK modems in both linear and hardlimited channels.

The demodulated in-phase and quadrature components are sampled at $kT_s+\Delta t$ where T_s is the symbol interval, k is an integer and Δt denotes the static timing error from the optimum sampling point.

The simulation results are shown in Figs. 6.12a,b,c in terms of E_b/N_o requirments for a given P_e versus the static timing error. The IJF double-interval pulse is $s(t) = \frac{1}{2}(1+\cos\frac{\pi t}{T_s})$ and the detection filter is a raised-cosine type filter described in Chapter 2.

The results indicate that for a given static timing error, the smaller is the roll-off factor (α) the higher the degradation. This can be understood by the fact that as the detection

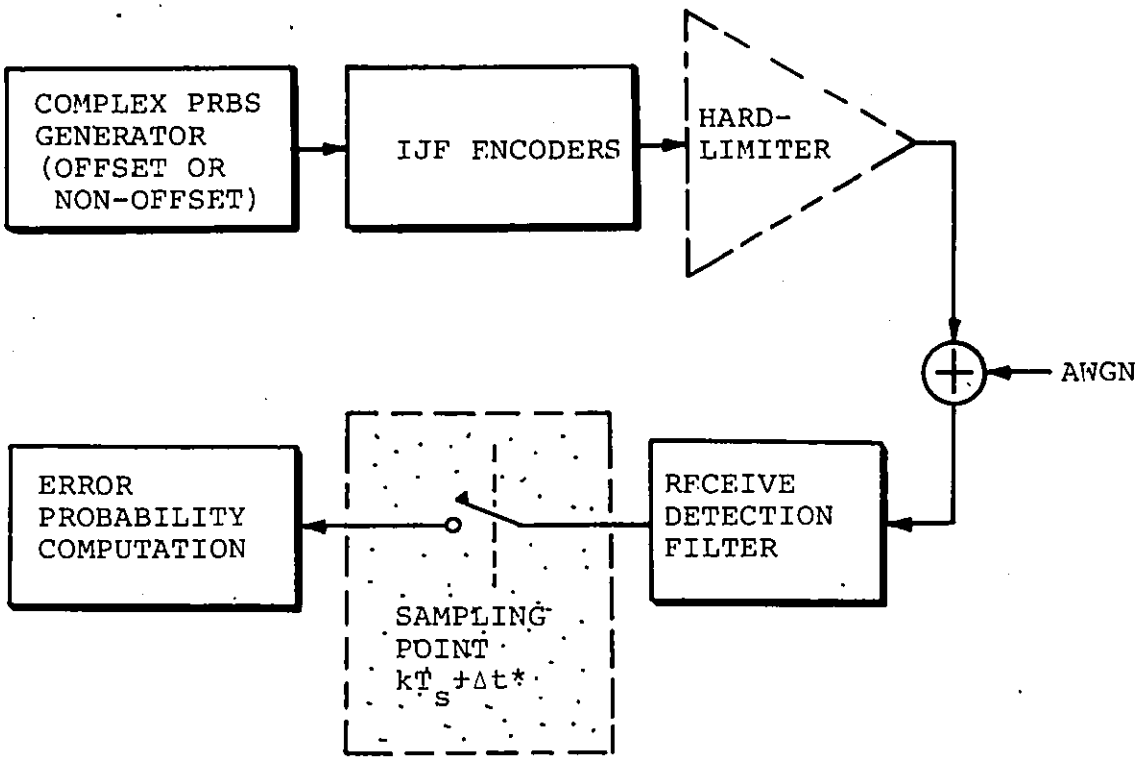

Fig. 6.11: SIMULATION MODEL USED TO STUDY THE EFFECT OF STATIC TIMING ERROR

*Δt: static timing error.

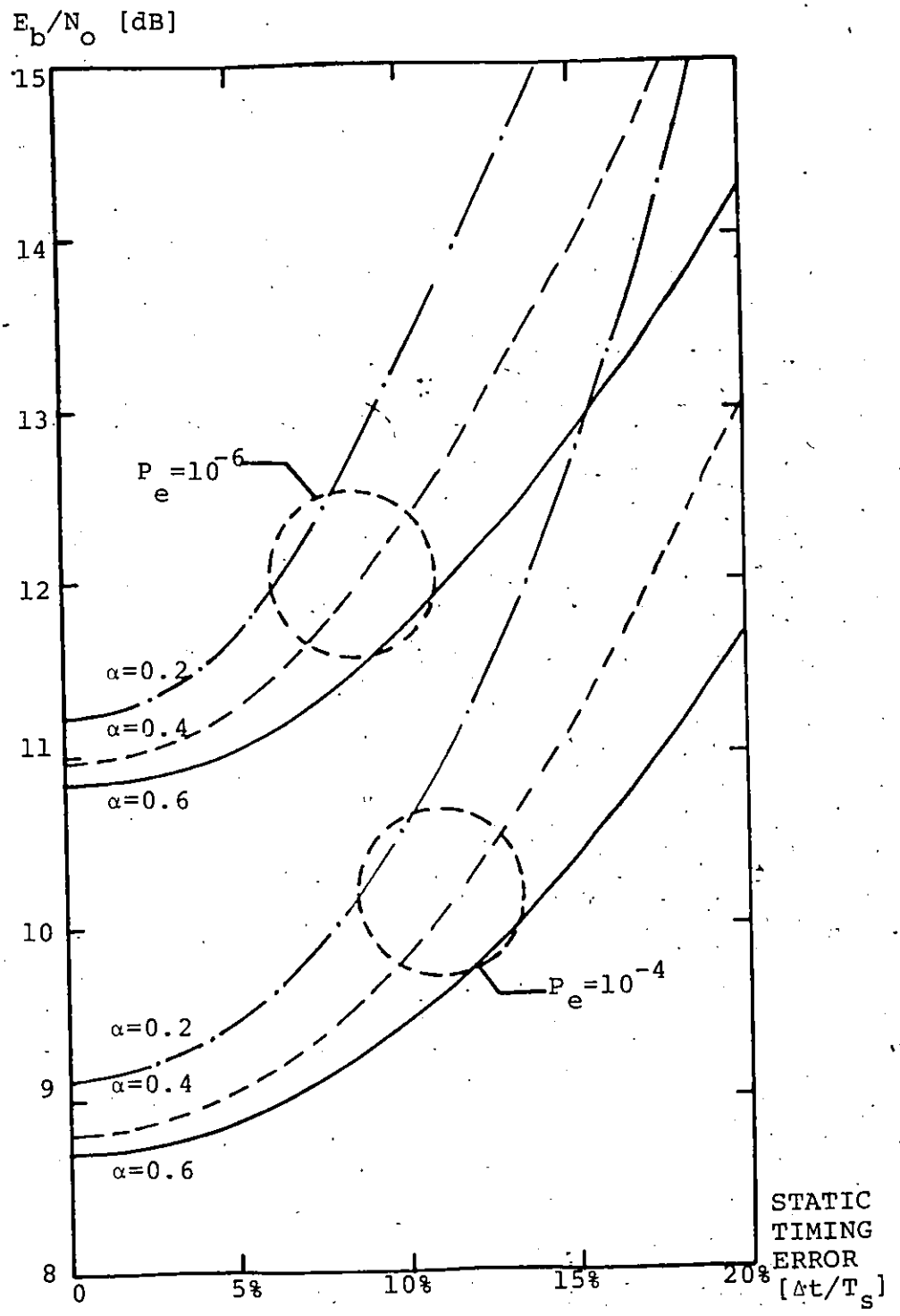

Fig. 6.12a: E_b/N_o VERSUS STATIC TIMING ERROR: IJF-QPSK AND IJF-OQPSK MODEMS IN A LINEAR CHANNEL

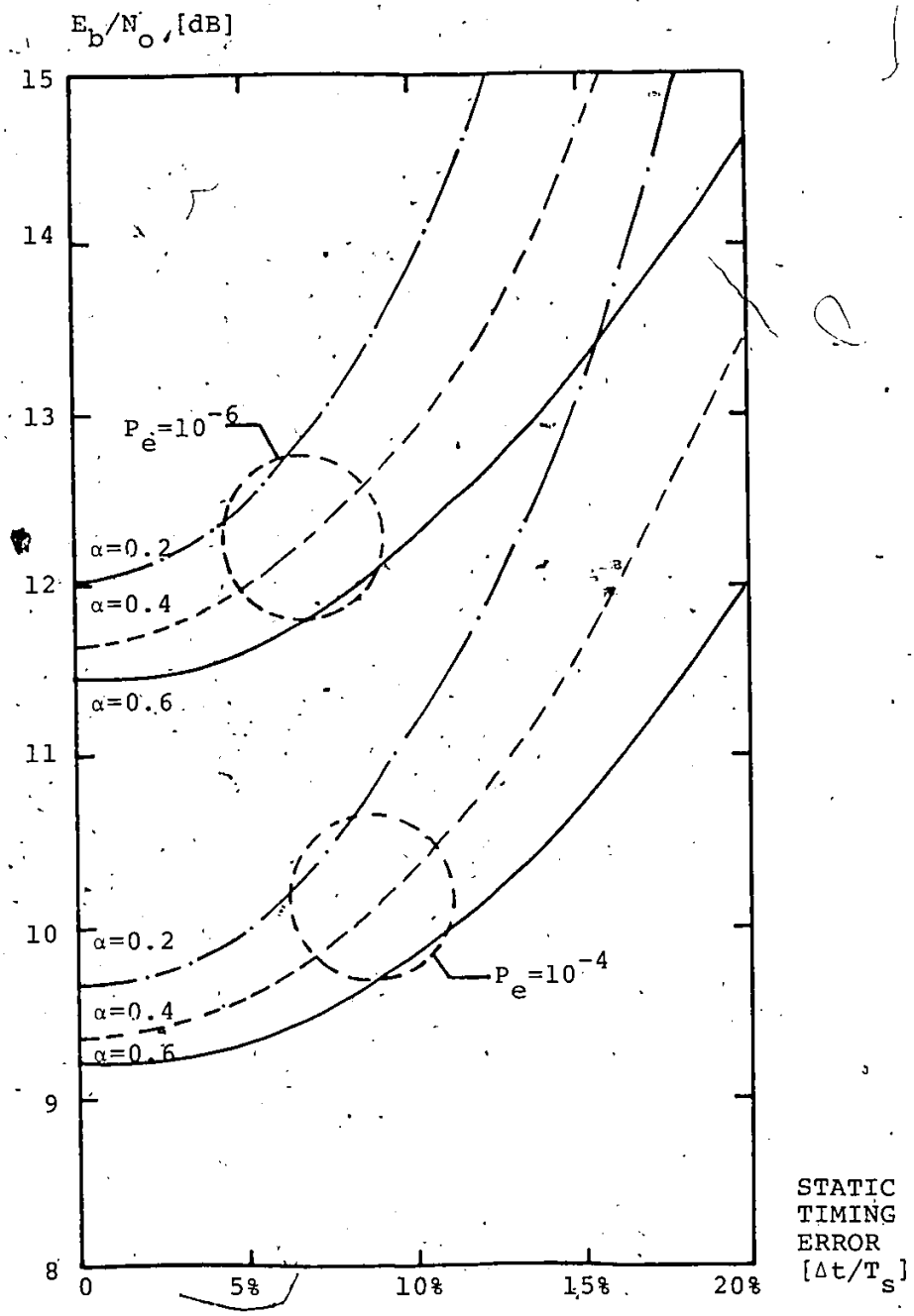

Fig. 6.12b: E_b/N_o VERSUS STATIC TIMING ERROR: IJF-QPSK MODEM IN A *HARDLIMITED* CHANNEL

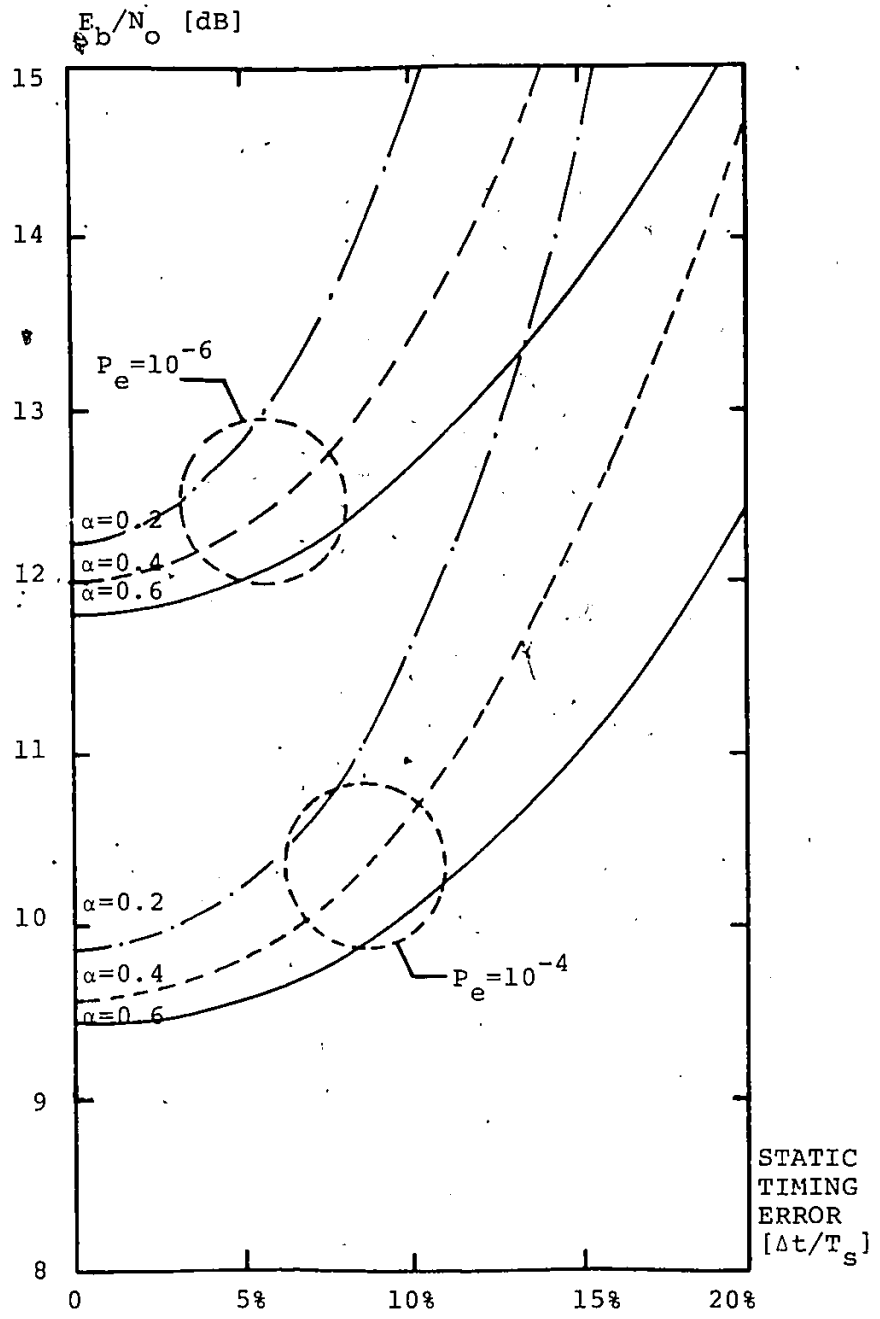

Fig. 6.12c: E_b/N_o VERSUS STATIC TIMING ERROR: IJF-OFFSET QPSK MODEM IN A *HARDLIMITED* CHANNEL

filter becomes narrower (i.e. α becomes smaller), the eye opening is less flat hence more sensitive to the static timing error. The results also show that the hardlimited IJF-Offset QPSK modem has a higher degradation than the hardlimited IJF-QPSK modem for the same amount of static timing error.

Figures 6.13a and b show the simulation results for combined static phase and timing errors. The results are presented in terms of equal E_b/N_o contours for $P_e=10^{-4}$ versus both static phase and timing errors. An IJF-Offset QPSK modem with filter roll-off factor $\alpha=0.4$ is used. The results indicate that for an allowable degradation of 0.2 dB, the static timing error should be less than 50% and the static phase error less than 10 degrees.

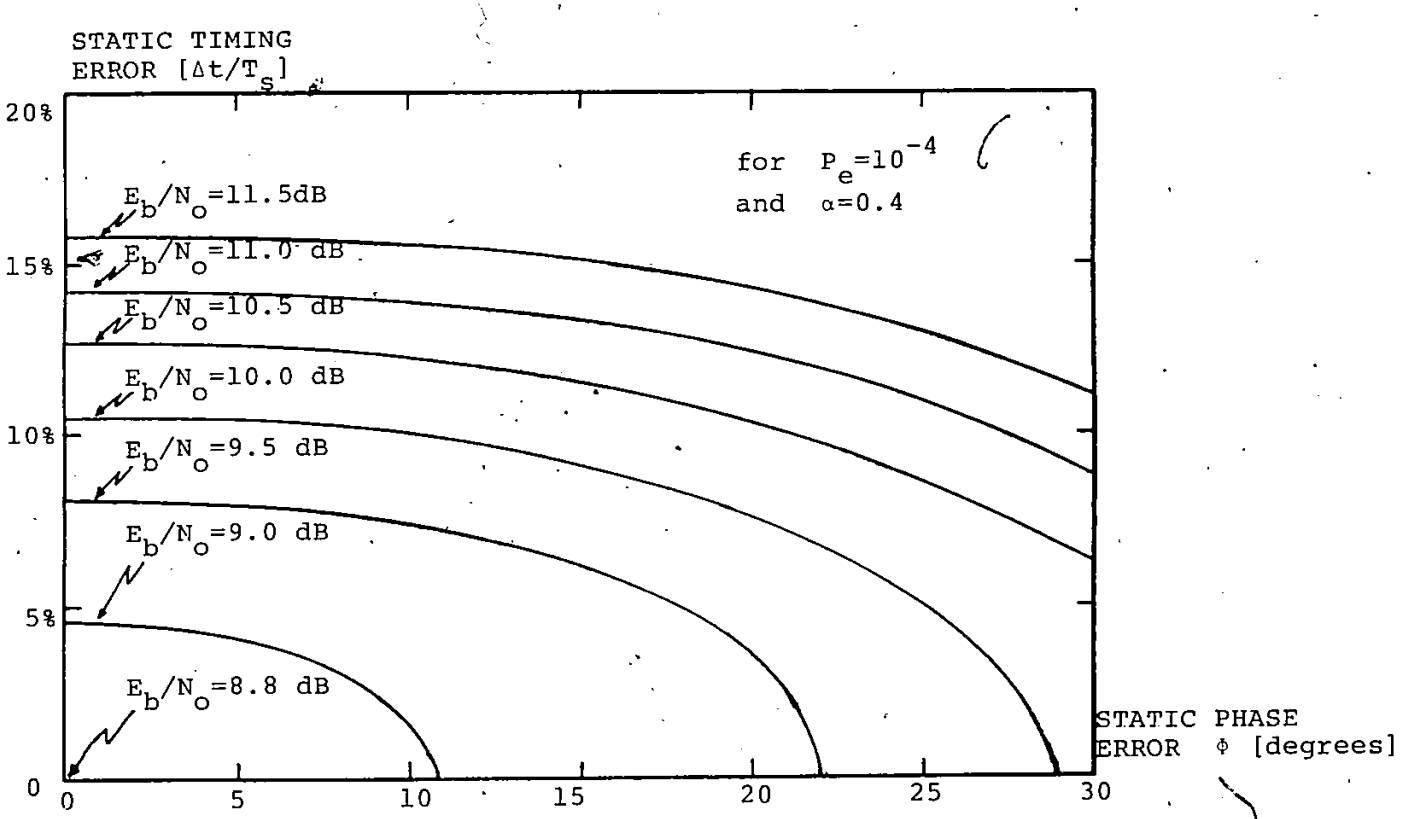

Fig. 6.13a: EQUAL-E_b/N_o CONTOURS VERSUS COMBINED STATIC PHASE AND TIMING ERRORS: IJF-OFFSET QPSK MODEM IN A *LINEAR* CHANNEL

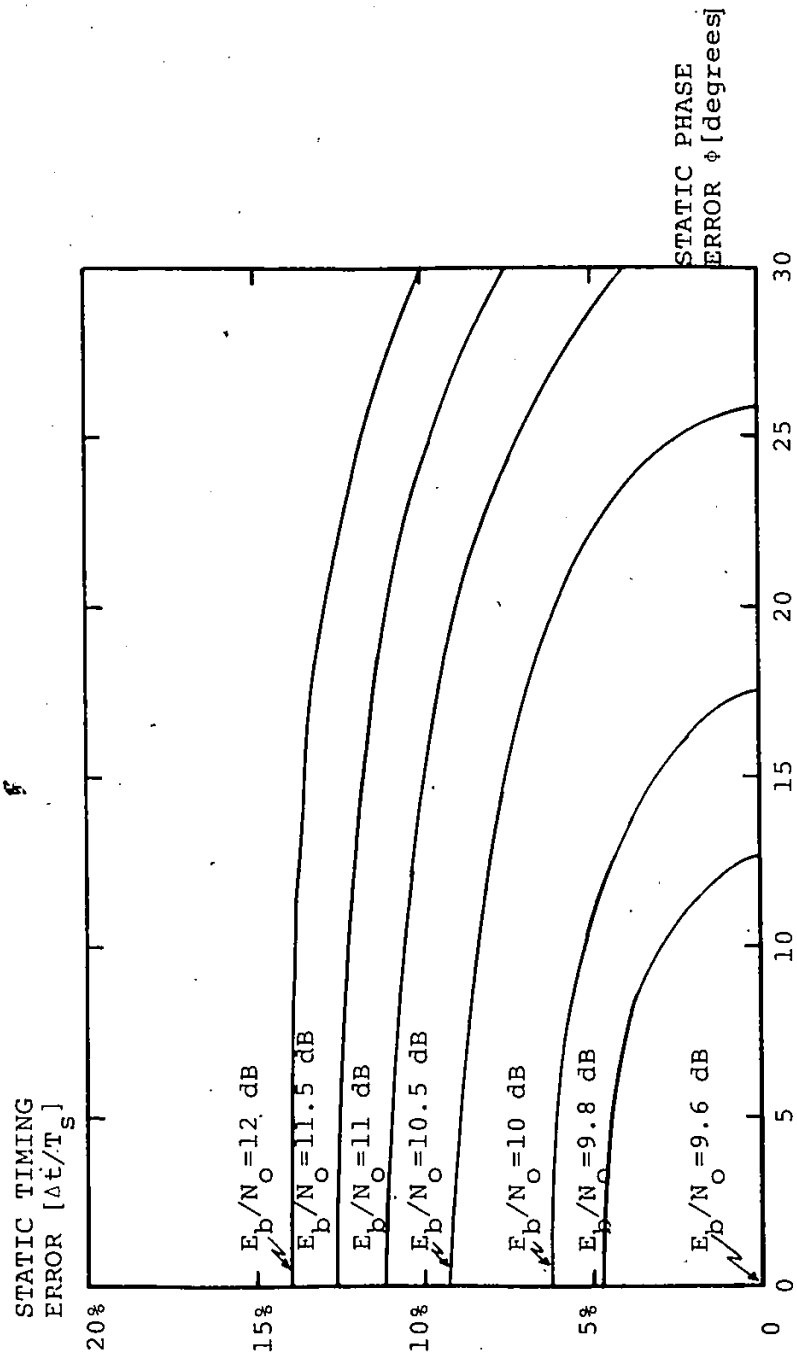

Fig. 6.13b: EQUAL-Eb/N_o CONTOURS VERSUS COMBINED STATIC PHASE AND TIMING ERRORS: IJF-OFFSET QPSK MODEM IN A *HARDLIMITED* CHANNEL

CHAPTER SEVEN:

IJF-QUADRATURE MODULATION TECHNIQUES: SOME MODIFIED SCHEMES

SUMMARY:

So far the spectral properties and P_e performance of IJF-QPSK and IJF-Offset QPSK modems have been studied. It was shown that IJF-Offset QPSK modulation techniques provide significant spectral advantages over QPSK, Offset QPSK and MSK, and a better performance in saturated channels.

In this chapter, additional techniques (modifications of the previous one) are introduced to further improve the spectral properties of IJF-Offset QPSK signals.

As an illustrative example, a 16-QAM scheme using IJF-Offset QPSK technique and saturated transmit high-power amplifiers is introduced. Spectral properties and signal space-diagram are investigated.

Higher spectral efficiency can also be accomplished by introducing controlled ISI into 2-level signals. Spectral efficiency is improved with the penalty in power efficiency. Two modified schemes having controlled ISI are presented. Spectral properties and P_e performance are evaluated.

7.1 A 16-QAM SCHEME USING THE IJF-OFFSET QPSK TECHNIQUE

Higher spectral efficiency can be achieved with multi-level QAM techniques. As an illustrative example, a 16-QAM scheme using the IJF-Offset QPSK technique is examined.

Figure 7.1 shows the block diagram of a 16-QAM modem using the IJF-Offset QPSK technique. The 16-QAM modulator contains two IJF-Offset QPSK modulators. The NRZ input signal is split into 4 parallel streams, $I_1(t)$, $I_2(t)$, $Q_1(t)$, and $Q_2(t)$. The signals $I_1(t)$, $I_2(t)$ and the delayed replica of $Q_1(t)$, and $Q_2(t)$ are encoded into IJF signals and fed to the in-phase and quadrature channels of the two IJF-Offset QPSK modulators.

The envelope fluctuations of the IJF-OQPSK signals, $y_1(t)$ and $y_2(t)$, are removed after hardlimiting. Hence, the hard-limited IJF-OQPSK signals, $z_1(t)$ and $z_2(t)$, suffer no major degradation due to nonlinear amplification. The output voltage of the first HPA is arranged to be twice that of the second HPA, i.e., 6 dB power difference. The outputs of HPA's are then added by a hybrid combiner, and filtered by the roofing band-pass filter to reject high order intermodulation products.

Since the shape of the power spectra of $z_1(t)$ and $z_2(t)$ is identical and the 16-QAM signal $v(t)$ results from the linear sum of $z_1(t)$ and $z_2(t)$, it can be shown that the power spectrum of $v(t)$ has the same shape as that of $z_1(t)$ or $z_2(t)$. Figs. 7.2a, b show the computed and measured spectra of $v(t)$ for the IJF double-interval pulse represented by Eq. (3.18b). The measured spectrum is in agreement with the computed one. It

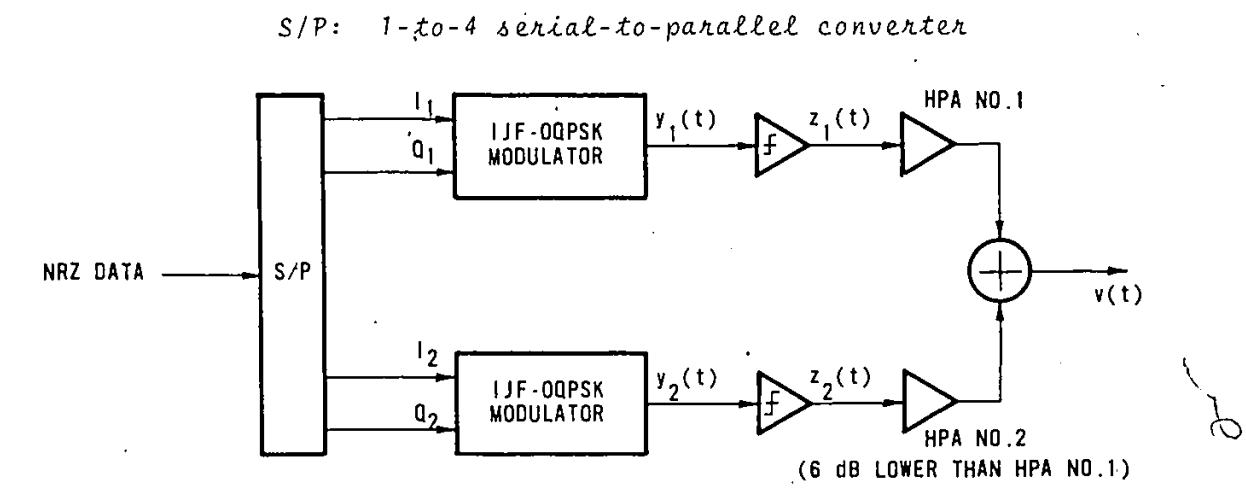

(a) MODULATOR

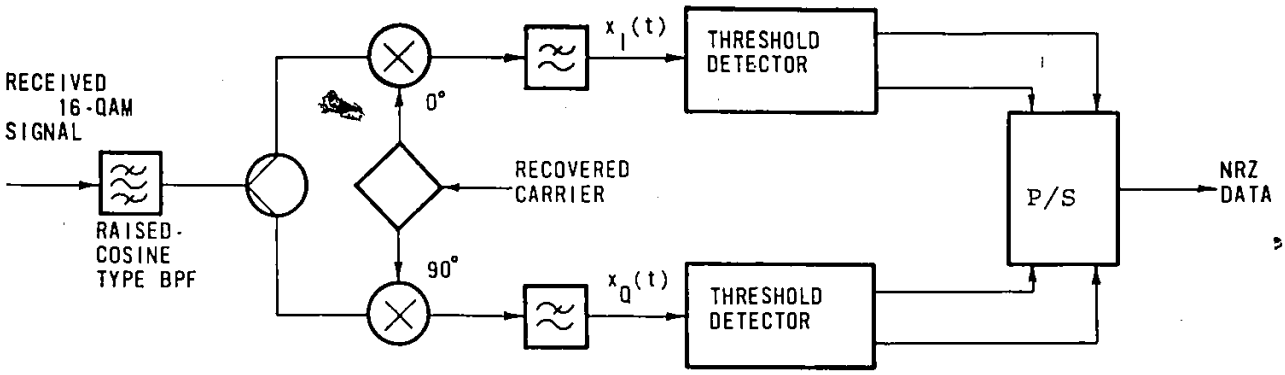

(b) DEMODULATOR

Fig. 7.1: BLOCK DIAGRAM OF A 16-QAM MODEM USING THE IJF-OQPSK TECHNIQUE

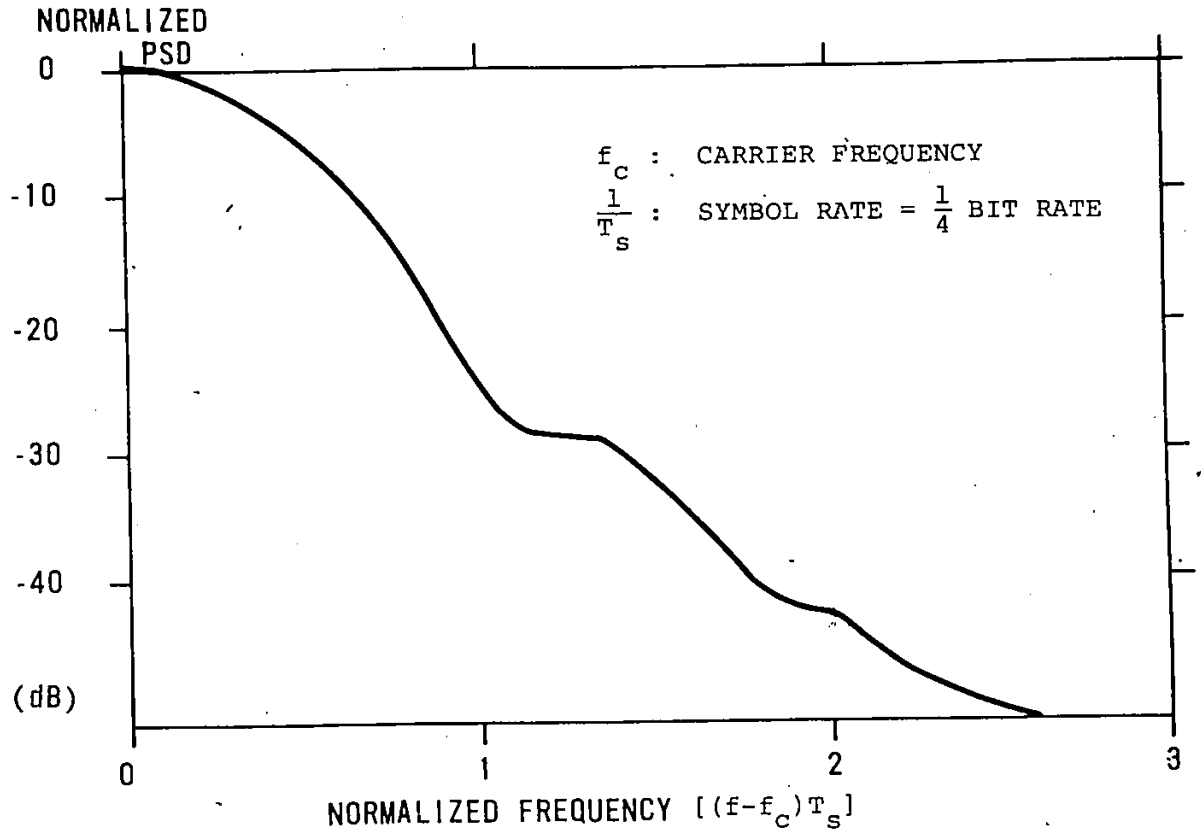

Fig. 7.2a: NORMALIZED PSD OF A 16-QAM SIGNAL USING THE IJF-OQPSK TECHNIQUE

(computed by using Eq. 4.14b)

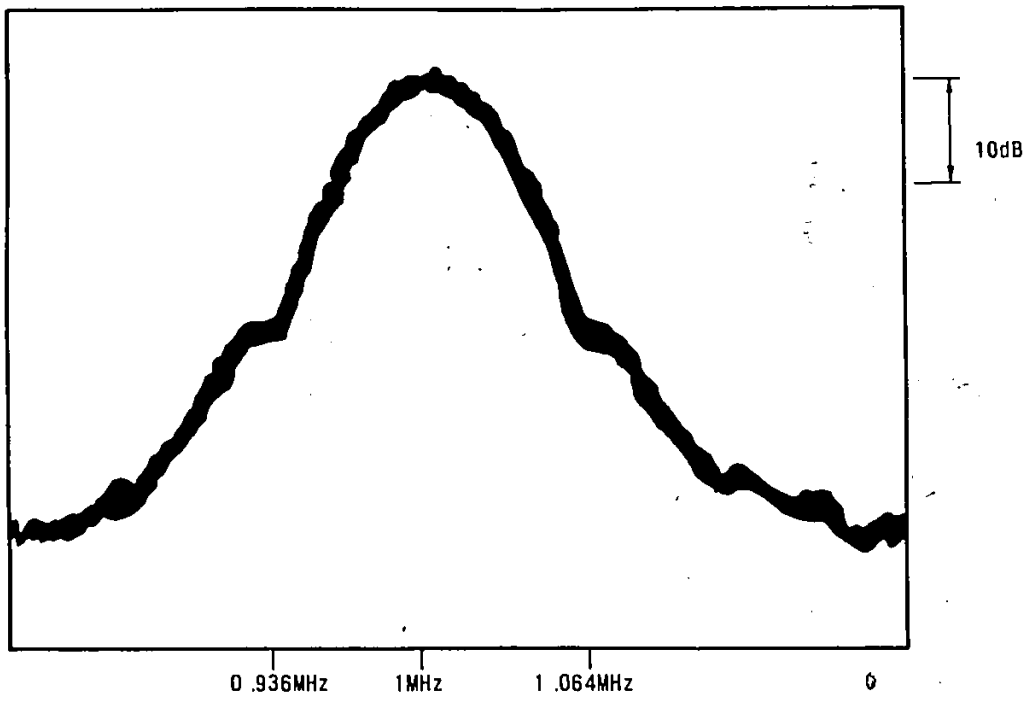

Fig. 7.2b: MEASURED POWER SPECTRUM OF A 16-QAM SIGNAL USING THE IJF-OQPSK TECHNIQUE

- *carrier frequency:* 1 MHz
- *bit rate:* 256 kb/s

also indicates that the spectral efficiency is double relative to IJF-OQPSK for the same bit rate. The signal space diagram of $v(t)$ can be derived from those of $z_1(t)$ and $z_2(t)$ using vector addition as shown in Fig. 7.3; $v(t)$ has a maximum envelope fluctuation of 4.8 dB.

The receive detection filter used in the 16-QAM demodulator (Fig. 7.1b) is a raised-cosine type bandpass filter as described in Chapter 3. Fig. 7.4 shows the measured eye diagrams of the in-phase and quadrature demodulated signals prior to the threshold detectors.

7.2. A BANDWIDTH-EFFICIENT ISI-CONTROLLED TRANSMISSION TECHNIQUE

Consider a NLSF output signal $y(t)$ represented by Eqs. (3.2a,b) with $s_e(t)$ and $s_o(t)$ represented by

$$s_e(t) = \begin{cases} 1+a, & \text{for } |t| < T_s/2 \\ \\ 0, & \text{elsewhere} \end{cases} \tag{7.1a}$$

$$s_o(t) = \begin{cases} \sin \frac{\pi t}{T_s}, & \text{for } |t| < T_s/2 \\ \\ 0, & \text{elsewhere} \end{cases} \tag{7.1b}$$

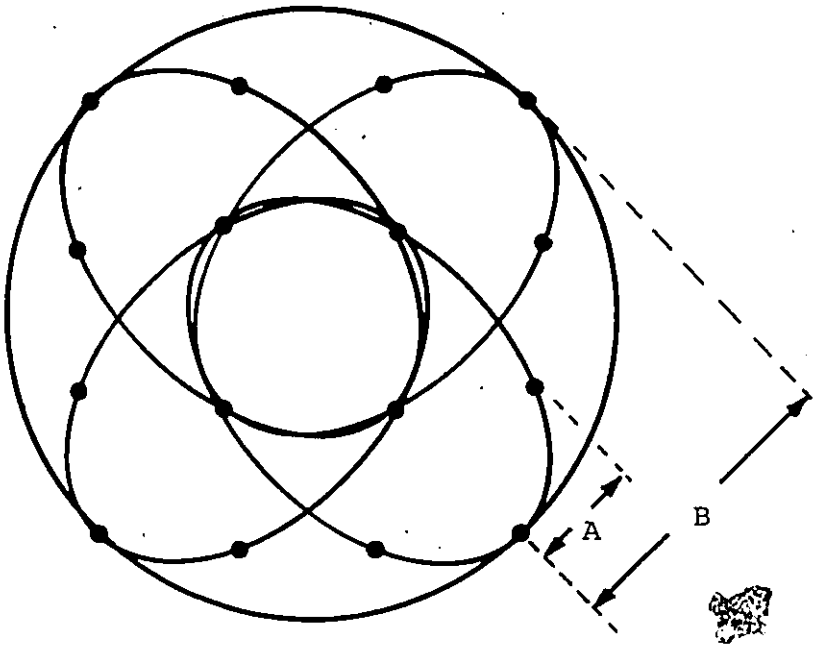

MAX. AMPLITUDE FLUCTUATION = $\frac{B}{A}$ = 3 or 4.8 dB

Fig. 7.3: SIGNAL SPACE DIAGRAM OF A 16-QAM SIGNAL USING THE IJF-OQPSK TECHNIQUE

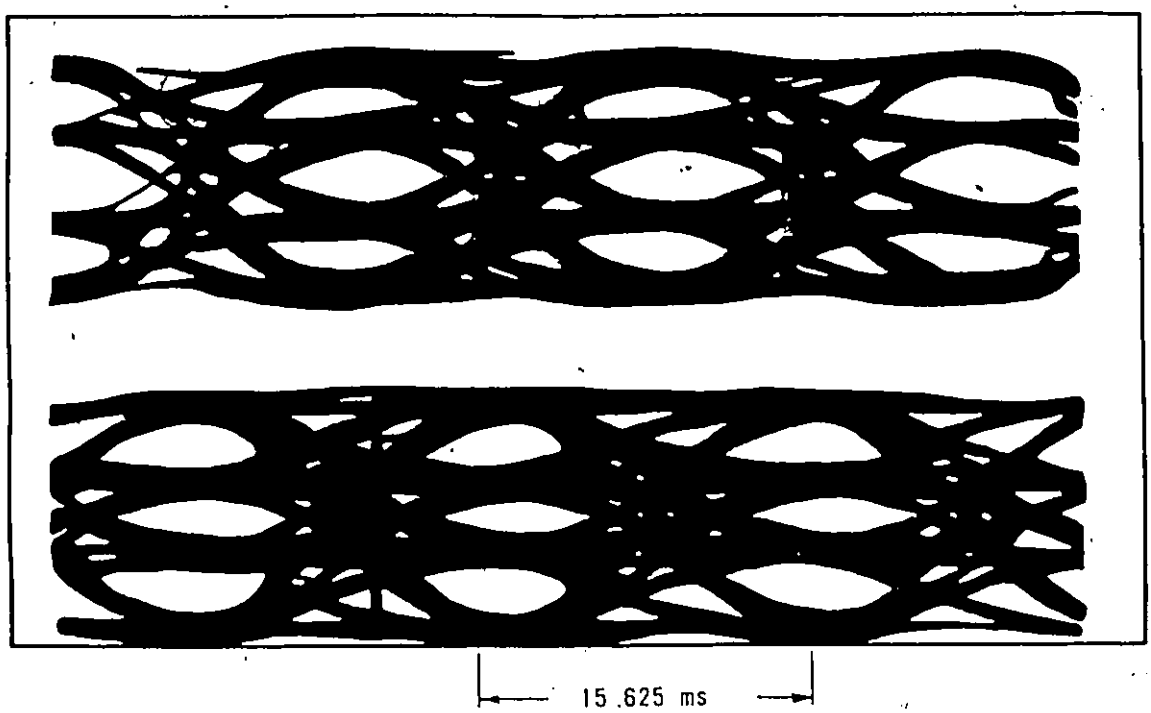

MEASURED EYE-DIAGRAMS OF THE DEMODULATED BASEBAND COMPONENTS

Fig. 7.4: MEASURED EYE-DIAGRAMS OF THE DEMODULATED BASEBAND COMPONENTS OF A 16-QAM SIGNAL USING THE IJF-OQPSK TECHNIQUE

bit rate: 256 kb/s

carrier frequency: 1 MHz

As shown in Fig. 7.5 the eye diagram of $y(t)$ exhibits an amount of *controlled* ISI represented by a. For $a=0$, there is no ISI and the resultant signal $y(t)$ corresponds to the IJF signal with the double-interval pulse represented by Eq. (3.18b).

The power spectral density (PSD) function of $y(t)$ is derived from Eq. (3.6). Taking the Fourier transforms of $s_e(t)$ and $s_o(t)$, and substituting them into Eq. (3.6), the normalized PSD function of $y(t)$ is simplified to

$$Y_n(x,a) = \{\frac{\sin 2\pi x}{(1+a)2\pi x}\ [\frac{1}{1-4x^2} + a]\}^2 \qquad (7.2)$$

where $x = fT_s$.

Figure 7.6 illustrates the normalized spectrum of the ISI-controlled binary signal, $y(t)$, for various values of a. As a increases, the main lobe of the corresponding power spectrum becomes *narrower*.

Following the same treatment given in Section 3.3.3, the performance of $y(t)$ in an additive white gaussian noise (AWGN) baseband channel can be derived. The receive detection filter is a raised-cosine type filter having a linear phase response and an amplitude response given by

$$H(x,a) = \frac{(1+a)\ 2\pi x}{[a+\frac{1}{1-4x^2}]\sin 2\pi x}\ R(x,\alpha) \qquad (7.3)$$

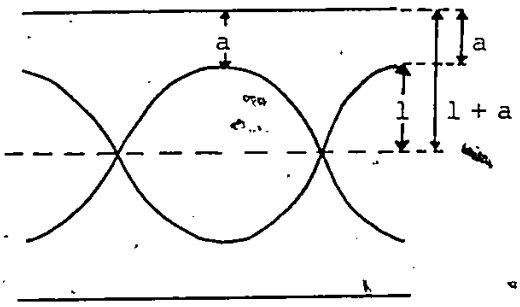

(a) computed eye diagram

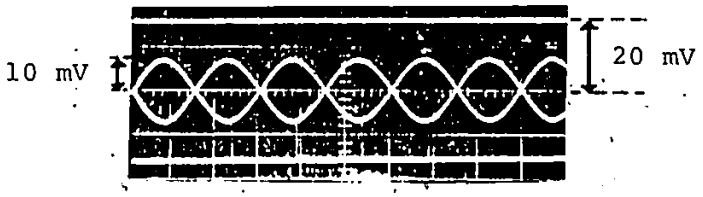

Measured eye diagram
with a = 1 and bit rate: 32 kb/s

Fig. 7.5: EYE DIAGRAM OF AN ISI-CONTROLLED BINARY SIGNAL

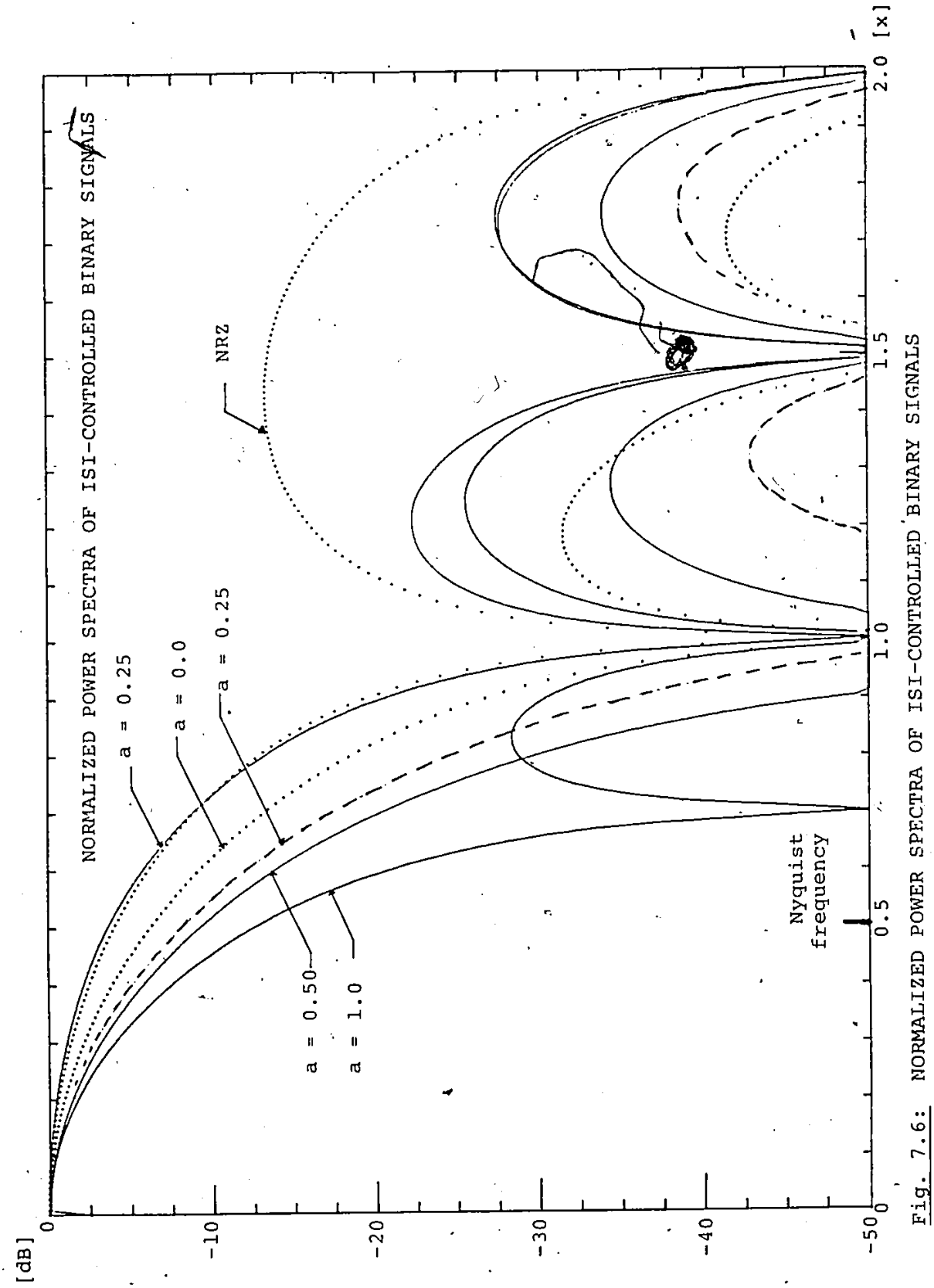

Fig. 7.6: NORMALIZED POWER SPECTRA OF ISI-CONTROLLED BINARY SIGNALS

where $R(x,\alpha)$ is the full raised-cosine filter (Section 3.3.3) and α is its roll-off factor.

Fig. 7.7 show the computed results. The degration factor d^2, represents the degradation in E_b/N_o relative to the optimum performance, i.e. 8.4 dB for $P_e=10^{-4}$. The performance degradation (d^2) *increases* with the controlled ISI value (a). Therefore the choice of the controlled ISI value depends on the trade-off between the spectral efficiency (Fig. 7.6) and the performance degradation (Fig. 7.7).

Figure 7.8a shows the block diagram of a modified Offset-QPSK modulator using this ISI-controlled binary transmission technique. The signal space diagram of the modulated signal $z(t)$ is illustrated in Fig. 7.8b. The modulated signal $z(t)$ contains envelope fluctuations. Its power spectrum has the same shape as that of the ISI-controlled baseband signal.

A constant-envelope modulated signal can be generated by adding a low-power ideal hardlimiter at the output of the modified Offset QPSK modulator. The power spectral density of the *hardlimited* (modulated) signal is computed using Equation (4.14b). The results are plotted in Fig. 7.9a. As the controlled ISI value (a) increases, the corresponding hardlimited (modulated) signal exhibits lower spectral spreading. For $a>0$, the modified Offset QPSK signal provides lower (better) spectral

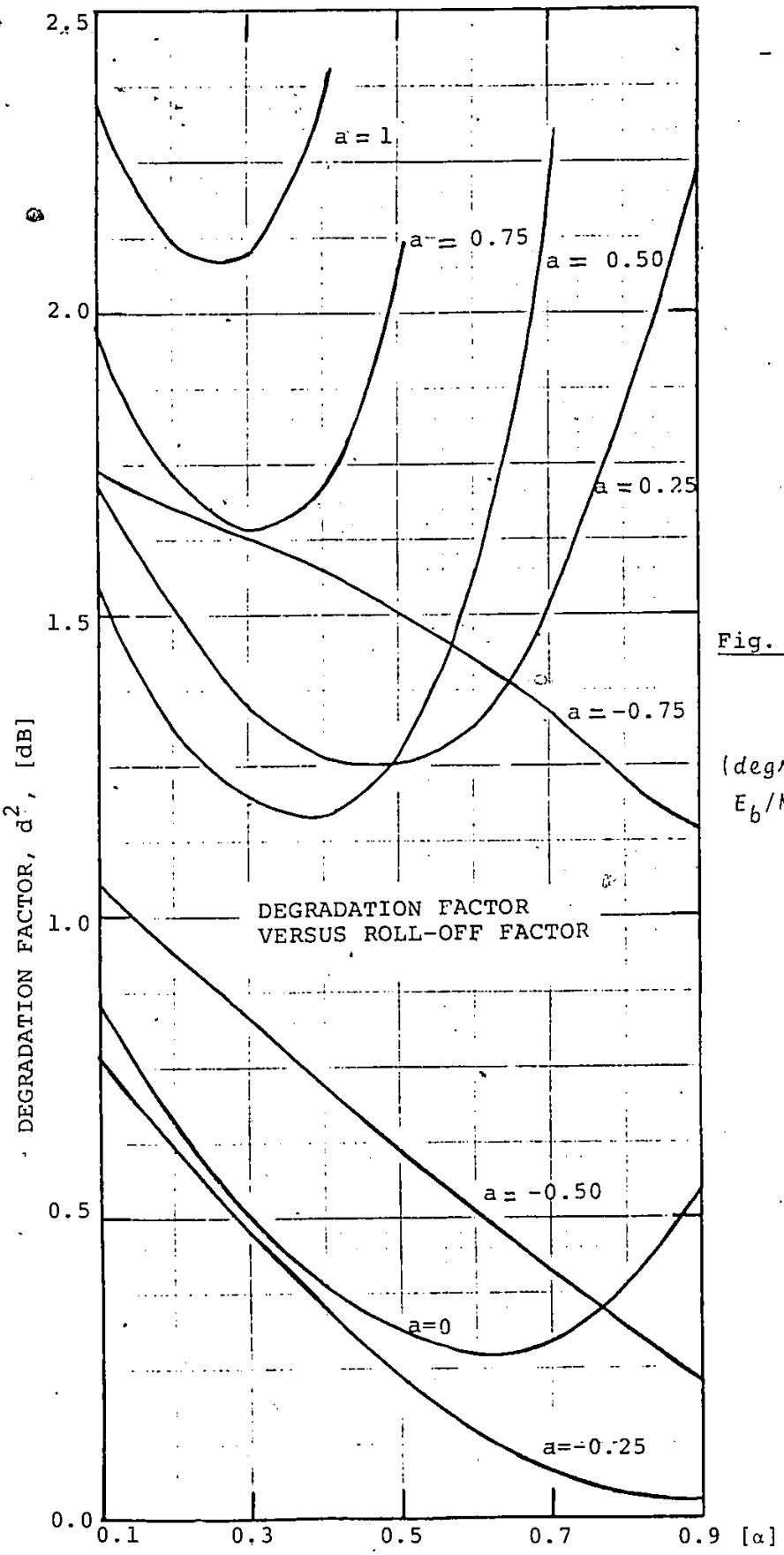

Fig. 7.7: DEGRADATION FACTOR VERSUS ROLL-OFF FACTOR

(degradation relative to E_b/N_o=8.4dB @ $P_e=10^{-4}$)

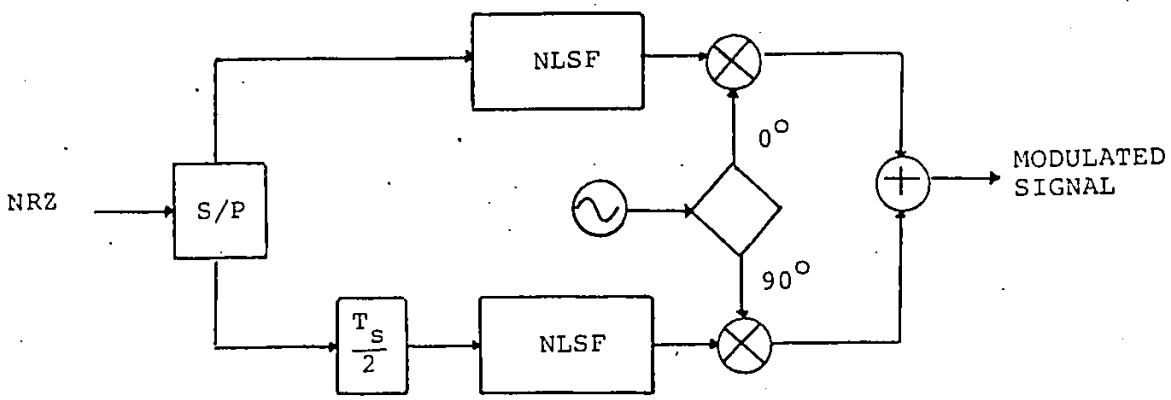

Fig. 7.8a: BLOCK DIAGRAM OF A MODIFIED OQPSK MODULATOR

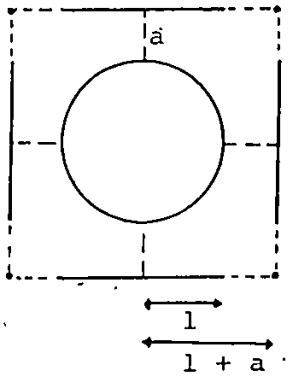

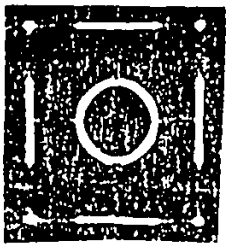

MEASURED RESULTS
bit rate: 64 kb/s
carrier frequency: 512 kHz

Fig. 7.8b: SIGNAL SPACE DIAGRAM OF AN OQPSK SIGNAL USING THE ISI-CONTROLLED BINARY TRANSMISSION TECHNIQUE

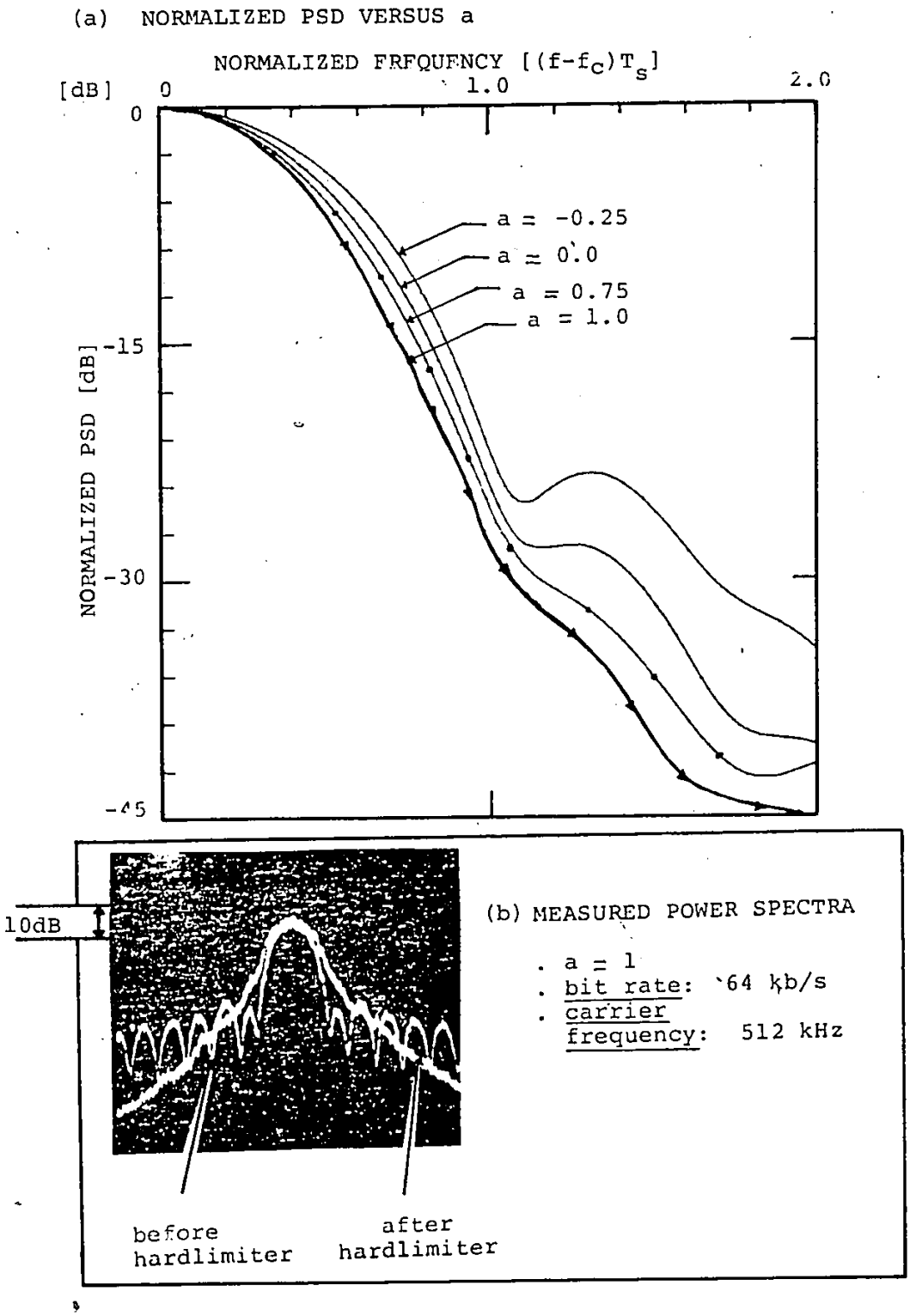

Fig. 7.9: POWER SPECTRA OF *HARDLIMITED* (MODULATED) SIGNALS

spreading than the IJF-OQPSK signal (i.e., case a=0).

Experiments are also used to verify the analytical results. As shown in Fig. 7.9b, the measured results are in agreement with the computed results.

7.3 A PARTIAL-RESPONSE IJF TRANSMISSION TECHNIQUE

Fig. 7.10 shows the block diagram of the Partial-Response (PR)-IJF encoder. The input to the encoder is an NRZ signal. The PR-IJF baseband signal, s(t), at the output of the partial-response filter, has the power spectral density S(f) represented by

$$S(f) = 2\, S_o(f)\, [1+\cos 2\pi fd] \tag{7.4}$$

where $S_o(f)$ is the power spectral density of the IJF baseband signal $s_o(t)$. The term $[1+\cos 2\pi fd]$ has a periodical attenuation centered at frequencies $1/2d + k/d$ where $k=0,1,2,...$ Thus the spectral roll-off of the original IJF signal is not affected and the out-of-band energy is reduced in the region depending on the choice of d.

As an illustrative example, for the IJF double-interval pulse represented by Eq. (3.18b) and $d=T_s/2$, the PSD function of the corresponding PR-IJF signal is

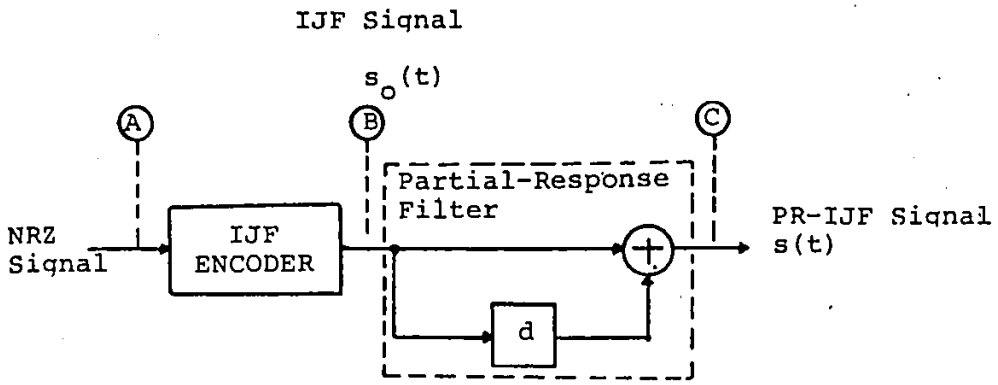

Fig. 7.10: BLOCK DIAGRAM OF A PR-IJF ENCODER

$$S(f) = \frac{1}{2}\left|\frac{\sin 2\pi fT_s}{\pi f(1-4f^2T_s^2)}\right|^2 (1+\cos\pi fT_s) \qquad (7.5)$$

Fig. 7.11 show the power spectra of $S_o(f)$ and $S(f)$. It is shown that the PR-IJF baseband signal has a better power spectrum than IJF baseband signal with the same IJF double-interval pulse. Figure 7.12 shows the out-of-band to total energy ratio of PR-IJF baseband signals with different values of d. It indicates that the out-of-band energy of the original IJF signal can be reduced in different regions according to the values of d.

The PR-IJF signalling technique is applied to the modified IJF-OQPSK modulation scheme called PR-IJF-OQPSK. The PR-IJF-OQPSK modem is illustrated in Fig. 7.13. The PR-IJF encoders are used to shape the transmitted power spectrum. Similar to IJF-OQPSK signal, the PR-IJF-OQPSK signal contains envelope fluctuation. Figure 7.14 shows the measured signal-space diagram of PR-IJF-OQPSK signals for the IJF pulse represented by Eq. (3.18b). The envelope fluctuation of these signals can be removed by a hardlimiter following the modulator. As shown in Fig. 7.15, the power spectrum of the hardlimiter PR-IJF-OQPSK signal is better (lower) than that of the hardlimiter IJF-OQPSK signal for the same IJF double-interval pulse.

The performance of a PR-IJF-OQPSK modem in a regenerative satellite system is evaluated using simulation techniques. The

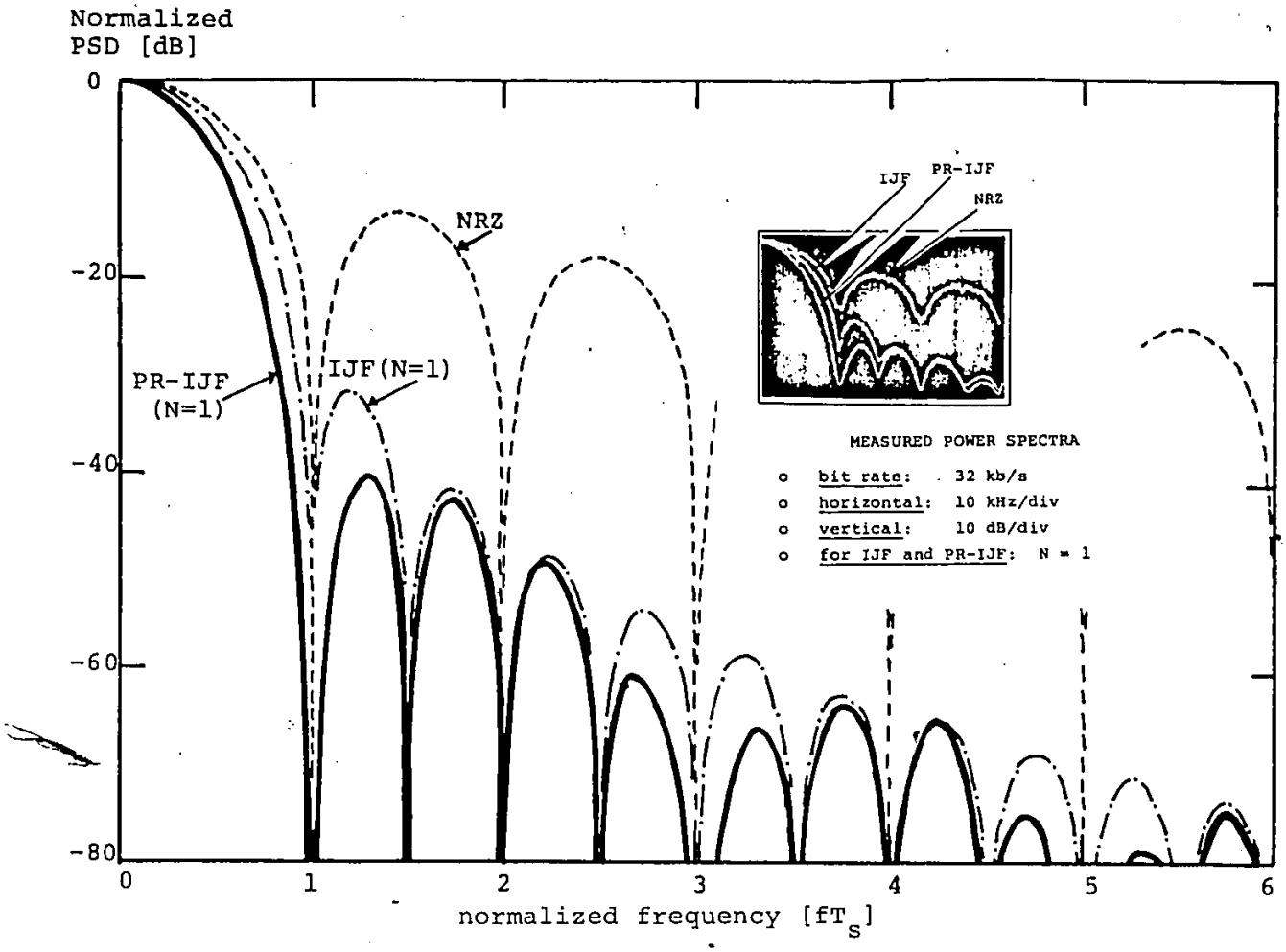

Fig.7.11: COMPARISON OF POWER SPECTRA OF NRZ, IJF AND PR-IJF SIGNALS, OBTAINED AT POINTS Ⓐ, Ⓑ, AND Ⓒ RESPECTIVELY.

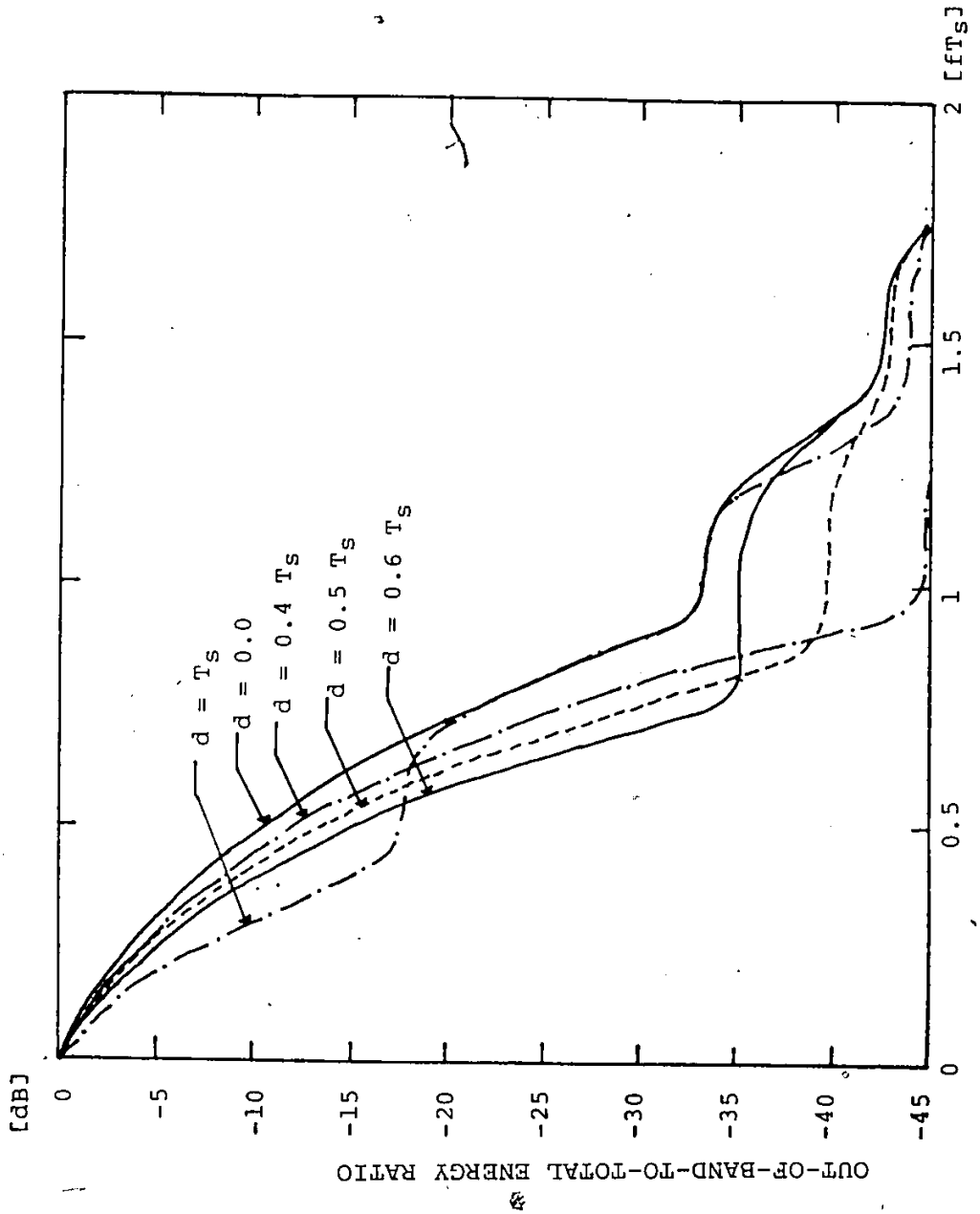

Fig.7.12: OUT-OF-BAND-TO-TOTAL ENERGY RATIO
(for PR-IJF signal with N = 1)

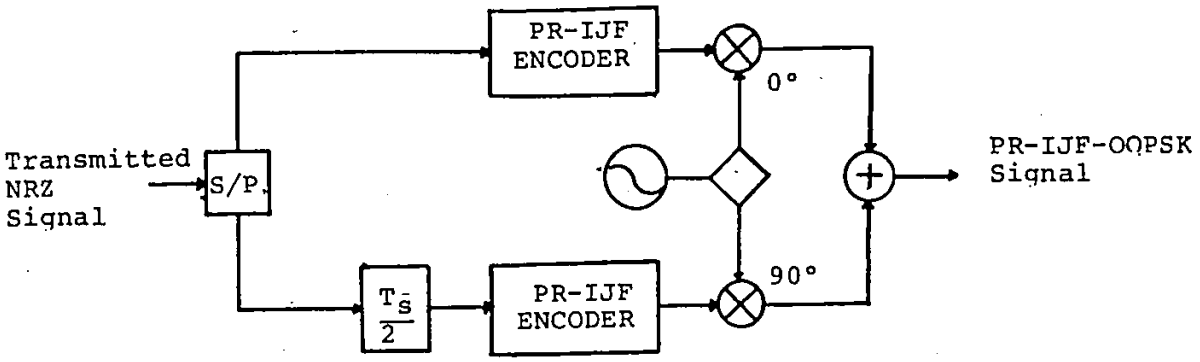

(a) PR-IJF-OQPSK MODULATOR

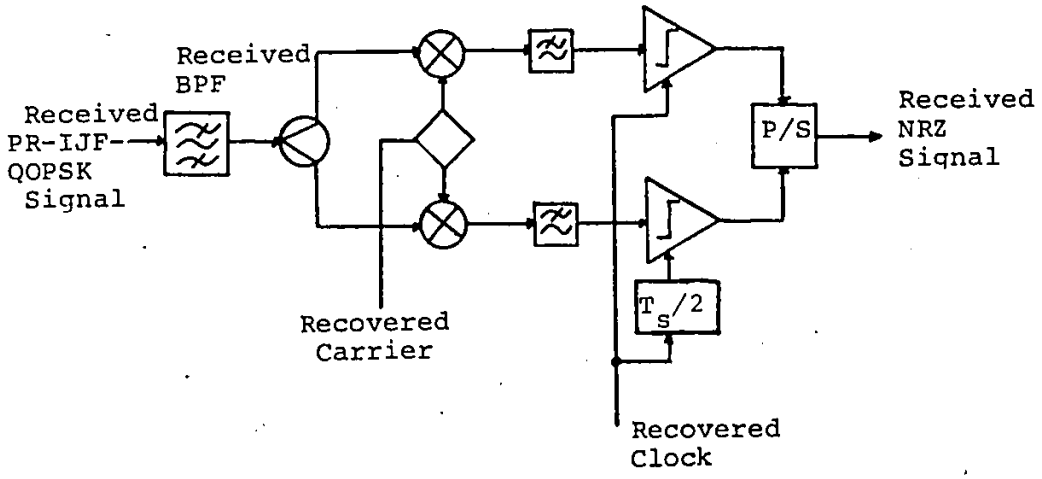

(b) PR-IJF-OQPSK DEMODULATOR

Fig. 7.13: BLOCK DIAGRAM OF A PR-IJF-OQPSK MODEM

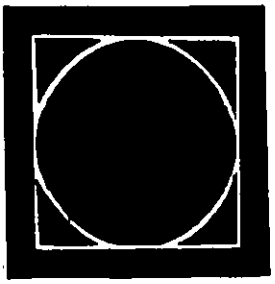

(a) IJF-OQPSK

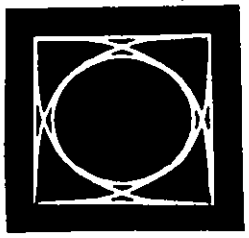

(b) PR-IJF-OQPSK

Fig. 7.14: MEASURED SIGNAL-SPACE DIAGRAMS (N=1)

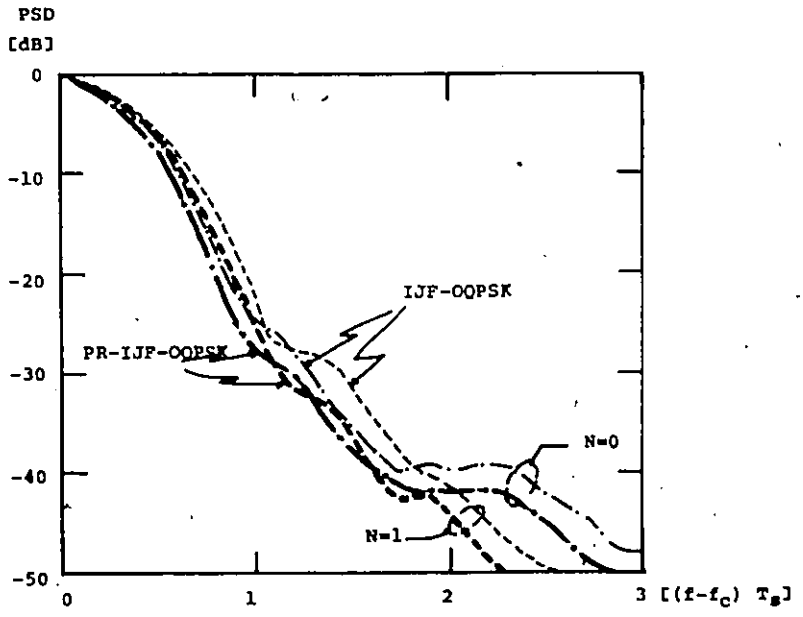

Fig. 7.15: NORMALIZED POWER SPECTRA OF *HARDLIMITED* IJF-OQPSK AND PR-IJF OQPSK SIGNALS

simulation model is similar to that given in Fig. 5.20. The results shown in Figs. 7.16a and b, indicate that the PR-IJF-OQPSK modem provides better performance than the IJF-OQPSK for a fade depth of 12 dB of the desired channel.

NOTES: *Parts of this chapter were published in [66,69,78-82].*

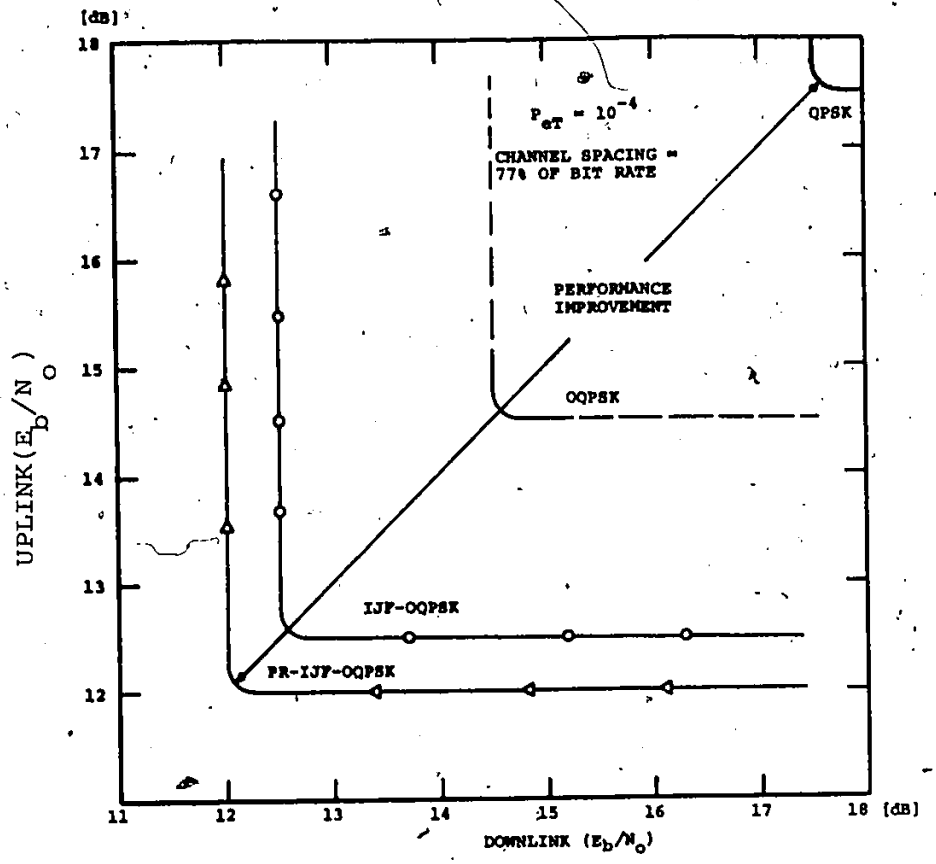

Fig. 7.16a: ISO-ERROR PROBABILITY PERFORMANCE OF A REGENERATIVE SATELLITE SYSTEM WITH ACI (EQUAL POWER CHANNELS)

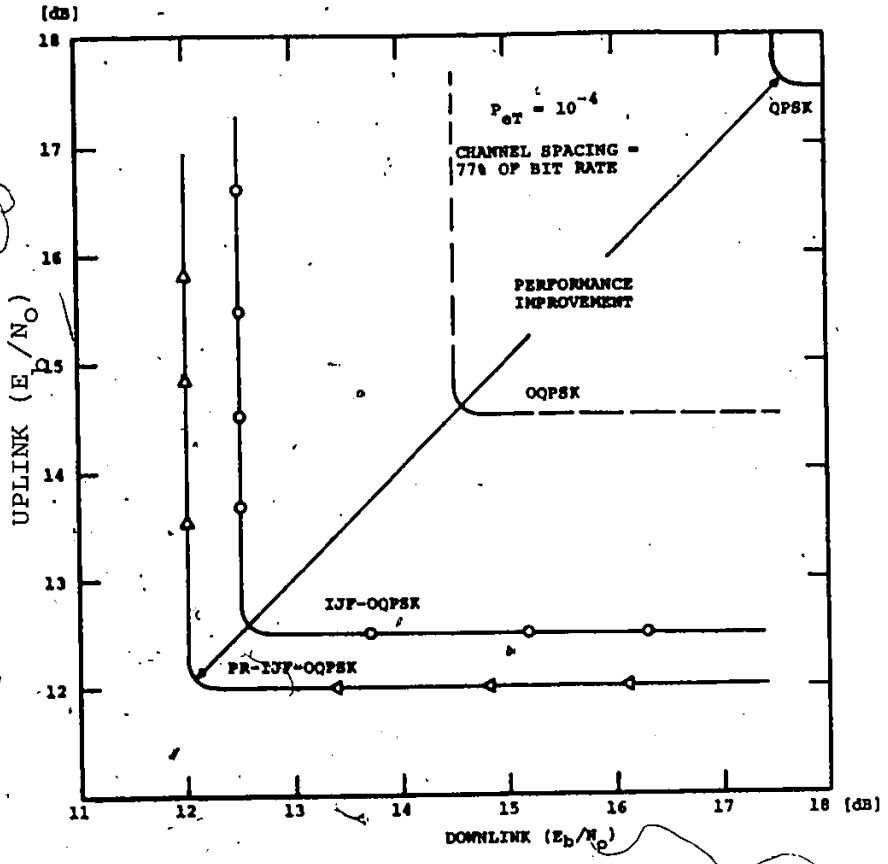

Fig. 7.16b: ISO-ERROR PROBABILITY PERFORMANCE OF REGENERATIVE SATELLITE SYSTEM WITH ACI (12 dB FADE DEPTH OF THE DESIRED CHANNEL)

CHAPTER EIGHT:

CONCLUSIONS AND SUGGESTIONS FOR FURTHER RESEARCH

8.1 CONCLUSIONS

In the previous chapters a new class of power and bandwidth efficient transmission techniques was presented and studied.

The power spectral density (PSD) function of a baseband signal generated by a generalized Nonlinear-Switching Filter (NLSF) was derived. It was shown that this PSD function can be expressed in terms of the Fourier transform of a double-interval even pulse when this baseband signal satisfies the Intersymbol-Interference and Jitter Free (IJF) conditions. This result stimulated the search of pulse shapes which yield IJF baseband signals having fast spectral roll-off and low out-of-band energy emission. Spectral properties and error probability (P_e) performance of these IJF signals were described and analyzed. Significant spectral advantages over the Non-Return-to-Zero (NRZ) signal and negligible degradation relative to the optimum performance (i.e. $P_e = \frac{1}{2}\,\mathrm{erfc}\,\sqrt{\frac{E_b}{N_o}}$) were discovered. Figures 3.7, 3.8a,b and 3.10a,b provide the necessary information to select an IJF signal for specific requirements of the spectral roll-off and out-of-band energy emission.

The IJF baseband signals were combined with quadrature phase modulation schemes. A 16-state Markov chain model was used to derive the PSD function of *hardlimited* IJF-quadrature modulated signals. The spectral regrowth due to nonlinear amplifiers and hardlimiter and effects of the time offset (d) between the in-phase and quadrature baseband components were investigated. The hardlimited IJF-quadrature modulated signal was found to have the lowest spectral regrowth for $d = T_s/2$ (T_s being the symbol interval). It was also shown that the IJF-quadrature modulated signal with $d = T_s/2$ (called IJF-OQPSK) has lower spectral regrowth than QPSK, Offset-QPSK and MSK signals in saturated channels.

The P_e performance of IJF-OQPSK modems in linear and nonlinear channels was studied. Effects of co-channel and adjacent-channel interference on the P_e performance were investigated. It was shown that a *low-power hardlimiter* introduced at the output of the IJF-OQPSK modulator can improve the spectral regrowth and performance when the transmit HPA operates in nonlinear mode. A spectral efficiency of 1.5 b/s/Hz can be achieved with IJF-OQPSK modems in a saturated multi-channel environment. This is a significant improvement compared to QPSK, OQPSK and MSK modems. Spectral advantages and good performance make the IJF-OQPSK modulation scheme a promising candidate for application in Single-Channel-Per-Carrier (SCPC), Time-Division-Multiple-Access (TDMA), and On-Board Regenerative systems with high-power amplifiers operating in saturation.

Results reported in Chapter 5 supply useful informations to select design parameters such as performance degradation, channel spacing, transmission efficiency, transmitted power requirements... in various system configurations.

Carrier and clock synchronization aspects of IJF-quadrature demodulators were studied. The PSD function of recovered clock and carrier signals was derived and used to investigate the pattern-noise in different carrier and clock synchronizers. The effects of static timing and phase error in recovered reference signals on the P_e performance were studied.

As an additional contribution modified techniques were introduced to further improve the spectral properties of IJF-OQPSK signals. It was shown that the spectral efficiency of these modified schemes could be improved with the penalty in power efficiency.

8.2 SUGGESTIONS FOR FURTHER RESEARCH

Although the spectral properties and P_e performance of IJF baseband signals and IJF-quadrature modulated signals were extensively studied in our research, there are undoubtedly other interesting aspects which were not covered. We make here the following suggestions for future research:

Non-coherent demodulation and detection of IJF-OQPSK signals: We assume coherent IJF-OQPSK demodulators throughout our studies. Non-coherent demodulators are desirable for their simple structures and in TDMA applications. They can provide faster detection and, as a result, the synchronization preamble in transmitted TDMA bursts can be shortened to increase the transmission throughput. The study of non-coherent IJF-OQPSK demodulator structures and their P_e performance may be desirable.

Effects of multipath fading: Multipath fading in microwave digital radio systems can be a major source of outage, specially for wideband, high-capacity transmission. The investigation of its effects on the P_e performance of IJF-OQPSK modems and equalization techniques for performance improvement is an interesting topic.

Correlated pulse shaping techniques: We considered only independent in-phase and quadrature baseband components of the modulated signals in this thesis. The envelope fluctuation of the modulated signal can be reduced by introducing cross-correlation between its in-phase and quadrature baseband components. Reduction in envelope fluctuation can lead to lower spectral regrowth due to nonlinear amplification (or hardlimiting). Appropriate

correlated pulse shaping techniques can provide more power and bandwidth efficient modulation schemes for nonlinear applications.

REFERENCES

[1] J.G. Smith, "Spectrally Efficient Modulation" *ICC '77*, pp. 31-41, Jun. 1977

[2] R.K. Kwan, "The Effects of Filtering and Limiting A Double-binary PSK Signal" *IEEE Trans on Aerospace and Electronic Systems*, Vol. AES-5 No. 4, pp. 587-594, Jul. 1969

[3] S.A. Rhodes, "Effects of Hardlimiting on Bandlimited Transmissions with Conventional and Offset QPSK Modem" *NTC '72*, pp. 26F/1-7, Dec. 1972

[4] M.L. Doelz and E.A. Heald, "Minimum-Shift Data Communication System" *U.S. Patent No. 2, 977, 417*, (assigned to Collins Radio Company) Mar. 28, 1961

[5] S.A. Gronemeyer, A.L. McBridge, "MSK and Offset QPSK Modulation" *IEEE Trans. Comm.*, Vol. COM-24, pp. 809-820, Aug. 1976

[6] M.G. Pelchat, R.C. Davis and M.B. Luntz, "Coherent Demodulation of Continuous Phase Binary FSK Signals" *Proc. Int. Telemetering Conf.*, pp. 187-190, Washington, D.C., 1971

[7] W.P. Osborne and M.B. Luntz, "Coherent and Noncoherent Detection of CPFSK" *IEEE Trans. Comm.* Vol. COM-22, pp. 1023-1036, Aug. 1974

[8] R. deBuda, "Coherent Demodulation of Frequency Shift Keying with Low Deviation Ratio", *IEEE Trans. Comm.*, Vol. COM-22, pp. 429-435, Aug. 1972

[9] J.D. Oetting, "A Comparison of Modulation Techniques for Digital Radio" *IEEE Trans. Commun.* Vol. COM-27, pp. 1752-1762, Dec. 1979

[10] S.A. Fredricsson, "Optimum Receiver Filters in Digital Quadrature-Phase-Shift-Keyed Systems With a Nonlinear Repeater", *IEEE Trans. Commun.* Vol. COM-23, pp. 1389-1399, Dec. 1975

[11] S.Y. Kwon and R.S. Simpson "Effect of Hard Limiting on a Quadrature PSK Signal", *IEEE Trans. Commun.*, Vol. COM-22, pp 955-958, Aug. 1973.

[12] C.A. Kunzinger, "An Evaluation of Digital PSK Signals Through a Nonlinear Satellite Repeater", *ICC '75*, pp 20/17-21, Jun. 1975

[13] D.P. Taylor, H.C. Chan, and S.S. Kaykin, "A Simulation Study of Digital Modulation Methods for Wideband Satellite Communications", *IEEE Trans. Commun.*, Vol. COM-24, pp 1351-1354, Dec. 1976

[14] S. Murakami, Y. Furuya, Y. Matsuo, M. Sugiyama, "Optimum Modulation and Channel Filters for Nonlinear Satellite Channels", *IEEE Trans. Commun.*, Vol. COM-27, pp 1810-1819, Dec. 1979

[15] E. Castellano, "Relative Performance of Conventional QPSK and Staggered QPSK Modulations in a Nonlinear Channel", *ESA Journal*, Vol. 2, pp 37-47, 1978

[16] S.A. Rhodes, "Effects of Noisy Phase Reference on Coherent Detection of Offset QPSK Signals", *IEEE Trans. Commun.*, Vol. COM-22, pp 1046-1055, Aug. 1974

[17] R.J.F. Fang, "Quaternary Transmission Over Satellite Channels with Cascaded Nonlinear Elements and Adjacent Channel Interference", *IEEE Trans. Commun.*, Vol. COM-29, pp 567-581, May 1981

[18] G. Robinson, O. Shimbo, and R. Fang, "PSK Signal Power Spectrum Spread Produced by Memoryless Nonlinear TWT's", *COMSAT Tech. Rev.*, Vol. 3, pp 227-256, Fall 1973

[19] M. Jones and M. Wachs, "Optimum Filtering for QPSK in Bandwidth-Limited Nonlinear Satellite Channels", *COMSAT Tech. Rev.*, Vol. 9, pp 465-507, Fall 1979

[20] D. Chakraborty, T. Noguchi, S.J. Campanella, and C.J. Wolejsza, "Digital Modem Design for Nonlinear Satellite Channels", *4th Int. Conf. on Dig. Sat. Commun.*, pp 123-130, Montreal, Oct. 1978

[21] R.A. Harris, "Transmission Analysis and Design for the ECS System", *4th Int. Conf. on Dig. Sat. Commun.*, pp 81-93, Montreal, Oct. 1978

[22] R.G. Lyons, "Effects of PSK Spectral Spreading in a Satellite Transponder", *ICC '74*, pp 36B-1/6, Minneapolis, Minn., Jun. 17-19, 1974

[23] D.J. Keenedy, "Optimum PSK Filtering in a Channelized Environment", *ICC '77*, pp. 43-22/28, Philadelphia, Penn. Jun. 14-16, 1976

[24] W.R. Bennett, J.R. Davey, *Data Transmission*, McGraw-Hill, N.Y., 1965

[25] R.W. Lucky, J. Salz, E.J. Weldon, Jr., *Principles of Data Communication*, McGraw-Hill, N.Y., 1968

[26] F. Amoroso, "Pulse and Spectrum Manipulation in the Minimum (Frequency) Shift Keying (MSK) Format", *IEEE Trans. Comm.*, Vol. COM-24, pp 381-384, Mar. 1976

[27] M.K. Simon, "A Generalization of Minimum-Shift Keying (MSK) - Type Signalling Based Upon Input Data Symbol Pulse Shaping", *IEEE Trans. Comm.*, Vol. COM-24, pp 845-856, Aug. 1976

[28] M. Rabzel, S. Pasupathy, "Spectral Shaping in Minimum Shift Keying (MSK) - Type Signals", *IEEE Trans. Comm.*, Vol. COM-26, pp 189-195, Jan. 1978 (corresp.)

[29] B. Bazin, "A Class of MSK Baseband Pulse Formats with Sharp Spectral Roll-Off", *IEEE Trans. Comm.*, Vol. COM-27, pp 826-829, May 1979 (corresp.)

[30] N. Boutin, S. Morisette, L. Dussault, "Constant Amplitude PSK Signal with Minimum Out-of-Band Energy", *NTC '78*, pp 6.3/1.3, Dec. 1978

[31] G.S. Deshpande, P.H. Wittke, "Optimum Pulse Shaping in MSK-Type Signals", *NTC '79*, pp 33.4/1-7, Dec. 1979

[32] T. Aulin, C-E Sundberg, "Continuous Phase Modulation-Part I: Full-Response Signalling, *IEEE Trans. Comm.*, Vol. COM-29, pp 196-209, Mar. 1981

[33] T. Aulin, N. Rydbeck and C-E Sundberg, "Continuous Phase Modulation - Part II: Partial-Response Signalling", *IEEE Trans. Comm.*, Vol. COM-29, pp 210-225, Mar. 1981

[34] H. Miyakawa, H. Harashina, and Y. Tanaska, "A New Digital Modulation Scheme-Multimode Binary CPFSK", *3rd Int. Conf. on Dig. Sat. Commun.*, pp 105-112, Kyoto, Japan, Nov. 1975

[35] J.G. Anderson, and D.P. Taylor, "A Bandwidth Efficient Class of Signal Space Codes", *IEEE Trans. Inf. Theory*, V-1. IT-24, pp 703-712, Nov. 1978

[36] T. Aulin, C-E Sundberg, "Binary CPFSK-Type of Signalling with Input Data Symbol Pulse Shaping-Error Probability and Spectrum", *NTC '78*, pp 6.5.1-6.5.5, Dec. 1978

[37] T. Aulin, N. Rydbeck, C-E Sundberg, "Bandwidth-Efficient Constant-Envelope Digital Signalling with Phase Tree Demodulation", *Electronic Letters*, Vol. 14, pp 487-489, Jul. 1978

[38] T. Aulin, N. Rydbeck, C-E Sundberg, "Further Results on Digital FM with Coherent Phase Tree Demodulation-Minimum Distance and Spectrum", *Technical Report TR-119*, University of Lund, Nov. 1978

[39] F. deJager, C.B. Dekker, "Tamed Frequency Modulation, A Novel Method to Achieve Spectrum Economy in Digital Transmission", *IEEE Trans. Comm.*, Vol. COM-26, pp 534-532, May 1978

[40] P. Galko, S. Pasupathy, "On a Class of Generalized MSK", *ICC'81* Denver, Jun.14-18, 1981

[41] D. Muilwijk, "Correlative Phase Shift Keying-A Class of Constant Envelope Modulation Techniques", *IEEE Trans. Comm.*, Vol. COM-29, pp 226-236, Mar. 1981

[42] G.S. Deshpande, P.H. Wittke, "The Spectrum of Correlative Encoded FSK", *ICC '78*, pp 25.3/1-5, Jun. 1978

[43] S. Rhodes, "FSOQ, A New Modulation Technique That Yields a Constant Envelope", *NTC '80*, pp 51.1/1-7, Dec. 1980

[44] G.J. Garrison, "A Power Spectral Density Analysis for Digital FM", *IEEE Trans. Comm.*, Vol. COM-25, pp 1228-1243, Nov. 1975

[45] L.J. Greenstein, "Spectra of PSK Signals with Overlapping Baseband Pulses", *IEEE Trans. Comm.*, Vol. COM-25, pp 523-530, May 1977

[46] V.K. Prabhu, "PSK-Type Modulation with Overlapping Baseband Pulses", *IEEE Trans. Comm.*, Vol. COM-25, pp 980-990, Sept. 1977

[47] M.C. Austin, M.V. Chang, "Quadrature Overlapped Raised-Cosine Modulation", *IEEE Trans. Comm.*, Vol. COM-29, pp 237-249, Mar. 1981

[48] F. Amoroso, "The Use of Quasi-Bandlimited Pulses in MSK Transmission", *IEEE Trans. Comm.*, Vol. COM-27, pp 1616-1624, Oct. 1979

[49] M. Gendron, K. Feher, "Une nouvelle famille de filtre nonlineaire", *Canadian Commun. & Power Conf.*, Montreal, Canada, pp 5-8, Oct. 1978

[50] J.C.Y. Huang, K. Feher, M. Gendron, "Techniques to Generate ISI and Jitter-Free Bandlimited Nyquist Signals and a Method to Analyze Jitter Effects", *IEEE Trans. Comm.*, Vol. COM-27, pp 1700-1711, Nov. 1979

[51] A. Lender, "Correlative Level Coding for Binary Data Transmission", *IEEE Spectrum*, Vol. 3, pp 104-115, Feb. 1966

[52] R. Bracewell, *The Fourier Transform and its Applications*, McGraw-Hill, New York, 1965

[53] R.R. Anderson and J. Salz, "Spectra of Digital FM", *Bell Syst. Tech. J.*, Vol. 44, pp 1165-1189, Jul.-Aug. 1965

[54] K. Feher, *Filter: Nonlinear Digital*, Canadian and U.S. Patent Disclosure, Canada No. 372-365, May 10, 1979, U.S. No. 119899, Feb. 1980

[55] W.C. Lindsey, M.K. Simon, *Telecommunication Systems Engineering*, Prentice-Hall, Inc., New Jersey, 1973

[56] R. Bracewell, *The Fourier Transform and its Applications*, McGraw Hill, New York, 1965

[57] J.H.H. Chalk, "The Optimum Pulse Shape for Pulse Communication", *Proc. IEE*, Vol. 97, No. 3, pp 88-92, Mar. 1950

[58] D. Slepian, E. Sonnenblick, "Eigenvalues Associated with Prolate Spheroidal Wave Functions of Zero Order", *BSTJ*, Vol. 44, No. 8, pp 1745-1959, Oct. 1965

[59] K.H. Mueller, "A New Approach to Optimum Pulse Shaping in Sampled Systems Using Time-Domain Filtering", *BSTJ*, Vol. 52, No. 5, pp 723-729, May-Jun. 1973

[60] K. Feher, R. deCristofaro, "Transversal Filter Design and Application in Satellite Communications", *IEEE Trans. on Communications*, pp 1262-1267, Nov. 1976

[61] T. Le-Ngoc, K. Feher, "Power and Bandwidth Efficient ISI-and-Jitter-Free (IJF) Transmission Techniques for Linear and Nonlinear Channels", *ICC '1981*, Denver, Colorado, Jun. 14-18, 1981

[62] Intelsat, *SCPC/PSK (40) and SCPC/PCM/PSK (40) System Specification*, BG-9-21E H/5/74 (rev. 2), Oct. 20, 1976

[63] G. Forney, "Maximum-Likelihood Sequence Estimation of Digital Sequences in the Presence of Intersymbol Interference", *IEEE Transactions on Information Theory*, Vol. IT-18, pp 363-378, May 1972

[64] R.C. Titsworth, L.R. Welch, "Power Spectra of Signals Modulated by Random and Pseudo-Random Sequences", *Technical Report No. 32-440*, Jet Propulsion Laboratory, Oct. 1961

[65] T. Le-Ngoc, K. Feher, H. Pham Van, "New Modulation Techniques for Low-Cost Power and Bandwidth Efficient Satellite Earth Stations", *IEEE Trans. on Comm.*, Vol. COM-30, pp 275-283, Jan. 1982

[66] T. Le-Ngoc, P. Vandamme, K. Feher, "Spectral Properties of IJF-OQPSK and PR-IJF-OQPSK Signals", *ICC '82*, Philadelphia, Jun. 13-17, 1982

[67] T. Le-Ngoc, K. Feher, "A New Class of IJF-OQPSK Modems for Regenerative Satellite Systems", *ICC '81*, Denver, Colorado, Jun. 14-18, 1981

[68] T. Le-Ngoc, K. Feher, "Performance of New IJF-OQPSK Modulation Schemes in the Presence of Noise, Inter-channel and Co-channel Interference", *NTC '81*, New Orleans, Louisiana, Nov. 29-Dec. 3, 1981

[69] P. Vandamme, T. Le-Ngoc, K. Feher, "Performance of IJF-OQPSK and PR-IJF-OQPSK Modems in a Nonlinear Multi-Channel Environment", *ICC '82*, Philadelphia, Jun. 13-17, 1982

[70] C.A. Belfiore & J.H. Park, "Decision Feedback Equalization", *Proceedings of IEEE*, Vol. 67, No. 8, pp 1143-1156, Aug. 1979

[71] K. Feher, *Digital Communications: Microwave Applications*, Prentice-Hall, Inc., Englewood Cliffs, N.J., 1981

[72] K. Feher, *Digital Modulation Techniques in an Interference Environment*, Vol. 9 of the EMC Encyclopedia, Don White Consultants, Inc., Gainesvilles, VA 1977

[73] *Intelsat TDMA/DSI Specification*, BG-42-65E, June 26, 1980.

[74] D.H. Morais, K. Feher, "The Effects of Filtering and Limiting on the Performance of PQSK, Offset QPSK and MSK Systems", *IEEE Trans. on Comm.*, Vol. COM-28, No. 12, pp 1999-2009, Dec. 1980

[75] S.J. Campanella, F. Assal, A. Berman, "Onboard Regenerative Repeater", *ICC 1977 Conference Record*, pp 6.2.121-125

[76] K. Feher, T. Le-Ngoc, R. Clewer, A. Guibord, "Fast acquisition methods for high-speed QPSK and OQPSK satellite systems", *International Electrical, Electronics Conference and Exposition*, Toronto, Oct. 2-4, 1979

[77] T. Le-Ngoc, K. Feher, "A digital approach to symbol timing recovery systems", *IEEE Canadian Communications and Power Conference*, Montreal, Oct. 15-18, 1980

[78] T. Le-Ngoc, K. Feher, "A Cost-Effective Modulation Technique for Digital Microwave Systems", *IEEE & E*, Toronto, Oct. 5-7, 1981

[79] P. Vandamme, T. Le-Ngoc, K. Feher, "Receiver Optimization for IJF and PR-IJF Signals", *GLOBECOM'82*, Miami, Nov. 29 - Dec. 2, 1982

[80] T. Le-Ngoc, K. Feher, "Power and Bandwidth Efficient Modulation Techniques", *GLOBECOM '82*, Miami, Nov. 29 - Dec. 2, 1982

[81] T. Le-Ngoc, K. Feher, "A Bandwidth-Efficient ISI-Controlled Binary Transmission Technique", *Canadian Communications and Energy Conference*, Montreal, Oct. 13-15, 1982

[82] P. Vandamme, T. Le-Ngoc, K. Feher, "Performance of IJF-OQPSK and Partial-Response (PR)-IJF-OQPSK Modems in a Nonlinearly Amplified and Adjacent-Channel Satellite Interference Environment", *IEEE Journal on Selected Areas in Communications*, special issue on Digital Satellite Communications, Jan. 1983

[83] T. Le-Ngoc, K. Feher, "Performance of IJF-OQPSK Modulation Schemes in a Complex Interference Environment", *IEEE Trans. on Commun.*, Jan. 1983

[84] T. Le-Ngoc, K. Feher, "Performance of an IJF-OQPSK Modem in Cascaded Nonlinear and Regenerative Satellite Systems", *IEEE Trans. on Commun.*, Feb. 1983

[85] T. Le-Ngoc, K. Feher, "A digital approach to symbol timing recovery systems", *IEEE Trans. Communication*, pp 1993-1999, Dec. 1980

[86] H. Yamamoto, K. Hirade, Y. Watanabe, "Carrier Synchronizer for Coherent Detection of High-Speed Four-Phase-Shift-Keyed Signals", *IEEE Trans. Commun.*, pp 803-807, Aug. 1972

[87] F.M. Gardner, *Phaselock Techniques*, 2nd Ed., New York, Wiley, 1979

[88] F.M. Gardner, "Self-noise in Synchronizers", *IEEE Trans. Commun.*, pp 1159-1163, Aug. 1980

[89] K. Feher, *Digital Communications: Satellite/Earth Station Engineering*, Englewood-Cliffs, N.J., Prentice-Hall, Dec. 1982

[90] F.M. Gardner, *Carrier and clock synchronization for TDMA digital communications*, ESATM-169 (ESTEC), Dec. 1976

APPENDIX:
LISTINGS AND DESCRIPTIONS OF MAJOR SIMULATION ROUTINES

SUMMARY:

This appendix includes the listings and descriptions of major routines used for simulating IJF-QPSK and IJF-Offset QPSK systems.

Section A1 describes the subroutines which represent basic portions of a communications system such as modulator, demodulator, filter, nonlinear devices..., as well as the signal processing procedures.

Section A2 presents two examples of the main programs to illustrate the use of simulation subroutines described in Section A1.

A.1 LISTINGS AND DESCRIPTIONS OF SIMULATION ROUTINES

A.1.1 General descriptions:

A modulated signal can be represented in the time domain by

$$y(t) = \mathrm{Re}\{z(t) \cdot e^{-j\omega_c t}\} \qquad (A.1)$$

where ω_c is the RF carrier frequency
and $z(t)$ is the complex envelope of $y(t)$.

The complex envelope $z(t)$ can be written as

$$z(t) = x_I(t) + jx_Q(t) \qquad (A.2)$$

where $x_I(t)$ and $x_Q(t)$ denote the in-phase and quadrature baseband components of the modulated signal $y(t)$ respectively.

The modulated signal, $y(t)$, is represented by its complex envelope, $z(t)$, in the simulation routines. This representation allows RF elements to be translated to baseband with retention of their RF amplitude and phase characteristics.

Channel filters are represented by their equivalent complex baseband frequency responses. The 0Hz point denotes the center frequency (which is also the carrier frequency).

Filtering process is performed by multiplication in the frequency domain with the aid of Fast Fourier Transform, i.e., the complex envelope of the filtered signal is given by

$$z'(t) = FFT^{-1}\{H(j\omega) \cdot FFT(z(t))\} \qquad (A.3)$$

where

- $z(t)$: Complex envelope of the filter input signal
- $H(j\omega)$: Equivalent complex baseband frequency response of the filter
- FFT: Fast Fourier Transform
- FFT^{-1}: Inverse Fast Fourier Transform

A.1.2 Signal Generation Routines

(a) Descriptions:

IJF-QPSK or IJF-Offset QPSK signals are generated by subroutine LOAD4 and its associated subroutine PULSE and function F(x). The in-phase and quadrature transmitted sequences, IPNI and IPNQ, are generated by two parallel shift registers of seven taps. The generating equation is

$$x_n = x_{n-7} \oplus x_{n-6}$$

Each shift register produces a pseudo-random sequence of 127 symbols with 16 samples per symbol (LSAMPL), i.e. the total number of samples per sequence is 2032. Since this total number of

samples should be an integer power of two for the Fast Fourier Transform (FFT), the first 16 samples are loaded into the last 16 samples to form a total number of 2048 samples for each sequence. The samples are loaded in the form of complex NRZ data (DATA) with the real part corresponding to the in-phase component and the imaginary part corresponding to the quadrature component.

The transmitted sequences, IPNI and IPNQ are stored to be used in the detection procedure (subroutine DECOD4). The input parameter IOFF can be either 0 or 8. IOFF=0 corresponds to QPSK schemes while IOFF=8 corresponds to Offset QPSK schemes.

Subroutine LOAD4 invokes the subroutine PULSE and function F(x) to generate the IJF double-interval sampled pulse P which is represented by

$$s(t) = \frac{1}{2}(1+\cos\frac{\pi t}{T_s}) \quad , \quad |t| \leq T_s$$

The pulse P has 48 samples defined as follows

$$P(i) = 0 \quad \text{for} \quad i=1,2,\ldots,8$$

$$P(i) = s([(i-25)+\tfrac{1}{2}]\Delta t)$$

$$\text{for} \quad i=25, 26, \ldots, 40$$

$$P(i) = s([i-24]-\tfrac{1}{2}]\Delta t)$$

$$\text{for} \quad i=9,10,\ldots, 24$$

where $\Delta t = T_s/16$

The complex data array (DATA) is properly multipled by the sampled pulse P to form the transmitted IJF-QPSK or IJF-Offset QPSK signal.

(b) Listings:

```
C*************************************************************
C      THIS SUBROUTINE GENERATES AN EQUIVALENT BASEBAND QPSK
C*************************************************************
C
      SUBROUTINE LOAD4(DATA,IPNI,IPNQ,LSAMPL,LDIM,     IOFF)
      COMPLEX DATA(1)
      DIMENSION NX(7),NY(7),IPNI(1),IPNQ(1),OF(2048),P(48)
      DATA NX(1),NX(2),NX(3),NX(4),NX(5),NX(6),NX(7)/-1,-1,-1,
     =-1,-1,-1,-1/
      DATA NY(1),NY(2),NY(3),NY(4),NY(5),NY(6),NY(7)/-1,-1,1,
     =1,1,1,-1/
      DATA JLAST,JTAP/7,1/
      KKK=2**JLAST
      I=0
      DO 1 K=1,KKK
      IF (I.EQ.JLAST) I=0
      I=I+1
      J=I-JTAP
      IF (I.LE.JTAP) J=J+JLAST
      NX(I)=NX(J)*NX(I)
      NY(I)=NY(J)*NY(I)
      IPNI(K)=NX(I)
1     IPNQ(K)=NY(I)
      CALL PULSE(P,LSAMPL     )
      DO 2 I=1,KKK
      J1=(I-1)*LSAMPL+1
      J2=I*LSAMPL
      J=0
      DO 3 L=J1,J2
      J=J+1
      L1=I-1
      L2=I+1
      PR=FLOAT(IPNI(I))*P(16+J)
      PQ=FLOAT(IPNQ(I))*P(16+J)
      IF(I.EQ.1) L1=KKK
      PR=PR+FLOAT(IPNI(L1))*P(32+J)
      PQ=PQ+FLOAT(IPNQ(L1))*P(32+J)
      IF(I.EQ.KKK) L2=1
      PR=PR+FLOAT(IPNI(L2))*P(J)
      PQ=PQ+FLOAT(IPNQ(L2))*P(J)
      DATA(L)=CMPLX(PR,0.)
      OF(L)=PQ
3     CONTINUE
2     CONTINUE
      DO 4 I=1,LDIM
      L=I+IOFF
      IF(L.GT.LDIM) L=L-LDIM
4     DATA(I)=DATA(I)+CMPLX(0.,OF(L))
      RETURN
      END
```

```
C*************************************************
C THIS SUBROUTINE STORES THE PULSE SAMPLES.
C*************************************************
      SUBROUTINE PULSE(P,LSAMPL     )
      DIMENSION P(1),Q(48)
      D=1./FLOAT(LSAMPL)
      K=2*LSAMPL
      KK=3*LSAMPL
      DO 10 I=1,KK
10    P(I)=0.
      DO 20 I=1,K
      AI=FLOAT(I-1)*D+(D/2.)-1.
20    P(I+8)=F(AI     )
      RETURN
      END
C
```

```
C*************************************************
C THIS SUBROUTINE DEFINES THE BASEBAND PULSE SHAPE
C*************************************************
      FUNCTION F(X   )

      B=(3.14159*ABS(X)-3.14159/2.)

      F=.5*(1.-SIN(B)   )
      RETURN
      END
```

A.1.3 Detection Filter Definition Routine

(a) Descriptions:

Subroutine RCOS generates the equivalent complex baseband frequency response of the raised-cosine type filter presented in Chapter 3.

- Input Variables
  - SBANDW: Sampling frequency (16 x symbol rate)
  - FBANDW: Nyquist frequency (symbol rate/2)
  - LDIM: Number of samples (2048)
  - ALPHA: Roll-off factor (α)
  - FOF: Frequency offset
- Output Variable
  - TF: Transfer function of the raised-cosine type filter (as shown in Fig. 3.15a)

The filter transfer function is presented in a sampled form (TF). The frequency difference between two samples is

Δf = symbol rate/128

TF(1) represents the filter response at the center frequency (f_c) and normalized to 1.

TF(i) represents the filter response at frequency $[f_c+(i-1)\Delta f]$ for i=2,3,...,1025.

TF(k) represents the filter response at frequency $[f_c-(2049-k)\Delta f]$ for k=1026, 1027, ... , 2048.

(b) Listing:

```
C*************************************************************************
C     RAISED COSINE FILTER WITH ARBITRARY ALPHA AND SHAPE CORRECTION
C*************************************************************************
      SUBROUTINE RCOS(SBANDW,FBANDW,TF,ALPHA,LDIM     ,FOF)
       COMPLEX TF(1)
      COMPLEX XX
C******* FF(X) IS THE INVERSE BASEBAND SPECTRUM
C
      FF(X)=2.*X*(1.-(4./(3.141592**2))*(X**2))/SIN(2.*X)
C
      NO=LDIM/2
      NO1=NO+1
       IF (ALPHA.EQ.0) ALPHA=0.0001
      FN=LDIM*(FBANDW/SBANDW)
      F1=(1.-ALPHA)*FN
      F2=(1.+ALPHA)*FN
      IFN=IFIX(FN)
      IF1=IFIX(F1)+1
      IF2=IFIX(F2)+1
       A1=3.141592/(2.*FLOAT(IFN))
      TF(1)=CMPLX(1.0,0.0)
      DO 8 I=2,IF1
       J=I-1
      A2=(FLOAT(J)*A1)
      A2=FF(A2     )
C
      TF(I)=CMPLX(A2,0.0)
    8 CONTINUE
      JK=IF1+1
      DO 9 J=JK,IF2
       I=J-1

        BBB=FN
                        A3=2.

        IF(I.NE.BBB) A3=FF(FLOAT(I)*A1     )
C
      A=(3.141592/(2.0*ALPHA))*((FLOAT(I)/FLOAT(IFN))-1.)
      TF(J)=CMPLX(0.5*(1.0-SIN(A)),0.0)
       TF(J)=TF(J)*CMPLX(A3,0.0)
    9 CONTINUE
      JH=IF2+1
      DO 10 I=JH,NO1
      TF(I)=CMPLX(0.0,0.0)
   10 CONTINUE
```

```
      NO2=NO1+1
      DO 5 I=NO2,LDIM
      TF(I)=TF(LDIM+2-I)
5     CONTINUE
      IFOF=IFIX(FOF*FLOAT(LDIM)/SBANDW)
      IF(IFOF.EQ.0)  RETURN
      IF(IFOF.LT.0) GO TO 50
      DO 20 K=1,IFOF
      XX=TF(LDIM)
      JJ=LDIM-1
      DO 30 I=1,JJ
      TF(LDIM+1-I)=TF(LDIM-I)
30    CONTINUE
      TF(1)=XX
20    CONTINUE
      RETURN
50    IFOF=-IFOF
      JJ=LDIM-1
      DO 70 K=1,IFOF
      XX=TF(1)
      DO 60 I=1,JJ
60    TF(I)=TF(I+1)
      TF(LDIM)=XX
70    CONTINUE
      RETURN
      END
```

A.1.4 Filtering Routine:

(a) Descriptions:

Subroutine FILTER simulates the filtering process

- Input Variables
  - SIGNAL: Sampled signal to be filtered
  - TF: Transfer function of the filter
  - LDIM: Number of samples (2048)
- Output Variables
  - SIGNAL: Filtered sampled signal

$$SIGNAL = FFT^{-1}\{TF * FFT\{SIGNAL\}\}$$

FFT and FFT^{-1} are the direct and inverse Fast Fourier Transforms respectively. They are performed by the library subroutine FFT2C.

(b) Listing:

```
C*************************************************************
C      THE FOLLOWING SUBROUTINE PERFORMS THE FILTERING
C      PROCESS ON THE DATA SEQUENCE.
C*************************************************************
C
       SUBROUTINE FILTER(SIGNAL,TF,LDIM)
       COMPLEX SIGNAL(1),TF(1)
       DIMENSION IWK(12)
       CALL FFT2C(SIGNAL,11,IWK)
       DO 1 I=1,LDIM
     1 SIGNAL(I)=CONJG(SIGNAL(I)*TF(I))
       CALL FFT2C(SIGNAL,11,IWK)
       DO 2 I=1,LDIM
     2 SIGNAL(I)=CONJG(SIGNAL(I))/FLOAT(LDIM)
       RETURN
       END
```

A.1.5 Transmitted Energy Computation Routine

(a) Descriptions:

Subroutine ENERGY computes the energy per bit E_b, of the transmitted signal x(t):

$$E_b = T_b \cdot \{\lim_{T\to\infty} \frac{1}{2T} \int_{-T}^{+T} |x(t)|^2 \, dt\}$$

* Input Variables:

- DATA: Transmitted signal x(t)

- BAUD: Symbol rate (1/2 T_b)

* Output Variable

- EB: E_b

$$EB = \frac{1}{2048} \{\sum_{i=1}^{2048} |DATA(i)|^2\}/(2*BAUD)$$

(b) Listing:

```
C*************************************************************
C CALCULATE EB
C *************************************************************
            SUBROUTINE ENERGY(DATA,EB,BAUD)
            COMPLEX DATA(1)
            WATTS=0.
            DO 1 I=1,2048
            WATTS=WATTS+((CABS(DATA(I)))**2.)
      1     CONTINUE
            WATTS=WATTS/2048.
            EB=WATTS/(2.*BAUD)
            WRITE (6,40) WATTS,EB
     40     FORMAT(10X,*ENERGY PER BIT*,F15.6,5X,E15.8)
            RETURN
            END
```

A.1.6 Noise Power Computation Routine

(a) Descriptions:

Subroutine HHGG computes the normalized noise power at the output of the receive detection filter

$$\sigma_n^2 = \frac{N_o}{2} \int_{-\infty}^{+\infty} |H(f)|^2 df$$

The power spectral density of the additive white gaussian noise, N_o, is normalized to unity.

. Input Variables

- TF: Filter response representing H(f)
- SBANDW: Sampling frequency
- LDIM: Number of samples (2048)
- LSAMPL: Number of samples/symbol

. Output Variable

- PNOISE: Normalized noise power

$$PNOISE = \frac{1}{2} \sum_{i=1}^{2048} |TF(i)| \cdot \Delta f$$

Δf = SBANDW/LDIM

SBANDW = 16 * (symbol rate)

(b) Listing:

```
C*************************************************************
C      THIS SUBROUTINE COMPUTES THE EFFECTIVE NOISE (PNOISE)
C      AT THE OUTPUT OF THE RECEIVE FILTER
C*************************************************************
C
      SUBROUTINE HHGG(TF,PNOISE,LSAMPL,LDIM,SBANDW)
      COMPLEX TF(1)
      SUM=0.0
      DO 1 L=1,LDIM
      HH=(CABS(TF(L)))**2
    1 SUM=SUM+HH
      PNOISE=SUM*SBANDW/FLOAT(LDIM)/2.
      WRITE (6,2) PNOISE
    2 FORMAT(5X,*PNOISE=*,F7.3,/)
      RETURN
      END
```

A.1.7 Bit Error Rate Computation Routine

(a) Descriptions

Subroutine DECOD4 simulates the quadrature demodulation and detection processes and computes the probability of bit error versus E_b/N_o.

The subroutine searches for the best sampling point corresponding to the lowest error probability.

The error probability is given by

$$P_e = \frac{1}{254} \{ \sum_{i=1}^{127} (P_{eQi} + P_{eIi}) \}$$

where

$$P_{eIi} = \frac{1}{2} \text{ erfc } (\frac{A_i}{\sigma\sqrt{2}})$$

$$P_{eQi} = \frac{1}{2} \text{ erfc } (\frac{B_i}{\sigma\sqrt{2}})$$

If A_i, B_i have the same signs as the i^{th} transmitted I,Q symbols

or

$$P_{eIi} = 1 - \frac{1}{2} \text{ erfc } (\frac{A_i}{\sigma\sqrt{2}})$$

$$P_{eQi} = 1 - \frac{1}{2} \text{ erfc } (\frac{B_i}{\sigma\sqrt{2}})$$

if A_i, B_i have the opposite signs to the i^{th} transmitted I,Q symbols.

A_i, B_i are the sampled values of the $i^{\underline{th}}$ symbols of the received I,Q baseband signals.

$$\sigma = \sqrt{PNOISE * EB * ratio}$$

PNOISE and EB are obtained from subroutines HHGG and ENERGY respectively,

$$ratio = 10^{-M/10}$$

M is a given E_b/N_o.

(b) Listing:

```
      SUBROUTINE DECOD4(DATA,LSAMPL,PNOISE,IPNI,IPNQ,NSYMB,
     1EBNO,PEI,NSNR,EB,ioff)
*****************************************************************
*                                                               *
*     THE FOLLOWING SUBROUTINE DECODES THE RECEIVED DATA        *
*                                                               *
*****************************************************************
C
      DIMENSION EBNO(50),PEI(50),IPNI(128),IPNQ(128)
      COMPLEX DATA(2048),AMP
      NERROR=0
C
C     synchronize the received data
C
        ldim=2048
        nold=0
        nof=0
        k=1


        IF(IOFF.EQ.0)GO TO 300
        DO 301 I=1,IOFF
        XX=AIMAG(DATA(LDIM))
        DO 302 J=2,LDIM
        JJ=LDIM+2-J
        DATA(JJ)=CMPLX(REAL(DATA(JJ)),AIMAG(DATA(JJ-1)))
302     CONTINUE
        DATA(1)=CMPLX(REAL(DATA(1)),XX)
301     CONTINUE
300     continue
        new=0
        do 200 j=1,nsymb
        j1=k+(j-1)*lsampl
        if(j1.gt.ldim)j1=j1-ldim
        xb=real(data(j1))
        yb=aimag(data(j1))
        if(sign(1.,xb).eq.ipni(j))new=new+1
        if(sign(1.,yb).eq.ipnq(j))new=new+1
200     continue

        if(nold.ge.new)go to 399
        nold=new
        nof=k

399     k=k+1

        if(nold.le.nsymb.and.k.le.ldim)go to 300
        if(nof.eq.0) go to 230
        lo=ldim-1

        do 250 i=1,nof
        amp=data(1)

        do 240 j=1,lo
        data(j)=data(j+1)
240     continue
```

```
      data(ldim)=amp
250   continue

230   mi=1

      eoi=2000.
      snr=pnoise*eb/5.
      sigma=sqrt(snr)
      do 110 j=1,16
      ei=0.

      do 100 k=1,nsymb
      j1=(k-1)*lsampl+j
      j11=j1+1

      if(j11.gt.ldim)j11=j11-ldim
      axbar=(real(data(j1))+real(data(j11)))/2.
      aybar=(aimag(data(j1))+aimag(data(j11)))/2.
      if(sign(1.,axbar).ne.ipni(k))ei=ei+1
      if(sign(1.,aybar).ne.ipnq(k))eq=eq+1
      argi=abs(axbar)/sigma
      argq=abs(aybar)/sigma
      ei=ei+erfc(argi)/2.+erfc(argq)/2.
100   continue

      if(eoi.le.ei) go to 110
      eoi=ei
      mi=j

110   continue

      off=float(ioff)/16.
      write(6,160) off
160   format(5x,'sampling points for i and q channels differ
     !  by',f6.1,'  of the symbol interval',/)

      noff=nof+mi
      off=float(noff)/16.-.5
      write(6,161) off
161   format(5x,'received data is delayed by',f6.1,' symbols',


      do 2 k=1,nsymb
      ji=(k-1)*lsampl+mi
      jii=ji+1
      if(ji.gt.ldim)ji=ji-ldim
      if(jii.gt.ldim)jii=jii-ldim
      axbar=(real(data(ji))+real(data(jii)))/2.
      aybar=(aimag(data(ji))+aimag(data(jii)))/2.
      indexx=0
      if(sign(1.,axbar).ne.ipni(k))indexx=1
      indexy=0
      if(sign(1.,aybar).ne.ipnq(k))indexy=1
      if((indexx.eq.1.).or.(indexy.eq.1))nerror=nerror+1
```

```
c       compute the probability of error for this symbol.

        do 4 m=1,nsnr
        xm=(6+.2*float(m))/10.
        snr=pnoise*eb/(10.**xm)
        sigma=sqrt(snr)
        arg=(abs(axbar))/(sigma*sqrt(2.))
        if(arg.gt.12)arg=12

        ex=erfc(arg)/2.
        if(indexx.eq.1)ex=1-ex

        arg=(abs(aybar))/(sigma*sqrt(2.))
        if(arg.gt.12) arg=12.
        ey=erfc(arg)/2.
        if(indexy.eq.1) ey=1-ey
        if(ex.lt.1.e-15)ex=0
        if(ey.lt.1.e-15)ey=0
4       pei(m)=pei(m)+((ex+ey)/2.)
2       continue

        do 5 i=1,nsnr
        pei(i)=pei(i)/float(nsymb)
5       ebno(i)=6+.2*float(i)

        write(6,150)
150     format(5x,' eb/no',10x,'prob. of error ',/)
        write(6,151)(ebno(i),pei(i),i=1,nsnr)
151     format(5x,f5.1,10x,e13.6)
        write(6,152) nerror
152     format(/,5x,' errors= ',i5,/)

c  centering the eye diagram

        if (mi.eq.7) go to 555
        if(mi.lt.7)mi=7-mi
        if(mi.gt.7)mi=23-mi
        if(mi.eq.0)mi=mi+1

        do 550 i=1,mi
        amp=data(ldim)
        do 551 j=1,lo
        jj=ldim-j+1
        data(jj)=data(jj-1)
551     continue
        data(1)=amp
550     continue
555     continue

        return
      END
```

A.1.8 Hardlimiting Process Routine

(a) Descriptions

Subroutine HLIM simulates the ideal hardlimiter using the following equation

$$z' = \frac{z}{|z|}$$

where

$z = x + jy$: input signal

$z' = x' + jy'$: output signal

- Input Variables
  - DATA: Input sampled signal of the hardlimiter
  - LDIM: Number of samples (2048)
- Output Variables
  - DATA: Output signal of the hardlimiter

(b) Listing:

```
C*************************************************
C THIS SUBROUTINE SIMULATES A HARD LIMITER
C*************************************************
      SUBROUTINE HLIM(DATA,LDIM)
      COMPLEX DATA(1)
      DO 10 I=1,LDIM
10    DATA(I)=DATA(I)/CABS(DATA(I))
      RETURN
      END
```

A.1.9 Signal Power Computation Routine

(a) Description:

Subroutine POWER computes the mean power (MP) of the signal (DATA)

$$MP = \frac{1}{2} \cdot \frac{1}{2048} \left\{ \sum_{i=1}^{2048} |DATA(i)|^2 \right\}$$

i.e.

$$P_{mean} = \frac{1}{2} \left\{ \lim_{T \to \infty} \frac{1}{2T} \int_{-T}^{+T} |s(t)|^2 \, dt \right\}$$

(b) Listing:

```
      SUBROUTINE POWER(DATA,LDIM,MP,PF)
      COMPLEX DATA(1)
       REAL MP
      PF=0.
      MP=0.0
      DO 10 I=1,LDIM
      MP=MP+((CABS(DATA(I)))**2.)
      IF(PF.LT.CABS(DATA(I))) PF=CABS(DATA(I))
   10  CONTINUE
       MP=MP/FLOAT(LDIM)/2.
      PF=(PF**2.)/MP
      PF=10.*ALOG10(PF)
      RETURN
        END
```

A.1.10 Nonlinear Device Simulation Routines

(a) Descriptions:

Subroutines HPA and TWT simulate the nonlinear characteristics of the HPA and TWT obtained from the data in Table 2 of attachement "INTELSAT TDMA/DSI system specifications" (BG-42-65E, June 1980).

The non-linearities can be described by two polynomials $p(r)$ and $q(r)$ so that if the input modulated signal is written as*

$$z_i(t) = [x(t)+jy(t)]e^{j\omega_c t}, \quad \omega_c: \text{ carrier frequency}$$

then the output signal of the non-linear device is

$$z_o(t) = [x'(t)+jy'(t)]e^{j\omega_c t}$$

where

$$x'(t) = x(t)p(r(t))-y(t)q(r(t))$$

$$y'(t) = x(t)q(r(t))+y(t)p(r(t))$$

and

$$r(t) = \sqrt{x^2(t)+y^2(t)} \quad : \text{ the envelope of incoming signal.}$$

AM/AM is represented by $\sqrt{(rp(r))^2+(rq(r))^2}$

and AM/PM is represented by $\tan^{-1}(\frac{q(r)}{p(r)})$.

The polynomials $rp(t)$ and $rq(t)$ are expressed as

$$rq(r) = \sum_{i=1}^{M} a_{2i-1} r^{2i-1}$$

and

$$rq(r) = \sum_{i=1}^{M} b_{2i-i} r^{2i-1}$$

where M is the order of polynomial, and all even coefficients are zero. The odd coefficients are determined using a polynomial fitting routine and are given in routines HPA and TWT.

The mean power is normalized such that the output power is unity at the 0 dB input/output backoff point. This normalization makes the scheme independent of the absolute saturated power of the devices. For the device operated at Q, dB backoff (BAKOFF), the normalized input signal becomes

$$z_i^N(t) = \frac{z_i(t)}{\sqrt{P}} .10^{-Q/10}$$

where P is the mean power (MP) of the input signal (DATA) calculated by subroutine POWER.

Input Variables: - DATA, LDIM, BAKOFF, MP

Output Variables: - DATA, PSHIFT

---

* M.J. Eric, "Intermodulation Analysis of Nonlinear Devices for Multiple Carrier Inputs", CRC Report No. 1234, Ottawa, Nov. 1972.

(b) Listing:

```
C*******************************************************
C      THIS SUBROUTINE SIMULATES THE EQUIVALENT BASEBAND
C      NONLINEARITY
C*******************************************************
C
       SUBROUTINE HPA(DATA,LDIM,BAKOFF,PSHIFT,MP1)
       COMPLEX DATA(1)
        REAL MP1
       DATA ZPMAX,ZQMAX,VMAX,VO/1.068,0.928,1.414,1./
       DATA A1,A3,A5,A7,A9,A11,A13,A15,A17/1.916288,-9.358132E-1,
      =1.942392E-1,-2.832262E-2,1.840305E-2,-4.282407E-3,0.0,0.0,0.0
       DATA B1,B3,B5,B7,B9,B11,B13,B15,B17/-5.9659E-2,1.907669,
      =-1.846724,8.615552E-1,-1.990954E-1,1.815157E-2,0.0,0.0,0.0/
       P(X)=((((((((A17*X**2+A15)*X**2+A13)*X**2+A11)*X**2+A9)*
      =X**2+A7)*X**2+A5)*X**2+A3)*X**2+A1
       ZP(X)=P(X)*X
       Q(X)=((((((((B17*X**2+B15)*X**2+B13)*X**2+B11)*X**2+B9)*
      =X**2+B7)*X**2+B5)*X**2+B3)*X**2+B1
       ZQ(X)=Q(X)*X
       Z(X)=SQRT(ZP(X)**2+ZQ(X)**2)
       TWTIN=VO*10.**(-BAKOFF/20.)
       TWTOUT=Z(TWTIN)
       PSHIFT=ATAN(ZQ(TWTIN*1.414)/ZP(TWTIN*1.414))
       WRITE (6,2) TWTIN,TWTOUT,PSHIFT
     2  FORMAT(5X,*TWTIN=*,F10.6,*  TWTOUT=*,F10.6,*  PSHIFT=*,F10.6
       FNORMI=TWTIN/SQRT(MP1)
          DO 11 I=1,LDIM
          DATA(I)=DATA(I)*FNORMI
    11     CONTINUE
       DO 10 I=1,LDIM

       X=REAL(DATA(I))
       Y=AIMAG(DATA(I))
       R=SQRT(X**2+Y**2)
       IF(R.GT.VMAX) GOTO 12
       DATA(I)=CMPLX(P(R)*X-Q(R)*Y,P(R)*Y+Q(R)*X)

       GO TO 10
    12  DATA(I)=CMPLX(ZPMAX*X-ZQMAX*Y,ZQMAX*X+ZPMAX*Y)/R

    10  CONTINUE
       RETURN
       END
```

```
      SUBROUTINE TWT(DATA,LDIM,BAKOFF,PSHIFT,MP2)
      COMPLEX DATA(1)
       REAL MP2,MPO
      DATA ZPMAX,ZQMAX,VMAX,VO/.986,1.017,1.414,1./
      DATA A1,A3,A5,A7,A9,A11,A13,A15,A17/2.185509,-1.934083,
     =9.807836E-1,-2.313386E-1,1.963255E-2,0.0,0.0,0.0,0.0/
      DATA B1,B3,B5,B7,B9,B11,B13,B15,B17/2.641891E-1,1.338875,
     =-9.973087E-1,2.675812E-1,-2.400961E-2,0.0,0.0,0.0,0.0/

       P(X)=((((((((A17*X**2+A15)*X**2+A13)*X**2+A11)*X**2+A9)*
     =X**2+A7)*X**2+A5)*X**2+A3)*X**2+A1
       ZP(X)=P(X)*X
       Q(X)=((((((((B17*X**2+B15)*X**2+B13)*X**2+B11)*X**2+B9)*
     =X**2+B7)*X**2+B5)*X**2+B3)*X**2+B1
       ZQ(X)=Q(X)*X
       Z(X)=SQRT(ZP(X)**2+ZQ(X)**2)
       TWTIN=VO*10.**(-BAKOFF/20.)
       TWTOUT=Z(TWTIN)
       PSHIFT=ATAN(ZQ(TWTIN*1.414)/ZP(TWTIN*1.414))
       WRITE (6,2) TWTIN,TWTOUT,PSHIFT
  2    FORMAT(5X,*TWTIN=*,F10.6,*   TWTOUT=*,F10.6,*   PSHIFT=*,F10.6
       FNORMI=TWTIN/SQRT(MP2)
            DO 11 I=1,LDIM
            DATA(I)=DATA(I)*FNORMI
 11         CONTINUE
            CALL POWER(DATA,LDIM,MPN)
100       FORMAT(10X,F15.6)
       DO 10 I=1,LDIM
       X=REAL(DATA(I))
       Y=AIMAG(DATA(I))
       R=SQRT(X**2+Y**2)
       IF(R.GT.VMAX) GOTO 12
       DATA(I)=CMPLX(P(R)*X-Q(R)*Y,P(R)*Y+Q(R)*X)

       GO TO 10
 12    DATA(I)=CMPLX(ZPMAX*X-ZQMAX*Y,ZQMAX*X+ZPMAX*Y)/R

 10    CONTINUE
       RETURN
       END
```

A.1.11 Power Spectrum Computation Routine

(a) Descriptions:

Subroutine SPECT computes the power spectrum of the signal (SIGNAL) by using the routine FTFPS of the IMSL library.

SIGNAL is loaded in such a way that Q channel samples follow I channel samples so that the total number of samples used for calculation is 4096. SIGNAL is sub-divided into 32 sections. Each section contains 128 points. The routine FTFPS uses the Parzen window in the computation of the power spectrum.

The trapezoidal rule for integration is used to find the area under the curve (total power normalized to 1). The output gives normalized power spectrum.

Input Variables

- SIGNAL, LDIM, IOFF

Output Variables

- PO

(b) Listing:

```
C*************************************************************
C       THIS SUBROUTINE COMPUTES THE POWER SPECTRUM
C*************************************************************
      SUBROUTINE SPECT(SIGNAL,LDIM,PO,IOFF)
      COMPLEX SIGNAL(2048)
      COMPLEX CWK(130)
      DIMENSION X(4096),PO(65),IWK(7),WK(64),TPO(65)
      S=0.
      DO 10 I=1,LDIM
      L=I-IOFF
      IF(L.LE.0) L=L+LDIM
      X(I)=REAL(SIGNAL(I))
      X(I+2048)=AIMAG(SIGNAL(L))
10    S=S+X(I)+X(I+2048)
      S=S/FLOAT(4096)
      DO 20 I=1,4096
20    X(I)=X(I)-S
      CALL FTFPS(X,Y,4096,128,0,PO,PSY,XPS,IWK,WK,CWK,IER)
      PMAX=PO(1)
      DO  30 I=1,65
30    TPO(I)=-10.*ALOG10(PO(I)/PMAX)
      WRITE(6,1) (TPO(I),I=1,65)
      TPO(65)=PO(65)
      DO 40 I=1,63
40    TPO(65-I)=TPO(66-I)+2.*PO(65-I)
      TPO(1)=TPO(2)+PO(1)
      TPMAX=TPO(1)
      DO 50 I=1,65
50    PO(I)=-10.*ALOG10(PO(I)/TPMAX)
      WRITE(6,2) (PO(I),I=1,65)
2     FORMAT(2X,*NORM. POWER SPECTRUM WITH TOTAL POWER=1*/
     +,10(2X,F6.1))
1     FORMAT(2X,*POWER SPECTRUM*/,10(2X,F6.1))
      RETURN
      END
```

A.1.12 Time Delay Routine

(a) Descriptions

Subroutine TIME introduces to the signal (DATA) a time delay IT.

IT is specified as a multiple number of steps of $T_s/16$ where T_s is the symbol interval.

(b) Listing:

```
C**********************************************
C THIS SUBROUTINE SHIFTS THE SIGNAL
C**********T***********************************
      SUBROUTINE TIME(DATA,IT,LDIM)
      COMPLEX DATA(1),DAT
      DO 10 I=1,IT
      DAT=DATA(1)
      DO 20 J=2,LDIM
20    DATA(J-1)=DATA(J)
10    DATA(LDIM)=DAT
      RETURN
      END
```

A.1.13 Phase Shift Routine

(a) Descriptions:

Subroutine PHASE shifts the phase of the signal (DATA) by a given amount (PSHIFT). PSHIFT is specified in radians.

$$DATA = DATA * e^{-j\ PSHIFT}$$

(b) Listing:

```
C*************************************************************
C  THIS SUBROUTINE COMPENSATES FOR THE PHASE SHIFT
C*************************************************************
      SUBROUTINE PHASE(DATA,PSHIFT,LDIM)
      COMPLEX EPS,DATA(1)
      EPS=CMPLX(COS(PSHIFT),-SIN(PSHIFT))
      DO 10 I=1,LDIM
10    DATA(I)=DATA(I)*EPS
      RETURN
      END
```

A.1.14 Signal Attenuation Routine

(a) Descriptions

Subroutine ATT introduces a given amount of attenuation (AT in dB) on the signal (DATA)

$$DATA = DATA * 10^{-AT/20}$$

(b) Listing:

```
C**********************************************************************
C THIS SUBROUTINE ATTENUATES THE SIGNAL
C**********************************************************************
      SUBROUTINE ATT(DATA,AT,LDIM)
      COMPLEX DATA(1)
      BB=10.**(-AT/20.)
      DO 10 I=1,LDIM
10    DATA(I)=DATA(I)*BB
      RETURN
      END
```

A.2 ILLUSTRATIVE EXAMPLES OF MAIN PROGRAMS

A main program is written to form a simulated system. This main program calls desired subroutines described in the previous section in a proper sequence.

The following examples illustrate the organization of a main simulation program for a given system.

A.2.1 Simulation of a Single-Channel Hardlimited IJF-QPSK System

(a) Descriptions:

Program SINGLE simulates a single-channel hardlimited IJF-QPSK system. Figure A.1 shows the block diagram of the simulation model and corresponding invoking statements.

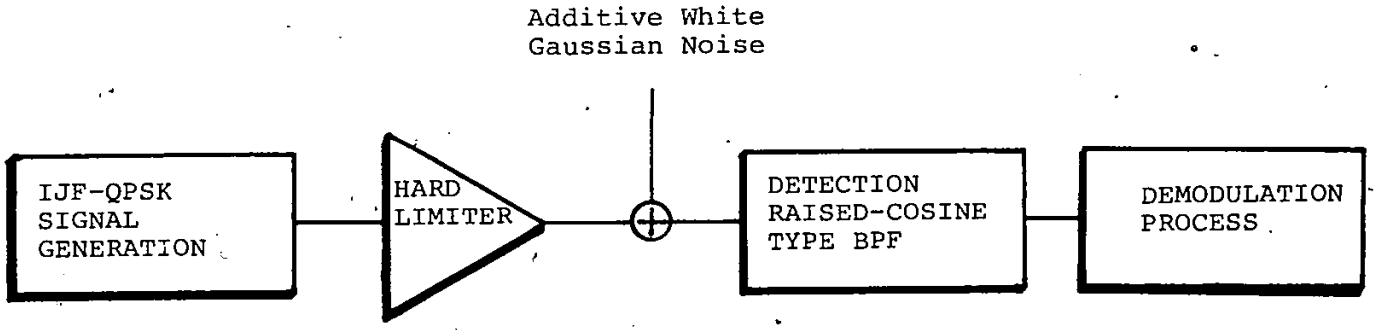

Fig. A.1: BLOCK DIAGRAM OF THE SIMULATION MODEL USED IN PROGRAM "SINGLE"

```
PROGRAM   SINGLE

      PROGRAM SINGLE(INPUT,OUTPUT,TAPE3,TAPE6=OUTPUT)
      COMPLEX DATA(2048),TF1(2048)
         COMPLEX DATA1(2048)
      DIMENSION PEI(25),EBNO(25),IPNI(128),IPNQ(128)
      DIMENSION IWK(12),PO(65),IPNI1(128),IPNQ1(128)
C
      REAL MP,MP1,MP2
C
C     INITIALIZE PROGRAM.
C
      DATA NSNR,NSYMB/25,127/
      DATA BAUD,LSAMPL,NRUNS,LDIM/60.,16,7,2048/
      DATA FBW1,FBW2,FBW3,FBW4/30.0,30.0,40.0,40.0/
      DATA ALPHA1,ALPHA2/0.0,0.4/

      DATA IOFF/0/


C

      OFF=FLOAT(IOFF)/FLOAT(LSAMPL)
C     END OF INITIALIZATION.
C
      PRINT 1
  1   FORMAT(5X,*SIMULATION OF IJF- QPSK ********************/)


      PRINT 12,ALPHA1
 12   FORMAT(5X,*THE COEFFICIENT ALPHA OF THE FILTER IS    = *,F3.1/
      WRITE(6,2)  OFF
2     FORMAT(5X,*OFFSET=*,F3.2,* T*)
      WRITE (6,6) BAUD,LSAMPL
  6   FORMAT(5X,*SYMBOL RATE:*,F7.2,* BAUD*/,
     +5X,I4,* SAMPLES PER SYMBOL*/)
C
C     START OF COMPUTATIONS.
      SBANDW=BAUD*LSAMPL
      CALL RCOS(SBANDW,FBW1,TF1,ALPHA1,LDIM,     FOF)
      CALL HHGG(TF1,PNOISE,LSAMPL,LDIM,SBANDW)
      CALL LOAD4(DATA,IPNI,IPNQ,LSAMPL,LDIM,     IOFF)
      CALL HLIM(DATA,LDIM)
      CALL ENERGY(DATA,EB,BAUD)
      CALL FILTER(DATA,TF1,LDIM)

C
      CALL DECOD4(DATA,LSAMPL,PNOISE,IPNI,IPNQ,
     =NSYMB,EBNO,PEI,NSNR,EB,IOFF)
      STOP
C*********************************
C       END OF MAIN PROGRAM.
C*********************************
      END
```

A.2.2 Simulation of a Multi-Channel Hardlimited IJF-Offset QPSK System

(a) Descriptions:

Program ACI simulates a multi-channel hardlimited IJF-Offset QPSK system. Figure A.2 shows the block diagram of the simulation model. The adjacent interfering signals, ACI No.1 and ACI No. 2, are also IJF-Offset QPSK signals. Attenuation is introduced in the adjacent channel paths to simulate the difference in received power between the desired and interfering channels. If the value of attenuation is negative, it means that the interfering channels have higher power than the desired channel.

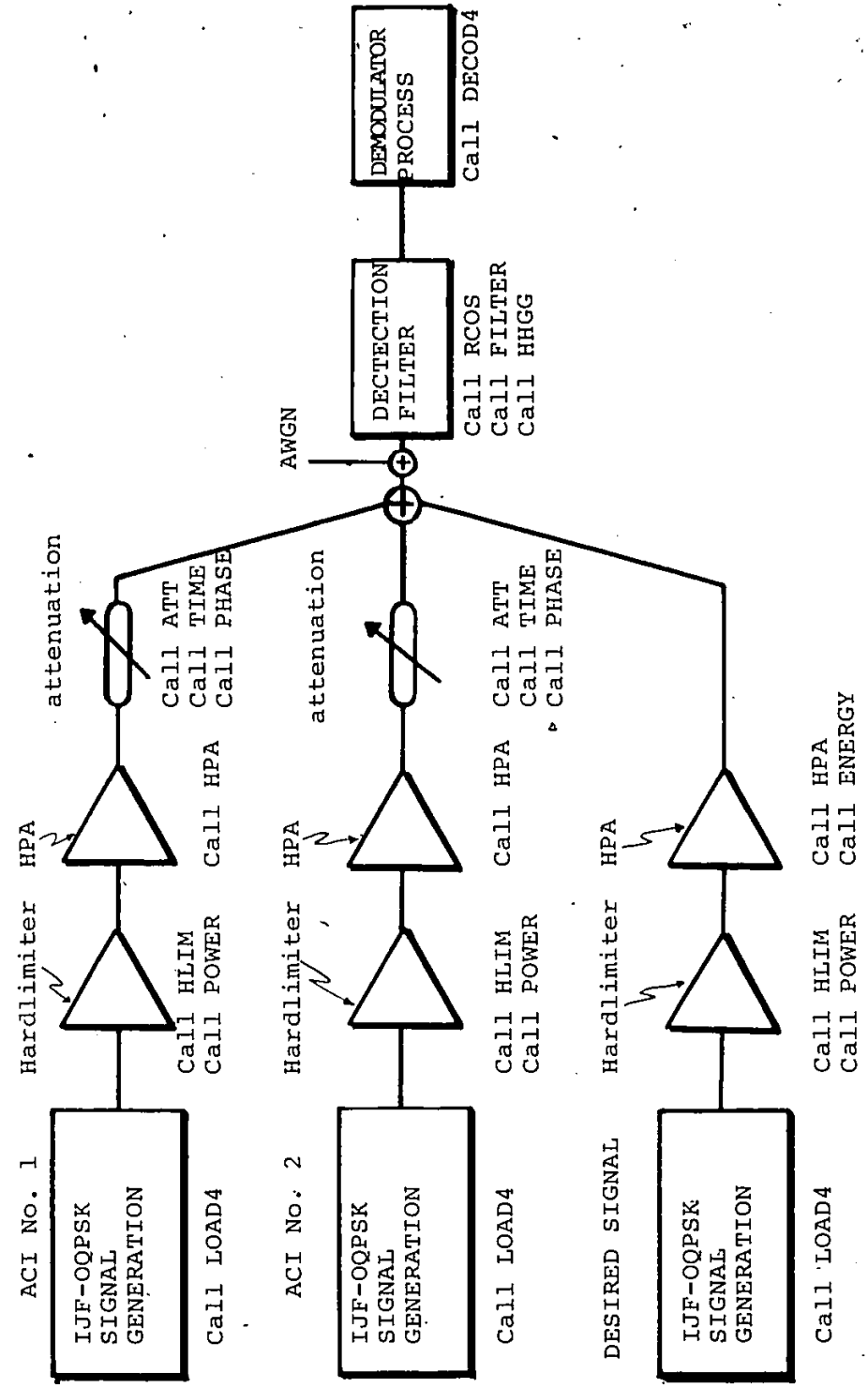

Fig. A.2: BLOCK DIAGRAM OF THE SIMULATION MODEL USED IN PROGRAM "ACI"

(b) Listing:

```
PROGRAM    ACI

      PROGRAM ACI(INPUT,OUTPUT,TAPE3,TAPE6=OUTPUT)
      COMPLEX DATA(2048),TF1(2048),TF2(2048),TF3(2048),TF4(2048)
         COMPLEX DATA1(2048)
      DIMENSION PEI(25),EHNO(25),IPNI(128),IPNQ(128)
      DIMENSION IWK(12),PO(65),IPNI1(128),IPNQ1(128)
C
      REAL MP,MP1,MP2
C
C     INITIALIZE PROGRAM.
C
      DATA NSNR,NSYMB/25,127/
      DATA BAUD,LSAMPL,NRUNS,LDIM/60.,16,5,2048/
      DATA FBW1,FBW2,FBW3,FBW4/30.0,30.0,40.0,40.0/
      DATA ALPHA1,ALPHA2/0.4,0.4/
      DATA BAKOFH,BAKOFT/0.0,2.0/
      DATA IOFF/8/
      DATA FOF,FOF1,FOF2/0.,70.0,-70.0/
      DATA PSHIF1,PSHIF2/1.7,3.14/
      DATA ITSH1,ITSH2/0,0/
C   INPUT THE VALUE OF N OF THE PULSE SHAPE
      DATA AT1,AT2/0.,0./
      DATA NNN/1/
      DO 501 KKK=1,1
      DO 500 KM=1,NRUNS
      SSS1=FLOAT(ITSH1)/(16.*.06)
      SSS2=FLOAT(ITSH2)/(16.*.06)
      ITSHI1=ITSH1+672
      ITSHI2=ITSH2+1344
      OFF=FLOAT(IOFF)/FLOAT(LSAMPL)
C     END OF INITIALIZATION.
C
      PRINT 1
    1 FORMAT(5X,*SIMULATION OF IJF-OQPSK **********************/)
      PRINT 11,NNN
   11 FORMAT(5X,*TYPE OF PULSE SHAPE    N = *,I1/)
      PRINT 12,ALPHA1
   12 FORMAT(5X,*THE COEFFICIENT ALPHA OF THE FILTER IS    = *,F3.1/
      WRITE(6,2)  OFF
    2 FORMAT(5X,*OFFSET=*,F3.2,* T*)
      WRITE (6,6) BAUD,LSAMPL
    6 FORMAT(5X,*SYMBOL RATE:*,F7.2,* BAUD*/,
     +5X,I4,* SAMPLES PER SYMBOL*/)
```

```
C       START OF COMPUTATIONS.
        SBANDW=BAUD*LSAMPL
        CALL RCOS(SBANDW,FBW1,TF1,ALPHA1,LDIM,      FOF)
        CALL RCOS(SBANDW,FBW1,TF2,ALPHA1,LDIM,      FOF1)
        CALL RCOS(SBANDW,FBW1,TF3,ALPHA1,LDIM,      FOF2)
        CALL HHGG(TF1,PNOISE,LSAMPL,LDIM,SBANDW)
        CALL LOAD4(DATA,IPNI,IPNQ,LSAMPL,LDIM,      IOFF)
        CALL HLIM(DATA,LDIM)
        CALL POWER(DATA,LDIM,MP1,PF)
        CALL HPA (DATA,LDIM,BAKOFH,PSHIFT,MP1)
        CALL ENERGY(DATA,EB,BAUD)
        CALL FILTER(DATA,TF1,LDIM)
        CALL POWER(DATA,LDIM,MP,PF)
        CALL LOAD4(DATA1,IPNI1,IPNQ1,LSAMPL,LDIM,      IOFF)
        CALL HLIM(DATA1,LDIM)
        CALL POWER(DATA1,LDIM,MP1,PF)
        CALL HPA(DATA1,LDIM,BAKOFH,PSHIFT,MP1)
        CALL FILTER(DATA1,TF2,LDIM)
        CALL PHASE(DATA1,PSHIF1,LDIM)
        CALL TIME(DATA1,ITSHI1,LDIM)
        CALL ATT(DATA1,AT1,LDIM)
        CALL POWER(DATA1,LDIM,MP1,PF1)
        DO 10 I=1,LDIM
10      DATA(I)=DATA1(I)+DATA(I)
C*******************************************************
        CALL LOAD4(DATA1,IPNI1,IPNQ1,LSAMPL,LDIM,      IOFF)
        CALL HLIM(DATA1,LDIM)
         CALL POWER(DATA1,LDIM,MP2,PF)
         CALL HPA(DATA1,LDIM,BAKOFH,PSHIFT,MP2)
C
        CALL FILTER(DATA1,TF3,LDIM)
        CALL PHASE(DATA1,PSHIF2,LDIM)
        CALL TIME(DATA1,ITSHI2,LDIM)
        CALL ATT(DATA1,AT2,LDIM)
        CALL POWER(DATA1,LDIM,MP2,PF2)
        DO 20 I=1,LDIM
 20     DATA(I)=DATA(I)+DATA1(I)
```

```
      ACI1=10.*ALOG10(MP/MP1)
      N=1
      PF1=PF1-3.0
      PF2=PF2-3.0
      ACI2=10.*ALOG10(MP/MP2)
      WRITE(6,3) N,FOF1,PSHIF1,SSS1,AT1,ACI1,PF1
      N=2
      WRITE(6,3) N,FOF2,PSHIF2,SSS2,AT2,ACI2,PF2
3     FORMAT(///,2X,*CHANNEL *,I1,* CHARACTERISTICS*//,2X,
     +*OFFSET FREQ.: *,F5.1,* MHZ*,*   OFFSET+PHASE*,F6.3,* RAD*,
     +/*   TIME OFFSET:  *,F6.2,* NS   ATTENUATION:*,F4.1,* DB*,
     +/*   CARRIER TO INT. RATIO: *,F5.1,* DB*,* PF: *,F5.1,* DB*)
C
C
C
      CALL PHASE(DATA,PSHIFT,LDIM)
      DO 45 I=1,LDIM
45     DATA1(I)=DATA(I)

      CALL DECOD4(DATA,LSAMPL,PNOISE,IPNI,IPNQ,
     =NSYMB,EBNO,PEI,NSNR,EB,IOFF)
C
       FOF1=FOF1+10.
       FOF2=FOF2-10.
500    CONTINUE
      AT2=AT2-1.
      AT1=AT1-1.
501   CONTINUE
      STOP
C*******************************
C       END OF MAIN PROGRAM.
C*******************************
      END
```